

**Central and peripheral mechanisms:
a multimodal approach to understanding and restoring
human motor control**

Présentée le 24 septembre 2020

à la Faculté des sciences et techniques de l'ingénieur
Chaire Fondation Bertarelli en neuro-ingénierie translationnelle
Programme doctoral en génie électrique

pour l'obtention du grade de Docteur ès Sciences

par

Nawal Noëlle KINANY

Acceptée sur proposition du jury

Prof. D. Ghezzi, président du jury
Prof. S. Micera, Prof. D. N. A. Van De Ville, directeurs de thèse
Prof. R. Barry, rapporteur
Prof. E. Ricciardi, rapporteur
Prof. F. Hummel, rapporteur

Abstract

All human actions involve motor control. Even the simplest movement requires the coordinated recruitment of many muscles, orchestrated by neuronal circuits in the brain and the spinal cord. As a consequence, lesions affecting the central nervous system, such as stroke, can lead to a wide range of motor impairments. While a certain degree of recovery can often be achieved by harnessing the plasticity of the motor hierarchy, patients typically struggle to regain full motor control. In this context, technology-assisted interventions offer the prospect of intense, controllable and quantifiable motor training. Yet, clinical outcomes remain comparable to conventional approaches, suggesting the need for a paradigm shift towards customized knowledge-driven treatments to fully exploit their potential. In this thesis, we argue that a detailed understanding of healthy and impaired motor pathways can foster the development of therapies optimally engaging plasticity. To this end, we develop and apply multimodal methodologies to investigate the central and peripheral mechanisms underlying motor control and recovery.

In the first part of this work, we concentrate on the transition from *one-suits-all* approaches to *patient-tailored* protocols, in the context of robot-assisted rehabilitation. We start addressing this question from a technical viewpoint and propose methods to assess individual dynamics of recovery in stroke patients. First, we demonstrate the applicability of a model-based approach to continuously personalize training based on kinematic motor improvement. Then, we show how complementary knowledge can be gleaned from kinematics, muscular and neural signals, and we introduce a versatile framework to distill this multimodal information into a set of clinically relevant variables. These results highlight the pivotal importance of multimodality, stressing the need for a comprehensive view of the human motor hierarchy.

To this end, the second part of this work focuses on the spinal cord, whose functional properties remain largely unexplored in humans. As this gap of knowledge primarily pertains to the dearth of non-invasive methods to assess its function *in vivo*, we first propose a pipeline for spinal cord functional magnetic resonance imaging (fMRI) and demonstrate its ability to capture cervical activation patterns during upper limb movements. We then present a dynamic functional connectivity framework to dissect spinal spontaneous fluctuations into fine-grained components mirroring neuroanatomical and physiological principles. Next, we extend the use of this approach to fMRI data acquired in the entire neural axis during motor sequence learning, hence shedding light on specific cortical, subcortical and spinal correlates of skill acquisition and consolidation. Finally, we glimpse into the implementation of these methodologies in the scope of translational applications, providing evidence of their potential to explore spinal plasticity following stroke.

These findings are a valuable contribution towards an extensive characterization of human motor control. This system-level view deepens our understanding of motor pathways, fully acknowledging the active and plastic nature of the spinal cord and emphasizing its key role in sensorimotor

functions. We envision that the synergy between technology and knowledge will open promising avenues for strategies leveraging each patient's residual function to optimize clinical outcome.

Keywords: human motor control, spinal cord, functional magnetic resonance imaging, dynamic functional connectivity, neurotechnology, neurorehabilitation, stroke

Résumé

Le contrôle moteur est au centre de chacune de nos actions. Même le plus simple mouvement nécessite l'activation coordonnée de multiples muscles, orchestrée par les circuits neuronaux du cerveau et de la moelle épinière. Par conséquent, les lésions affectant le système nerveux central, telles que les accidents vasculaires cérébraux, amènent un éventail de déficits moteurs. Bien que la plasticité du système moteur permette un certain degré de récupération, la plupart des patients ne parviennent pas à récupérer leur motricité initiale. Dans ce contexte, des technologies innovantes, appliquées à la rééducation, laissent entrevoir le potentiel de traitements intenses, contrôlés et quantifiables. Malgré ces avantages, les résultats restent actuellement similaires à ceux obtenus avec un entraînement conventionnel. Afin de pouvoir pleinement exploiter le potentiel de ces technologies, il apparaît dès lors primordial d'évoluer vers une approche personnalisée, prenant en compte les spécificités de chaque patient. Dans cette thèse, nous soutenons qu'une compréhension détaillée du système moteur humain peut favoriser le développement de nouvelles thérapies mettant efficacement à profit la neuroplasticité. Dans ce but, nous développons et évaluons des méthodologies multimodales afin d'étudier les mécanismes centraux et périphériques du contrôle moteur, ainsi que leurs possibles dysfonctionnements.

En premier lieu, nous proposons des méthodes permettant de capturer des dynamiques individuelles de récupération motrice, afin d'appuyer la transition vers des protocoles adaptés à chaque patient, dans le contexte de rééducations robotisées. Dans une première étude, nous démontrons l'efficacité d'une approche modélisant l'amélioration motrice grâce à des données cinématiques, ainsi que sa capacité à personnaliser l'entraînement en conséquence. Ensuite, nous soulignons la complémentarité des informations obtenues grâce à d'autres modalités, telles que des signaux musculaires ou neuronaux. Nous présentons un cadre d'analyse permettant de combiner ces informations multimodales afin de caractériser de manière synthétique l'état neuro-moteur et mécanique de chaque patient.

Afin de parvenir à une évaluation exhaustive de cet état, il est néanmoins primordial d'y intégrer la moelle épinière, jusqu'alors peu explorée chez l'humain. Cette méconnaissance s'explique notamment par le manque de méthodes visant à évaluer sa fonction *in vivo*. Ainsi, nous établissons d'abord un protocole d'imagerie fonctionnelle par résonance magnétique ciblant la moelle épinière, dont nous validons la capacité à détecter l'activité cervicale liée à des mouvements du membre supérieur. Par la suite, nous nous intéressons à la fonction spinale au repos, mettant en lumière son caractère dynamique. Nous proposons une méthodologie d'analyse détaillée de ses fluctuations et de leurs propriétés neuroanatomiques. Notamment, l'extension de cette approche à l'ensemble du système nerveux central nous permet d'identifier des changements fonctionnels spécifiquement associés à l'apprentissage moteur. Pour finir, nous donnons un aperçu des applications cliniques de ces méthodologies, suggérant leur potentiel pour explorer la neuroplasticité découlant d'un accident vasculaire cérébral.

Ces études permettent d'évoluer vers une vision globale des mécanismes du contrôle moteur. Grâce à cette approche multimodale, reconnaissant l'importance de la moelle épinière, nous espérons pouvoir atteindre une meilleure compréhension des circuits impliqués dans la récupération motrice, en vue du développement de nouvelles thérapies ciblées.

Mots-clés: contrôle moteur humain, moelle épinière, imagerie fonctionnelle par résonance magnétique, connectivité dynamique fonctionnelle, neurotechnologies, neurorééducation, accident vasculaire cérébral

Acknowledgements

First and foremost, I would like to express my deepest gratitude to my thesis advisors, Prof. Silvestro Micera and Prof. Dimitri Van De Ville, for giving me the opportunity to carry out this exciting interdisciplinary project. Thank you for your supervision, your kindness and your trust. I am particularly grateful for the freedom you gave me throughout these years, which helped me grow as a scientist and develop my own research.

A very special thanks to Elvira, for being a mentor and a friend, who supported me from the very beginning and through all the steps of my PhD (and beyond!). Working with you has always been a pleasure, and this thesis would clearly not be the same without your continuous guidance, your never-ending energy and your countless ideas.

I would also like to thank Prof. Julien Doyon, for welcoming me in his lab, for giving me this chance to work with unique datasets, and for sharing his valuable experience. Thanks as well to all members from his group, it was great to be a part of your team!

Then, I would like to recognize the precious assistance provided by Loan Mattera and Roberto Martuzzi, who helped me find my way through the challenges of spinal cord fMRI, so that we could establish the protocols presented in this thesis.

A huge thanks to my fellow labmates in the TNE and the MIPLAB, I feel very lucky to have had you around! Thanks for the stimulating discussions, the coffee breaks, the travels and for all the nice times we had during these years. It was great sharing the ups and downs of the PhD life with you all, and I really hope this is not the end of our adventures together, in this part of the world or another!

Finally, I am deeply thankful to my friends and family, who supported me in this journey. Thanks for believing in me, for all the fun, all the discussions and all the joy that you bring to my life! A particular thanks to my brother, Soufyane, for being such an amazing person and for always being by my side.

Contents

Abstract.....	i
Résumé.....	iii
Acknowledgements.....	v
Contents.....	vii
List of abbreviations.....	x
Chapter 1 Introduction	1
1.1 Human motor control	2
1.2 Neuromotor disorders and rehabilitation	4
1.3 Exploring brain mechanisms	6
1.4 Exploring peripheral mechanisms	8
1.5 The missing link: the spinal cord	9
1.6 Outline of the thesis.....	13
PART I Towards personalized rehabilitation	15
Chapter 2 Kinematic-based personalization	17
2.1 Introduction	18
2.2 Methods	20
2.3 Results	27
2.4 Discussion	35
2.5 Conclusion.....	39
Chapter 3 Multimodal framework	41
3.1 Introduction	42
3.2 Methods	43
3.3 Results	52
3.4 Discussion	58
3.5 Conclusion.....	61

Summary and outlook.....	63
PART II Bridging the gap between the brain and the periphery	65
Chapter 4 Towards a pipeline for spinal cord fMRI	67
4.1 Introduction.....	67
4.2 Methods	68
4.3 Results.....	73
4.4 Discussion.....	77
4.5 Conclusion	79
Chapter 5 Motor output and spinal activity	81
5.1 Introduction.....	82
5.2 Methods	83
5.3 Results.....	90
5.4 Discussion.....	96
5.5 Conclusion	99
Chapter 6 Spinal cord's functional architecture	101
6.1 Introduction.....	101
6.2 Methods	103
6.3 Results.....	108
6.4 Discussion.....	114
6.5 Conclusion	118
Chapter 7 Cerebro-spinal dynamics of motor learning	119
7.1 Introduction.....	119
7.2 Methods	120
7.3 Results.....	125
7.4 Discussion.....	131
7.5 Conclusion	136
Chapter 8 Clinical applications of spinal cord fMRI	137
8.1 Introduction.....	137
8.2 Methods	138
8.3 Results.....	140
8.4 Discussion.....	143
8.5 Conclusion	145
Summary and outlook.....	146
Chapter 9 General conclusion.....	148

9.1	Summary and discussion.....	148
9.2	Perspectives	151
A.	Supplementary material for Chapter 2.....	155
B.	Supplementary material for Chapter 3.....	161
C.	Supplementary material for Chapter 5.....	163
D.	Supplementary material for Chapter 6.....	167
E.	Supplementary material for Chapter 7.....	173
F.	Supplementary material for Chapter 8.....	175
	References.....	177
	Curriculum vitae	208

List of abbreviations

General

3D	3-dimensional
ALE _x	arm light exoskeleton
ALFF	amplitude of low frequency fluctuations
ANOVA	Analysis of variance
BOLD	blood oxygenation level-dependent
CDF	cumulative distribution function
CSF	cerebrospinal fluid
CNS	central nervous system
dFC	dynamic functional connectivity
DOF	degrees of freedom
EEG	electroencephalography
EPI	echo-planar imaging
FC	functional connectivity
FD	framewise displacement
FM/FMA	Fugl-Meyer assessment
FOV	field-of-view
EMG	electromyography
fMRI	functional magnetic resonance imaging
FWHM	full width half maximum
GE	gradient-echo
GLM	general linear model
GM	grey matter
HRF	hemodynamic response function
ICA	independent component analysis
iCAP	innovation-driven co-activation pattern
MAS	Modified Ashworth Scale
MI	motor improvement
MNI	Montreal Neurological Institute
MRI	magnetic resonance imaging
MN	motoneuron
MS	multiple sclerosis
NNMF	non-negative matrix factorization
PCA	principal component analyses
PD	Parkinson's disease
ROI	region of interest

RS	resting-state
RSN	resting-state networks
SCI	spinal cord injury
SD	standard deviation
SE / SEM	standard error of the mean
SNR	signal-to-noise ratio
SVD	singular value decomposition
TA	total activation
TE	echo time
TR	repetition time
tSNR	temporal signal-to-noise ratio
VAF	variance accounted for
WM	white matter

Brain and muscles

ABDM	abductor digiti minimi
ACC	anterior cingulate cortex
ADPT	adductor pollicis transversus
BIC(S/L)	biceps brachii short/long head
BRA	brachialis
BRAD	brachioradialis
DANT	deltoid anterior
DMED	deltoid medialis
DPOS	deltoid posterior
EXCL	extensor carpi radialis longus
EXCU	extensor carpi ulnaris
EXDC	extensor digitorum communis
EXPB	extensor pollicis brevis
FLCR	flexor carpi radialis
FLCU	flexor carpi ulnaris
FLDS	flexor digitorum superficialis
FLPB	flexor pollicis brevis
INFRA	infraspinatus
LAT	latissimus dorsi
M1	primary motor cortex
PEC	pectoralis major
PRO	pronator teres
S1	primary somatosensory cortex
TRILAT	lateral head of triceps brachii
TRILONG	long head of triceps brachii
TRAPM	medial trapezius
TRAPS	superior trapezius

Chapter 1 Introduction

The human motor system relies on the dynamic interplay between multiple organs distributed throughout the body (Baker *et al.*, 2015). Briefly, motor commands from different brain regions travel down to spinal circuits, where active integration of sensorimotor information continuously ensures accurate movement execution through the coordinated activation of multiple muscles (Arber and Costa, 2018). This sophisticated arrangement of subsystems is capable of generating an impressive variety of motor behaviors. Nonetheless, its dispersed organization leaves it particularly fragile against imbalance, as damages can potentially occur at many levels of the circuitry. Among the disorders that can perturb this exquisite machinery, neurological conditions impairing the central nervous system (CNS) occupy a prominent place, as they affect the life of millions of people worldwide every year (Feigin *et al.*, 2017). The associated physical consequences are numerous, ranging from sensory to motor impairments affecting several parts of the body. Patients may experience difficulties in performing voluntary movements, or even complete paralysis, hence significantly affecting their life and reducing their independence.

Yet, the dispersed nature of the motor system also confers it a considerable capacity of resilience. Regaining a certain degree of motor function can be achieved through spontaneous recovery or facilitated by a rehabilitation process. The conventional view suggests that an efficient training should start as early as possible and actively engage patients in an intensive and goal-directed manner (Feys *et al.*, 2004; Kwakkel *et al.*, 2004; Kwakkel, 2006; Buma *et al.*, 2013). The final aim of such approaches is to stimulate neuroplasticity, the innate ability of the nervous system to reorganize its connections and to use secondary pathways to bypass damaged circuits (Rossini *et al.*, 2003; Winstein and Kay, 2015).

In the last decades, innovative neurorehabilitative treatments such as technology-assisted therapies have emerged (Micera *et al.*, 2020). By allowing therapy to be given over longer periods of time and in a more reproducible manner, they aim to optimally engage the remaining neural pathways in order to promote better and faster recovery. Regardless of those developments, recovering from a neurological condition is still very challenging and most patients struggle to translate their improvements to activities of daily living (Winstein and Kay, 2015). For instance, following a stroke, 80% of patients experience acute paresis of the upper extremity and only approximately one-third achieve full functional recovery (Lawrence *et al.*, 2015). One of the limitations of the current rehabilitative approaches could stem from the lack of personalization. Indeed, treatments are often provided in a standardized manner and the adjustment of the task is based solely on the therapist's evaluation, relying mainly on kinematics and task performance.

In this regard, a better understanding of the mechanisms underlying motor recovery is pivotal to further improve existing therapies and to foster the development of novel rehabilitative treatments (Buma *et al.*, 2013). This requires to focus on the neural and muscular processes involved in healthy

and impaired motor function and to integrate this multimodal information in order to design new tailored treatments based on the specific neuro-biomechanical state of each patient. Therapeutic approaches could, thus, leverage new knowledge on residual function, in order to optimally promote reorganization of the spared connections and networks.

Importantly, it is necessary to characterize not only the underlying cortico-muscular processes, but the whole path of events that occur from the generation of motor commands in the brain, to the activation of motoneurons in the spinal cord, and to the actual execution of the movement. In this context, it is necessary to go beyond an encephalo-centered view of motor control and to recognize the spinal cord as an active and plastic part of the central nervous system, considering its unequivocal importance as the final common pathway of the musculoskeletal system (Giszter *et al.*, 2012). Accordingly, new exploration should focus on its central role in human sensorimotor function, as well as on its integration with cerebral circuits. To this end, neuroimaging approaches, such as functional magnetic resonance imaging (fMRI), can provide valuable insights into the dynamics of motor recovery and the reorganization of spared neural circuits to subserve improvements in function (Grefkes and Fink, 2014).

In the following, I will first give an overview of the principles underlying healthy human motor control. Then, I will elaborate on the nature of neurological disorders impairing motor circuits, along with considerations on recovery and rehabilitation, placing the emphasis on stroke. In this context, the factors limiting the clinical efficiency of rehabilitative treatments will be highlighted. Finally, I will introduce techniques that could foster our understanding of the central and peripheral mechanisms involved in healthy and impaired motor control. Here, a strong focus will be put on approaches aiming to probe spinal cord function.

1.1 Human motor control

Motor actions are associated with almost all human behaviors, from simple everyday tasks such as picking up a glass, to fine skilled movements involved, for instance, in piano performance. Even the most seemingly trivial task actually requires the precise and coordinated regulation of muscle activities (Levine *et al.*, 2012). In this context, all levels of the central nervous system, from cortical to spinal networks, are dynamically interacting to ensure the vast repertoire of human behaviors (Nielsen, 2016) (Figure 1.1).

Brain mechanisms: In the brain, it is now widely accepted that several areas contribute to distinct aspects of movement generation (Lemon, 2008; Feher, 2012; Miall, 2013). The primary motor cortex (M1) is directly involved in eliciting motor commands associated with voluntary movements, but other cortical areas also play important roles. The premotor cortex (PMC) and supplementary motor area (SMA) are participating in movement planning, while the posterior parietal cortex (PPC) provides spatial information about the body and the surrounding environment (Miall *et al.*, 2004). Upper motoneurons originating in these motor regions give rise to the pyramidal tract, a descending pathway carrying motor-related signals from the cortex to the brainstem and the spinal cord. Its main component is the corticospinal tract (CST), which first descends through the brainstem, where its fibers divide into two subpathways: 80% decussate to the opposite side of the body (lateral corticospinal tract), while the remaining fibers continue to travel down along the same side (anterior corticospinal tract) and only decussate in the spinal cord (Welniarz *et al.*, 2017). Importantly, decussation implies that muscles are controlled by the contralateral side of the brain.

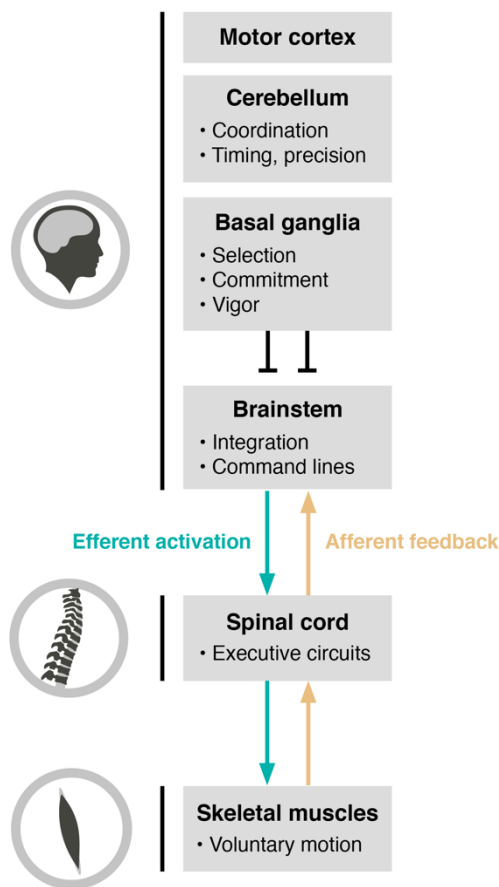


Figure 1.1 – Schematic view of the systems and pathways underlying human motor control. Adapted with permission from Arber and Costa, 2018.

Of note, other brainstem-mediated descending pathways exist (e.g., reticulospinal tract) and they are mainly involved in involuntary movements, such as postural control or balance. Although sub-cortical structures, such as the basal ganglia, do not directly participate in generating voluntary motor commands, they play a dominant role in controlling if, and how intensely, these commands should be activated under specific circumstances (Arber and Costa, 2018). Similarly, the cerebellum is engaged in timing motor commands, notably by adjusting movement based on sensory feedback so as to ensure proper limb coordination (Manto *et al.*, 2012).

Spinal mechanisms: The signals originating from cortical areas travel down the corticospinal tract and project to different levels of the spinal cord. Corticospinal neurons can make direct monosynaptic connections to lower motoneurons located in the ventral horns of the spinal cord grey matter or, alternatively, indirect connections through interneurons (Lemon, 2008; Nielsen, 2016) (see 1.5.1). The axons of spinal motoneurons innervate muscle fibers, hence sending electrical impulses that activate skeletal muscles (Barbara and Clarac, 2011). Sensory neurons, instead, are found in the dorsal horns and convey information from the periphery to supraspinal structures. Although motor and sensory spinal circuits may seem to act as a mere relay, the striking complexity of their intrinsic organization is slowly being unravelled (Poppele and Bosco, 2003; Giszter *et al.*, 2012; Arber and Costa, 2018). This sophisticated circuitry enables the integration of the stream of motor commands from supraspinal structures with continuous information from the periphery, so as to

produce goal-directed behaviors adapted to the specificities of the immediate environment (Wolpert and Ghahramani, 2000; Christiansen *et al.*, 2017). In particular, spinal interneuron circuits are actively involved in processing sensory and supraspinal inputs into motoneuron outputs (Levine *et al.*, 2012; Baker *et al.*, 2015). For instance, their complex connection patterns appear to perform substantial intrinsic processing to support hand dexterity (Takei and Seki, 2010; Takei *et al.*, 2017; Tohyama *et al.*, 2017).

Peripheral mechanisms: Voluntary movements are mediated by motor units, which are the functional elements involved in muscle contraction. A motor unit corresponds to a lower motoneuron together with the muscle fibers it innervates (Feher, 2012). Of note, skeletal muscles contain two types of fibers: extrafusal fibers, which are responsible for the majority of muscle power, and intrafusal fibers, which have a limited contractile power but provide afferent sensory feedback related to stretch. The arrangement of motoneurons along the spinal cord exhibit specific organizational principles with respect to the targeted muscles, with an orderly spatial arrangement, termed musculotopic map (Romanes, 1964; Levine *et al.*, 2012). In particular, different muscles are innervated by different spinal levels, located at distinct rostrocaudal positions along the spinal cord. For instance, motor pools involved in biceps contraction are located more rostrally than the ones linked to wrist muscles (Kendall *et al.*, 2005).

In summary, the coordinated action of distinct structures, from the brain to the periphery, supports the wide range of movements we readily learn and perform in our everyday lives. Yet, this smooth and complex machinery, by its distributed nature, appears vulnerable to damages, notably those occurring at different levels of the CNS (Baker *et al.*, 2015). From focal brain injury to spinal cord trauma, a wide range of conditions can indeed affect neural structures and, consequently, perturb motor control (Dobkin, 2009) (Figure 1.2).

1.2 Neuromotor disorders and rehabilitation

Lesions associated with cerebrovascular accidents, such as strokes, can result in tissue loss in cerebral regions. About 70% of stroke survivors are affected by chronic motor impairments (Lawrence *et al.*, 2015) that can substantially limit their ability to perform activities of daily living. Consequences range from loss of muscle strength or sensation, limited selectivity in muscle recruitment, velocity-dependent spasticity, to paralysis (Buma *et al.*, 2013). Due to the aging of the population, coupled with an increased incidence of stroke in young people in low- and middle-income countries, this impact is likely to increase considerably in the coming years (Katan and Luft, 2018; Gorelick, 2019). While stroke is a leading cause of adult long-term disabilities worldwide, other neurological disorders can perturb or interrupt the pathways through which motor commands generate movements. For instance, traumatic events such as spinal cord injuries (SCI) (Ahuja *et al.*, 2017), as well as neurodegenerative diseases, such as Parkinson's disease (PD) (Poewe *et al.*, 2017) or multiple sclerosis (MS) (Filippi *et al.*, 2018), can also lead to sensorimotor deficits having devastating impacts on patients' ability to voluntarily control movement. As such, neurological disorders constitute an enormous social and economic burden and recovery represents a major challenge for our society.

In this context, the distributed character of motor systems can be harnessed, as alternative routes can emerge to overcome motor-related disruptions and restore movement (Baker *et al.*, 2015). In general, the term *recovery* encompasses mechanisms leading to "true" recovery (i.e., a restitution of function) and mechanisms involved in compensation (i.e., relying on adaptation, for instance using alternate muscle groups) (Zeiler and Krakauer, 2013). Although spontaneous recovery can rely

on these mechanisms, it is often insufficient to regain full function. Besides, neurological changes might also lead to unwanted behavior (e.g., spasticity) (Baker *et al.*, 2015).

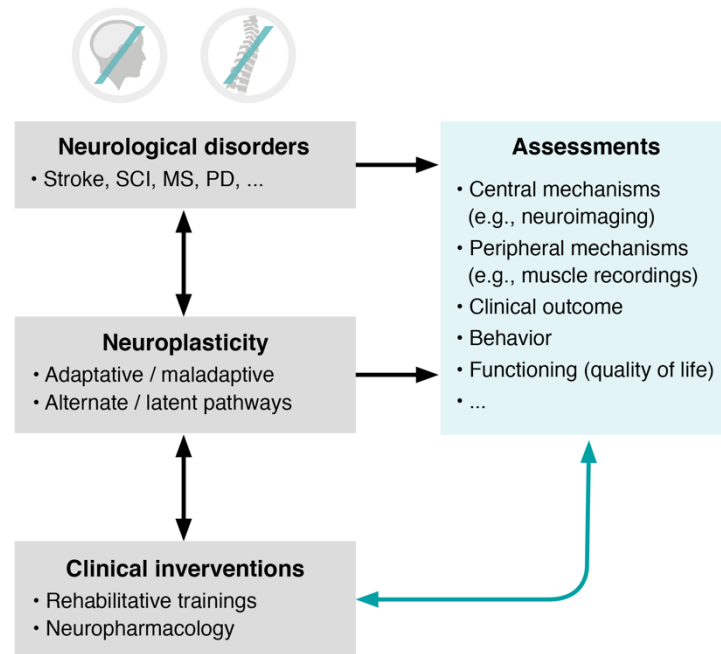


Figure 1.2 – Conceptual overview of the interplay between neurological disorders, neuroplasticity, clinical interventions and assessments of function. Inspired from (Cramer *et al.*, 2011).

Rehabilitation, therefore, should help enhance recovery in order to maximize the regaining of motor control while minimizing maladaptive compensatory strategies (Dobkin, 2009). To this end, rehabilitative treatments capitalize on plasticity, a fundamental ability of neuronal circuits to adapt in response to experience or training (Figure 1.2) (Cramer *et al.*, 2011). Although pathophysiological processes underlying neurological disorders can differ, neuroplasticity is a crucial factor to tackle loss of CNS tissue and the associated sensorimotor deficits (Dobkin, 2009). It comprises synaptic changes, axonal sprouting and changes of intracellular properties and can take place at different levels of the CNS (i.e., cortex, brainstem and spinal cord) (Fouad and Tse, 2008; Murphy and Corbett, 2009; Demarin *et al.*, 2014). In particular, recent reports have suggested that spinal plasticity can contribute to post-stroke recovery (Sist *et al.*, 2014; Tennant, 2014). For instance, sprouting of axons from the contralesional motor cortex into the spinal cord was shown in rodent models (Reitmeir *et al.*, 2011; Ueno *et al.*, 2012). While the importance of the corticospinal tract integrity has been widely acknowledged in humans (Ward *et al.*, 2006; Zhu *et al.*, 2011; Puig *et al.*, 2013; Maraka *et al.*, 2014; Karbasforoushan *et al.*, 2019), the spatial and temporal properties of spinal rewiring remain largely unexplored (Tennant, 2014). Nevertheless, engaging spinal cord plasticity could play a major role in function restoration following neurological disorders (Wolpaw, 2012).

In recent years, numerous approaches relying on technology have been proposed to facilitate neuroplasticity (Micera *et al.*, 2020). Neurotechnologies can potentially be leveraged to specifically target central and peripheral motor systems, in a way that will optimally engage functional reorganization and lead to adaptive changes supporting recovery (Figure 1.2). In the framework of stroke rehabilitation, different interventions have been suggested to deliver treatment or training in a controlled way (Coscia *et al.*, 2019). Among those approaches, non-invasive brain stimulation can be

deployed to modulate brain function, most commonly using transcranial magnetic stimulation (TMS) or transcranial direct-current stimulation (tDCS) (Hummel and Cohen, 2006). Various parameters (e.g., location, stimulus intensities, duration, etc.) can be tuned to induce changes in neuronal excitability at the sites of stimulation with the aim to efficiently steer neuroplasticity (Morishita and Hummel, 2017). While these methods directly target the central nervous system, other neurotechnologies, instead, act at the peripheral level to promote use-dependent plasticity (Coscia *et al.*, 2019). Evidence from animal and human studies suggests that plasticity is most efficiently harnessed when goal-directed training is performed early and intensively (Cramer *et al.*, 2011). For instance, technology-assisted rehabilitation can exploit robotic devices to allow therapy to be given over longer periods of time, in a more reproducible manner, while quantitatively monitor patient's improvement (Reinkensmeyer and Boninger, 2012). Several categories of robotic devices can be used, from end-effector devices to exoskeletons enabling control at the level of each individual joint (Colombo *et al.*, 2017). Besides, different control strategies are available to adapt training and severely affected patients can benefit from an active support provided by the robot, while challenge can be increased with resistance or error-augmentation when necessary (Marchal-Crespo and Reinkensmeyer, 2009).

Although these technology-based approaches have emerged as promising tools to improve rehabilitation, their clinical impact has so far been relatively limited, suggesting that a paradigm shift is essential to fully exploit their potential (Micera *et al.*, 2020). The main limitation hindering clinical improvement likely pertains to the *one suits all* strategy that is commonly employed, with rehabilitation being provided in a standardized manner. In this regard, neurotechnologies should be better optimized and personalized to meet each patient's individual needs and abilities (Borton *et al.*, 2013; Raffin and Hummel, 2018; Micera *et al.*, 2020). Alternatively, clinical outcome could be enhanced thanks to the coordinated combination of multiple therapies (Coscia *et al.*, 2019; Micera *et al.*, 2020). However, further progress towards patient-tailored strategies requires a comprehensive understanding of the mechanisms underlying functional and clinical recovery (Cramer *et al.*, 2011). Not only such knowledge could help stratify patients towards specific treatments (or combinations of treatments), it could also be harnessed to inform parameter selection, hence fine-tuning rehabilitation to substantially improve long-term outcome (Figure 1.2).

Therefore, overcoming the challenges hampering recovery implies efforts to better understand and manipulate motor circuits, so that they can be optimally engaged to compensate for injury-induced loss of function (Murphy and Corbett, 2009). It is thus of primary importance to investigate how peripheral and central mechanisms contribute to motor control and recovery.

1.3 Exploring brain mechanisms

In order to probe brain function, non-invasive recordings can be deployed and can offer valuable insights into cerebral mechanisms in healthy and impaired individuals.

1.3.1 Brain fMRI

Since its development in the 90s, functional magnetic resonance imaging (fMRI) has been widely used to non-invasively monitor brain activity (Poldrack *et al.*, 2011). This technique relies on changes in blood oxygenation following neural activity, yielding a measurable signal called the blood oxygenation level dependent (BOLD) signal. Upon local neural activation, blood flow carrying oxygenated hemoglobin increases to meet the metabolic demand in this particular region (Figure 1.3). Only a partial amount of this oxygen is actually consumed, leading to a temporary increase of

oxygenated hemoglobin compared its deoxygenated form. This relation between the neural activity and the cerebral blood flow is termed neurovascular coupling (Attwell *et al.*, 2010). Importantly, hemoglobin has different magnetic properties depending on its state (i.e., diamagnetic, as most of the brain tissues, when it is oxygenated and paramagnetic when it is deoxygenated) (Linus and Coryell, 1936). As a result, deoxygenated hemoglobin is more attracted to magnetic fields, resulting in B0 inhomogeneities when placed in an MRI scanner. This affects T2* relaxation, since the magnetization of paramagnetic molecules will decay faster, resulting in less signal where the concentration of deoxygenated hemoglobin is higher (Arthurs and Boniface, 2002). These processes imply that the BOLD signal is much slower than the actual neural activity. Specifically, it can be described using the hemodynamic response function (HRF) (Poldrack *et al.*, 2011), whose main peak occurs approximately after 5 seconds post-stimulus, before slowly returning back to baseline. Typically, fMRI scans cover the entire brain with a spatial resolution at the scale of millimeter and a temporal repetition of 1-3 seconds.

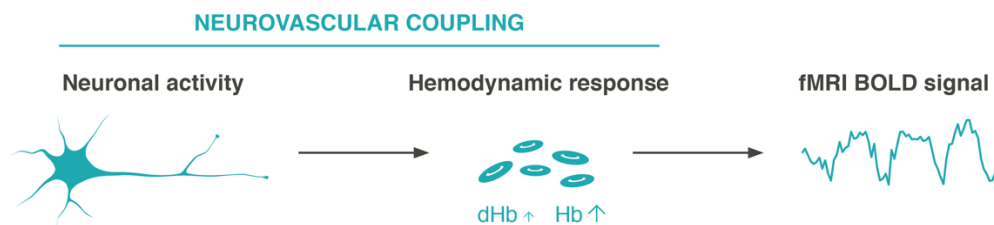


Figure 1.3 – Neuronal activity leads to an increased energy demand. Blood flow increases to carry oxygenated hemoglobin (Hb), which results in a temporary increase of Hb compared to the deoxygenated form (dHb). As these two molecules have different magnetic properties, it generates a detectable signal change, used to measure the BOLD signal.

Although most fMRI studies have initially focused on the observation of brain activity following a stimulation (i.e., task-based fMRI), it was demonstrated in 1995 that the brain maintains meaningful functional activity even when no task is actively performed (Biswal, 2012). Indeed, the brain consists of spatially distributed, but functionally linked regions, undergoing long-range interactions (Van Den Heuvel and Hulshoff Pol, 2010). Resting-state functional connectivity (RSFC) can be described as the coherent activation of those anatomically distinct brain regions. Resting-state (RS) recordings are particularly attractive in the scope of translational applications, where patients' impaired mobility can prevent the execution of motor tasks (Krakauer, 2007). The simplest approach to study RSFC is to measure the correlation between RS fMRI time-series (Poldrack *et al.*, 2011). Practically, this can be done by extracting the time-series of a region-of-interest (ROI) defined based on a priori knowledge of function and structure and to compute its correlation with other voxels or regions. Other methods do not rely on a priori hypotheses, such as principal component analysis (PCA) (Friston *et al.*, 1993) or independent component analysis (ICA) (Calhoun *et al.*, 2001; Beckmann *et al.*, 2005), which have been widely used to identify RS networks (RSNs). Although these approaches only give a measure of stationary connectivity (i.e., averaged over the whole scanning session), recent evidence has highlighted the dynamic nature of functional connectivity, suggesting that its temporal features can inform on cognition and behavior (Hutchison *et al.*, 2013; Liégeois *et al.*, 2019; Bolton *et al.*, 2020). Consequently, new methods aiming at capturing time-varying properties of neural networks, using dynamic functional connectivity (dFC), have also been developed (Prete *et al.*, 2016).

As functional connectivity offers a system-level view of cerebral activity, it is particularly suited to investigate the widespread reorganizations occurring following brain lesions (Grefkes and Fink, 2014). Indeed, RSFC demonstrated that strokes cause network disturbances not only close to the lesion, but also between distinct cortical areas in both hemispheres (Rehme and Grefkes, 2013). The main findings highlighted a disruption of interhemispheric FC between homologous motor areas, which is linearly correlated with the severity of the neurological deficits (Carter *et al.*, 2010; Wang *et al.*, 2010; Park *et al.*, 2011). Overall, the global motor network efficiency was reported to be reduced, even in patients with good clinical recovery (Rehme and Grefkes, 2013).

1.3.2 Electroencephalography

In this thesis, fMRI is the modality of choice to assess brain function, but it should be mentioned that other approaches can be deployed for similar purposes. Among them, electroencephalography (EEG) has the notable advantage of enabling data acquisition with a milliseconds temporal resolution. On the other hand, its spatial resolution is relatively poor (a few centimeters) (Burle *et al.*, 2015). Briefly, EEG measures changes in electrical activity along the scalp, related to neuronal activity and can also highlight pathological interactions (Dubovik *et al.*, 2012). EEG connectivity can be described using the coherence in different frequency bands. For instance, alpha oscillation synchrony at rest has been shown to be a marker of network function, linearly associated with behavioral performance (Westlake *et al.*, 2013) and beta oscillation synchrony was demonstrated to be a marker of stroke recovery, correlated with better subsequent motor improvement (Nicolo *et al.*, 2015). EEG signals can also be studied by probing topographical changes (Brunet *et al.*, 2011). As opposed to frequency analyses, these techniques are reference independent and can give insights into large-scale patterns of activity. Remarkably, such analyses have revealed that spontaneous activity is organized in short time periods of stable patterns of coherent neural activation, termed EEG microstates (Michel and Koenig, 2018). Deviant patterns have notably been linked to unilateral spatial neglect in stroke patients (Pirondini *et al.*, 2020).

1.4 Exploring peripheral mechanisms

1.4.1 Muscle synergies

Skilled limb manipulation, such as grasping, requires the spatial and temporal coordination of dozens of muscles. How the nervous system deals with the complex problem of movement generation is still debated. One theory is that muscle synergies, defined as common patterns of muscle activations, could be used as a strategy to alleviate this complexity. According to this hypothesis, movements would be constructed through a combination of motor modules, allowing for the simultaneous activation of sets of muscles (Mussa-Ivaldi *et al.*, 1994). This idea is supported by findings obtained from the decomposition of simultaneously acquired electromyographic (EMG) signals, where a large fraction of the variance of the activity of many muscles can be accounted for by combining few muscle synergies (D'Avella *et al.*, 2003, 2006; Tresch *et al.*, 2006). Decomposing muscular activity offers a valuable tool to probe muscle coordination and these approaches can be used to infer how motor control is affected by an impairment (Ting *et al.*, 2015). Notably, muscle synergies were shown to be altered after a stroke (Roh *et al.*, 2013), with a merging of motor modules in the paretic limbs, corresponding to the severity of the motor deficits (Cheung *et al.*, 2009, 2012).

1.4.2 Spinal maps

Other approaches, such as spinal maps, can also be used to provide a synthetic view of muscular organization. These EMG-based maps have been proposed as a way to estimate the spatiotemporal activation of ensembles of motoneurons in the spinal cord (Yakovenko *et al.*, 2002). This is typically done by combining EMG recordings with knowledge about the rostro-caudal location of motoneurons pools innervating different muscles, found in published charts of segmental localization (Kendall *et al.*, 2005). Therefore, this approach provides an indirect estimation of spinal cord activity, without the need of an imaging technique. As a matter of fact, spinal maps have been extensively studied in healthy subjects (Ivanenko *et al.*, 2006, 2008, 2013; Cappellini *et al.*, 2010; La Scaleia *et al.*, 2014; Pirondini *et al.*, 2016) and neurological patients, such as after a spinal cord injury or a stroke (Grasso *et al.*, 2004; Coscia, 2011; Coscia *et al.*, 2015).

1.5 The missing link: the spinal cord

The aforementioned approaches give insights into central and peripheral mechanisms, but they overlook an essential part of the CNS: the spinal cord. While its primary function is to provide the necessary link to support motor and sensory information flow between the brain and the periphery, it is also known to incorporate local processing essential for motor control, proprioception or pain (Levine *et al.*, 2012). Fundamental and clinical neurosciences would largely benefit from new insights into the mechanisms and organizational principles of spinal cord function, still largely unknown today (Wheeler-Kingshott *et al.*, 2014). Current knowledge on this topic is mostly based on invasive neurophysiology experiments on animal models or on indirect measurements in humans (see 1.4.2). In this regard, spinal cord fMRI appears as a potential tool to non-invasively study spinal mechanisms. Here, I will discuss the challenges that have hindered the development of this approach, as well as the current state of research.

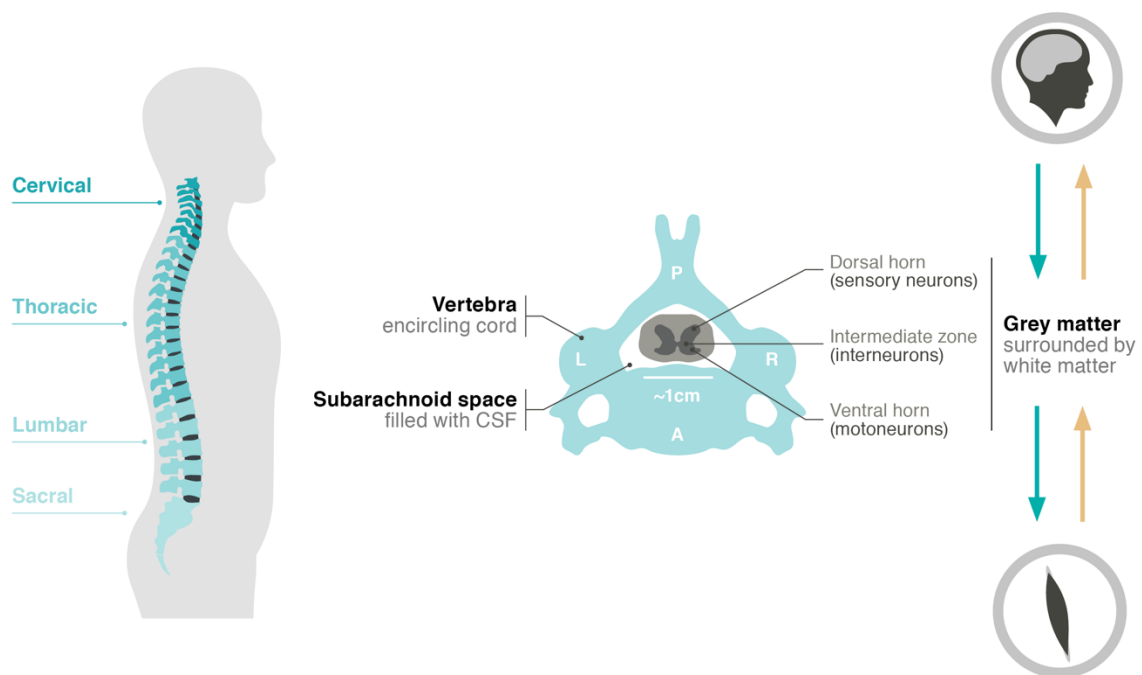


Figure 1.4 – Principles of spinal cord neuroanatomy.

1.5.1 Neuroanatomy

The human spinal cord is a long and curved structure, enclosed in the vertebral column, of about 45 cm (Cramer and Darby, 2014). As illustrated in Figure 1.4, the spinal cord is encircled by vertebrae and is surrounded by a cavity called the subarachnoid space, containing cerebrospinal fluid (CSF). As opposed to the brain, the white matter composed of myelinated axons is found around the grey matter, which presents a typical butterfly shape. The grey matter structure can be divided in horns with different types of neurons. The dorsal horns contain neurons processing sensory information, whereas ventral horns contain motoneurons linked to skeletal muscles. Interneurons, making connections within or between spinal levels, are also present. The cord contains 31 pairs of spinal nerves, exiting superior or inferior to the corresponding vertebra and organized in the rostrocaudal direction in four different parts: cervical, thoracic, lumbar and sacral. As mentioned in 1.1, different nerves are linked to different parts of the body; e.g., cervical to upper limbs, lumbar to lower limbs. Importantly, these anatomical differences between the brain and the spinal cord have a substantial impact in terms of functional imaging in this region.

1.5.2 Challenges

Spinal cord fMRI relies on the same principles as brain fMRI, as spinal neurons also depend on the delivery of oxygen via blood flow to support their metabolic demands (Summers *et al.*, 2014). Although successful reports of spinal cord activation have emerged already since the 90s (Yoshizawa *et al.*, 1996), their reproducibility has long remained an open question. Besides, spinal cord fMRI suffers from a number of additional challenges that have limited the interest and progress in the field (Giove *et al.*, 2004; Stroman *et al.*, 2014; Summers *et al.*, 2014).

Dimensions: The cross-sectional dimensions of the spinal cord are in the order of a centimetre and, as such, substantially smaller than the 15 centimeters of the brain. As a consequence, achieving high spatial resolution is essential to obtain meaningful images and to avoid partial volume effect. Conversely, this negatively affects the signal, as signal-to-noise ratio is proportional to the voxel size (Murphy *et al.*, 2007; Summers *et al.*, 2014). This small size, in addition, implies a limited tolerance to motion.

Inhomogeneous magnetic field: MRI-based techniques rely on the application of an homogeneous magnetic field B_0 to ensure good data quality. However, inhomogeneities can be arise from differences in magnetic susceptibility between adjacent tissue types (Finsterbusch, 2014). In this regard, the spinal cord is a very challenging environment, where bones, muscles, fluids as well as air are present. If not dealt with appropriately, this may lead to various image artifacts (distortion or signal dropout) with standard $T2^*$ -weighted fMRI, in particular at the level of the intervertebral disks (Cooke *et al.*, 2004; Finsterbusch *et al.*, 2012).

Physiological noise: The close proximity of the lungs, the heart and other visceral organs is an important source of motion (Brooks *et al.*, 2008; Piché *et al.*, 2009; Fratini *et al.*, 2014; Eippert *et al.*, 2017a). Furthermore, the cardiac activity is generating a pulsatile flow in the cerebrospinal fluid (CSF) around the spinal cord.

Several solutions have been proposed in order to overcome those limitations, both in terms of data acquisition and processing (Stroman *et al.*, 2014; Summers *et al.*, 2014; Eippert *et al.*, 2017a). Different imaging sequences have been compared, such as gradient-echo (GE) and spin-echo sequences (SE) (Jochimsen *et al.*, 2005; Parkes *et al.*, 2005; Stroman, 2005; Bouwman *et al.*, 2008).

Although SE sequences offer a better image quality, thanks to the refocusing pulse that makes them less sensitive to the venous signal, GE sequences offer a higher signal sensitivity and reproducibility. As regards slice orientation, it may seem interesting to use sagittal or coronal slices, in order to have a large rostro-caudal coverage with a limited number of slices. Nevertheless, isotropic voxels, e.g., $2 \times 2 \times 2 \text{ mm}^3$, should be preferentially used with this orientation to limit bias for the spatial mapping of activations (Summers *et al.*, 2014). As this will impose constraints on the in-plane resolution, most recent studies used axial slices, where they could take advantage of the spatial organization of the cord by having anisotropic voxels (typically $1 \times 1 \times 5 \text{ mm}^3$) (Sprenger *et al.*, 2012; Kong *et al.*, 2014; Van de Sand *et al.*, 2015; Weber *et al.*, 2016b). Therefore, high in-plane resolution can be obtained, with less variation in field intensity, while keeping a sufficient signal-to-noise ratio (SNR), proportional to the voxel size and, thus, to the slice thickness (Murphy *et al.*, 2007). Regardless of the acquisition scheme, a particular care should be devoted to the “shimming”, which refers to the procedures aiming to adjust the magnetic field so as to limit the detrimental effects of field inhomogeneities (Finsterbusch, 2014). Finally, different methods have been proposed to limit the impact of physiological noise, mostly using nuisance regressors based on physiological recordings or directly derived from the data (Eippert *et al.*, 2017a).

Simultaneous brain and spinal cord imaging is also achievable, although even more challenging. Indeed, the ideal MRI setup differs considerably for the brain and the spinal cord, notably as regards resolution, field-of-view, coils and shimming. As a result, several solutions have been proposed, such as custom-made coils (Cohen-Adad *et al.*, 2011) or sequences (Finsterbusch *et al.*, 2013; Islam *et al.*, 2018). As these options are not readily available, some researchers rather resorted to protocols employing regular equipment and sequences provided by the manufacturer, which can simplify their deployment and generalization (Vahdat *et al.*, 2015).

Although spinal cord fMRI has mainly been conducted using field strengths of 1.5 or 3T, a few studies have extended this approach to a higher field of 7T (see Barry *et al.*, 2018b for a review). The sub-millimetric in-plane resolution that can be achieved, along with the higher BOLD sensitivity, are indeed particularly appealing and promising results were previously reported using resting-state scans (Barry *et al.*, 2014). Nevertheless, higher fields are also more sensitive to field inhomogeneities, hence further complicating the shimming procedure. In addition, the higher contribution of physiological noise at 7T may also have a detrimental effects on the BOLD signals (Triantafyllou *et al.*, 2005).

1.5.3 Imaging motor control with spinal cord fMRI

Since the seminal work of Yoshizawa in 1996 (Yoshizawa *et al.*, 1996), several studies have confirmed the potential of spinal cord fMRI to monitor task-related activity, mainly with tasks involving the upper extremity (Madi *et al.*, 2001; Govers *et al.*, 2007; Maieron *et al.*, 2007; Bouwman *et al.*, 2008; Ng *et al.*, 2008; Vahdat *et al.*, 2015; Weber *et al.*, 2016b). Not only did the different studies highlighted the feasibility of spinal cord fMRI, they also shed light on different properties of the task-related activity. First, a linear relationship was observed between the applied force and the signal amplitude during an isometric task (Madi *et al.*, 2001). The effect of the side and rate of finger tapping was then investigated, and a larger ipsilateral effect was observed, as expected, as well as a rate-dependent increase in spinal cord fMRI signal (Maieron *et al.*, 2007). More recently, the reliability of signal lateralization was demonstrated across runs at the group level (Weber *et al.*, 2016b). Although these studies underlined the link between motor output and spinal activity, it should be noted that this is not the only factor determining spinal signal. For instance, Ng *et al.*,

(2008) pointed out an effect of task complexity, even for similar muscular demands. Another evidence that spinal activity is not a mere reflection of motor output lies in the work of Vahdat *et al.*, 2015, in which simultaneous brain-cervical cord fMRI was employed during a motor sequence learning task. Learning-related modulation of activity was observed in the spinal cord, independently from the modulation of supraspinal structures, hence suggesting that the spinal cord is capable of local plasticity and contributes distinctively from the brain to motor learning. Although the upper limb, most particularly the hand, has been preferred in order to minimize motion, spinal cord fMRI was also employed during active and passive ankle movements and generated anatomically consistent activations in the lumbar region (Kornelsen and Stroman, 2004).

1.5.4 Imaging spontaneous spinal cord activity

In the spinal cord, spontaneous signal fluctuations during resting state have only been explored in the last decade. In 2010, Wei *et al.* first attempted to retrieve spinal RSNs using single-subject ICA (Wei *et al.*, 2010). The resulting findings were equivocal, as networks exhibited dominant frequencies in the range of the respiratory rhythm, potentially hinting at their artifactual nature. This relative success may pertain to technological constraints, such as low field strength (1.5 T), absence of group template or lack of correlation of physiological noise. A few years later, Barry *et al.* leveraged improved acquisition protocols and processing techniques, along with ultra-high field fMRI (7 T), and delineated for the first time spinal sensory and motor networks using a seed-based approach (Barry *et al.*, 2014). An investigation at 3 T, using ICA-derived networks, further corroborated the existence of organized spinal RS fluctuations (Kong *et al.*, 2014). Following these results, the reproducibility and robustness of the connectivity patterns against variations of the processing pipelines were confirmed (Barry *et al.*, 2016; Eippert *et al.*, 2017b). Building on these promising observations, new analyses aiming to characterize spinal RSNs were performed. For instance, network features were probed using graph theory-based metrics (Liu *et al.*, 2016b), shedding light on their small-world properties (i.e., efficient local and global connectivity), previously reported for cortical networks (Bullmore and Bassett, 2011). Expanding on this work, the effect of experimental manipulation on spinal cord resting-state patterns was also explored (Weber *et al.*, 2018). One major finding was the state-dependency of dorsal networks, which were disrupted upon thermal stimulation. Interestingly, neither the small-worldness properties nor the global clustering coefficient were affected by the change of state, while modularity was decreased and global efficiency increased. In recent work, structural equation modelling with a predefined underlying backbone was applied to characterize interactions between time-courses of regions-of-interest in the brainstem and the spinal cord revealed a complex connectivity network between those regions (Harita *et al.*, 2019). The aforementioned observations, along with recent research demonstrating that BOLD timecourses reflect electrophysiological measures such as local-field potentials and multiunit spiking (Wu *et al.*, 2019), support the genuine character of spinal RSNs. In order to fully harness the potential of spinal cord fMRI to unravel these fluctuations, efforts are now deployed to optimize protocols and provide robust guidelines (Barry *et al.*, 2018a).

1.5.5 Spinal cord fMRI and clinical applications

So far, applications of spinal cord fMRI to clinics have been relatively limited (Kornelsen and Mackey, 2010; Wheeler-Kingshott *et al.*, 2014). During thermal stimulation, lumbar spinal activity was shown to present similar stimulus-response patterns between spinal-cord injured (SCI) patients and healthy subjects (Stroman *et al.*, 2002, 2004). However, there were differences in the patterns of activity, as subjects with complete SCI exhibited an altered dorsal grey matter activity, alongside an enhanced ventral activity. Interestingly, activity was detected even when the patients

could not feel the stimulation. Spinal activity in SCI patients during passive and active lower limb movements was also investigated (Kornelsen and Stroman, 2007) and activity was observed regardless of the extent of injury, in all participants. In particular, activity was detected caudal to the injury site, more intensely during active movements. As for RS recordings, their clinical potential was first demonstrated in non-human primates, where injuries to the cord disrupted interhorn connectivity, thus hinting at the functional relevance of those connections and suggesting their potential as a biomarker of functional integrity (Chen *et al.*, 2015). In humans, the amplitude of low frequency fluctuations (ALFF) was found to be affected in patients suffering from cervical spondylotic myelopathy (Liu *et al.*, 2016a) and fibromyalgia (Martucci *et al.*, 2019). Similarly, spinal lesions resulting from multiple sclerosis were shown to be associated with focal abnormalities in intrinsic connectivity (Conrad *et al.*, 2018). Of note, spinal cord fMRI has so far not been employed in stroke patients.

1.6 Outline of the thesis

This thesis is organized in two parts, whose contents are summarized in Figure 1.5. **PART I** presents methods aiming to foster the development of personalized approaches for motor neuro-rehabilitation. Specifically, **Chapter 2** introduces a model-based approach to adapt robot-assisted therapy in real-time based on the subject's motor performances. Then, **Chapter 3** proposes a multivariate methodology to combine quantitative neurophysiological metrics into a multimodal index that can be used to track the patients' neuro-biomechanical state. **PART II** aims to address the gap in knowledge regarding spinal cord's function, so as to achieve a comprehensive view of the central and peripheral mechanisms involved in motor control and recovery. In order to establish a pipeline enabling the non-invasive study of spinal cord activity in humans, **Chapter 4** is devoted to an initial exploration of potential fMRI acquisition schemes. **Chapter 5** elaborates on this analysis and demonstrates the robustness of the selected pipeline to detect motor-related activity during upper limb movements. Capitalizing on the potential of this fMRI pipeline to image spinal mechanisms and in an effort to unravel their functional architecture, **Chapter 6** then proposes a framework for the study of spinal resting-state fluctuations using dynamic functional connectivity. Following this thorough characterization of spinal signals, the focus is extended to the entire central nervous system and **Chapter 7** investigates cerebro-spinal processes involved in motor sequence learning, thanks to simultaneous brain and spinal cord fMRI. Finally, **Chapter 8** shows how spinal neuroimaging can be translated to clinical applications, in the context of stroke and spinal cord injury.

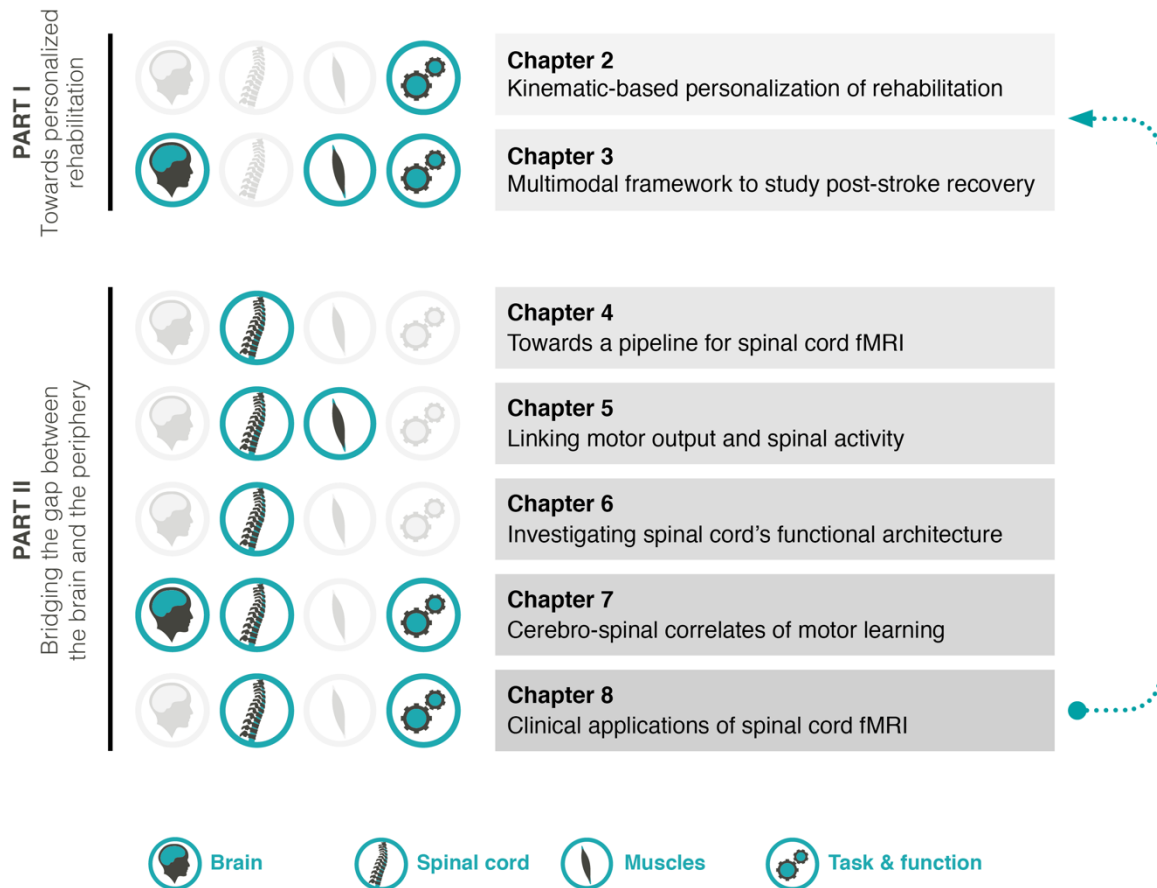


Figure 1.5 – Overall summary of thesis content

PART I

Towards personalized rehabilitation

Although conventional motor rehabilitation following a stroke encompasses a wide array of treatment solutions, therapies typically include completion of movements, possibly assisted by a clinician (Winstein and Kay, 2015). In particular, repetitive and goal-directed motor practice has been suggested to improve function in stroke patients, granted that the neuromuscular system is sufficiently and adequately challenged (Woldag and Hummelsheim, 2002; Langhorne *et al.*, 2011). In the last decades, robotic devices have become increasingly deployed in neurorehabilitation, as they have an indubitable potential to provide intense, controllable and quantifiable motor training (Weber and Stein, 2018). Despite these auspicious abilities, clinical outcomes after intensive robot-aided rehabilitation have so far been reported to be similar to intensive traditional therapies, or only marginally better (Lo *et al.*, 2010; Klamroth-Marganska *et al.*, 2014). Besides, it remains unclear whether improvements due to robotic rehabilitation can readily be transferred to activities of daily living (Veerbeek *et al.*, 2017; Weber and Stein, 2018). This relative efficacy suggests that providing a high dose of therapy through highly repetitive movements may not be sufficient to significantly promote motor recovery (Winstein *et al.*, 2016). Consequently, the use of robotic devices should be further optimized to deliver compelling evidence of their clinical relevance.

In that regard, personalization of the intervention has been advocated as a pivotal factor to fully exploit robot-based rehabilitation (Winstein and Kay, 2015; Raffin and Hummel, 2018; Micera *et al.*, 2020). Instead of delivering training following a *one-suits-all* approach, motor recovery and re-learning are presaged to be optimized when the task difficulty matches the level of ability (Guadagnoli and Lee, 2004), and when the therapy is impairment-oriented (Duret *et al.*, 2019). The embedded sensors integrated in robotic devices can be leveraged in that respect, in order to monitor task performance and to adjust training accordingly. Exoskeletons, in particular, enable continuous quantification of limb kinematics at the level of individual joints (Frisoli, 2018). Nevertheless, how to design personalized tasks tailored to the needs of individual patients is still an open issue, as many parameters can be foreseen, both as regards performance assessments and task adaptation. Besides, patient-tailored strategies should also consider the multifaceted neuro-biomechanical state of each patient so as to develop pathophysiologically-driven treatments (Raffin and Hummel, 2018; Guggisberg *et al.*, 2019).

From that perspective, the aim of the research presented in this section is twofold: first, we want to explore the feasibility of treatment personalization in real-time within a rehabilitative session, using simple kinematic measures. Secondly, we zoom out and focus on the dynamics of recovery over multiple sessions, with the aim of proposing a multimodal framework enabling the combination of kinematic, muscle and brain measurements into a single variable reflecting patient's neuro-biomechanical state and residual motor function.

Chapters 2 and 3 correspond to postprint versions of articles published under:

“Motor improvement estimation and task adaptation for personalized robot-aided therapy: a feasibility study”, Giang C., Pirondini E.*, **Kinany N.***, Pierella C.*, Panarese A., Coscia M., Miehlabrad J., Magnin C., Nicolo P., Guggisberg A. and Micera S., BioMedical Engineering OnLine, May 2020, doi:10.1186/s12938-020-00779-y

* Equally contributing authors

Contributions as second author: design of the experiments, implementation of the training task (exoskeleton control), data collection, development of the analysis plan, revision of the analysis, writing of the manuscript

“A multimodal approach to capture post-stroke temporal dynamics of recovery”, Pierella C., Pirondini E., **Kinany N.**, Coscia M., Giang C., Miehlabrad J., Magnin C., Nicolo P., Dalise S., Sgherri G., Chisari C., Van de Ville D., Guggisberg A. and Micera S., Journal of Neural Engineering, July 2020, vol. 17(4), doi.org/10.1088/1741-2552/ab9ada

Contributions as third author: organization of the clinical trial, planning and coordination of experiments involving patients and healthy subjects, implementation of the training task (exoskeleton control), data collection, development of the analysis plan, revision of the analysis, writing of the manuscript

Chapter 2

Kinematic-based personalization

Motor improvement estimation and task adaptation for personalized robot-aided therapy: a feasibility study

Christian Giang¹, Elvira Pirondini^{2,3,*}, Nawal Kinany^{1,2,3,*}, Camilla Pierella^{1,*}, Alessandro Panarese⁴, Martina Coscia⁵, Jenifer Miehlebradt⁶, Cécile Magnin⁷, Pierre Nicolo^{7,8}, Adrian Guggisberg^{7,8} and Silvestro Micera^{1,4}

¹Bertarelli Foundation Chair in Translational Neuroengineering, Center for Neuroprosthetics and Institute of Bioengineering, School of Engineering, École Polytechnique Fédérale de Lausanne (EPFL), Lausanne, 1015, Switzerland; ²Institute of Bioengineering/Center for Neuroprosthetics, Ecole Polytechnique Fédérale de Lausanne (EPFL), Lausanne, Switzerland; ³Department of Radiology and Medical Informatics, University of Geneva, Geneva, Switzerland; ⁴Translational Neural Engineering Area, The Biorobotics Institute, Scuola Superiore Sant'Anna, Pisa, 56025, Italy; ⁵Wyss Center for Bio- and Neuro- Engineering, Geneva, 1202, Switzerland; ⁶Brain Electrophysiology Attention Movement Laboratory, Institute of Psychology, University of Lausanne, Lausanne, Switzerland; ⁷Division of Neurorehabilitation, Department of Clinical Neurosciences, University Hospital Geneva, Geneva, Switzerland; ⁸Laboratory of Cognitive Neurorehabilitation, Department of Clinical Neurosciences, Medical School, University of Geneva, Geneva, Switzerland

** Equally contributing authors*

Abstract – Background: In the past years, robotic systems have become increasingly popular in upper limb rehabilitation. Nevertheless, clinical studies have so far not been able to confirm superior efficacy of robotic therapy over conventional methods. The personalization of robot-aided therapy according to the patients' individual motor deficits has been suggested as a pivotal step to improve the clinical outcome of such approaches. **Methods:** Here, we present a model-based approach to personalize robot-aided rehabilitation therapy within training sessions. The proposed method combines the information from different motor performance measures recorded from the robot to continuously estimate patients' motor improvement for a series of point-to-point reaching movements in different directions. Additionally, it comprises a personalization routine to automatically adapt the rehabilitation training. We engineered our approach using an upper limb exoskeleton. The implementation was tested with seventeen healthy subjects, who underwent a motor-adaptation paradigm, and two subacute stroke patients, exhibiting different degrees of motor impairment, who participated in a pilot test undergoing rehabilitative motor training. **Results:** The results of the exploratory study with healthy subjects showed that the participants divided

into fast and slow adapters. The model was able to correctly estimate distinct motor improvement progressions between the two groups of participants while proposing individual training protocols. For the two pilot patients, an analysis of the selected motor performance measures showed that both patients were able to retain the improvements gained during training when reaching movements were reintroduced at a later stage. These results suggest that the automated training adaptation was appropriately timed and specifically tailored to the abilities of each individual. **Conclusions:** The results of our exploratory study demonstrated the feasibility of the proposed model-based approach for the personalization of robot-aided rehabilitation therapy. The pilot test with two subacute stroke patients further supported our approach, while providing encouraging results for the applicability in clinical settings.

2.1 Introduction

With the increase of life expectancy, it is estimated that stroke related impairments will be ranked fourth most important cause of disability in western countries by 2030 (Donnan *et al.*, 2008). Despite early rehabilitative interventions, 55% to 75% of the patients still suffer from upper limb impairments in the chronic state of the injury (Carod-Artal *et al.*, 2000; Lawrence *et al.*, 2001; Clarke *et al.*, 2002). The recovery of reaching and grasping movements is therefore a crucial therapeutic goal in stroke rehabilitation (Veerbeek *et al.*, 2017).

Post-stroke rehabilitation usually relies on task-oriented repetitive movements that help improving motor function and training new control strategies. In this regard, the amount of goal-directed and challenging practice, rather than daily intensity alone, seems to be the most effective factor in neurorehabilitation (Dobkin, 2004). In the last two decades, robot-aided motor training has shown potential for the recovery of lost motor abilities in upper limbs after stroke (Marchal-Crespo and Reinkensmeyer, 2009; Wagner *et al.*, 2011; Di Pino *et al.*, 2014). While providing intense and highly repeatable motor training, robotic devices also offer means to control and quantify movement performance. Despite this strong potential, controlled clinical trials have so far not been able to confirm whether robotic therapy is more effective than conventional methods in restoring motor abilities (Lo *et al.*, 2010; Klamroth-Marganska *et al.*, 2014; Rodgers *et al.*, 2019). It has been argued that this might be related to saturation effects in the patients' motor performances and a lack of automatic methods to promptly detect them (Grimm *et al.*, 2016). Indeed, a recent review analyzing 38 studies on this topic (Ferreira *et al.*, 2018), concluded that robotic therapy had rather small effects on patients' motor control compared to other interventions.

The automatic and personalized adaptation of the rehabilitation training has been suggested as a pivotal step to improve the outcome of robot-aided rehabilitation and the clinical relevance of such solutions (Krakauer, 2006). As a matter of fact, motor learning is known to be maximized when the difficulty level of the training task matches the patient's level of ability (Guadagnoli and Lee, 2004). Recent advances in the field of personalized robotic rehabilitation have therefore focused on the design of customized training protocols, including individualized selection of upper limb movements (Rosenthal *et al.*, 2019). One of the pivotal aspects underlying the development of a personalized rehabilitation training is the definition of performance measures that can correctly capture the different aspects of motor recovery, as well as their specific dynamics. Different measures have been used to assess the patient's "status" during training (i.e., motor performance, engagement, etc.) in order to adjust the proposed tasks accordingly. Kinematic performance measures, such as movement accuracy, smoothness, velocity, inter-joint coordination, range of motion and stiffness

(Krebs *et al.*, 2003; Wolbrecht *et al.*, 2008; Kan *et al.*, 2011; Papaleo *et al.*, 2013; Metzger *et al.*, 2014; Wittmann *et al.*, 2015; Wu *et al.*, 2017a), game-related statistics (Octavia and Coninx, 2014; Grimm *et al.*, 2016), measures of muscle activity (Krebs *et al.*, 2003), or the combination of kinematic and psychophysiological measurements (Rodriguez Guerrero *et al.*, 2010; Novak *et al.*, 2011; Badesa *et al.*, 2016) have been among the measures used for the design of patient-tailored training protocols. However, those approaches either focused on a single performance measure describing a specific aspect of rehabilitation or used multiple measures but lacked the ability to meaningfully synthesize the information from these variables. Integrating this information into a single measure, yet representative of the patient's multidimensional rehabilitation response, would facilitate the monitoring of the multifaceted progress of the patient and provide a way to trigger task adaptation while enormously simplifying the design of personalized rehabilitation training.

A first approach addressing this issue was presented in our previous work (Panarese *et al.*, 2012a). Previously, we have used a state-space model to merge the information from different kinematic measures and, in this way, estimated motor improvement (MI) of chronic stroke patients exercising with a planar robotic device for upper limb rehabilitation. In this previous work, we used four performance measures to estimate the MI: (1) the movement velocity (MV); (2) the movement accuracy (nMD); (3) the movement smoothness (nPK); (4) the percentage of successful tasks executed during each session (%SUCC). Following post-hoc analyses on the recorded performance measures, we showed that such model would be capable of mimicking decision rules applied by physical therapists regarding the adaptation of the task difficulty. In most cases, the model even appeared to be faster than the therapists in detecting when the patients' motor performance had reached a plateau and when more challenging tasks should have been proposed. Yet an automatic task adaptation based on such a model was lacking from our previous implementation.

In the current study, we therefore build on these results to implement a method able to continuously detect patient's motor improvement and adapt the training task for three-dimensional movements using an upper limb exoskeleton. Indeed, most of the adaptive approaches mentioned before, were restricted to planar workspaces, hindering their applications to functional movements exploring three-dimensional workspaces, that better resemble those performed during daily life activities. Evaluating and estimating motor improvement is particularly complex in three-dimensional training workspaces, where the visual evaluation of motor performance becomes more challenging. Under these circumstances, a method able to autonomously estimate patient training progress, in particular for movements in different directions, could provide fundamental support to therapists. In contrast to our previous work, here we employed a continuous implementation of the motor improvement estimation and the training adaptation routine. Indeed, the immediate task adaptation within the same training sessions could not only increase patients' engagement, but also foster their attention control, possibly leading to improved reaching performances (Rinne *et al.*, 2017).

However, in order to enable the use of such methods for clinical applications, it is first necessary to validate their feasibility and safety under controlled experimental conditions. The main objective of this exploratory study was hence to demonstrate feasibility and safety for the proposed method and to comprehend whether such approach could possibly be applied in clinical settings. We, therefore, devised an experiment to test our model in a group of healthy subjects. In order to mimic the recovery of motor performance observed in stroke patients, we inverted the visual feedback for the point-to-point reaching movements that the healthy subjects had to perform in a three-dimensional training environment using a robotic upper-limb exoskeleton. Previous studies on visually

manipulated motor tasks showed that most people could cope with similar manipulations after training (Harris, 1965; Miall *et al.*, 2004; Krakauer, 2009; Shabbott and Sainburg, 2010; Werner and Bock, 2010). Accordingly, we hypothesized that performances would drop after the introduction of the inverted visual feedback (i.e., movements would become slower and jerkier), but would then gradually improve and eventually reach a plateau - with temporal dynamics resembling the ones occurring in robot-aided rehabilitation of stroke patients (Colombo *et al.*, 2008, 2010; Panarese *et al.*, 2012a). Moreover, previous work has demonstrated that for reaching movements in planar setups, participants showed better performance for targets lying on the axis perpendicular to the inversion (Cunningham and Pavel, 1991; Werner and Bock, 2010). Though in this study we used a three-dimensional setup, we also hypothesized that participants would have less difficulties with the targets lying on one of three coordinate axes (on-axis targets), as they involved inversions in only one dimension (in contrast to inversions in two dimensions for off-axis targets, i.e., targets not lying on the axes). Using this setup, we tested whether our model was capable of tracking individual motor improvement induced by motor adaptation, and whether it was able to personalize the training by identifying “recovered” (i.e., adapted) movements in real-time.

To provide further evidence about the clinical usability of the presented approach, we finally performed a pilot test with two subacute stroke patients. The objective of this pilot test was to evaluate the model in an authentic clinical context and with two patients exhibiting different degrees of motor impairment. The patients underwent four weeks of robot-aided rehabilitation training, performing the same point-to-point reaching movements as the healthy subjects. In this case however, visual feedback was provided normally, without inversion. We hypothesized that the model would suggest two distinct training adaptation schemes for the patients, optimizing their motor recovery by proposing reaching movements that match the individual abilities of each patient.

2.2 Methods

In the current study, we developed a model to continuously estimate motor improvement (MI) in three-dimensional workspaces using kinematic performance measures, based on the results of our previous work (Panarese *et al.*, 2012a). Moreover, we designed a personalization routine, that automatically adapts the difficulty of the rehabilitative motor task (i.e., a point-to-point reaching task) based on the MI estimates. Both the MI model and the personalization routine were integrated in the control algorithm of an upper-limb exoskeleton and tested with a group of 17 healthy participants. The presented approach was then tested with two subacute stroke patients.

2.2.1 Participants

Healthy participants

Seventeen right-handed subjects (eight males, nine females, 25.4 ± 3.3 years old) participated in the experimental validation of our approach. The participants did not present any evidence or known history of skeletal and neurological diseases and they exhibited normal ranges of motion and muscle strength. All participants gave their informed consent to participate in the study, which had been previously approved by the Commission Cantonale d'Éthique de la Recherche Genève (CCER, Geneva, Switzerland, 2017-00504).

Subacute stroke patients

Two subacute stroke patients from the inpatient unit of the Hôpitaux Universitaires de Genève (HUG, Geneva, Switzerland) were included in the study. A summary of the patient information is reported in Table 2.1. Both patients suffered from a right hemiplegia with at least 10° of residual motion in shoulder and elbow joints. The patients were enrolled in the study within two to eight weeks after the stroke. Both patients received standard therapy at the stroke unit during the acute phase, and an individually tailored multidisciplinary rehabilitation program in the subacute and chronic phases. The patients received two times 30 minutes of physical therapy per day on five days per week and five times 30 minutes of occupational therapy per week on an inpatient basis for 8 to 16 weeks, followed by outpatient treatment of 1 to 4 hours of physical and occupational therapy per week. Therapy was adapted by the therapists to the current capacities of the patients by choosing from a list of appropriate exercises comprising upper-extremity relaxation techniques, unilateral task-specific mobilizations, bilateral upper limb exercises with a wand, ball exercises, active ante/retropulsion exercises, active pronation/supination exercises and grasping exercises. Therapists were assigned to the patients based on their availability; hence different therapists took care of the patients throughout the therapy sessions. In addition to the standard therapy, the patients received robot-aided treatment following the adaptive robotic rehabilitation protocol described in Section 2.2.2. All patients gave their informed consent to participate in the study. This study is registered in ClinicalTrials.gov (NCT02770300) and the experimental protocols were approved by Swissmedic and Swissethics.

Table 2.1 – Demographics and information of the stroke patients included in the study

Patient	Gender	Age	Weight (kg)	Height (cm)	Hand dominancy	Stroke diagnosis	Enrolment after lesion
P01	Male	86	66	165	Right	Ischemic, middle cerebral artery left, cerebellum right	3 weeks
P02	Male	65	81	180	Right	Ischemic, corona radiata left	2 weeks

2.2.2 Robotic exoskeleton and motor task

We implemented the motor improvement model and the personalization routine in the robotic upper-limb exoskeleton ALEx (Wearable Robotics srl., Bergamasco *et al.*, 2013; Pirondini *et al.*, 2016). During the experiments, the patients and the healthy participants were instructed to perform point-to-point reaching movements at their comfortable velocity (Figure 2.1a). All reaching movements started from the center of the workspace and the goal was to reach one of the eighteen targets equally distributed over the three planes of a sphere of 19 cm of radius (Figure 2.1b). The selected radius of the sphere allows for a maximum exploration of the workspace, while maintaining the reaching movements executable for people of most body sizes. Each movement towards a target represented a subtask. This design allowed exploiting an extensive three-dimensional workspace and provided means to easily identify all subtasks of the exercise. The sphere was positioned so

that its center was aligned with the acromion of the right arm mid-way between the center of the target panel and the subject's acromion. The targets were displayed on a screen mounted in front of the subjects and visual feedback was provided by means of a cursor mapping the position of the exoskeleton's handle to the screen. In order to preserve the depth perception, the dimensions of the target spheres were modified in accordance with their position in the 3D space. If a subject was unable to reach a target (i.e., the subject did not move for more than 3 seconds), ALE_x activated its assistance mode to guide the subject towards the target according to a minimum jerk speed profile (Sadaka-Stephan *et al.*, 2015).

2.2.3 Experimental protocols

Healthy participants

The healthy participants attended a single experimental session, which comprised seven blocks of reaching movements (Figure 2.1c). Breaks of one minute were scheduled after each block to prevent fatigue. The session started with an initial assessment block consisting of three runs ($A_{I,1-3}$). During each run all 18 targets were presented once and in a randomized order. The purpose of the assessment block was i) to allow familiarization with the robotic system and the motor task and ii) to record a baseline for the performance measures. This block was followed by five blocks B_{1-5} during which the visual feedback was inverted (i.e., an upward movement was displayed as downward and vice versa, likewise for left/right and forward/backward movements). This vision inversion was introduced to induce motor performances with temporal dynamics resembling the ones observed in robot-aided rehabilitation of stroke patients (Colombo *et al.*, 2008, 2010; Panarese *et al.*, 2012a). At the onset of the five inversion blocks, participants were not informed about the inversion of the visual feedback, but they were told that the task difficulty was changed. Each of the five inversion blocks B_{1-5} consisted of five runs, each one composed of eight point-to-point reaching movements for a total of 40 reaching movements per block.

The initial set of training targets for each participant was generated following a semi-randomized procedure: based on the hypothesis presented in the Introduction, we expected movements towards on-axis targets (i.e., targets 1, 3, 5, 7, 10 and 13, see Figure 2.1b) to be easier. Therefore, the initial set of training targets always contained all six on-axis and two randomly selected off-axis targets (i.e., targets 2, 4, 6, 8, 11, 14, 15, 16, 17 and 18). The presentation order of the eight initial training targets was randomized. The remaining ten off-axis targets were placed randomly in the training queue.

During the five inversion blocks B_{1-5} , MI was continuously estimated for each training target and a target was removed from the current set of training targets if the MI estimates for this subtask satisfied the replacement conditions (see section 2.2.6). In this case, the target was replaced by the next one in the training queue. The inversion blocks B_{1-5} were followed by a final assessment block which was composed of three runs ($A_{F,1-3}$) and followed the same procedure as the initial assessment block (i.e., neither vision inversion nor training adaptation were applied). The data acquired during the assessment blocks (i.e., $A_{I,1-3}$ and $A_{F,1-3}$) were not considered for the motor improvement estimation.

Subacute stroke patients

The experimental protocol for the patients consisted of four weeks of robot-aided rehabilitation therapy (Figure 2.1d), with three sessions of 30 minutes per week. The training comprised the

regular point-to-point reaching task (see section 2.2.2). In order to evaluate the outcome of their rehabilitation training, the patients completed two assessment sessions before ($A_{I,1-2}$) and after ($A_{F,1-2}$) the therapy. The initial assessment sessions $A_{I,1-2}$ were completed two weeks and one week before the beginning of the therapy. The final assessment sessions $A_{F,1-2}$ were completed one week and one month after the end of the therapy. During the initial and final assessment sessions, all eighteen targets of the point-to-point reaching task were presented to the patients in a randomized order. The total amount of reaching movements for each session was determined by the physical therapist while encouraging the patient to perform as many movements as possible (numbers reported in Section 2.2). Breaks of varying durations were scheduled based on the patient's condition. In addition, the patients were evaluated using the upper extremity section of the Fugl-Meyer assessment (FMA-UE, Fugl-Meyer *et al.*, 1975). The data acquired during the assessment blocks (i.e., $A_{I,1-2}$ and $A_{F,1-2}$) were not considered for the motor improvement estimation.

For the treatment sessions, we first identified the patient-specific difficulty for each of the 18 targets following the initial assessment sessions $A_{I,1-2}$. Specifically, we analyzed the mean values of the performance measures MV, SAL and %SUCC (see Section 2.2.5) for each of the eighteen training targets. The targets were first ordered by descending values of %SUCC (i.e., starting from easier targets). If several targets had equal values for %SUCC, the order amongst them was determined by their mean values for MV and SAL, while giving both measures equal weight. The first eight targets of the resulting list were selected as the initial training targets. The remaining targets were placed in a training queue while conserving the determined order of difficulty. During the therapy (W_1 - W_4 , Figure 2.1d), MI was continuously estimated for each training target separately. The replacement of a training target based on the MI estimates followed the procedure presented in Section 2.2.6. The current set of training targets was saved after the completion of each training session, ensuring continuity between sessions. The total amount of reaching movements for each session was determined by the physical therapist while encouraging the patient to perform as many movements as possible. However, no decisions were taken by the therapist regarding the choice of the specific training targets. Breaks of varying durations were scheduled based on the patient's condition.

2.2.4 Motor improvement model

In order to continuously track patients' MI at subtask level (i.e., for a series of point-to-point reaching movements in different directions), we used a state-space model. MI was modelled as a random walk:

$$MI_k = MI_{k-1} + \epsilon_k \quad (1)$$

where k are the different repetitions for a movement direction and ϵ_k are independent Gaussian random variables with zero mean and variance σ_ϵ^2 . A set of observation equations $z_{j,k}$ was defined in order to estimate MI. These equations related MI to continuous performance measures r_j , which were computed from kinematic recordings provided by the robotic device (see section 2.2.5 for details on the performance measures). The continuous variables r_j (with $j = 1, \dots, J$ representing the different performance measures) were defined by the log-linear probability model

$$z_{j,k} = \log(r_{j,k}) = \alpha_j + \beta_j MI_k + \delta_{j,k} \quad (2)$$

where $\delta_{j,k}$ are independent Gaussian random variables with zero mean and variance $\sigma_{\delta,j}^2$. The use of log-linear models allowed capturing rapid increases (or decreases) of the performance measures during the training, as well as the expected convergence towards subject-specific upper (or lower) bounds at the end of the training. The suitability of such probability models for motor performance measures in stroke patients was previously demonstrated (Panarese et al., 2012a, 2016). Similarly, an observation equation for a discrete performance measure n_k was defined. The binary discrete variable $n_k \in \{0, 1\}$ was used to track the completion of the exercised subtask, with 1 meaning that the subtask was performed successfully and 0 meaning failure. The observation model for n_k was assumed to be a Bernoulli probability model:

$$Pr(n_k | p_k) = p_k^{n_k} (1 - p_k)^{1-n_k} \quad (3)$$

where p_k , the probability of performing the subtask successfully at repetition k , was related to MI_k by a logistic function:

$$p_k = \frac{\exp(MI_k)}{1 + \exp(MI_k)} \quad (4)$$

ensuring that p_k was constrained in $[0, 1]$. Furthermore, this formulation guaranteed that p_k would approach 1 with increasing MI .

The model parameters $\{\alpha_j, \beta_j, \sigma_{\delta,j}, \sigma_\epsilon, p_k\}$ were estimated for each individual subject using the recordings of $r_{j,k}$ and n_k (i.e., kinematic recordings from the robotic device, see Section 2.2.5) and by applying Bayesian Monte Carlo Markov Chain methods. The estimation of the parameters resulted in an estimate for MI . In order to ensure accuracy of the model, it was necessary that the number of recordings of $r_{j,k}$ and n_k exceeded the number of parameters. Based on simulations performed with varying number of data points (detailed description can be found in the Supplementary material), the minimum number of data points for MI estimation was set to 8. In order to validate the capability of the proposed approach to appropriately capture variable dynamics of the performance measures, we simulated different rehabilitation scenarios under varying conditions (see Supplementary material). As we aimed at estimating MI at subtask level, separate MI models were used for each movement direction of the training exercise.

2.2.5 Performance measures

Previous studies have shown that mechanisms of post-stroke recovery can be described by factors related to movement velocity, smoothness, and efficiency (Bosecker et al., 2010; Panarese et al., 2012a, 2016). Unlike physiological signals, these kinematic performance measures can be easily recorded and processed in real-time, promoting their use in clinical settings. In this study, we selected two continuous performance variables r_j for the use with the MI model: i) the mean velocity of a movement (MV) and ii) the spectral arc length (SAL), a robust and consistent measure of movement smoothness (Balasubramanian et al., 2012). MV was calculated using the x , y , and z

coordinates of the robotic handle recorded by the exoskeleton for each movement. SAL is a dimensionless measure quantifying movement smoothness by negative values, where higher absolute values are related to jerkier movements. It was calculated using the position of the robotic handle recorded by the exoskeleton for each movement and the mathematical equations presented in (Balasubramanian *et al.*, 2012). Regarding rehabilitation training, values of SAL close to zero are desirable, as well as high values of MV. The discrete variable n_k , instead, was denoted as success (SUCC) and defined separately for the experiments with the healthy participants and the patients. For the patients, the value of SUCC was determined by the robotic assistance (i.e., SUCC = 1 if the patient performed the movement without robotic assistance, SUCC = 0 otherwise). On the other hand, the healthy participants were expected not to rely on the robotic assistance, although it was also provided if necessary. This assumption was supported by preliminary experiments with healthy subjects (see Supplementary material). Therefore, in order to have an equivalent discrete variable for the experiment with healthy subjects, we defined the value of SUCC based on the execution time (i.e., SUCC = 1 if a healthy participant completed the movement within the time threshold t_{th} , SUCC = 0 otherwise). The time threshold t_{th} was set to 4 seconds based on preliminary experiments with healthy subjects (see Supplementary material).

2.2.6 Training adaptation routine

Using the model described in the previous section, MI was continuously tracked for each subtask (i.e., a movement towards a specific target) and used to implement a personalized training routine (Figure 2.1e). At the beginning of the training, we identified the subject-specific difficulty level for each subtask of the training exercise based on an initial assessment of the performance measures. The subtasks were then ordered by increasing difficulty and the easiest ones were selected as the initial training set. During the training, a subtask was removed from the set of current training subtasks when the MI estimates for this movement exceeded a given threshold and approached a plateau. Specifically, the probability of performing the subtask successfully p_k , had to be greater than 0.5, and the difference between two consecutive MI values (i.e., between two repetitions of the same subtask) had to be smaller than 5% for at least four repetitions. Given the observation equation for p_k , the former condition ($p_k > 0.5$) can be equally expressed in terms of the motor improvement: $MI_k > 0$. Once these conditions were satisfied, the subtask was replaced by a more difficult one from the training queue. The removed subtask was placed back into the training queue, so that it could be reintroduced at a later stage.

2.2.7 Statistical analysis

Healthy participants were grouped into fast ($n = 9$) and slow ($n = 8$) adapters by a post-hoc median split based on the total number of replaced targets during the inversion blocks.

For the healthy subjects, statistical tests were performed to support the following hypotheses:

- i) The introduction of the vision inversion degrades the performance of fast and slow adapters for the reaching movements
- ii) Performances for reaching movements with vision inversion improve with training for both groups.
- iii) Even after training, performances for reaching movements with vision inversion of both groups do not reach the levels of the initial assessment (without inversion).

-
- iv) There is a performance difference between fast and slow adapters, which is observable in the moment the vision inversion is introduced and also at the end of the vision inversion.

For the blocks $A_{I,1-3}$, B_1 and B_5 , movements towards all presented training targets were combined to calculate mean values for MV, SAL and %SUCC for each healthy subject. Each individual performed 54 movements in $A_{I,1-3}$ and 40 movements in B_1 and B_5 . Using the Shapiro-Wilk normality test, mean values for MV, SAL, %SUCC for fast and slow adapters were tested for normal distribution separately. The data were not normally distributed. In order to support the first three claims, a Friedman test was performed for the mean values of MV, SAL and %SUCC for the three time blocks (i.e., for $A_{I,1-3}$, B_1 and B_5). Following the Friedman tests, post-hoc tests were performed between pairs of blocks using Wilcoxon signed-rank tests with Holm-Bonferroni correction (for three comparisons) to illustrate the differences between the blocks. Specifically, point i) was verified by comparison between $A_{I,1-3}$ and B_1 ; point ii) was verified by comparison between B_1 and B_5 ; and point iii) was verified by comparison between $A_{I,1-3}$ and B_5 . To verify point iv), we used Wilcoxon rank-sum tests with Holm-Bonferroni correction (for three comparisons) to compare the mean values of MV, SAL and %SUCC between fast and slow adapters in the blocks $A_{I,1-3}$, B_1 and B_5 .

For the patients, statistical tests were performed to support the following hypotheses:

- i) Motor performance in the reaching task improved for both patients following the completion of the robot-aided rehabilitation training.
- ii) The motor improvement is retained four weeks after the end of the training for both patients.
- iii) Motor performance right before the replacement of a target and after reinsertion of the same target is comparable.

For the assessment blocks, all movements performed by the patients in the session were combined, resulting in 36 observations for P01 in each block and 54 observations for P02, respectively. To verify the two first claims, Friedman tests were performed for MV, SAL and %SUCC between the initial assessment session right before the treatment sessions ($A_{I,2}$), the final assessment session right after the training ($A_{F,1}$), and the follow-up session ($A_{F,2}$). Following the Friedman test, pairwise comparisons were performed, between these blocks using Wilcoxon signed-rank tests with Holm-Bonferroni correction (two comparisons). Specifically, we compared $A_{I,2}$ and $A_{F,1}$ to verify claim i) and $A_{F,1}$ and $A_{F,2}$ to verify claim ii). Friedman tests and pairwise comparisons were performed for each patient separately. To verify claim iii), we analyzed the values of MV, SAL and %SUCC before the replacement of the targets and after their reinsertion. For each target, mean values of improvement were calculated with respect to the first four repetitions in $A_{I,2}$ for the last four repetitions before replacement and for the first four repetitions after reinsertion. We then used Wilcoxon signed-rank tests to analyze differences in MV, SAL and %SUCC for all targets before replacement and after reinsertion. The analyses were performed for each patient separately. The power of the statistical tests was computed using z-tests and approximations of normal distributions of the data. All analyses were performed using MATLAB (The MathWorks, Natick, Massachusetts). The significance levels were set to $\alpha < 0.05$ (type I error) and $\beta < 0.2$ (type II error).

2.3 Results

2.3.1 Experimental validation with healthy participants

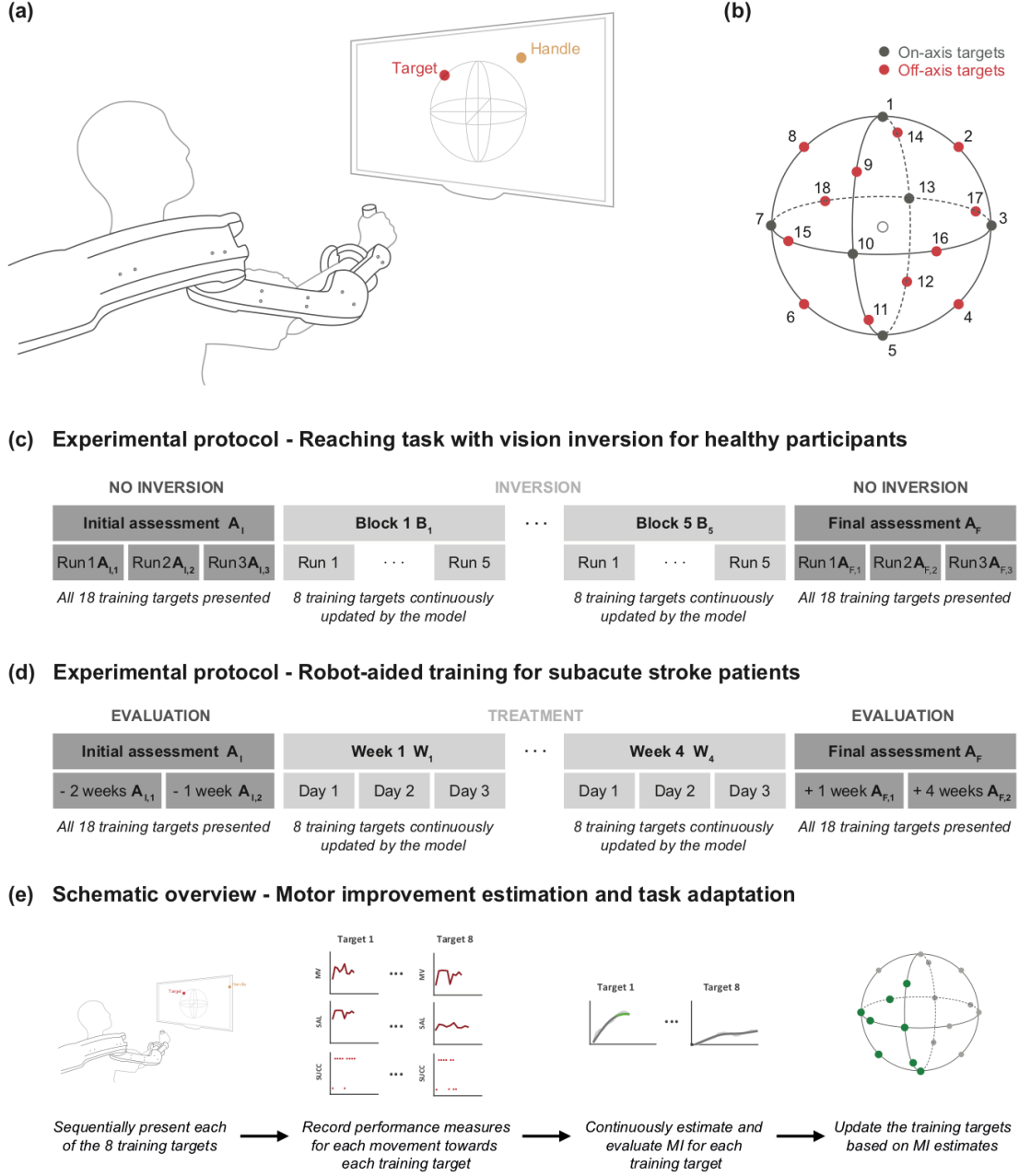


Figure 2.1 – Experimental setup and protocols. (a) Schematic overview of experimental setup. (b) Design of the three-dimensional point-to-point reaching task. Eighteen targets (representing the different subtasks) are positioned over a sphere of 19 cm of radius (equally distributed on the three planes). The empty circle represents the center of the workspace (starting position). (c) Experimental protocol for healthy participants. Experiments were completed in a single session and were divided into blocks (one initial assessment block $A_{i,1-3}$, five inversion blocks B_{1-5} , one final assessment block $A_{f,1-3}$). The assessment blocks consisted of three runs, each composed of 18 reaching movements (one towards each target). The inversion blocks consisted of five runs, each composed of eight reaching movements. The training targets for the inversion blocks were automatically selected by the implemented personalization routine. Breaks were allowed between the blocks

to prevent fatigue. **(d)** Experimental protocol for the patient. During the initial ($A_{I,1-2}$) and final ($A_{F,1-2}$) assessment sessions, all eighteen targets were presented to the patient. For each treatment session eight training targets were selected by the implemented personalization routine. The total number of repetitions performed in each session was determined by the physical therapist. **(e)** Schematic overview of the different steps performed for the adaptive scheduling of the reaching task with vision inversion for healthy participants and the reaching task without vision inversion for patients.

The model was first tested with 17 healthy subjects, who performed a point-to-point reaching task using an upper-limb exoskeleton (ALEX, Figure 1a-b). As an additional constraint, the healthy subjects had to complete the task with a vision inversion implemented in the blocks B_{1-5} (Figure 1c). During these five blocks, we tested whether our model was capable to continuously adapt the reaching task according to the performances of each individual. For each participant, the performance measures recorded by the exoskeleton were deployed in a state-space model to continuously estimate the motor improvement (MI) for each direction of movement independently. When the MI values for a movement direction passed a certain threshold and remained stable for a given time window (see Section 2.2.6), the movement was replaced with a new target from the training queue (Figure 1e). The latter contained eighteen directions of movement (i.e., targets) and it was generated for each individual at the beginning of the training based on a semi-randomized procedure (see Section 2.2.3).

Task adaptation at subject level

Despite a general improvement for all participants, the healthy subjects differed considerably in their adaptation speed, as quantified by the number of new targets introduced during the inversion blocks B_{1-5} . Since this study was exploratory in nature, we did not expect *a priori* such a variety of adaption speeds. However, a post-hoc analysis of the number of new introduced targets allowed to identify two groups of participants using a median split. Specifically, participants were classified into fast adapters ($n = 9, 7.7 \pm 1.1$ new targets) and slow adapters ($n = 8, 2.6 \pm 2.0$ new targets). This result emerged as an unforeseen opportunity to highlight the model's capability to differentiate varying motor adaptation rates. As hypothesized, the performance measures (i.e., movement velocity (MV), movement smoothness (SAL) and task completion rate (%SUCC)) degraded for both groups after the introduction of the vision inversion in B_1 (Figure 2.2a-c).

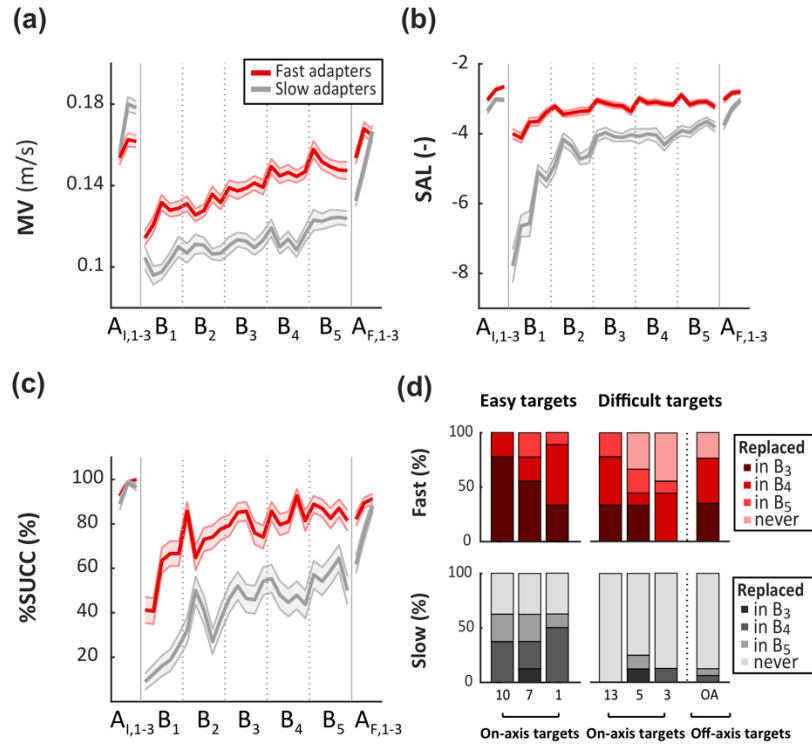


Figure 2.2 – Analysis of performance measures for the experiment with healthy participants. Average values of mean velocity (MV, panel a), spectral arc length (SAL, panel b) and rate of success (%SUCC, panel c) for each run (eight reaching movements) of fast (red) and slow (grey) adapters. Measures were averaged for all targets presented during a run and for all subjects of a group. Shaded areas depict standard error of the mean (sem). Vertical bars (panel d) depict the percentage of subjects in each group for which a target was replaced in B₃₋₅ or was not replaced at all. No targets were replaced in and B₁₋₂ due to lack of data needed for proper estimation of motor improvement.

Participants in both groups gradually improved from B₁ to B₅, although they did not reach their initial motor performances (i.e., performances during A_{I,1-3}). Friedman tests confirmed the differences between the blocks A_{I,1-3}, B₁ and B₅, for both groups and for all performance measures (Table 2.2). Post-hoc analyses were performed using Wilcoxon signed-rank tests with Holm-Bonferroni corrections for three comparisons. The analyses confirmed pairwise differences between different pairs of blocks (A_{I,1-3} and B₁, B₁ and B₅, A_{I,1-3} and B₅) within both groups and for all performance measures, except for MV between A_{I,1-3} and B₅. When introduced to the vision inversion in B₁, fast adapters outperformed slow adapters as measured by all performance measures. A statistical comparison of the performance measures in A_{I,1-3} between the two groups (Table 2.3) showed that there were no statistically significant differences for SAL and %SUCC (statistical power of 0.99 and 0.85 respectively), while no conclusions could be drawn for MV (statistical power 0.42). The performance difference was still observable in B₅, the last block with vision inversion.

Table 2.2 – Within-group comparisons of healthy subjects at three different time points

	Performance measures (mean \pm standard error of the mean, sem)			Friedman's test		Wilcoxon signed-rank test (Holm-Bonferroni correction for $n = 3$)		
	$A_{1,1-3}$	B_1 (inversion)	B_5 (inversion)	Chi-Square	p	p_{corr} $A_{1,1-3}-B_1$	p_{corr} B_1-B_5	p_{corr} $A_{1,1-3}-B_5$
Fast Adapters (n = 9)								
<i>MV</i> (m/s)	0.16 \pm 0.01	0.13 \pm 0.01	0.15 \pm 0.01	10.89	0.0043	0.0156	0.0117	0.3594
<i>SAL</i>	-2.81 \pm 0.07	-3.77 \pm 0.12	-3.09 \pm 0.19	16.22	0.0003	0.0117	0.0078	0.0117
<i>%SUCC</i>	97.1 \pm 1.1	55.8 \pm 3.4	85.4 \pm 2.8	18.0	0.0001	0.0117	0.0117	0.0117
Slow Adapters (n = 8)								
<i>MV</i> (m/s)	0.17 \pm 0.01	0.10 \pm 0.01	0.12 \pm 0.01	13.0	0.0015	0.0156	0.0156	0.1094
<i>SAL</i>	-3.13 \pm 0.10	-6.39 \pm 0.34	-3.82 \pm 0.11	16.0	0.0003	0.0234	0.0234	0.0234
<i>%SUCC</i>	94.7 \pm 1.5	16.3 \pm 3.9	57.0 \pm 5.6	16.0	0.0003	0.0234	0.0234	0.0234

Task adaptation at subtask level

We then analyzed which initial training targets were replaced by the algorithm during the inversion blocks and when this replacement occurred (Figure 2.2d). The insertion of new targets did not start before B_3 , as in B_{1-2} the amount of data for each training target was not sufficient to obtain proper MI estimations (see section 2.2.4). Overall, movements towards the off-axis targets (Figure 2.1b) seemed to be more difficult: the algorithm replaced these targets for 13% of the slow adapters and for 77% of the fast adapters. The on-axis targets instead, were replaced for 38% of the slow adapters and 87% of the fast adapters. However, we also observed differences within the on-axis targets: targets 3, 5 and 13 were replaced for 13% of the slow adapters and for 74% of the fast adapters, while the replacement for targets 1, 7 and 10 was achieved by 63% of the slow adapters and by 100% of the fast adapters. Following this analysis, we classified the targets into easy (1, 7 and 10) and difficult (3, 5, 13 and off-axis) subsets. The results suggested that despite the differences in the overall performance, the subsets of easy and difficult targets appeared to be similar for both groups. Nevertheless, we observed an earlier replacement of the easy targets for the fast adapters: 56% of the easy targets were replaced in B_3 (4% for slow adapters), 33% were replaced in B_4 (38% for slow adapters), and 11% were replaced in B_5 (21% for slow adapters). In contrast, for the difficult targets, the fast adapters also needed more time to achieve a replacement (if they were replaced eventually): 26% of the difficult targets were replaced in B_3 (3% for slow adapters), 35% were replaced in B_4 (5% for slow adapters) and 14% were replaced in B_5 (5% for slow adapters).

Table 2.3 – Between-group comparisons of healthy subjects at three different time points

	Fast Adapters (n = 9)	Slow Adapters (n = 8)	Wilcoxon rank-sum test (Holm-Bonferroni correction for n = 3)
Performance measures in A_{1,1-3} (mean ± sem)			p_{corr}
<i>MV (m/s)</i>	0.16 ± 0.002	0.18 ± 0.003	0.2359
<i>SAL</i>	-2.69 ± 0.03	-3.03 ± 0.04	0.0619
<i>%SUCC</i>	99.3 ± 0.5	97.3 ± 1.0	0.2973
Performance measures in B₁ (mean ± sem)			p_{corr}
<i>MV (m/s)</i>	0.11 ± 0.002	0.10 ± 0.002	0.0360
<i>SAL</i>	-3.77 ± 0.06	-6.34 ± 0.18	0.0002
<i>%SUCC</i>	55.6 ± 2.9	16.0 ± 2.3	0.0002
Performance measures in B₅ (mean ± sem)			p_{corr}
<i>MV (m/s)</i>	0.15 ± 0.002	0.12 ± 0.002	0.0360
<i>SAL</i>	-3.09 ± 0.04	-3.82 ± 0.07	0.0002
<i>%SUCC</i>	85.4 ± 2.1	57.3 ± 3.1	0.0002

To illustrate the behavior of individual participants at subtask level, we present the data of one exemplary subject from each group for the movements towards the same two targets (Figure 2.3). We selected one target from the subset of the easy (target 10) and one target from the subset of the difficult (target 13) targets. The examples illustrate the different adaptation rates observed between subjects and targets. For the easy target, the performance measures for the fast adapter quickly improved and approached a plateau. The slow adapter, instead, showed difficulties until the fourth repetition, reflected particularly by SAL and SUCC. Nonetheless, starting from the fifth repetition, they also managed to adapt the movements to the visual inversion and finally reached the conditions for the target replacement at the twelfth repetition. The difficult target instead, appeared to be more challenging for both subjects. For this target, the fast adapter showed an improvement in all performance measures only after the tenth repetition and finally reached the conditions for the target replacement after eighteen repetitions. In contrast, the slow adapter did not manage to satisfy the conditions for a replacement. Despite a trend of improvement, the motor performance was not yet sufficient to trigger a replacement of the target.

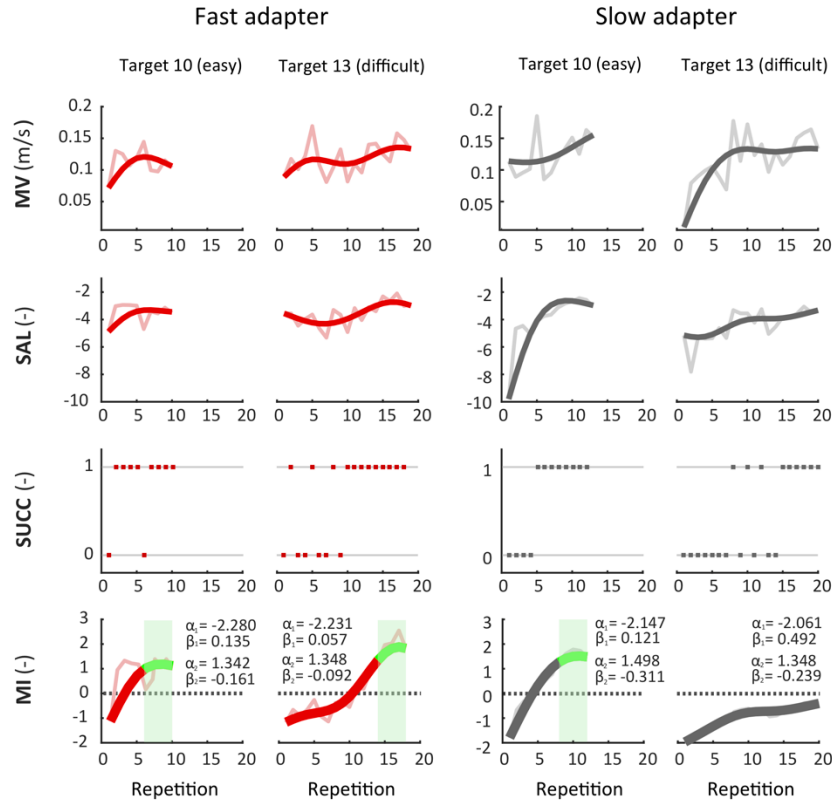


Figure 2.3 – Examples of MI estimates and performance measures at subtask level. Data is presented for a fast adapter and a slow adapter for the same two targets. Repetitions for each target are concatenated for all inversion blocks and presented in chronological order. Data for mean velocity (MV), spectral arc length (SAL) and MI were low pass filtered for visualization purposes (raw data shown in light red/grey). Dotted lines depict one of the necessary conditions ($MI > 0$) for triggering a target replacement. Green areas indicate the time span where the model detected a performance plateau and triggered a target replacement. Estimated model parameters (α_i , β_i) for each target and subject are presented next to the corresponding MI curves (a summary and analysis on the model parameters can be found in the Supplementary material).

2.3.2 Pilot test with subacute stroke patients

To provide further evidence about the feasibility of the presented approach in clinical settings, we finally performed a pilot test with two subacute stroke patients, who completed four weeks of personalized robot-aided training complementing standard rehabilitation therapy (Figure 2.1d, see Section 2.2.1 for details). During the robot-aided training, the patients performed the reaching tasks without vision inversion and the set of targets was automatically adapted based on a continuous evaluation of the MI estimates for each training target.

Based on the initial assessment of their scores on the Fugl-Meyer assessment for upper extremities (FMA-UE), we observed a remarkable difference in the degree of motor impairment of patient P01 (22 points at $A_{1,2}$, Figure 2.4a) compared to patient P02 (59 points at $A_{1,2}$). This difference was equally reflected by the number of movements (nMov) performed in the initial assessment sessions, which was notably lower for P01 (31 movements compared to 69 movements for P02 at $A_{1,2}$). The different degrees of initial impairment allowed us to evaluate the feasibility of our approach for two patients exhibiting disparate initial motor abilities.

Following the training, both patients showed improvements for MV, SAL, and %SUCC (Figure 2.4a). Comparing the performances between the second initial assessment session $A_{I,2}$ and the first final assessment session $A_{F,1}$ we found that both patients improved on all measures (Table 2.4). One month after the training, both patients performed a follow-up assessment $A_{F,2}$. During this session we observed that both patients managed to retain the improvements observed in $A_{F,1}$. These differences were confirmed by Friedman tests between the three sessions ($A_{I,2}$, $A_{F,1}$, and $A_{F,2}$) for both patients, except for the %SUCC measure for P02. This can be related to the fact that the values for %SUCC for patient P02 already started at a very high level (98.6% at $A_{I,2}$) and thus left smaller room for improvement. Post-hoc Wilcoxon tests with Bonferroni correction for multiple comparisons (i.e., two pairwise comparisons), confirmed the differences between $A_{I,2}$ and $A_{F,1}$ for the performance measures for both patients. For comparisons between $A_{F,1}$ and $A_{F,2}$ (i.e., differences between end of treatment and follow-up one month later), the only statistically significant difference was found for MV values of P01. Though no clear differences could be observed between $A_{F,1}$ and $A_{F,2}$ for the other measures, no further conclusions can be drawn due to the low statistical power of the tests (smaller than 0.8).

Table 2.4 – Performance measures of the two stroke patients (P01 and P02) before and after the treatment sessions

	Performance measures by session (mean \pm sem)			Friedman's test		Wilcoxon rank-sum test (Holm-Bonferroni correction for $n = 2$)		
	$A_{I,2}$	$A_{F,1}$	$A_{F,2}$	Chi-Square	p-value	p_{corr} $A_{I,2}-A_{F,1}$	p_{corr} $A_{I,2}-A_{F,2}$	p_{corr} $A_{F,1}-A_{F,2}$
P01								
MV (m/s)	0.08 ± 0.004	0.11 ± 0.005	0.13 ± 0.005	32.44	9.01e-08	5.89e-04	5.89e-04	0.015
SAL	-6.92 ± 0.65	-5.31 ± 0.26	-5.15 ± 0.23	6.33	0.041	0.035	0.031	0.892
%SUCC	77.8 ± 7.3	100 ± 0.0	94.4 ± 5.6	10.18	0.006	0.031	0.033	> 0.99
P02								
MV (m/s)	0.09 ± 0.003	0.12 ± 0.002	0.11 ± 0.004	18.78	8.36e-05	0.001	0.002	0.586
SAL	-5.49 ± 0.29	-4.04 ± 0.21	-3.99 ± 0.19	16.33	0.0003	0.004	0.003	0.844
%SUCC	98.6 ± 1.4	100 ± 0.0	100 ± 0.0	4.0	0.1353	> 0.99	> 0.99	> 0.99

Along with the improvements of the performance measures, we also observed higher FMA-UE scores for both patients following the training. In that respect, we observed a lower increase for patient P02 (+3 points between $A_{I,2}$ and $A_{F,1}$) compared to patient P01 (+8 points). Both patients further improved their FMA-UE scores when assessed in the follow-up session $A_{F,2}$. Finally, we also observed an increase in the number of performed movements per session (nMov) for both patients.

As for this measurement, patient P02 (+40 movements at $A_{F,1}$ and +76 movements at $A_{F,2}$ compared to $A_{I,2}$) improved more than patient P01 (+23 movements at both $A_{F,1}$ and $A_{F,2}$ compared to $A_{I,2}$).

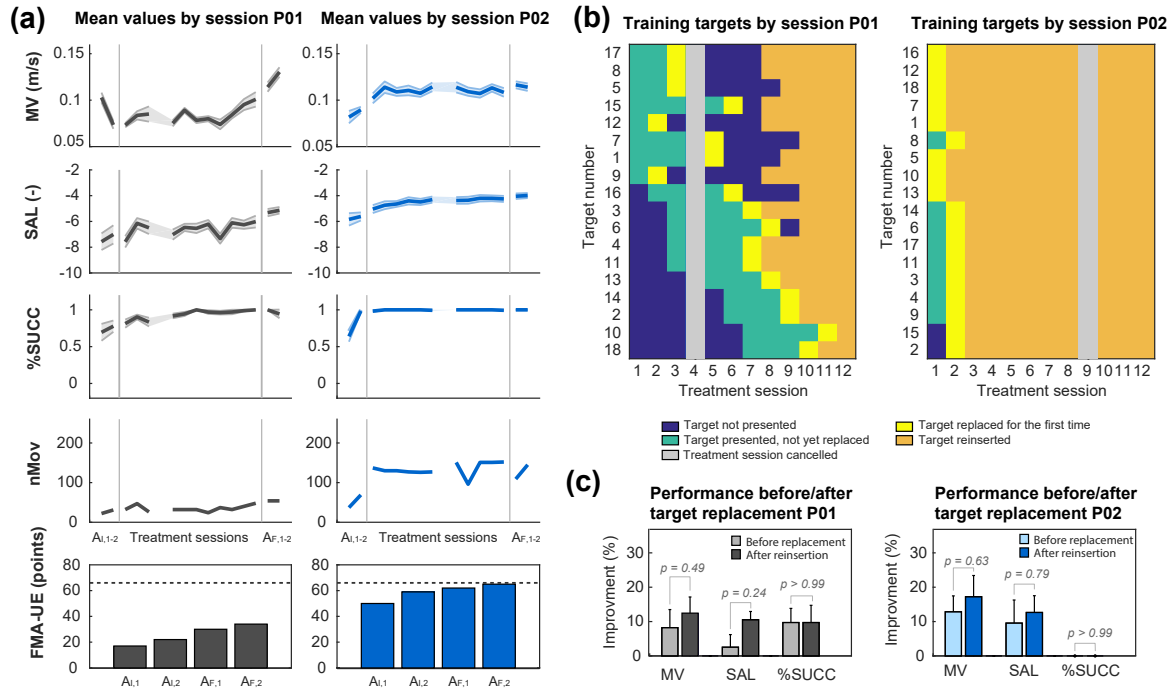


Figure 2.4 – Summary of the results from the pilot test with two subacute stroke patients. **(a)** The first three rows show the mean values for mean velocity (MV), spectral arc length (SAL) and rate of success (%SUCC) for each assessment and treatment session of both patients. Measures were averaged for all targets presented during a session, shaded areas depict standard error of the mean (sem). The fourth row shows number of movements performed by the patients in each session. The fifth row shows the scores on the Fugl-Meyer scale for upper extremities (FMA-UE) for initial ($A_{I,1-2}$) and final ($A_{F,1-2}$) assessment sessions. The dotted line indicates the maximum achievable score for FMA-UE (66 points). **(b)** Summary of the training targets presented to the patients in each treatment session. Targets are listed by the order as presented to the patients (first eight targets from the top are the initial training set). **(c)** Analysis of performance measures for two different time points (before replacement and after reinsertion). Values are compared between the last four movements towards a training target before its replacement and the first four movements towards the target after it has been reinserted for training. The data shows the mean improvement for MV, SAL and %SUCC averaged for all targets at both time points. Improvements were calculated with respect to the mean values obtained from the first four movements towards each target in $A_{I,2}$. Error bars depict standard error of the mean (sem). P-values of Wilcoxon signed-rank tests are reported above the bars.

Both patients progressed during the rehabilitation training and eventually achieved a replacement of all eighteen training targets. However, the temporal dynamics of these replacements appeared to be strongly different (Figure 2.4b). In line with the lower degree of motor impairments observed from the performance measures and the FMA-UE scores, patient P02 achieved a replacement of all training targets after only two training sessions. Patient P01, instead, needed considerably more time to achieve the replacement of all eighteen targets. While some of the initial training targets (i.e. targets 9 and 12) were already replaced after two treatment sessions, other targets (i.e. targets 1, 7 and 15) needed more than 4 training sessions to trigger a replacement. It was only after eleven treatment sessions that all eighteen training targets were presented to patient P01. These observations emphasized the ability of our model to differentiate between both subject- and subtask-specific time courses of motor improvement, also in a real clinical setting. The examples illustrate how

the model adapted the training schedules according to the patients' individual abilities, granting patient P01 enough time to practice certain movements, and at the same time, responding to the fast recovery of patient P02 by continuously introducing new training targets.

Upon completion of the full set of training targets (i.e., when all targets had been replaced at least once), the therapy was carried on by reintroducing all targets and presenting them alternately in the order in which they were replaced. This allowed us to assess whether the patients' performance was retained once a training target was reintroduced, so as to validate that the replacements orchestrated by the algorithm had occurred when the movements towards the targets had actually recovered. In order to do so, we compared the mean values for MV, SAL, and %SUCC from the last four repetitions of a movement before a target was replaced by the algorithm with the mean values of the four repetitions of the same movement after the first reinsertion as a training target (Figure 2.4c). Both values are calculated with respect to the mean values obtained from the first initial four repetitions of the movements towards a training target. The overall analysis for all eighteen targets showed that compared to the initial movements towards the targets, all values for the three performance measures were higher right before the targets were replaced by the algorithm. Moreover, both patients retained the improvements gained during the training or even further improved their performance for a movement when the corresponding training target was reintroduced at a later stage. Using a Wilcoxon signed-rank test, we did not find statistically significant differences ($p > 0.24$) for any value of the three performance measures of both patients between the two time points (i.e., before replacement and after reinsertion). However, no further conclusions can be drawn due to the low statistical power of the tests (smaller than 0.8). Nevertheless, the results indicate that the algorithm only replaced training targets when motor performance had stably improved and that patients' performances did not degrade when training targets were reintroduced at a later stage.

2.4 Discussion

In this study, we demonstrated the feasibility of a model-based approach for the personalization of robotic rehabilitation training based on motor performance during three-dimensional training tasks. Differently from previous work in this field, the model was designed to allow estimation of motor improvement (MI) in subacute stroke patients, allowing to capitalize on the enhanced potential for plasticity in the early stage after the injury (Biernaskie, 2004; Cramer, 2008). A first experimental validation in healthy subjects demonstrated the ability of our model to capture MI linked to visual motor adaptation. The results were further validated by a clinical pilot test with two subacute stroke patients, in which motor recovery was tracked and harnessed by our adaptive personalization routine.

2.4.1 Direction dependent training adaptation for three-dimensional reaching movements

We first sought to validate the model's ability to continuously track MI and dynamically adapt the training task under controlled conditions. To this end, we tested our approach in a group of seventeen healthy subjects. In order to mimic the motor deficits observed in stroke patients, we introduced a manipulation of the visual feedback, by inverting the directions of the 3D environment. While the physiological mechanisms underlying motor adaptation and motor recovery are most likely not equivalent, the main objective of this experimental design was merely to obtain an

adaptation curve that resembles post-stroke motor recovery, on which we could validate the efficacy of our model. Our results suggest that motor adaptation to vision inversions in healthy subjects may exhibit similar temporal dynamics for the selected performance measures as previously observed for stroke patients undergoing robot-aided rehabilitation (Panarese *et al.*, 2012a, 2016). Indeed, when introduced to the vision inversion (during the blocks B1 to B5), the performance of the participants dropped drastically and gradually improved throughout the training (Figure 2.2).

During the experiments, the MI model tracked when a movement towards a target was performed efficiently despite the vision inversion, and dynamically adjusted the training by replacing this target with a more difficult one from the training queue. Based on the number of new inserted training targets, we divided the healthy population into two separate clusters: fast and slow adapters. The analysis on the performance measures showed that the fast adapters learned to cope with the manipulated environment very quickly, while the slow adapters needed considerably more time to reach similar performances (Figure 2.3). The MI model was able to capture these individual performance differences for different movement directions and introduced new training targets in a well-timed manner, i.e., targets were replaced when subjects reached a performance plateau. The advantages of monitoring motor improvement at subtask level were supported by additional post-hoc analyses (see Supplementary material). The analyses illustrated that if motor improvements were estimated for the reaching task overall (i.e., chronologically combining the recorded data for movements in all directions), improvements for individual subtasks would have been obscured by inferior performances of other, more difficult, subtasks. Moreover, the detection of performance plateaus would not correspond to the actual performances for each subtask. As a result, some subtasks would be kept too long, while others would be replaced too soon, potentially leading to a less efficient training schedule. Likewise, individual training progressions for specific subtasks were also observed for the two stroke patients participating in this study (Figure 2.4b). We therefore, believe that the current study further supports the approach to specifically consider MI estimation at subtask level, as it has been proposed in our previous work (Panarese *et al.*, 2012a). The results of the current study suggest that this subtask dependency does not only apply to planar movements, but also extends to three-dimensional movements. In order to optimize robotic treatment protocols, future studies should therefore specifically aim at evaluating motor performance at subtask level.

When comparing the performances for each subtask, we observed that off-axis targets were replaced less often than on-axis targets and they, thus, seemed to be more difficult (Figure 2.2d). This finding appears to be in line with results from similar studies involving vision inversion in planar setups (Cunningham and Pavel, 1991; Werner and Bock, 2010). These studies demonstrated that participants showed better performance for reaching movements lying on the axis perpendicular to the inversion. The present study extends these insights to three-dimensional reaching movements. However, the results showed that there were also remarkable performance differences among the on-axis targets. An analysis on the replaced training targets demonstrated that the subsets of easy (1, 7 and 10) and difficult (3, 5, 13 and off-axis) targets appeared to be similar for both types of adapters. Easy targets were mostly replaced earlier and more frequently than the difficult ones (Figure 2.2d). It could be that the medial and proximal movements towards targets 7 and 10 tended to be easier for the participants. However, since these tendencies were not observed in the patients or the healthy subjects involved in the preliminary study (see Supplementary material), we presume that the performance differences for the on-axis targets could be linked to the visually inverted environment. Previous studies have investigated vision inversion in reaching movements and suggested that the adaptation to such manipulations involves a complex mixture of implicit and

cognitive processes (Werner and Bock, 2010; Lillicrap *et al.*, 2013). For instance, it has been argued that for reaching tasks involving left-right reversal, new control policies need to be acquired by the motor system, as opposed to visual rotations (i.e., rotating the visual feedback around the movement origin in one direction by less than 90°), which only require a recalibration of an existing control policy (Telgen *et al.*, 2014). The implicit adaptation to such inversions has previously been assessed by aftereffects (Wilterson and Taylor, 2019). In the current study, we have observed that especially fast adapters had more initial difficulties in readapting their movements when the vision inversion was removed (between B5 and AF,1). Although this was mainly observed for a few initial movements after removing the inversion, it could suggest that fast adapters were more likely to learn the new control policy through implicit adaptation and therefore, were more successful in completing the inverted reaching task. However, to this day, these phenomena have only been investigated for planar reaching movements, mostly involving a one-dimensional inversion (mirror-reversal). Further research would be necessary to examine these phenomena in three-dimensional reaching movements involving multi-dimensional inversions. In this context, it would also be interesting to determine why the reaching movements towards some on-axis targets appeared to be more challenging in the inverted environment, independent from the individual adaptation speed of the subjects.

Finally, we would also like to raise the question of motivational implications resulting from the automated training adaption. From informal observations made during the experiments with the healthy subjects, we noticed that many participants showed increased motivation and verbalized satisfaction when new training targets were introduced. Motivation is known to be a crucial factor in rehabilitation and finding ways to maintain and improve it has always been a matter of interest (Maclean *et al.*, 2000, 2002; Colombo *et al.*, 2007). With regard to this issue, it seems like the automated character of our approach, enabling dynamic and well-timed task adaptation, may have positive impacts on training engagement.

2.4.2 Personalization of rehabilitation therapy

The potential of our implementation was finally evaluated in a clinical pilot test with two subacute stroke patients, who completed four weeks of robot-aided rehabilitation training following our adaptive approach. Based on the devised method, the training of these two patients was continuously monitored and the point-to-point reaching task was adapted in real-time to match their level of ability.

The results obtained from these two patients suggested that in general, the selected performance measures (MV, SAL and SUCC) appeared to be suitable for the estimation of motor improvement in subacute stroke patients. Moreover, the temporal dynamics of the performance measures (Figure 2.4a) appeared to be similar to the ones previously reported for chronic stroke patients (Panarese *et al.*, 2012a, 2016). In past studies, the selected measures have been shown to correlate with clinical scores (Bosecker *et al.*, 2010) and they have been linked to distinct post-stroke deficits and mechanisms of recovery (Nordin *et al.*, 2014; Panarese *et al.*, 2016). Specifically, the percentage of accomplished tasks was mostly associated to paresis (i.e., the decreased ability to volitionally modulate motor units activation (Lang *et al.*, 2013)), whereas movement velocity and smoothness were related to an abnormal muscle tone (Nordin *et al.*, 2014). Although continuous adaptation of the difficulty for reaching tasks has been explored before (Metzger *et al.*, 2014; Octavia and Coninx, 2014; Grimm *et al.*, 2016), the decisions to change task difficulty were mainly based on one or

multiple task completion variables, measuring whether the patient was able to complete tasks or not. The present study extends the decision rules by additionally integrating two variables related to movement kinematics, namely movement velocity and smoothness, which also characterized the neuro-biomechanical status of the patients (Murphy *et al.*, 2011). Nevertheless, some tuning of the parameters could be considered to further enhance the efficacy of the motor improvement model. For instance, we observed that the patient with a lower degree of initial impairments (P02) barely made use of the robotic assistance provided by the exoskeleton, leading to almost no variance in the variable SUCC. In this regard, future studies may explore other performance measures and models, to achieve a more exhaustive evaluation of the patients' status. In this context, the use of a model-based approach, such as the one proposed in the current work, can facilitate the integration of other measures which have been explored before, such as for example muscle activity (Krebs *et al.*, 2003) or psychophysiological signals (Badesa *et al.*, 2016).

The results for the two patients showed as well that targets were replaced by the model at appropriate moments, i.e., when the patients' performance had improved and started to saturate. Indeed, it could be argued that a replacement of a subtask occurring too soon would have led to degraded motor performances in further evaluations. However, motor performances of both patients were retained when targets were reintroduced (Figure 2.4c), indicating that the estimated recovery was preserved. Nevertheless, other methods for task scheduling could be introduced to further optimize the training progression. Indeed, previous work has suggested that effective scheduling of multi-task motor learning should be based on prediction of long-term gains rather than on current performance changes (Lee *et al.*, 2016). Along these lines, we have implemented the time window of the last four repetitions, which are always taken into account for the evaluation of motor performance. However, it should be acknowledged that other, more sophisticated, methods to adapt the schedules may lead to higher gains in rehabilitation and are therefore worth exploring. For instance, task difficulty could be increased by introducing new subtasks depending on more complex movements within the same workspace, in order to exploit generalization effects (Dipietro *et al.*, 2007, 2009). Another possible approach could be a semi-automatic implementation of the training adaptation, where the physical therapists remains in charge of the task adaptation, in order to benefit from their expertise, while in parallel harnessing the real-time MI estimates provided by the model as a decision support. Such solutions could further improve engagement and enhance the rehabilitative treatment by providing training tasks specifically adapted to the ability level of the patient.

The retention of improvements at target reinsertion together with the increase in FMA-UE scores for both patients are promising indications for the usability and efficacy of the presented approach in clinical settings. Nevertheless, it has to be acknowledged, that it is also known that subacute patients often report motor improvements even with limited training (Kwakkel *et al.*, 2006). Therefore, at the current state of this research, it cannot be presumed that improvements were merely elicited by the adaptive robot-aided therapy. However, several pieces of evidence suggested that the period immediately after the lesion, normally characterized by spontaneous neurological recovery, represents the critical time window in which the delivery of high dose and intense neurorehabilitation can elicit crucial improvements in functional tasks (Murphy and Corbett, 2009; Zeiler and Krakauer, 2013). Therefore, more and more robot-aided rehabilitation trainings should be targeting subacute stroke populations. In this context, our results illustrate the feasibility of using a personalization method to continuously monitor the status of both mild and severely impaired subacute stroke patients and to automatically adapt their motor retraining within practice sessions by continuously challenging their neuromuscular system.

2.4.3 Limitations of the study

Although the results of this study suggest that the proposed approach might be interesting for clinical applications, the limited sample size as well as the lack of an experimental control group receiving standardized robotic therapy, constrain the generalizability of the reported results. Yet clinical efficacy was not probed in this work. Moreover, the very different severities of initial impairment observed in the two patients of the pilot study do not allow for a controlled comparison. Therefore, further studies including larger cohorts of participants would be necessary to draw meaningful conclusions about the clinical relevance of the presented approach. Yet the results obtained from the present study may provide a useful basis for the design and implementation of such clinical studies. In this context, it would be particularly interesting to compare the clinical outcomes of the personalized approach presented in this study with non-adaptive robotic or conventional rehabilitation trainings. This is important, since previous work has suggested that pseudo-random scheduling of multiple tasks may be almost as effective as adaptive scheduling approaches (Lee et al., 2016).

2.5 Conclusion

In this work, we presented a model-based approach to personalize robot-aided rehabilitation therapy within rehabilitation sessions. The feasibility of this approach was demonstrated in experiments with seventeen healthy subjects and a pilot test with two subacute stroke patients providing promising results. However, due to the limited sample size, larger studies would be needed to demonstrate clinical relevance of the presented approach. While we implemented the proposed method for the use in upper limb rehabilitation of stroke patients, the usage is certainly not limited to such applications. The presented model can be adapted for the use with other robotic rehabilitation devices and training tasks, exploiting different performance measures and/or different observation equations. The real-time functionality and the identification of subject-specific abilities at subtask level could enhance robot-aided rehabilitation training, making it more purposive and efficient for the patients.

Chapter 3

Multimodal framework

A multimodal approach to capture post-stroke temporal dynamics of recovery

Camilla Pierella¹, Elvira Pirondini^{2,3}, Nawal Kinany^{1,2,3}, Martina Coscia⁴, Christian Giang¹, Jenifer Miehlbradt¹, Cécile Magnin⁵, Pierre Nicolo^{5,6}, Stefania Dalise⁷, Giada Sgherri⁷, Carmelo Chisari⁷, Dimitri Van de Ville², Adrian Guggisberg^{5,6} and Silvestro Micera^{1,8}.

¹ Bertarelli Foundation Chair in Translational Neuroengineering, Center for Neuroprosthetics and Institute of Bioengineering, School of Engineering, École Polytechnique Fédérale de Lausanne (EPFL), Lausanne, 1015, Switzerland; ² Medical Image Processing Laboratory, Ecole Polytechnique Fédérale de Lausanne (EPFL), Lausanne, 1015, Switzerland; ³ Department of Radiology and Medical Informatics, University of Geneva, Geneva, 1202, Switzerland; ⁴ Wyss Center for Bio- and Neuro-Engineering, Geneva, 1202, Switzerland; ⁵ Division of Neurorehabilitation, Department of Clinical Neurosciences, University Hospital Geneva, Geneva, 1206, Switzerland; ⁶ Laboratory of Cognitive Neurorehabilitation, Department of Clinical Neurosciences, Medical School, University of Geneva, Geneva, 1206, Switzerland; ⁷ Department of Translational Research and of new Technologies in Medicine and Surgery, University Hospital of Pisa, Pisa, Italy; ⁸ Translational Neural Engineering Area, The Biorobotics Institute, Scuola Superiore Sant'Anna, Pisa, 56025, Italy

Abstract – Objective. Several training programs have been developed in the past to restore motor functions after stroke. Their efficacy strongly relies on the possibility to assess individual levels of impairment and recovery rate. However, commonly used clinical scales rely mainly on subjective functional assessments and are not able to provide a complete description of patients' neuro-biomechanical status. Therefore, current clinical tests should be integrated with specific physiological measurements, i.e. kinematic, muscular, and brain activities, to obtain a deep understanding of patients' condition and of its evolution through time and rehabilitative intervention. **Approach.** We proposed a multivariate approach for motor control assessment that simultaneously measures kinematic, muscle and brain activity and combines the main physiological variables extracted from these signals using principal component analysis (PCA). We tested it in a group of six sub-acute stroke subjects evaluated extensively before and after a four-week training, using an upper-limb exoskeleton while performing a reaching task, along with brain and muscle measurements. **Main results.** After training, all subjects exhibited clinical improvements correlating with changes in kinematics, muscle synergies, and spinal maps. Movements were smoother and faster, while muscle synergies increased in numbers and became more similar to those of the healthy controls. These findings were coupled with changes in cortical oscillations depicted by EEG-topographies. When combining these physiological variables using PCA, we found that i)

patients' kinematic and spinal maps parameters improved continuously during the four assessments; ii) muscle coordination augmented mainly during treatment, and iii) brain oscillations recovered mostly pre-treatment as a consequence of short-term subacute changes. **Significance.** Although these are preliminary results, the proposed approach has the potential of identifying significant biomarkers for patient stratification as well as for the design of more effective rehabilitation protocols.

3.1 Introduction

Stroke is the leading cause of adult long-term disability in Western societies. More than 1.5 million people are affected every year in Europe (WHO, 2008). Even though acute stroke care and intensive rehabilitation are improving, two-thirds of chronic stroke survivors have to cope with persisting neurologic deficits, and only 20% of them are able to go back to their normal professional and private life (Di Carlo, 2009).

The most common impairments in the acute and chronic stages are cognitive conditions and motor deficits contralateral to the affected brain hemisphere (Lee *et al.*, 2015). A profound neuromuscular reorganization occurs after stroke (Levin, 1996; Cirstea *et al.*, 2003). The affected limb is typically characterized by spasticity (Bourbonnais *et al.*, 1989), stereotyped movement patterns, mainly caused by abnormal muscle co-activation and an enlarged activity of the antagonist muscles (Brunnström, 1970), which result in a reduced range of motion against gravity (Levin, 1996), and, thus, to a limited workspace in three-dimensional reaching movements (Ellis *et al.*, 2007; Sukal *et al.*, 2007).

A key factor in stroke recovery is the intensity of training, especially in the acute phase, to enhance functional restoration and prevent inactivity-related complications (Kwakkel *et al.*, 2004). Yet because of the patient-specific clinical picture, treatment programs might vary in duration, intensity, and frequency (Lo *et al.*, 2010). Therefore, the success of the rehabilitation processes depends on the ability of the clinician to discern the individual levels of impairment and responses to treatment with simple, robust, and effective methods.

Currently, patients are evaluated mainly using clinical scales, with Fugl-Meyer being one of the most adopted measures of motor impairment after stroke. Yet, the precision of these clinical tests are limited by inter-rater and intra-rater reliability (Bosecker *et al.*, 2010; Harrison *et al.*, 2013; Krebs *et al.*, 2014), as well as by floor and ceiling effects (Lamers *et al.*, 2014; Murphy *et al.*, 2015). Moreover, some of them require a consider amount of time to be administered. Clinical scales should, therefore, be integrated with targeted neuro-biomechanical assessments, in order to provide a more detailed description of the patients' clinical status.

Many instrumental approaches that investigate different domains of the hierarchical organization of the neuromusculoskeletal system can be employed for this purpose, including measures of kinematics, muscular, and brain activities.

In a recent work, Thrane and colleagues coupled standard clinical tests with upper extremity kinematics to reduce the ceiling effects of the Fugl-Meyer Assessment (Thrane *et al.*, 2019). They showed that post-stroke participants with near or fully recovered sensorimotor function still showed deficits in movement kinematics that were not captured by the clinical assessment. These kinematic measures provide a detailed and quantitative description of motor behaviors.

However, the neural deficits may be masked at the kinematic level by compensatory strategies and similar movements may be produced through different neuromuscular mechanisms. Therefore, muscular control strategies should be also considered in the patients' clinical picture. Indeed, several behavioral studies on animals and humans (Mussa-Ivaldi *et al.*, 1994; D'Avella *et al.*, 2003; Ivanenko *et al.*, 2004; Bizzi and Cheung, 2013) have showed that muscle synergies extracted from the factorization analysis of electromyographic signals (EMG) can reveal underlying patterns in muscle activity that may reflect different levels of neural functions and their integrity has been proposed as a physiological marker of cortical damage. For instance, Cheung *et al.* observed that in severe stroke patients there is a lack of preservation of muscle synergies in the affected side (Cheung *et al.*, 2012), and their level of preservation correlates with the level of motor impairment (Tropea *et al.*, 2013). Finally, recordings of neural activity can also inform about the central nervous system reorganization after brain damage. Indeed, previous electrophysiological studies in post-stroke patients showed that compromised cortical areas are characterized by augmented slow potentials, which are predictive of long-term post-stroke outcome (Finnigan and van Putten, 2013; Woo *et al.*, 2017).

Despite these interesting and promising results, each of the proposed approach investigates a specific domain of the neuro-musculoskeletal system. Therefore, each methodology provides a detailed but sectorial assessment. Conversely, merging all the domains may provide a comprehensive framework for a more complete and quantitative patient profiling (Bulea *et al.*, 2013; Belfatto *et al.*, 2018).

To this end, the main goal of this study was to develop a multivariate analysis method to couple clinical evaluations with multimodal instrumental evaluations in order to provide a deeper characterization of the neuro-biomechanical status of stroke patients undergoing different rehabilitation protocols. We first introduced an exhaustive and diverse set of measures extracted from different sources, including motor performance as well as muscle activity during a motor task and brain activity at rest. Then, we presented a methodological approach combining and integrating these parameters, which allowed to identify neuro-biomechanical features modifications at different time points during intervention and recovery. We tested this methodology on a small cohort of stroke subjects that went through a period of intense motor training using a 3D reaching task. We believe that the features extracted with our comprehensive multivariate analysis can increase the understanding of the mechanisms underlying motor impairments and recovery, and, additionally, they can potentially help design more effective rehabilitative interventions and monitor the progress of the disease as well as the effects of rehabilitative treatments (Allali *et al.*, 2018; Coscia *et al.*, 2019).

3.2 Methods

3.2.1 Subjects

Six stroke subjects (4 females, age 68 ± 18 yo) between 2 and 6 weeks from the occurrence of the stroke lesion, all with right hemiplegia and at least 10° of residual motion in shoulder and elbow joints (details in Table 3.1), and six healthy subjects (4 females, age 58 ± 16 yo) were enrolled in the study. All subjects were right-handed. The healthy subjects did not present any evidence or known history of skeletal or neurological diseases, and they exhibited intact joint range of motion and muscle strength.

Table 3.1 – Demographics of the stroke population recruited in the study

Subject	Age	Gender	Time after stroke	Lesion type and location	FMA
S1	79	female	3 weeks	Ischemic, left middle cerebral artery	24
S2	82	female	4 weeks	Ischemic, left corona radiata, internal capsule and putamen	16
S3	34	female	2 weeks	Ischemic, left middle cerebral artery	17
S4	78	male	4 weeks	Ischemic, left paramedian pontine	5
S5	65	male	2 weeks	Ischemic, left corona radiata	50
S6	73	female	6 weeks	Ischemic, left parasagittal pontine	54

The study was carried out in the Neurorehabilitation Unit of the University Hospital of Geneva (HUG), Switzerland and of the University Hospital of Pisa (Cisanello hospital), Italy. It was approved by the Commission Cantonale d’Ethique de la Recherche (CCER) de Genève, Switzerland, and by the Comitato Etico Area Vasta Nord Ovet (CEAVNO) in Pisa. The recordings were carried out in agreement with the Declaration of Helsinki and Good Clinical Practice norms. The study is registered with the number NCT02770300 in ClinicalTrials.gov. The participants were informed of the procedure and they signed an informed consent, which included the consent for the use of all data collected during the experiment in scientific publications.

3.2.2 Experimental set-up and procedure

The experimental protocol for the stroke patients consisted of four sessions of clinical and robotic assessment interleaved by four weeks of experimental training - three sessions of 30 minutes per week - proposed in addition to the habitual physical rehabilitative treatment of the patient. The stroke population completed two assessment sessions before (A1 and A2) and two after (A3 and A4) the experimental training. The initial assessment sessions were completed two weeks (A1, baseline) and one week (A2) before the beginning of the training. A2 was done in order to estimate the rate of the changes due to spontaneous recovery and inpatient therapy, since the patients were in the subacute phase of the stroke. The final two assessment sessions were completed one week after the end of the training (A3), in order to evaluate the effects of the rehabilitation protocol, and one month after the end of the training (A4) to evaluate the retention of the changes induced by the experimental training (Figure 3.1a).

The enrolled stroke participants were receiving different therapies during the period of experimental training, including extra sessions of conventional therapy without the use of robotic devices; or standard robot-assisted rehabilitation therapy with an upper-limb exoskeleton; or automatic personalized robot-assisted rehabilitation therapy with an upper-limb exoskeleton (Giang *et al.*, 2020) (see Supplementary material for details on patients’ division during the experimental training).

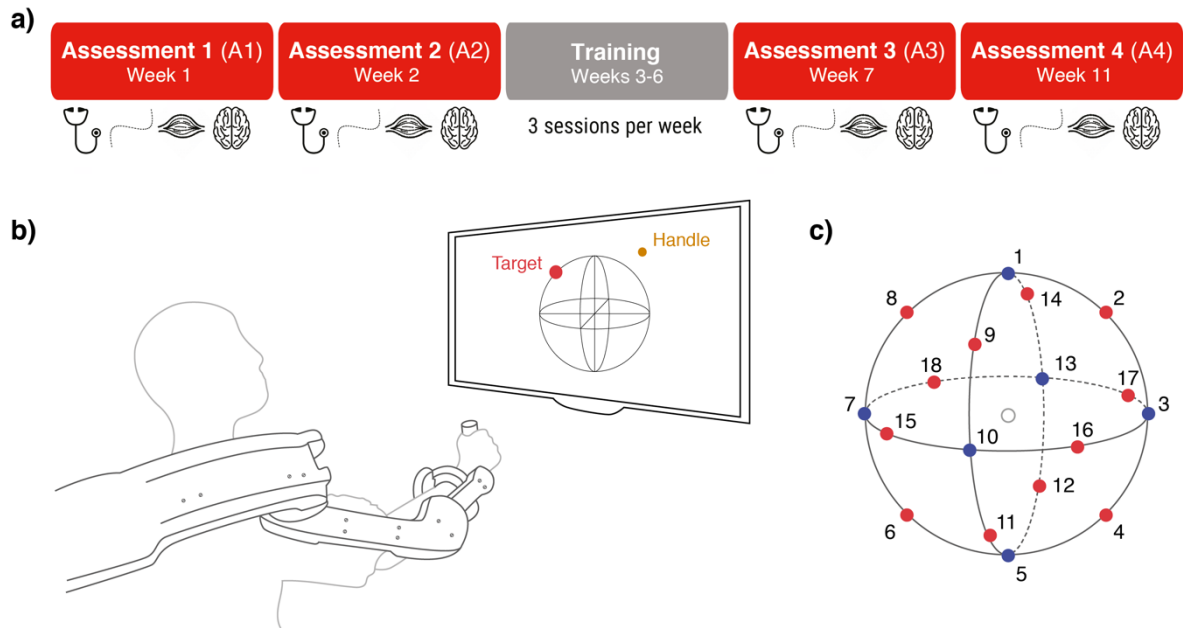


Figure 3.1 – a) experimental protocol: the protocol was organized in four assessments (A1 to A4) and four weeks of training. During the assessments, clinical scales were measured along with kinematic, muscular activity and brain activity before and while training with the exoskeleton. **b)** experimental set up: the subject was sitting in front of a computer screen while wearing the exoskeleton and was given a visual feedback of the end effector of the robot in the shape of a yellow sphere. A red sphere indicated the position of a target that the subject had to reach for. **c)** reaching task: the reaching task consisted in center-out reaching movements towards 18 targets equally distributed along a sphere. The blue targets were the ones considered in the multimodal performance analysis, while the set of blue and red targets together constituted the full training target set.

During the robotic assessment sessions and the treatment sessions involving a robot, the subjects were assisted by an exoskeleton for the upper limb (Arm Light Exoskeleton Rehab Station, ALEx RS) developed by Wearable Robotics srl (Lenzo *et al.*, 2015; Pirondini *et al.*, 2016). The task proposed while working with ALEx RS was a 3D point-to-point reaching task. Specifically, the participants were instructed to start from the center of the workspace, reach one of the eighteen outer targets, and then move back to the starting position at a comfortable speed. Visual feedback was displayed on a monitor placed in front of the subjects (Figure 3.1b). A yellow sphere corresponded to the position of the exoskeleton's end-effector, while a red sphere indicated the target to be reached. The outer targets were in total eighteen, equally distributed along a spherical workspace of 19 cm radius (Figure 3.1c). The selected radius of the sphere allows for a maximum exploration of the workspace, while maintaining the reaching movement executable for people of most body sizes. This design of the motor task allowed exploiting an extensive three-dimensional workspace. The spherical workspace was positioned so that its center was aligned with the acromion of the right arm (i.e., arm trained with the exoskeleton) mid-way between the center of the target panel and the subject's acromion. In order to preserve the depth perception, the dimensions of the target spheres were modified in accordance with their position in the 3D space. If a subject was unable to reach a target (i.e., the subject did not move for more than 3 seconds), ALEx RS activated its assistance mode to guide the subject towards the target according to a minimum jerk speed profile (Sadaka-stephan *et al.*, 2015; Pirondini *et al.*, 2016). During the assessment sessions, the subjects were asked to reach all the eighteen targets as many times as possible within 30 minutes, while

during the robotic training the subjects practiced only a subsection (8 targets) of the available workspace. During each training session, the choice of which target to reach among the available eighteen was done either by the physical therapist (standard robot-assisted rehabilitation therapy) or by an automatic-personalized algorithm. The algorithm was embedded in the control scheme of ALEx RS and selected the targets at the beginning of each session and changed them within the same session accordingly to the subject's performance (automatic personalized robot-assisted rehabilitation therapy) (Giang *et al.*, 2020). Patients that performed standard rehabilitation without ALEx RS were trained with a similar amount of upper limb movements.

In addition to the experimental training sessions described above, all the patients received habitual physical therapy at the stroke unit during the acute and sub-acute phase, while hospitalized. Specifically, all patients received two times 30 minutes of physical therapy per day on five days per week and five times 30 minutes of occupational therapy per week on an inpatient basis for 8 to 16 weeks. Following the end of the hospitalization, patients continued receiving outpatient treatments consisting of 1-4 hours of physical and occupational therapy per week. Therapy was adapted by the therapists to the current capacities of each patient by choosing from a list of appropriate exercises comprising upper-extremity relaxation techniques, unilateral task-specific mobilizations, bilateral upper limb exercises with a wand, ball exercises, active ante/retropulsion exercises, active pronation/supination exercises and grasping exercises.

All subjects were hospitalized until the assessment performed at the end of the experimental treatment (A3). At the time of A4 all subjects were no longer hospitalized and participated at the assessment as outpatients. Therefore, we can consider the dosage of inpatient and outpatient therapies globally equivalent across subjects.

The healthy subjects went through a single robotic assessment session where they were asked to reach the eighteen targets 5 times.

During each robotic assessment session, both for stroke patients and healthy controls, muscular (EMG) and brain (EEG) activity were recorded. Resting state eye-closed EEG was recorded for 5 minutes before the beginning of each robotic assessment session. Kinematic data acquisition was synchronized with EMG signals acquisition by using trigger signals sent from ALEx RS at the following events: movement start, movement end, and at the occurrence of robotic-assistance.

For the goal of this study we considered all 6 stroke subjects together independently from the therapy received during the experimental training period. Therefore, we are going to compare motor performance of two groups: healthy and stroke subjects.

3.2.3 Clinical evaluation

Along with the robotic assessments, and at the same time points (A1, A2, A3 and A4), the stroke subjects were evaluated with clinical tests by a therapist not directly involved in the study and blind to the group allocation. The sensorimotor status of the patient was evaluated using the upper limb section of the Fugl-Meyer Assessment (FMA) scale (Fugl-Meyer *et al.*, 1975); and the grip force measured using a Jamar dynamometer (Bertrand *et al.*, 2015).

3.2.4 Data analysis

For the data analysis of all subjects, stroke and healthy, we considered only the 6 targets (Figure 3.1c, blue spheres) that all the stroke patients were able to actively reach, which were, in addition, representative of the 3 main movement directions: up and down (target 1 and target 5), right and left (target 3 and target 7), near to and far from the body (target 10 and target 13). We only considered the movements going from the center of the workspace to the outer targets. The selected set of movements differed in terms of elbow and shoulder joints combination in order to fully capture subjects' impairment. In particular, target 13 elicited elbow extension, which is generally more difficult than elbow flexion (i.e., target 10). Target 7 required extension of both elbow and flexion of the shoulder as opposite to target 3, which involved a coordination of elbow extension and shoulder flexion. Finally, movements toward target 5, the one placed at the bottom of the spherical workspace, were facilitated by gravity. All reaching movements performed by the subjects were requiring active gravity compensation of the subject's arm, while the exoskeleton was compensating only for the weight of its components. In all further analyses, we did not consider each selected target separately but we pulled all movements together.

For the healthy subjects the total number of movements was 30 (i.e. 5 repetitions of 6 targets), while for the stroke subjects it depended on the level of residual mobility at each assessment. The session lasted 30 minutes, during which the stroke subjects could perform a minimum number of one repetition of each target and a maximum of 5 repetition of 6 targets.

3.2.5 Kinematic analysis and measures

Kinematic parameters were computed from the handle (i.e., exoskeleton's end-effector) positions recorded by ALEx RS during each reaching movement. The start and end of the reaching movement were defined as the time points when the speed profile of the EE of the exoskeleton respectively exceeded or dropped below 2 % of the local maximum value (Pirondini *et al.*, 2016). We adopted the following parameters (Panarese *et al.*, 2012a; Giang *et al.*, 2020): MV, the mean tangential velocity of the handle; nMD, the mean absolute value of the distance between the actual trajectory and the straight line connecting the starting position with the target (theoretical path) normalized by the length of the theoretical path, which is a measure of movement accuracy; nPK, the number of peaks in the speed profile, a well-known parameter quantifying movement smoothness; the spectral arc-length metric (SAL), (expressed as a negative value), that uses a movement speed profile's Fourier magnitude spectrum to quantify movement smoothness (Balasubramanian *et al.*, 2012); the distance from target when the exoskeleton started to assist the movement normalized by the distance between the target and the center of the workspace (D_{tgt}); the robot assistance frequency, i.e., the number of assisted movements (RAF, in percentage); the percentage of workspace explored without the help of the robotic-assistance normalized by the ideal workspace corresponding to the volume of a sphere of radius 19cm (WS); and the time to complete the task (t_{task} , i.e., reaching of the outer target). MV, nMD, nPK have been computed only over the path's trajectory in which the patient moved actively.

3.2.6 EMG analysis

Data acquisition and pre-processing

We recorded the activity of 15 upper limb muscles: upper trapezius, TRAPS, trapezius medialis, TRAPM, anterior deltoid, DANT, medial deltoid, DMED, posterior deltoid, DPOS, pectoralis major, PECM, latissimus dorsi, LAT, infraspinatus, INFRA, rhomboid major, RHO, biceps brachii long head, BICL, biceps brachii short head, BICS, brachioradialis, BRAD, triceps brachii lateral, TRILA, triceps brachii long head, TRILO, and pronator, PRO. The EMG were recorded with a Noraxon Desktop DTS wireless system at a sampling rate of 1.5 kHz by using superficial Ag-AgCl electrodes (Kendall H124SG, ECG electrodes 30x24 mm) after appropriate skin preparation. Electrodes were placed according to guidelines of the Surface Electromyography for the Non-Invasive Assessment of Muscles European Community project (SENIAM) (Hermens *et al.*, 2000) and Anatomical guideline (Delagi and Perotto, 1980).

EMG data were preprocessed offline using MATLAB (MathWorks, Natick MA). The raw EMG signals were detrended, band-pass filtered 50-500 Hz (Butterworth filter, 7th order), rectified, low-pass filtered with a cut-off frequency of 10 Hz (Butterworth filter, 7th order) to obtain the envelopes (Cheung *et al.*, 2009; Kieliba *et al.*, 2018). To correct the EMG-amplitude differences due to electrode placement and to ensure that the extraction of the synergies would not be biased against the low-amplitude muscles, the envelope of each muscle signal was normalized by the median computed for each individual across each session. The normalization based on the median value instead of the maximum is more robust to outliers (Cheung *et al.*, 2009). Then, for each subject and session, EMG data were epoched considering the 6 different directions and were concatenated for muscle synergies analysis.

Muscle synergies extraction and measures

For each subject, muscle synergies were extracted by using the non-negative matrix factorization algorithm (NNMF) (Lee and Seung, 2001). The NNMF algorithm decomposes the EMG envelope in a defined number of positive components or muscle synergies. The organization of a synergy is determined by the contribution (weight coefficient) of each muscle, as specified by the weight matrix W . Its activation profile is defined by the activation coefficients, specified by the matrix H (Lee and Seung, 2001). Since, the iterative algorithm can find a solution as a local and not global minimum, each extraction was repeated 50 times, and the repetition with the solution explaining the highest overall amount of EMG variance was selected. For each subject, to objectively determine the minimum number of muscle synergies required to reconstruct the data set, we used the variance accounted for by the synergies model and chose as threshold the number of synergies at which the VAF was higher than 95% (Cheung *et al.*, 2009). The same number of muscle synergies was retained for all healthy subjects to allow an easy intra-task comparison (i.e., mean number of muscle synergies across healthy subjects). For the patients, instead, the individual number of muscle synergies was considered. Indeed, the number of retained synergies has been proposed as a biomarker of cortical damage and recovery (Cheung *et al.*, 2012).

Muscle synergies were matched among subjects and sessions according to their similarity (determined by using normalized scalar products) with a set of reference synergies. The set of reference synergies was obtained by grouping the muscle synergies of the healthy subjects with a hierarchical clustering procedure based on minimization of the Minkowski distance between weighting coefficient vectors (Cheung *et al.*, 2009).

Muscle synergies structure was compared within the healthy population and between the stroke patients and the healthy subjects by using the scalar products ($\text{dot}_{\text{HEALTHY}}$ and $\text{dot}_{\text{STROKE}}$ respectively). When a stroke subject presented a lower number of synergies, the value of the dot product between the healthy synergy and the correspondent missing synergy of the stroke was set to zero.

Spinal maps extraction and measures

The same preprocessed EMG data were resampled on the minimum number of time points (2 seconds) across directions, sessions and subjects and were used to estimate the spinal maps along the rostro-caudal direction related to C2-T1. The spinal maps describe the spatiotemporal organization of the peripheral EMG signals at the level of the spinal cord, by estimating the motoneuronal (MN) activity for each spinal segment as previously described in literature to investigate the muscle activity in the lower and upper extremities (Ivanenko *et al.*, 2008; Cappellini *et al.*, 2010; Coscia *et al.*, 2015). The weight coefficients approximating the rostro-caudal distribution of the MN pools innervating the upper limb muscles included in the study were located in the segments from C2 to T1, as reported by Kendall (Kendall *et al.*, 2005) (see Table B1 in Supplementary material).

In order to assess the similarity between two different spinal maps, we used the 2D correlation coefficient between two maps (Coscia *et al.*, 2015) ($R_{\text{MAP,H}}$ and $R_{\text{MAP,S}}$ when comparing respectively the spinal maps within the healthy population and between the healthy population and the stroke patients) and the root mean square error ($\text{RMSE}_{\text{MAP,H}}$ and $\text{RMSE}_{\text{MAP,S}}$), calculated as

$$\text{RMSE}_{\text{MAP}} = \sqrt{\frac{1}{N * M} * \sum_{m=1}^M \sum_{n=1}^N (\text{MAP}_1(n, m) - \text{MAP}_2(n, m))^2}$$

where MAP_1 and MAP_2 are the two spinal maps under comparison. N (i.e., number of spinal segments) is equal 8 and M (i.e., time samples) is equal 3000 samples.

We first computed these measures comparing the maps within the healthy population. Then, we compared the maps of each stroke subject and for each session with those of the healthy subjects.

3.2.7 EEG analysis

Data acquisition and pre-processing

EEG data were continuously acquired at 500Hz using an Active II EEG system (Biosemi, Amsterdam) with 64 pre-amplified (active) EEG channels with standard 10-20 configuration. EEG data were preprocessed offline using MATLAB (MathWorks, Natick MA) and EEGLAB toolbox (Delorme and Makeig, 2004). The raw EEG data were filtered (1 Hz to 40 Hz, Butterworth zero-phase 8th order IIR filter (Britz *et al.*, 2010; Van De Ville *et al.*, 2010; Dipietro *et al.*, 2014)) and down-sampled to 128 Hz. EEG electrodes with prolonged prominent artifacts (assessed by visual inspection) were removed and interpolated using spherical interpolation (Pirondini *et al.*, 2017, 2020). The data were, then, re-referenced to a common average. Finally, the data were visually inspected to remove periods contaminated by artifacts (i.e., amplitude > 80µV) and the remaining data were concatenated.

Resting-state EEG measures

Resting-state EEG measures were obtained by singular value decomposition (SVD) of the EEG signals (Balasubramanian *et al.*, 2012; Pirondini *et al.*, 2019). We followed the same approach of our previous work (Pirondini *et al.*, 2019, 2020). The SVD of a real matrix is a factorization of the form $E = MSN'$. In this case, $E \in \mathbb{R}^C \times \mathbb{R}^T$ was the matrix of the pre-processed EEG signals concatenated across sessions and participants with C equals to 64 EEG channels and T equal to the total time of recordings summed over sessions and participants. The left-singular vectors of $M \in \mathbb{R}^C \times \mathbb{R}^C$ are a set of orthonormal eigenvectors that in our case represented the group-level EEG-SVD topographical maps. The right-singular values vectors of $N \in \mathbb{R}^T \times \mathbb{R}^C$ represented the group-level temporal courses. They are ranked according to their non-zero singular values (i.e., diagonal values of S). In order to obtain the subject-specific temporal courses of each EEG-SVD topography for each participant and session, the EEG activity of each individual for each session was projected on the group-level EEG-SVD topographical maps corresponding to 75% of the explained variance (Pirondini *et al.*, 2019, 2020), which was calculated from the singular values as: $VAR_j = \sum_j^C \frac{s_j^2}{\sum s_j^2} * 100$. For instance, the time courses for the first $\{1, \dots, p\}$ SVD components for one subject was obtained as $\tilde{E}_1 = M_{1,\dots,p}^T E_1$.

We assessed reproducibility of the group-level topographies by a split-half reproducibility analysis. We randomly split the original set of subjects and sessions (i.e., the six healthy controls and the four assessments of the patients) into 2 groups, each with 14 sessions. We generated ten different random splits. Subsequently, for each split, EEG-SVD topographies were computed for each group concatenating the data of all subjects and sessions within the group. EEG-SVD topographies obtained from the two groups were then matched using Hungarian algorithm, and their similarity was assessed by Pearson correlation (Munkres, 1957).

For each topographical map and each subject/session, a time-frequency representation of the corresponding subject-specific temporal course was calculated from 1 to 64 Hz by convolving the signals with a complex-valued Morlet wavelet with 3 cycles. Time-frequency power was calculated as the squared magnitude of the complex wavelet-transformed data. We then computed coefficient of variation (CVs - i.e., ratio between variance and mean spectral power over time) for four typical frequency bands (i.e., δ : 1-4Hz; θ : 4-8Hz; α : 8-12Hz; β : 15-30Hz).

In order to identify whether these resting-state EEG measures represented reliable biomarkers of motor recovery, we deployed a multivariate analysis of correlation, i.e., canonical correlation (CCA), between the FMA score and the CVs of each EEG-SVD topography and frequency band. If we consider the CVs of the EEG-SVD and the Fugl-Meyer scores as vectors of random variables ($X = (x_1, \dots, x_n)$ with $n = 1$ and $Y = (y_1, \dots, y_m)$ with $m = 12$ - i.e., 4 frequency bands per 3 EEG-SVD components), and there are correlations among these variables, then the CCA would find linear combinations (i.e., canonical components) of the CVs that have maximum correlation with the Fugl-Meyer. Specifically, the CCA seeks vectors $a \in \mathbb{R}^n$ and $b \in \mathbb{R}^m$ such that the random variables $a^T X$ and $b^T Y$ maximize the correlation $\rho = \text{corr}(a^T X, b^T Y)$. We used a permutation test to verify the significance of the found canonical components. In details, the CVs of each EEG-SVD topography and frequency band were permuted over subjects and we then used CCA to find correlation between these permuted data and the Fugl-Meyer. We repeated this procedure 1000 times and considered the 99th percentile of the resultant distribution of correlation as a significance threshold. Once identified the significant canonical components, the brain canonical scores (V) were obtained

by projections over the canonical correlation vectors ($V = b^T Y$). We then evaluated the changes of the brain canonical scores over assessment sessions for each individual patient.

3.2.8 Multimodal analysis

In order to quantitatively assess the presence of a relationship between the various parameters extracted from the different sources (kinematic, muscle and brain activity) we ran a correlation analysis among all of them. In this way, links between specific pairs of parameters extracted not only from the same type of signal but also from different ones (i.e. kinematic and brain, or muscle and brain) can be highlighted. In particular, we extracted Pearson correlation coefficients from a matrix Q [28x18], where each column was a parameter and each row an observation. Data of stroke and healthy subjects were pulled together. We obtained a matrix of correlation coefficients resulting from pairwise comparisons between the columns of Q and we retained only the correlation coefficients that resulted significant (p-value < 0.05).

To identify the neuro-biomechanical parameters that were most important for post-stroke motor recovery, we applied a multistep statistical procedure based on principal component analysis (PCA) (Musienko *et al.*, 2011). Specifically, PCA was applied to all the parameters extracted from the kinematic, EMG and EEG analysis for all healthy and stroke subjects together. To avoid introducing bias due to the different scales of the various parameters, we normalized measures before running PCA, so as to have zero mean and a standard deviation equal to 1 (z-score). We retained the first three principal components (PCs), which explained more than 50% of the total variance, and we projected the original dataset in the 3D space defined by the constructed PC1-3. For each distribution, the coordinates of the centroid were computed by averaging all the coordinates of the points included in that distribution. We then computed the distance between the centroid of the distribution of the healthy controls and the projection of the data of each stroke subject in the identified PCs space, for each session. The distance was computed in the 3PCs space ($dist_{ALL}$) but also along each individual PC ($dist_{PC1}$, $dist_{PC2}$, $dist_{PC3}$). Finally, to determine the relation between the clinical outcome and the identified neuro-biomechanical measures, we correlated the PC scores with the clinical scores computing Pearson correlations coefficients.

3.2.9 Statistical procedures

In order to summarize the information, the results reported were averaged across subjects. All data are reported as mean values \pm standard error (SE) of the mean. Results of the Kolmogorov-Smirnov normality test for all the extracted indicators confirmed that the later were not normally distributed. For this reason, in order to verify if there were significant changes over the four assessments we performed a Friedman test. Post-hoc analysis, two-sided Wilcoxon signed rank test with no correction for multiple comparisons due to the small sample size, was used to verify statistically significant differences obtained with Friedman test. We used instead the Wilcoxon rank-sum test when comparing stroke data with those of the healthy controls. The significance level was set to $p < 0.05$.

Table 3.2 – Clinical scales results. Upper limb Fugl-Meyer assessment scale (FMA) and grip strength test performed in the four assessment sessions (A1 to A4). Subject 1 (S1) did not have the follow-up session. EEG data of subject (S2) were not considered because of contaminated by artifacts.

Subjects	FMA				Grip strength			
	A1	A2	A3	A4	A1	A2	A3	A4
S 1	24	27	29	n/a	0	0	0	n/a
S 2	16	16	30	34	0	0	0	0.5
S 3	17	34	46	52	0	4.00	6.3	8.1
S 4	5	7	19	19	0	0	0	0
S 5	50	59	62	65	0	1	3.33	6.3
S 6	54	59	63	62	9.72	11.41	13.27	13.71

3.3 Results

3.3.1 Clinical outcome improvement

Patients showed a reduction of impairment along with an increase of grip forces during the evaluation time. Significant improvements in the FMA ($\chi^2=16.68$, $p<0.001$) and in the grip strength ($\chi^2=9$, $p=0.020$) occurred throughout the four assessments for all 6 patients. Changes in the clinical scores ensued between the first (A1) and the second assessment (A2) (on average 6 ± 2.5 points, $p=0.031$, in the FMA and 1.12 ± 0.64 Kg, $p=0.250$, in the grip strength) and likely reflect the short-term changes typical of the subacute phase (see Table 3.2). Yet, stronger improvements occurred between A2 and the assessment after the training (A3). On average all subjects increased of 7.8 points (±2.1 SE, $p=0.031$) in the FMA and 1.08 Kg (±0.49 SE, $p=0.250$) in the grip strength. Finally, these measures did not change significantly at the assessment performed one month following the end of the training (A4; on average 2.4 ± 1.2 points, $p=0.250$ in the FMA and 1.14 ± 0.49 Kg, $p=0.250$, in the grip strength).

Table 3.3 – Results of the Friedman test on the kinematic metrics

metric	MV	SAL	RAF	WS	nMD	nPK	D _{trgt}	t _{task}
χ^2	14.04	11.88	10.95	6.12	9.24	11.88	16.77	13.77
p-value	0.003	0.008	0.012	0.106	0.026	0.008	<0.001	0.003

3.3.2 Motor performances improvement is captured by the kinematic measures

Motor performances significantly improved in all patients, with the exception of the dimension of the workspace (Figure 3.2, Table 3.3). Between A1 and A2 patients' movement increased in speed

(on average from 0.074 ± 0.012 m/s in A1 to 0.094 ± 0.012 m/s in A2) with a concurrent reduction, yet not significant, of the jerkiness and of the robotic-assistance (respectively from -5.44 ± 0.60 to -5.11 ± 0.36 and from $57.95 \pm 18.84\%$ to $47.15 \pm 20.40\%$).

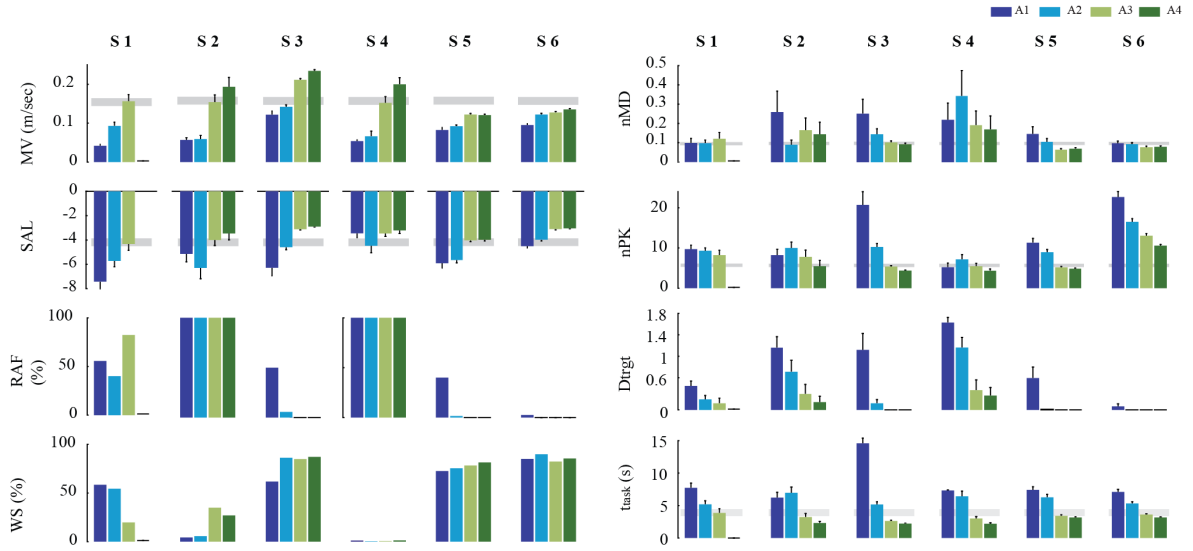


Figure 3.2. – Kinematic parameters. Mean velocity (MV), spectral arc length (SAL), percentage of movement assisted by the robot, percentage of the workspace explored without robotic assistance (WS), linearity index (nMD), number of peaks in the velocity profile (nPK), distance from the target when the assistance started normalized by the distance of the external target from the central one (D_{trgt}) and reaching time (t_{task}) extracted from the trajectories of the end-effector of the exoskeleton during the four robotic assessments (A1 and A2 in the shades of blue and A3 and A4 in the shades of green). The behavior of the healthy, mean \pm standard error of the mean, is shown in grey.

After the month of training these improvements were stronger and statistically significant. Mean velocity and SAL reached level comparable with those of the controls (respectively 0.151 ± 0.013 m/s and -3.67 ± 0.21 for stroke and 0.153 ± 0.011 m/s and -4.18 ± 0.37 for healthy subjects, differences between the two groups were not significant: for the velocity $p=0.589$ and SAL $p=0.240$) and subjects S3, S5, and S6 did not require anymore the robotic assistance. Noticeably, subjects S2 and S4, even if they still needed robotic-assistance in all the assessments, they were able to complete a larger portion of the workspace without the robot, as highlighted by a decrease in D_{trgt} , (overall along the four assessment from 1.39 ± 0.15 to 0.42 ± 0.07 for S2 and from 1.61 ± 0.75 to 0.25 ± 0.11 for S4). Finally, along the four assessments, patients performed straighter movements (i.e. reduction of nMD: from 0.191 ± 0.029 at A1 to 0.094 ± 0.011 at A4, $\chi^2=9.24$ $p=0.026$) in a shorter amount of time (from 0.191 ± 0.029 at A1 to 0.094 ± 0.011 at A4, $\chi^2=13.77$ $p=0.003$).

3.3.3 Muscle coordination improves with training as highlighted by muscle synergies

Six (5.8 ± 0.5) muscle synergies were found for each healthy participant, when considering the movements from the center of the workspace to the six main outer targets (Figure 3.3a). The muscle synergies structure was similar to that already reported in literature for analogous tasks (Pirondini *et al.*, 2016).

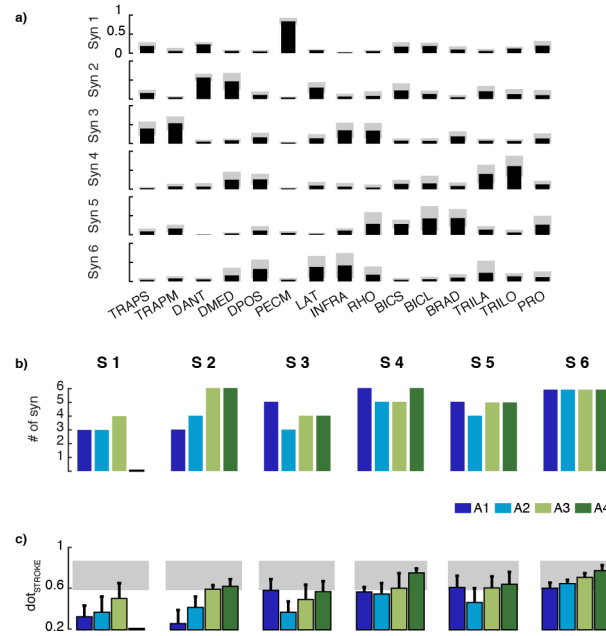


Figure 3.3. – Muscle synergies. **a)** Muscle synergies structure of the healthy subjects presented as mean (black) and standard deviation (in grey) computed across the healthy population. Each row is a muscle synergy, ordered from the one that was more similar across the healthy to the less similar one. **b)** Number of synergies that explained more than the 95% of the VAF. **c)** Mean similarity index ($\text{dot}_{\text{STROKE}}$) between all the synergies of the stroke subjects and the ones of the healthy population. Data of the two assessments before the training (A1 and A2) are presented in the shades of blue and in the shades of green are the data of the assessments after the training (A3 and A4). The grey areas in section c) is the mean \pm std of $\text{dot}_{\text{HEALTHY}}$ resulting from averaging across all the 6 identified synergies of the healthy population.

Specifically, synergy 1 involved mainly the pectoralis, which was responsible for the arm flexion. Synergies 2 and 4 were dedicated to the extension of the arm and included respectively the anterior and medial part of the deltoid (Syn 2), and the two triceps and the posterior part of the deltoid (Syn 4). Synergy 5 was mostly composed of the activation of the forearm muscles (i.e., BRAD and PRO). Finally, synergies 3 and 6 accounted for the activity of the postural muscles (i.e., both trapezii, INFRA and RHO for Syn 3, and LAT, INFRA and RHO for Syn 6) involved in the elevation of the arm against gravity. The stroke subjects presented a significant increase in the number of synergies from A1 to A4, $\chi^2=8.54$ and $p=0.036$. Specifically, the number of synergies augmented between A2 (4.1 ± 0.4) and A3 (5.0 ± 0.3) and it was maintained at A4 (5.4 ± 0.4 synergies modules) (Figure 3.3b). This change highlights an increased level of complexity of muscle activity as expected during motor recovery (Tropea *et al.*, 2013). Additionally, through time and training the structure of the synergies of the stroke subjects became more similar to the structure of the controls. Indeed, the $\text{dot}_{\text{STROKE}}$ augmented significantly for each stroke subject, $\chi^2=9.49$ and $p=0.023$. Specifically, it was stable during the first two assessments ($\text{dot}_{\text{STROKE}}=0.48 \pm 0.07$ and $\text{dot}_{\text{STROKE}}=0.47 \pm 0.04$ at A1 and A2, respectively). At A3, instead, there was a significant improvement of this indicator with respect to A2 ($\text{dot}_{\text{STROKE}}=0.58 \pm 0.03$, $p=0.031$), and it continued to significantly evolve also at follow-up ($\text{dot}_{\text{STROKE}}=0.67 \pm 0.03$, $p=0.031$).

3.3.4 Motoneuronal activity in the spinal circuits increases with training

We further investigated the global muscular strategies adopted by the participants by computing spinal maps, which estimate spatiotemporal motoneuronal activation. For the controls, spinal maps

were characterized by a main period of activation towards the end of the reaching task, localized around C7-T1 (Figure 3.4a). For the stroke subjects, instead, at A1 and A2 the motoneuronal activity was either almost absent because they were not able to accomplish the task without the help of the exoskeleton or it was diffused across all the spinal segments and not localized, in contrast to the controls (Figure 3.4b).

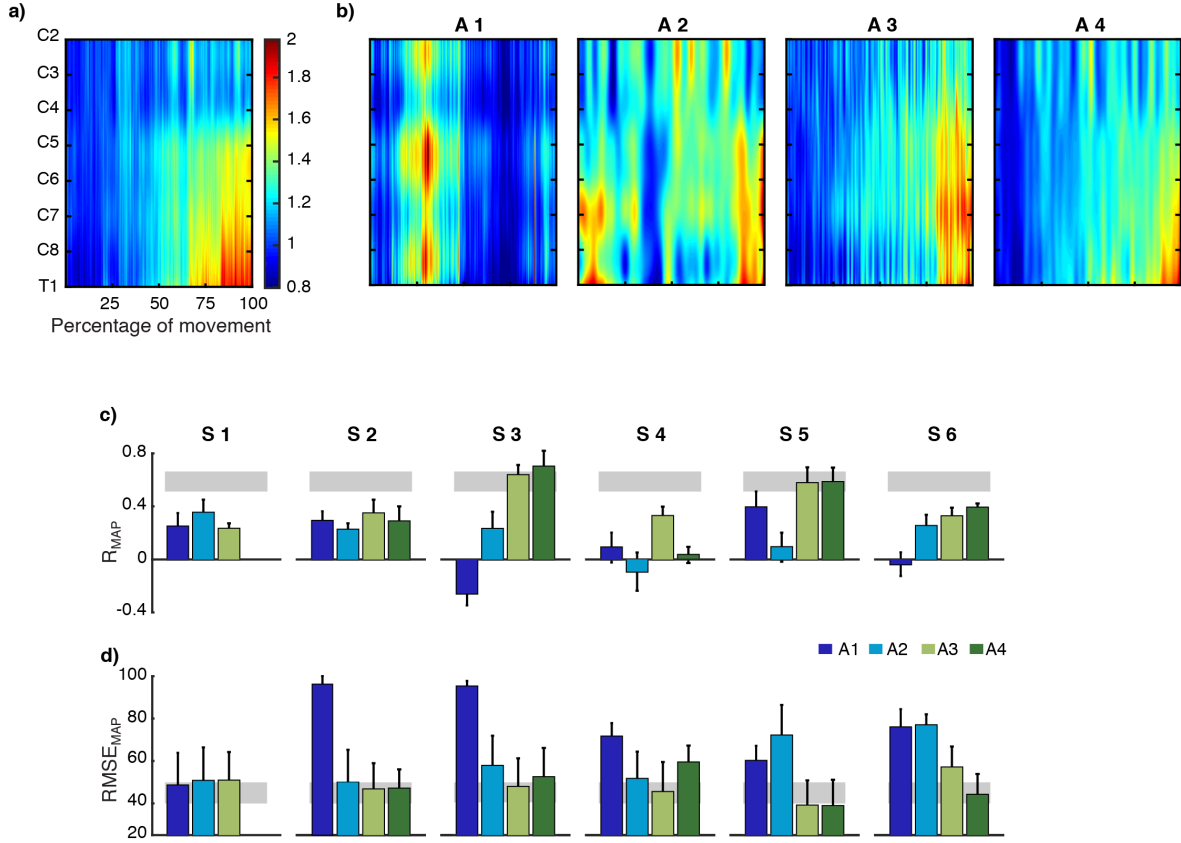


Figure 3.4. – Spinal maps. **a)** Temporal activation of the spinal map extracted from the EMG activities of the healthy population. **b)** Temporal activation of the spinal map extracted from the EMG activities of S 3 in the four assessments. **c)** Mean and standard deviation of the 2D correlation (R_{MAP}) between the spinal map of each stroke subject and the healthy subjects at the different assessments. Mean and STD of the correlation across the healthy population is showed with the grey area. **d)** Mean and standard deviation of the distance ($RMSE_{MAP}$) between the spinal map of each stroke subject and the healthy subjects at the different assessments. Mean and STD of the correlation across the healthy population is showed with the grey area. In the shades of blue are presented the results of assessment 1 and 2 (A1 and A2) while in the shades of green the data concerning assessments 3 and 4 (A3 and A4).

Along the four assessments, the spinal maps of the stroke subjects became significantly more similar to those of the controls, both in term of correlation $R_{MAP,S}$, $\chi^2=9.56$ and $p=0.022$, and of root mean square error $RMSE_{MAP,S}$, $\chi^2=10.62$ and $p=0.014$. Yet, the greatest and the only significant changes for both metrics occurred between A2 and A3 (i.e., with training), where $R_{MAP,S}$ augmented from 0.18 ± 0.06 to 0.42 ± 0.08 ($p=0.031$) and $RMSE_{MAP,S}$ diminished from 60.50 ± 5.17 to 46.33 ± 3.23 ($p=0.031$). Importantly, the improvement remained stable at follow-up as indicated by a non-significant difference of the values of $R_{MAP,S}$ and $RMSE_{MAP,S}$ between A3 and A4.

3.3.5 Cortical activity gets closer to healthy level with training as highlighted by EEG topographies

We utilized SVD decomposition of the EEG signals concatenated in time across participants and sessions to identify reliable and reproducible topographical maps (Pirondini *et al.*, 2019, 2020). We selected the first three EEG-SVD components, which accounted for 75% of the variance (Figure 3.4a). We tested the consistency of the maps by split-half reproducibility analysis. All the three components were highly reproducible (average correlation \pm STD across splits and components: 0.98 ± 0.01).

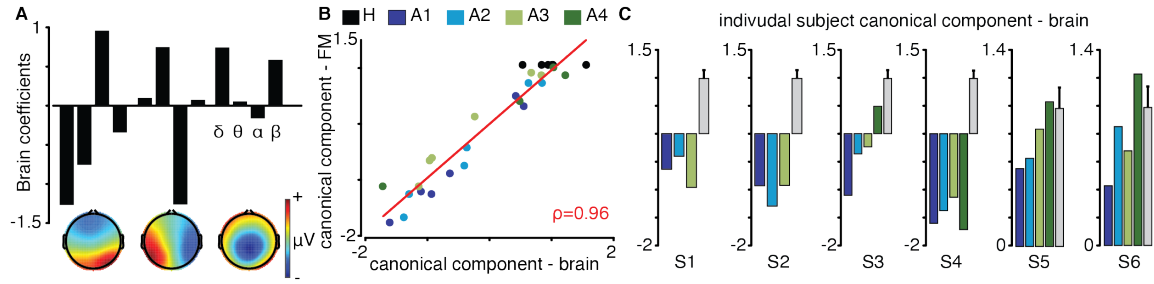


Figure 3.5. – EEG topographies. a) Canonical correlation coefficients for the coefficients of variation of the first three EEG-SVD topographies and the four frequency bands (delta, theta, alpha, and beta). **b)** 2D correlation plot of canonical correlation scores for FMA (y-axis) and resting-state EEG measures (y-axis). Black dots represent healthy subjects. Blue, cyano, and light and dark green dots represent stroke patients at A1, A2, A3, and A4, respectively. **c)** Brain canonical scores for each subject for A1 (blue bars), A2 (cyano bars), A3 (light green bars), and A4 (dark green bars) and for controls (grey bars).

We computed canonical correlation between the FMA scores and the coefficients of variation of each EEG-SVD topography and frequency band. We found one significant canonical correlation component ($p < 0.01$ permutation test; correlation: 0.96, Figure 3.5b) with highest coefficients for CV of delta and alpha bands for the 1st EEG-SVD component, theta and alpha bands for the 2nd component, and delta and beta bands for the 3rd component (Figure 3.5a). Through time and training the CVs got closer to those of the healthy controls, in particular for S3, S5, and S6. Yet, no significant difference was found between the three assessments when considering all subjects together.

3.3.6 Multimodal analysis reveals different temporal dynamics of recovery

Before running the multimodal analysis, we looked for correlations between specific pairs of parameters obtained both from the same domain and from different domains. Results are summarized in Figure 3.6a. We found that there were some significant correlations between couples of parameters extracted from the same domain, like between the nPK and time to reach the target or the linearity index (nMD) and the robotic assistance (RAF) obtained from the kinematic domain. Similarly, we found significant correlations between $\text{dot}_{\text{syn}1}$ and $\text{dot}_{\text{syn}3}$ or between the number of synergies and $\text{dot}_{\text{syn}6}$. Interestingly, we noticed significant correlations also between parameters of different domains, for example the percentage of workspace explored without robotic assistance and the number of muscle synergies or the time to reach the target and the RMSE_{MAP} extracted from the spinal maps. Nevertheless, despite these significant correlations, the value of the correlation coefficient was, on average, relatively modest: $r = \text{mean } 0.53 \pm \text{STD } 0.12$.

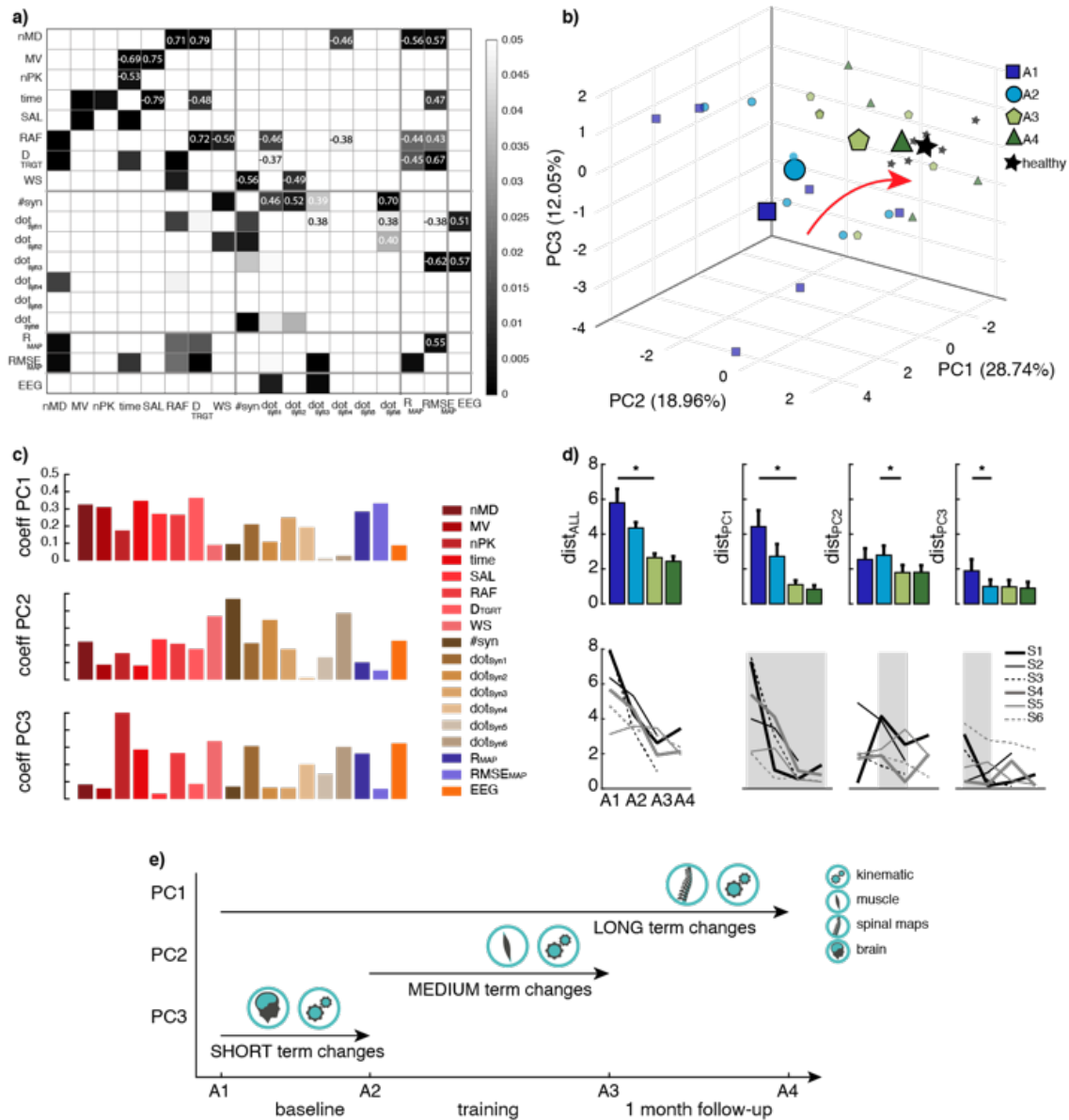


Figure 3.6. – Multimodal analysis. **a)** Matrix of Pearson correlation coefficients resulting from pairwise comparisons between each parameter extracted from healthy and stroke population for each assessment. The grey intensity of the figure corresponds to the value of the p-values of the correlations, only the correlations that resulted significant are reported. The bold lines are delimitating the area of features extracted from the same source. **b)** Projection of the dataset in the 3D space identified by the first three principal components (PCs). The data relative to the healthy subjects are in black, the data of the stroke subjects at A1 in blue, A2 light blue, A3 light green and A4 dark green. The centroid of each group of data is highlighted by a marker of bigger size and higher intensity with respect of the majority. **c)** Coefficients of the three PCs. In the shades of red data relative to the kinematic, in the shades of brown data relative to muscle synergies, shades of purple data relative to the spinal maps and in orange data relative to EEG. **d)** Top: Distance between the healthy and the stroke group in the space of PCs1-2-3 ($dist_{ALL}$) and along each PC separately ($dist_{PC1}$, $dist_{PC2}$, $dist_{PC3}$). Bottom: Distance between the healthy group and each stroke subject in the space of PCs1-2-3 ($dist_{ALL}$) and along each PC separately ($dist_{PC1}$, $dist_{PC2}$, $dist_{PC3}$). Highlighted in grey the regions where there was a significant change. **e)** Summary image illustrating the different temporal dynamics of recovery identified by the proposed methodology.

We then combined together all the measures extracted from the robotic assessment (kinematic, EMG and EEG metrics) in a multimodal analysis using PCA. The explained variance for the first three PCs was 59.75%. The metrics extracted from the kinematic and spinal maps were those mostly contributing to PC1. The second PC, instead, was mainly associated with the workspace coverage, the number of synergies, and the similarity of synergy 2 and 6. Finally, the factor loadings associated with the third PC were the number of peaks in the speed profile, movement duration, the workspace coverage, the structure of synergy 1, and the EEG scores (Figure 3.6c). When projecting the individual data points into the 3D space defined by the newly constructed variables PC1–3, clear differences emerged between the healthy subjects and the stroke patients (Figure 3.6b). Importantly, these differences were, also, affected by time and training (Figure 3.6b and d). Indeed, the distance between the patients' and controls' data points in the 3D space significantly decreased along the four assessments, $\chi^2=10.22$ and $p=0.016$. In particular, the distance decreased significantly ($p=0.031$) from A2 ($\text{dist}_{\text{ALL}}=4.07\pm0.32$) to A3 ($\text{dist}_{\text{ALL}}=2.52\pm0.37$), and it remained stable at A4 ($\text{dist}_{\text{ALL}}=2.17\pm0.36$). Interestingly, we found different temporal dynamics of recovery for the three principal components, summarized in Figure 3.6e. Indeed, the distance along PC1 changed along the four assessments, $\chi^2=9.61$ and $p=0.022$, with a significant decrease in particular between A1 and A2 ($\text{dist}_{\text{PC1}}=4.73\pm0.98$ and $\text{dist}_{\text{PC1}}=2.43\pm0.56$ at A1 and A2, respectively - $p=0.031$) and between A2 and A3 ($\text{dist}_{\text{PC1}}=0.80\pm0.17$ - $p=0.031$). PC2 significantly decrease between A2 and A3 ($\text{dist}_{\text{PC2}}=2.76\pm0.29$ and $\text{dist}_{\text{PC2}}=1.51\pm0.23$ at A2 and A3, respectively - $p=0.031$). Instead, the distance along PC3 decreased throughout the four assessments, $\chi^2=8.39$ and $p=0.03$, yet mainly between A1 and A2 ($\text{dist}_{\text{PC3}}=1.91\pm0.53$ and $\text{dist}_{\text{PC3}}=0.95\pm0.14$ at A1 and A2, respectively - $p=0.031$). When correlating the 3 PCs with the clinical scores we found a significant correlation between PC1 and the FMA, $r=0.74$ $p<0.001$, and between PC1 and grip force, $r=0.54$ $p=0.003$.

3.4 Discussion

The current study aimed to introduce a comprehensive set of movements, muscle, and brain measures as well as to present a multivariate methodological approach combining them in a unique framework. This approach can be applied to any dataset containing multidomain measures. Here we applied this method to a multidomain dataset, including a small group of subacute stroke subjects that went through a month of intense motor rehabilitation.

3.4.1 Multimodal assessment

Motor rehabilitation aims at maximizing the recovery and independence in daily living by discouraging dysfunctional compensatory behaviors and promoting the re-learning of appropriate motor control strategies (Micera *et al.*, 2020). For this, rehabilitation protocols have to adapt to the individual dynamics of recovery (Winstein and Kay, 2015). However, because of the multifaceted nature of stroke, recovery assessments should explore different aspects of the nervous system. For this reason, in this study, we simultaneously recorded kinematic, EMG, and EEG signals to gather a general understanding of the neuro-biomechanical state of the subjects and of its evolution over time after a rehabilitative treatment, independently from the nature of the latter (e.g., robotic or conventional therapy). Importantly, all domains of the neuromuscular system - kinematic, muscle, and neural activity - were affected by the motor training. Besides, significant correlations could also be observed across them, although they could not fully capture the complex variations pertaining to the different domains. As such, these observations support the feasibility and the need for a multimodal approach that could efficiently summarize these factors in a single metric. For this purpose, we deployed principal component analysis. We projected the individual data points into the 3D

space defined by the first three principal components explaining a high percentage of variance, and we computed the distance between the healthy controls and the stroke subjects at each assessment. During the training, the distance between the patients' and controls' data points in the 3D space significantly decreased, yet with different dynamics. Previous studies already reported different evolutions of the recovery factors for movement speed, efficiency, and accuracy (Murphy *et al.*, 2011; Nordin *et al.*, 2014; Panarese *et al.*, 2016). We here extended these findings to new physiological measures, hence providing a more complete characterization of the neuro-biomechanical status of the patients and of its evolution. We found that patients' kinematic and spinal maps parameters were mainly clustered over the first principal component (PC1) and improved continuously during the four assessments. These quantitative measures were also those exhibiting a higher correlation with the post-stroke impairments captured by the FMA assessment and by the grip force. A strong correlation between kinematics and the patient status as described by clinical scales is in general well accepted and expected since they measure similar parameters (Anne *et al.*, 2019; Shirota *et al.*, 2019). A more striking observation is, instead, the strong correlation with the spinal maps, as they have been so far rarely used to describe upper limb movements (Pirondini *et al.*, 2016; Barra *et al.*, 2018) and levels of impairment after stroke (Coscia *et al.*, 2015).

Together with spinal maps, we also estimated muscle synergies as metrics of motor coordination extracted from electromyographic signals. Interestingly, muscle synergies features clustered in a separated principal component (PC2), as compared to spinal maps, and they normalized already in the shorter period of the training, highlighting that motoneuronal activity and muscle coordination evolve differently over time.

Finally, the third component mainly included metrics related to some kinematics measures (speed profile, movement duration, and workspace coverage), the structure of synergy 1, and the brain features that normalized in the shorter period post-lesion (i.e., between A1 and A2).

Overall these results highlighted that post-stroke recovery develops at different stages for different aspects of the nervous systems. A short-term recovery (between A1-A2) likely due to a combination of spontaneous recovery and inpatient therapy; a medium-term recovery (between A2-A3) probably as result of our intervention and the inpatient rehabilitative therapy and finally, a long-term recovery (between A3-A4) that showed a maintenance of the functional improvements achieved at A3 probably supported as well by the outpatient therapy. While further studies should confirm these preliminary results in larger datasets, these different dynamics were previously not captured when considering standard clinical approaches or mono-parameter analysis and should be taken in consideration when designing new rehabilitation protocols.

3.4.2 Specific unimodal analysis

Stroke subjects performed the 3D point-to-point reaching task worst as compared to healthy controls. In accordance with previous studies (Levin, 1996; Cirstea *et al.*, 2003; Belfatto *et al.*, 2018; Pila *et al.*, 2018) patients' movements were less smooth and slower, and often required assistance from the exoskeleton, especially during the A1 assessment, a few weeks after the injury. Already at the second assessment, which was performed before the extra dose of rehabilitative intervention (either robotics or standard therapy), performances improved. This progress immediately after the injury is typical of the recovery that usually arises in the acute phase (Cramer, 2008). Moreover, in this period patients were already receiving inpatient physical and occupational therapy. Yet, the

strongest improvement occurred between A2 and A3 (i.e., after the treatment). At A3, kinematic performances became comparable to those of the controls and maintained an analogous pattern at follow-up (i.e., assessment A4).

The multimodal set-up deployed in this study linked this trend of kinematic improvements to the motoneuronal changes estimated using spinal maps. The use of spinal maps to characterize upper limb movements had so far been limited (Pirondini *et al.*, 2016; Barra *et al.*, 2018; Kibleur *et al.*, 2019) and they were never exploited in stroke patients to explore upper limb impairments. Moreover, we recently demonstrated a strong correlation between spinal maps activation and blood-oxygen-level-dependent signal of the spinal cord captured by functional magnetic resonance imaging, which further supports the use of this analysis technique to infer motoneuronal activity (Kinany *et al.*, 2019). In our stroke population, the motoneuronal activity described by the spinal maps was reduced after the stroke lesion with respect to the one of healthy participants, both in terms of temporal activation (R_{STROKE}) and magnitude of activation ($\text{RMSE}_{\text{STROKE}}$), but it increased during the training, getting closer to the one of the healthy participants at A3 and A4.

The number and structure of the patients' muscle synergies also became more similar to those of the healthy controls, in particular after the month of intense training. Similarly to observations reported in previous studies, the number of synergies for the stroke subjects increased through time with the recovery of motor functions (Cheung *et al.*, 2009, 2012; Tropea *et al.*, 2013; Coscia *et al.*, 2015) and this increase was also accompanied by changes in their structure. The synergies structure improved also for the subjects that did not recover all the six synergies characteristic of the healthy population (see also Figure B1 in Supplementary material for more details). These results are in accordance with studies showing that the conjunction between the spontaneous recovery and the intensive treatment improved motor performance, both in terms of kinematics and muscle activation patterns (Fasoli *et al.*, 2003; Riener *et al.*, 2005; Tropea *et al.*, 2013). Interestingly, muscle synergies related to the control of the shoulder (i.e., Syn 2 and 4) were those with the strongest changes particularly after training with the exoskeleton (see Figure B1 in Supplementary material) paralleling our previous findings (Tropea *et al.*, 2013).

The kinematic and muscle factors explored in this study provide a detailed description of the biomechanical status of the patients. Yet, they do not tap into the complex neural reorganization processes that occur after brain insult. To capture these changes, we deployed topography-based analysis of the EEG signals acquired at rest. We opted for a topography-based approach, in contrast to traditional EEG waveform analysis, as we believe this approach can better capture post-stroke large-scale neural processes without any a priori hypothesis on the spatial location of abnormal brain activity (Pirondini *et al.*, 2017; Zappasodi *et al.*, 2017). Indeed, stroke has been nowadays reconsidered as a distributed network disease with structural and functional changes occurring between brain areas distant to the lesion (Carrera and Tononi, 2014; Siegel *et al.*, 2016; Allali *et al.*, 2018). We deployed singular-value decomposition to extract EEG topographies that resemble previously identified microstates, whose preserved occurrence and duration has been shown to correlate with a better effective motor recovery (Zappasodi *et al.*, 2017). Specifically, in our approach we concatenated in time the data recorded for healthy subjects and patients and subsequently derived group-level spatial maps that come with subject-specific time courses. Indeed, we were interested in preserving the subject-specificity only in the time courses, while considering the same spatial subspace across subjects. We further supported this assumption by performing SVD decomposition of the EEG signal of each participant and every session (see Supplementary Figure B2), which showed a high correlation across all subjects for all top-three components. We recently deployed similar analysis to discriminate patients with spatial neglect of different severity levels (Pirondini

et al., 2020). Here, we paralleled these previous results showing that spectral power of the SVD topographies, which has a typical $1/f$ fall-off typical of the EEG spectral power for all components, and particularly delta and alpha rhythms, correlated with level of motor impairments. Interestingly, through time and training the aberrant brain oscillation patterns were restored, in particular for the subjects that showed a stronger motor improvement. Indeed, the three patients (S1, S2, and S4) for which brain rhythms remained abnormal not only had lower FMA scores, but also aberrant monotoneuronal activation. Furthermore, they still needed robotic assistance after the intensive training and at follow-up.

Overall kinematic, muscle, and cortical activity showed an improvement particularly evident during the training and correlated with the clinical status of the patients. Yet, when summarizing these affinities across the different physiological measures using a multivariate approach, the latter highlighted that post-stroke recovery develops at different stages for different aspects of the nervous systems, suggesting that kinematic, muscle, and brain features should be taken into consideration when designing new rehabilitation protocols. For this, our approach could be an effective method to summarize the different psychological measures in few metrics that could be monitored over time to personalize the treatment (Panarese *et al.*, 2012a; Giang *et al.*, 2020)

3.4.3 Limitations of the study

Although the findings presented in this study suggest that the proposed multimodal approach has the capacity to provide additional information regarding the evolution of the recovery after stroke, the limited sample size limits the generalizability of the results. Nevertheless, the main goal of this study was to propose a potential comprehensive method that included various types of information rather than probing its clinical efficacy. Moreover, the heterogeneity of the stroke subjects included in the study does not allow for an ideal homogeneous stratification of the population. However, this could not be precisely controlled, as we were working with sub-acute stroke and the recruitment was done on a continuous basis one patient at the time. Therefore, further studies including larger cohorts of participants would be necessary to draw meaningful conclusions about the clinical efficacy of the presented approach. One further limitation regards the number of movements performed by the patients recruited in the three different groups. To ensure comparability among the groups, we proposed the same duration of the session and we asked the therapist to provide a training with a similar intensity as the one provided by the robot. Yet, the number of movements performed highly depended on the ability level of each stroke subject.

3.5 Conclusion

The use of an instrumental assessment followed by a multimodal approach identified quantitative neurophysiological metrics correlating with clinical measures such as the FMA and grip force, as well as clustered metrics that evolve distinctly during recovery, underlining their functional and clinical relevance. A combined analysis of kinematic, muscular, and brain activity seems to be able to provide a good and accurate patient characterization in line with the outcome of the clinical scales. In the future, similar methods should be implemented in order to track the evolution of the neuro-biomechanical state of the patients after brain damage, to define suitable personalized rehabilitative intervention strategies and to provide a deeper insight into the recovery process after stroke.

Summary and outlook

In this section, we explored approaches to quantify motor recovery, in the broader context of the personalization of rehabilitative interventions. In the first study (**Chapter 2**), we validated a model-based methodology to estimate motor improvement and continuously adapt training based on this quantitative variable. In practical terms, we tested this approach in a group of healthy subjects performing a visual adaptation task in a three-dimensional environment, using an upper-limb exoskeleton. We demonstrated that motor improvement could successfully be captured for each individual subject, at the subtask level, and that the subsequent task adaptation was timely and accurate. Furthermore, we showed that this approach could be deployed to enable personalized rehabilitation in two sub-acute stroke patients with significantly disparate motor symptoms, thus providing preliminary evidence of its applicability in clinical settings. While kinematic-based personalization has an undeniable potential as regards the customization of the training procedure itself, a thorough investigation of recovery mechanisms is necessary to fully understand and harness patients' residual function. In the second study (**Chapter 3**), we thus probed the temporal evolution of motor function using a novel multimodal framework. Specifically, we used a PCA-based approach to combine measures reflecting movement execution, motor output, muscle coordination and neural activity into a clinically meaningful metric. We applied this analysis to longitudinal data of sub-acute stroke patients undergoing rehabilitation and illustrated the ability of the proposed framework to provide a synthetic view of the physiological processes underlying post-stroke motor recovery. In particular, our findings emphasized their multifaceted nature, as heterogeneous temporal dynamics were observed for multimodal variables reflecting central and peripheral mechanisms. This suggested that functional changes at different levels occurred at multiple time scales to support the regaining of motor function. Consequently, our findings pointed out the importance of integrating measures from different sources in order to accurately identify the correlates of stroke recovery.

All in all, technology-assisted rehabilitative strategies offer avenues for precise and efficient therapies, provided that they are employed so as to optimally manipulate the physiological circuitry involved in motor recovery. How this should be implemented in practice is still a matter of debate, but developments should rely on comprehensive evaluations of the cerebral, spinal, muscular and mechanical status of the patients in order to establish science-driven paradigms. Advances in this regard can have numerous benefits, both in terms of prognosis and treatments. Notably, this could highlight biomarkers to inform patient stratification, hence ensuring that the most adapted combination of treatments is provided, with the most appropriate timing.

PART II

Bridging the gap between the brain and the periphery

In Part I, we acknowledged the importance of considering central and peripheral motor-related mechanisms to better characterize post-stroke recovery. Despite the multimodal nature of this work, the involvement of the CNS was merely limited to cortical processes, apart from indirect estimation of spinal motoneuronal activity using muscular recordings. This encephalo-centered view of the CNS is, actually, a common limitation in studies investigating motor function. Nevertheless, evidence is accumulating to emphasize the key role of the spinal cord in motor control, as well as the sophisticated character of its circuitry (Poppele and Bosco, 2003; Giszter *et al.*, 2012; Arber and Costa, 2018). Contrary to the long-standing view of a passive and hard-wired organ, the spinal cord is actually a major site of activity-dependent plasticity throughout life (Wolpaw and Tennissen, 2001; Grau, 2014; Zholudeva *et al.*, 2018). As such, engaging and guiding spinal neuroplasticity could have substantial implications in the development of new therapies (Wolpaw, 2012). At the core of the interplay between afferent and efferent pathways, it undoubtedly occupies an ideal position to contribute to functional recovery (Tennant, 2014).

Considering this central position of the spinal cord, at the interface between the brain and the periphery, it may appear surprising that it has so rarely been investigated. The answer to this question partly lies in the limited availability of methods to efficiently probe spinal cord function in humans (Wheeler-Kingshott *et al.*, 2014). Indeed, most knowledge on that topic has so far been gained from animal models. Given that spinal circuits are not entirely preserved across species (Lemon, 2008; Nielsen, 2016), there is however a considerable need for approaches enabling non-invasive assessments of human spinal pathways. In this context, imaging methods, such as fMRI, could potentially be leveraged (Stroman *et al.*, 2014; Powers *et al.*, 2018).

The work presented in this section is articulated around two main axes: methodology development and applications. Accordingly, the purpose of Chapters 4, 5 and 6 is essentially to establish a robust framework to study spinal cord activity using fMRI, during task and at rest. We then capitalize on these advances to investigate fundamental and clinical neuroscientific questions. In Chapter 7, we show how distinct cerebro-spinal correlates support short- and long-term motor sequence learning (Chapter 7). Finally, Chapter 8 focuses on the potential for clinical translation of spinal functional imaging and we present preliminary results in two patient populations. First, we explore the reorganization of spinal pathways in stroke patients. Then, we illustrate how fMRI can be used to inform patient-tailored rehabilitation in the context of a case study with a spinal cord injured patient.

Chapter 4 corresponds to unpublished results.

Contributions: responsible of the project, design and organization of the experiments, establishment of the MRI protocols (supported by the MR technical staff from the Fondation Campus Biotech Geneva), data collection, development of the analysis plan, data processing and analysis, presentation of the results.

Chapter 5 corresponds to a postprint version of the article published under:

"Functional imaging of rostrocaudal spinal activity during upper limb motor tasks", **Kinany N.**, Pirondini E., Martuzzi R., Mattera L., Micera S.* and Van de Ville D.*, *NeuroImage*, 2019, vol. 200, doi:10.1016/j.neuroimage.2019.05.036

* Equally contributing authors

Contributions as first author: responsible of the project, design and organization of the experiments, data collection, development of the analysis plan, data processing and analysis, preparation of the figures and writing of the manuscript

Chapter 6 corresponds to a postprint version of an article accepted in *Neuron*:

"Dynamic functional connectivity of resting-state spinal cord fMRI reveals fine-grained intrinsic architecture", **Kinany N.**, Pirondini E., Micera S.* and Van de Ville D.*, *Neuron*, 2020

* Equally contributing authors

Contributions as first author: responsible of the project, design and organization of the experiments, data collection, development of the analysis plan, data processing and analysis, preparation of the figures and writing of the manuscript

Chapter 7 is adapted from a manuscript in preparation:

"Dynamics of cerebral and spinal networks during acquisition and consolidation of motor skills", **Kinany N.**, Khatibi A., Lungu O., Micera S., Van de Ville D., Marchand-Pauvert V. and Doyon J.

Contributions as first author: development of the analysis plan, data processing and analysis, preparation of the figures and writing of the manuscript

Chapter 8 corresponds to unpublished results.

Contributions: design and organization of the experiments (in collaboration with the clinical centers), data processing and analysis, presentation of the results.

Chapter 4

Towards a pipeline for spinal cord fMRI

4.1 Introduction

In the brain, fMRI studies have been widely deployed to map neural activity. While the first report of spinal cord fMRI in humans dates from 1996 (Yoshizawa *et al.*, 1996), spinal cord fMRI has not, however, followed the same development (Stroman *et al.*, 2014). This limited rate of progress mainly stems from additional challenges associated with imaging this region (Giove *et al.*, 2004), hence implying that spinal cord fMRI cannot be considered as a straightforward extension of its brain counterpart. Among the challenges impeding spinal cord fMRI, most arise from its anatomy. In particular, the spinal cord has a small cross-sectional diameter, in the order of a centimeter, along with a long rostro-caudal extent, approximately 45 centimeters in adults. This implies that high spatial resolution and large coverage would ideally be required, although this is not easily achievable in practice (Summers *et al.*, 2014). Moreover, these dimensions entail a limited tolerance to motion artifacts. In this regard, an important source of motion is linked to physiological noise, with cardiac-related noise being a major issue, as the dilation of the arteries and the CSF pulsatile flow can both induce signal variations (Piché *et al.*, 2009). The close proximity of the lungs can also lead to time-varying changes in the magnetic field homogeneity, in turn impacting signal changes (Vannesjo *et al.*, 2018). Finally, the spine is surrounded by different tissue types, whose distinct boundaries cause field inhomogeneities, potentially resulting in distortion or signal losses (e.g., susceptibility artifacts at the level of intervertebral disks, Cooke *et al.*, 2004; Finsterbusch *et al.*, 2012).

Despite these impediments, a number of studies have investigated different methodologies to circumvent the aforementioned limitations (see Eippert *et al.*, 2017a; Powers *et al.*, 2018; Stroman *et al.*, 2014; Summers *et al.*, 2014, 2010; Wheeler-Kingshott *et al.*, 2014 for reviews). While they underlined the technical feasibility of spinal cord fMRI, the heterogeneity of the employed strategies has hampered the emergence of standard guidelines. This variety of approaches has also raised concerns about their reliability. In this regard, it should be mentioned that most of the early studies were conducted using non-standard techniques (Cohen-Adad, 2008). In particular, several studies favored the use of a contrast mechanism termed signal enhancement by extravascular water protons (SEEP), in place of the well-established BOLD contrast. This contrast was first introduced in 2001 by Stroman *et al.* (Stroman *et al.*, 2001a, 2001b), who suggested that T2-weighted imaging could provide a better quality than standard T2*-weighted acquisitions, by imaging signals resulting from proton-density changes associated with cellular swelling instead of perfusion. Nevertheless, the findings related to this contrast mechanism are controversial and several groups unsuccessfully tried to reproduce these results (Jochimsen *et al.*, 2005; Moffitt *et al.*, 2005; Bouwman *et al.*, 2008). For instance, Jochimsen *et al.* (Jochimsen *et al.*, 2005) reported a potential statistical explanation, suggesting that the SEEP contrast might be linked to the inclusion of false-positive voxels in the analysis. In line with these observations, another aspect that may have affected early studies pertains to the detection of task-related activity using cross-correlation analysis (i.e., correlation

between the stimulus and the time course of every voxel) (e.g., Stroman *et al.*, 2001a, 2001b, 2005, Kornelsen and Stroman, 2004, 2007; Stroman, 2005), which was often not accompanied by proper statistical evaluations of the results significance. Fortunately, methodologies have evolved during the last decade and general linear model (GLM) approaches (Friston *et al.*, 1995) have generalized in more recent studies, allowing to map task-related activity using regression and statistical testing (Valsasina *et al.*, 2008), while possibly accounting for motion or physiological artifacts (Brooks *et al.*, 2008; Eippert *et al.*, 2017a). Nevertheless, correction for multiple comparisons was mostly bypassed in spinal cord fMRI studies, despite its primary importance (Martin *et al.*, 2016). As a matter of fact, the transition towards more systematic and quantitative evaluations, with standards more at par with brain fMRI procedures, only started in the last years (Weber *et al.*, 2016a, 2016b, 2020; Tinnermann *et al.*, 2017).

Altogether, these observations emphasize the limitations that precluded the emergence of a standardized pipeline for spinal cord fMRI. Considering that there is yet no consensus, we present a pilot study evaluating various acquisition approaches adapted from literature (Eippert *et al.*, 2009; Sprenger *et al.*, 2012; Weber *et al.*, 2016b), using simple motor paradigms previously demonstrated to elicit detectable activity (finger tapping and ankle extension). Furthermore, we capitalized on the advent of novel processing tools tailored to the spinal cord (e.g., common template, slice-wise motion correction, etc.) (De Leener *et al.*, 2017) and we provide, in the methods, support for the choices that were made with respect to these processing steps. In sum, this chapter introduces the methodological pipeline (cervical or lumbosacral fMRI) deployed in the following chapters.

4.2 Methods

4.2.1 Participants

Four young healthy volunteers were enrolled in this study (details are presented in Table 4.1). All subjects were right-handed and all participants had normal or corrected-to-normal vision and no history of neurological disorders. All participants gave their written informed consent to participate, and the study had been approved by the Commission Cantonale d’Ethique de la Recherche Genève (CCER, Geneva, Switzerland, 2016-01566).

4.2.2 Experimental protocols

Different experimental tests were performed, during four imaging sessions.

Experiment A: Exploration of spinal cord fMRI sequences

For this first experiment, six acquisition schemes for spinal cord fMRI were tested on one subject (S01). Sequence parameters are presented in Table 4.2 (Sequences 1 to 6) and adapted from acquisition protocols most commonly deployed in recent years (see 4.2.3 for details). One functional run was performed for each sequence, during which the subject executed a bilateral finger-tapping task, known to elicit observable spinal activity (Govers *et al.*, 2007; Maieron *et al.*, 2007; Ng *et al.*, 2008; Vahdat *et al.*, 2015), at an individually fixed rhythm. The movements were performed in blocks of 15 seconds (8 blocks of rest alternated with 8 blocks of movement and a final block of rest) and an entire run lasted 4 min and 15 s. Instructions were displayed on a screen (fixation cross ‘+’ during the rest blocks and text indicating ‘movement repetitions’ during the task blocks). Auditory cues were used to inform the subject of the different phases. The paradigm was performed once for each sequence.

Experiment B: Re-test of ZOOMit sequence

The same subject (S01) was scanned three months later, using the most promising sequence of Experiment A (Sequence 4), as well as the same experimental paradigm.

Experiment C: ZOOMit VS Z-shimmed

Three subjects were enrolled in this experiment (S01, S02 and S03). Two functional sequences (5 and 7, see Table 4.2) were used. Each subject performed three runs for each sequence, in a random order, with the same experimental paradigm as Experiments A and B.

Experiment D: Lumbosacral fMRI

One participant (S04) was enrolled in this experiment, which involved a unilateral isometric ankle extension (right limb), a movement previously shown to evoke detectable spinal signals (Kornelsen and Stroman, 2004, 2007). The task paradigm was similar to Experiments A to C, although the duration of the experiment was increased (6 min and 15 s), as we expected activity to be weaker using a unilateral task. Each extension was performed in blocks of 15 seconds (12 blocks of rest alternated with 12 blocks of movement and a final block of rest).

Table 4.1 – Participants demographics and experiments details

Experiment	Subject	Age	Gender	Task
A	S01	29	F	Bilateral finger tapping
B	S01	29	F	Bilateral finger tapping
	S01	29	F	Bilateral finger tapping
C	S02	23	M	Bilateral finger tapping
	S03	30	F	Bilateral finger tapping
D	S04	31	F	Unilateral ankle extension

4.2.3 Data acquisition

Several experiments aiming to compare various acquisition schemes were performed. In all instances, a Siemens Prisma scanner (3 Tesla) was used (Erlangen, Germany), with the subjects positioned in supine position. In order to permit functional to structural registration, a high-resolution T2-weighted anatomical image was also acquired for all subjects using a SPACE sequence (single slab 3D turbo spin echo sequence with a slab selective, variable excitation pulse, TR = 1500 ms, TE = 135 ms, echo train length = 74, flip angle = 140, resolution = 0.4 x 0.4 x 0.8 mm, sagittal orientation). The imaged region extended from the upper cervical to the upper thoracic spine for the cervical acquisitions (Experiments A, B and C) and from T11 to L5 for the lumbosacral acquisition (Experiment D).

As for the functional scans, details of the acquisition parameters are summarized in Table 4.2. All pulse sequences used echo planar imaging (EPI), which allows rapid imaging and high SNR (Samson *et al.*, 2016). However, it should be mentioned that EPI is prone to distortions and signal losses in case of magnetic field shifts (Powers *et al.*, 2018). The shimming of the magnetic field is therefore crucial to limit such artifacts. The approach adopted in the following experiments was to manually set the shim volume to be focused on the spinal cord (Ellingson and Cohen-Adad, 2014; Eippert *et al.*, 2017a).

As previously mentioned, there is no established method for spinal cord fMRI acquisition. As a result, our first focus was to compare potential sets of acquisition parameters (Experiments A and B). To this end, we performed a literature review and proposed six acquisition schemes (Sequences 1 to 6), based on sequences most frequently used in recent years (Eippert *et al.*, 2009; Sprenger *et al.*, 2012; Geuter and Büchel, 2013; Kong *et al.*, 2014; Van de Sand *et al.*, 2015; Weber *et al.*, 2016a, 2016b), which we adjusted to our setup. Note that these pulse sequences all relied on built-in Siemens protocols. Thus, a second focus was to compare one such built-in approach, proven to be efficient in Experiment A, with a custom approach attempting to dynamically optimize shimming on a slice-by-slice basis (Finsterbusch *et al.*, 2012) (Experiment C). In a last experiment (D), a sequence targeting the lumbosacral region of the spinal cord was tested. Sequence 4 was adapted for this purpose, as a wider field-of-view was required to account for the additional tissue volume present in this region (i.e., at the levels of the hips). In-plane resolution was thus changed from 1 to 1.1 mm to avoid aliasing artifacts.

Table 4.2 – Sequence parameters

#	TR/TE	FA	FOV	Resolution	Slices	Region	Notes	Experiment
1	1170/39	62°	140x140	1x1x5 mm	11	Cervical		A
2	1890/39	72°	140x140	1x1x5 mm	18	Cervical		A
3	1500/39	72°	140x140	1x1x5 mm	14	Cervical		A
4	2500/34	80°	44x144	1x1x3 mm	32	Cervical	ZOOMit	A,B
5	1500/30	90°	44x144	1x1x5 mm	21	Cervical	ZOOMit	A,C
6	1170/37	62°	128x128	1x1x5 mm	10	Cervical	PACE	A
7	1500/31	50°	144x144	1x1x5 mm	17	Cervical	Dynamic Z Shim	C
8	2500/34	80°	44x144	1.1x1.1x3mm	27	Lumbosacral	ZOOMit	D

4.2.4 Data processing

As the processing pipeline cannot rely on conventional brain-based methods, different options were investigated in order to establish a processing procedure tailored to the spinal cord. The details of the selected approach are presented below, along with supporting information.

Motion correction

In conventional brain imaging, motion correction is commonly performed using a 6 degrees of freedom (translations and rotations of the volume) rigid-body transformation (Poldrack *et al.*, 2011) or using Friston's 24-motion model (Friston *et al.*, 1996). However, such transformations do not yield satisfying results when applied to the spinal cord, as its anatomy affects the nature of motion artifacts (Stroman *et al.*, 2014; Summers *et al.*, 2014). In particular, the articulated structure of the spinal cord implies minimal motion in the rostro-caudal direction (z direction), while distortions might not be identical in each spinal segment. For this reason, rigid transformations alone cannot fully account for movements and slice-wise motion correction should be preferred (De Leener *et al.*, 2017). Moreover, regions outside the vertebral column, that may move independently from the cord, should be excluded from the correction procedure. Here, this was done using a cylindrical mask drawn along the spinal cord and slice independent motion correction was performed with the mean functional image as the target image, using the Spinal Cord Toolbox (SCT) (De Leener *et al.*, 2017). While this procedure is helpful to reduce the noise in BOLD time courses, severe artifacts linked to large volume-to-volume movements are not fully removed by this approach (Caballero-Gaudes and Reynolds, 2017; Parkes *et al.*, 2018). A censoring approach, termed motion scrubbing (Power *et al.*, 2014), was therefore employed to identify such outliers and to include the corresponding frames as noise regressors during the GLM analysis (see 4.2.5). Specifically, variations in image intensity between volumes were computed using the FSL outlier detection tool (DVARS metrics: root mean square intensity difference of volume N to volume N+1). This was done within the spinal cord, and using a box-plot cutoff (75th percentile + 1.5 x the interquartile range). The global level of motion was evaluated for all experimental runs, indicating a mean framewise displacement inferior to 0.5mm in all instances. As a result, all runs were included in the analysis.

Spatial smoothing

Spatial smoothing of fMRI volumes is routinely performed in order to improve the signal-to-noise ratio, to minimize the structural differences between subjects as well as to increase the validity of statistical testing. The common practice in brain imaging is to use an isotropic Gaussian smoothing kernel, but applying this approach in the spinal cord is not recommended. An isotropic smoothing may, indeed, lead to problematic partial volume effects between the CSF and the cord, as well as between the white and grey matter. Although the use of an anisotropic kernel could partly limit this issue by diminishing the in-plane smoothing, this solution remains suboptimal, as it does not take into account the curved structure of the spine and may induce mixing of signals from different regions. In order to preserve anatomical consistency, we therefore opted to apply smoothing on a straightened spinal cord (i.e., along the centerline of the cord, using a 3D Gaussian kernel with a full width half maximum (FWHM) of $2 \times 2 \times 6 \text{ mm}^3$) before un-straightening it back (De Leener *et al.*, 2017).

Physiological noise modelling

In the spinal cord, the impact of physiological noise is particularly pronounced, due to the surrounding respiratory and cardiac organs (Piché *et al.*, 2009; Vannesjo *et al.*, 2018). Data-driven approaches that directly derive noise from fMRI recordings can be used to remove these signals without involving additional external measurements (e.g., using approaches such as CORSICA, Perlberg *et al.*, 2007, or CompCor, Behzadi *et al.*, 2007). Nevertheless, noise identification is not trivial and should be performed with caution to avoid removing task-related signals (Eippert *et al.*, 2017a). For this reason, a model-based approach relying on the independent acquisition of physiological

signals was preferred in our experiments. Physiological recordings were performed using a photoplethysmograph and a respiratory belt (Biopac MP150 system, California, USA), synchronized with the scanner triggers. These signals were then used to model physiological noise, with an approach based on the RETROspective Image CORrection (RETROICOR) procedure (Glover *et al.*, 2000a). This method assumes that the physiological processes are quasi-periodic, which means that cardiac and respiratory phases can be uniquely assigned for each image in the time series. The signals are then modeled using a low-order Fourier expansion based on the phases at the time of image acquisitions. This technique has been specifically tailored to spinal cord imaging and improved by including higher order Fourier terms, as well as by taking into account the interactions between cardiac and respiratory cycles (Brooks *et al.*, 2008; Kong *et al.*, 2012). This adapted version is referred to as physiological noise modeling (PNM) and is available as an FSL toolbox (Jenkinson *et al.*, 2012). The physiological model can then be used as noise regressors in the GLM analysis (see 4.2.5). In these experiments, we modelled 18 voxelwise noise regressors, but it is worth mentioning that 32 regressors have been most commonly used in most spinal cord fMRI studies (Kong *et al.*, 2012). The choice of a lower number was driven by the short length of the runs (102 volumes), and corresponds to the model proposed by Harvey *et al.* (Harvey *et al.*, 2008), which was successfully employed in the brainstem and the spinal cord (Tinnermann *et al.*, 2017). As cardiac activity implies pulsatile movement in the CSF, including a CSF noise regressor is also advised (Kong *et al.*, 2012). This can be done using the slice-wise averaged time courses from the 10 % of CSF voxels showing the highest variance.

Spatial normalization

Using a common reference space is crucial to reliably compare activation maps obtained in multiple runs. While this has been available in the brain for decades, for instance in the form of the MNI template (Mandal *et al.*, 2012), spinal cord analyses have long lacked such a common framework. Fortunately, recent developments in this regard have been made and the PAM50 template, which spans the entire length of the human spinal cord with a resolution of 0.5 x 0.5 x 0.5 mm, is now available (De Leener *et al.*, 2018). Here, we normalized functional images with a two-step procedure using the SCT (De Leener *et al.*, 2017): (i) Anatomical-to-template: First, the spinal cord was automatically segmented on the T2-weighted anatomical image. Vertebrae were then automatically labelled to generate the landmarks used to perform non-rigid registration to the PAM50 template. (ii) Functional-to-anatomical: Non-rigid transformations were used to register the mean motion-corrected functional images to the corresponding anatomical scan. Finally, the warping fields obtained in both steps were concatenated to obtain the functional-to-template transformation. Note that the lumbosacral scan was not normalized to the template, as only one scan was performed.

4.2.5 Data analysis

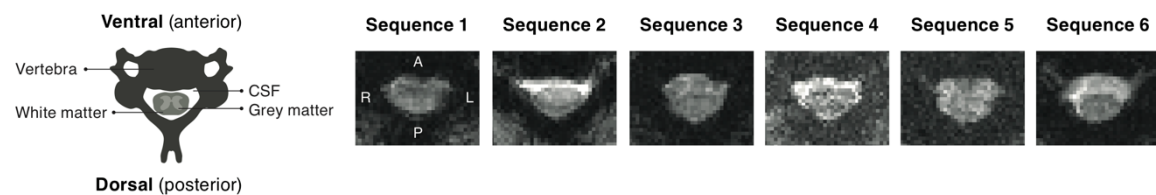
For each run, the temporal signal-to-noise ratio (tSNR) was computed to inform on signal quality (mean signal intensity across time divided by its standard deviation) at three steps of the analysis: (i) raw images, (ii) after motion correction and (iii) after spatial and temporal filtering. Values were then averaged within the spinal cord. In order to identify task-related activity, a general linear modelling (GLM) approach was used for each individual run. The preprocessed images (after motion correction and smoothing) were highpass filtered (sigma = 45.0 s) and analyzed using the FST's FEAT tool (FMRI Expert Analysis Tool) (Jenkinson *et al.*, 2012). The explanatory variables were defined as the task blocks convolved with a set of three basis functions defined by FSL's Linear Optimal Basis Set (FLOBS) tool (Woolrich *et al.*, 2004b). This allows to account for potential variations in the hemodynamic response function. The second and third FLOBS waveforms, respectively

modelling temporal and dispersion derivatives, were orthogonalized to the first waveform. The noise regressors (i.e., physiological noise and motion outliers) were also included as confounds in the GLM. Time-series statistical analysis was carried out using FMRIB's Improved Linear Model (FILM) with local autocorrelation correction (Woolrich *et al.*, 2001). Indeed, all fMRI time-series suffer from autocorrelation, which can be addressed using pre-whitening (i.e. making the noise 'white', in order to turn it into uncorrelated noise). Kong *et al.* (Kong *et al.*, 2012) observed that this procedure, applied to spinal fMRI data, efficiently removed non-white noise and also helped in controlling false-positive rates. The contrast opposed task against rest (first FLOBS regressors). Z statistic images were thresholded using clusters determined by $Z > 2$ and a cluster-defining threshold of $p < 0.01$ to account for multiple comparisons. These thresholded maps were then normalized to the PAM50 template to allow between-runs comparison. For Experiment A, an ICA was carried out using FSL's MELODIC tool (Multivariate Exploratory Linear Decomposition into Independent Components), in order to confirm the results found with the GLM analysis. The dimensionality was defined using Probabilistic Principal Component Analysis where the number of dimensions was estimated using the Laplace approximation to the Bayesian evidence of the model order (Minka, 2001; Beckmann and Smith, 2004).

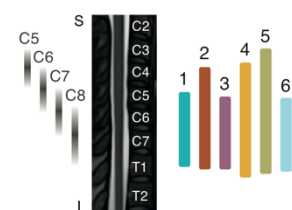
4.3 Results

4.3.1 Task-related activity can be efficiently imaged using spinal cord fMRI (Experiments A and B)

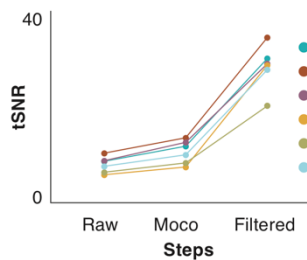
A. Raw images



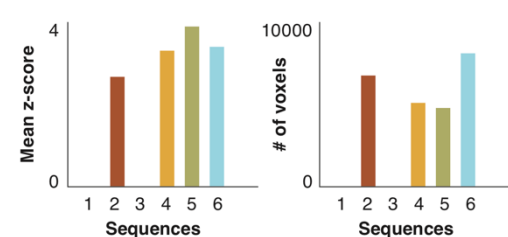
B. Imaged regions



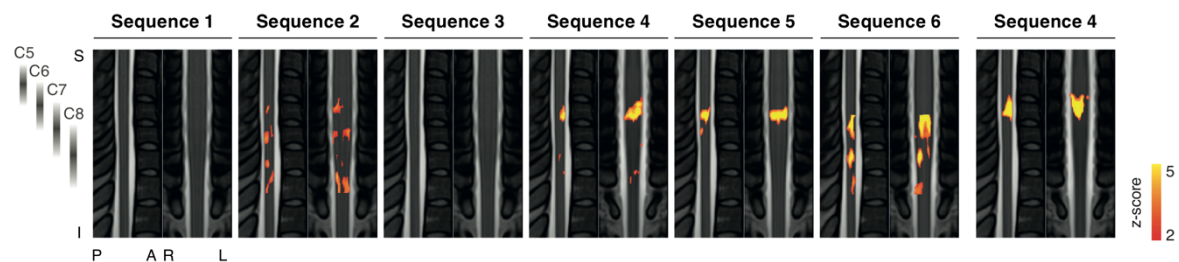
C. Temporal SNR



D. Task-related activity (summary)



E. Task-related activity (maps)



F. Re-test

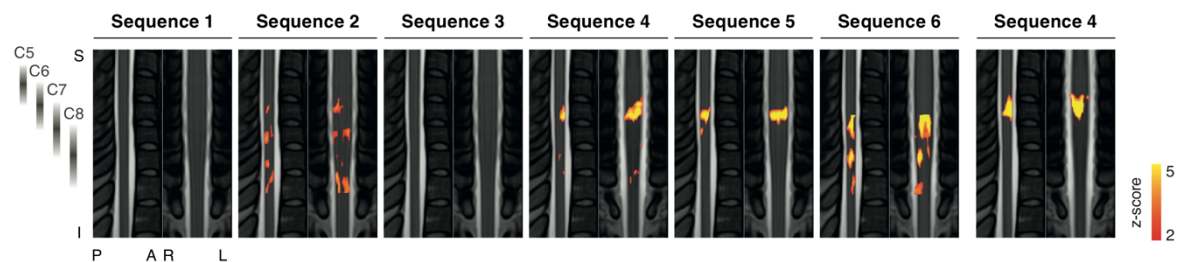


Figure 4.1 – Comparison of different sequences (Experiments A and B, S01). A. One example axial slice, extracted from the raw time series, is presented for the six sequences used in Experiment A (right panel). A

schematic view of the spinal cord is shown (left panel) to indicate the different regions. **B.** The coverage of each sequence is indicated using color bars. A sagittal view of the PAM50 template is used as a reference (De Leener *et al.*, 2018). The vertebral bodies are labelled, as well as the corresponding probabilistic spinal levels (Cadotte *et al.*, 2015). **C.** Temporal signal-to-noise ratio (tSNR) was computed for (i) the raw signals (Raw), (ii) following motion correction (Moco), and (iii) following spatial and temporal filtering (Filtered). **D.** Task-related activity was evaluated using a GLM approach (see panel D. for the associated spatial maps). The average z-score, as well as the number of active voxels, are presented. **E.** Activation maps for the contrast task VS baseline. **F.** Detection of task-activity using Sequence 4 was re-tested after three months on the same subject (Experiment B). All statistical maps are thresholded at a Z-score > 2 (cluster-defining threshold of $p < 0.01$ to account for multiple comparisons) and normalized to the PAM50 template. Representative coronal and sagittal views are presented for each sequence. S = superior, I = inferior, L = left, R = right, A = anterior, P = posterior.

An initial visual inspection of image quality was performed for the six sequences (see Figure 4.1A for example slices). As expected, differences could be observed depending on the acquisition parameters, notably as regards the delineation between the spinal cord and the surrounding CSF. The rostrocaudal extent of the imaged regions were also different between sequences, with Sequences 2, 4 and 5 extending from C5 to C8, while Sequences 1, 3 and 6 did not include C5 (Figure 4.1B). Signal quality was also probed by computing the tSNR at different steps of the processing (Figure 4.1C). Values increased between the raw (range 5.84 - 10.35), motion corrected (range 7.46 - 13.55) and filtered signals (range 20.27 - 34.46), hence emphasizing the efficiency of the processing procedure. Although image quality (i.e., sufficient contrast, limited distortion, etc.) and tSNR are important factors to evaluate signal integrity, they do not fully inform on BOLD sensitivity.

To this end, we sought to investigate task-related activity using a GLM approach. Significant task activity could be detected for four of the acquisition schemes (Sequences 2, 4, 5 and 6) (Figure 4.1D), with distinct spatial patterns (Figure 4.1E). In particular, Sequences 2 and 6 demonstrated a spread of the activity on several spinal levels, from C6 to C8, as opposed to the highly localized C6-C7 cluster observed using Sequence 4 (58% of voxels in C6, 23% in C7) and Sequence 5 (44% of voxels in C6, 56% in C7) (i.e., using the ZOOMit sequences), in line with knowledge regarding innervation of finger muscles, as well as with previous fMRI studies (Govers *et al.*, 2007; Vahdat *et al.*, 2015). In all instances, voxels were present in both the left and right hemicords, as expected for bilateral movements. Activity was also found in both the anterior and posterior hemicords, consistently with the fact that finger tapping involves both muscle activation and sensory feedback (e.g., tactile and proprioception).

The GLM approach relies on the availability of the experimental paradigm and is, as such, model-based. In order to further confirm our findings, we employed an ICA approach to probe whether task-related activity could be retrieved using a data-driven strategy. Timecourses of all independent components were visually inspected for each acquisition scheme. For Sequences 1, 2 and 3, no task-related patterns were detected. In contrast, temporal timecourses following the task paradigm could be recovered for Sequences 4, 5 and 6 (Figure 4.2). Moreover, the associated spatial maps showed clusters focused on the spinal cord and located in the C6-C7 spinal levels, hence in agreement with anatomic knowledge. This highly localized activity also supported the neural origin of the detected signal, while ruling out the hypothesis of task-related noise. Interestingly, independent components obtained with the ZOOMit sequences (4 and 5) were the most informative, with task-related components accounting for, respectively, 10.07% and 6.14% of the explained variance, as opposed to Sequence 6, for which this component represented 4.46% of the explained variance. Altogether, this model-free approach strongly supported the findings of the GLM analysis, as well

as the ability of spinal cord fMRI to reflect neural activity, provided that adequate parameters are employed.

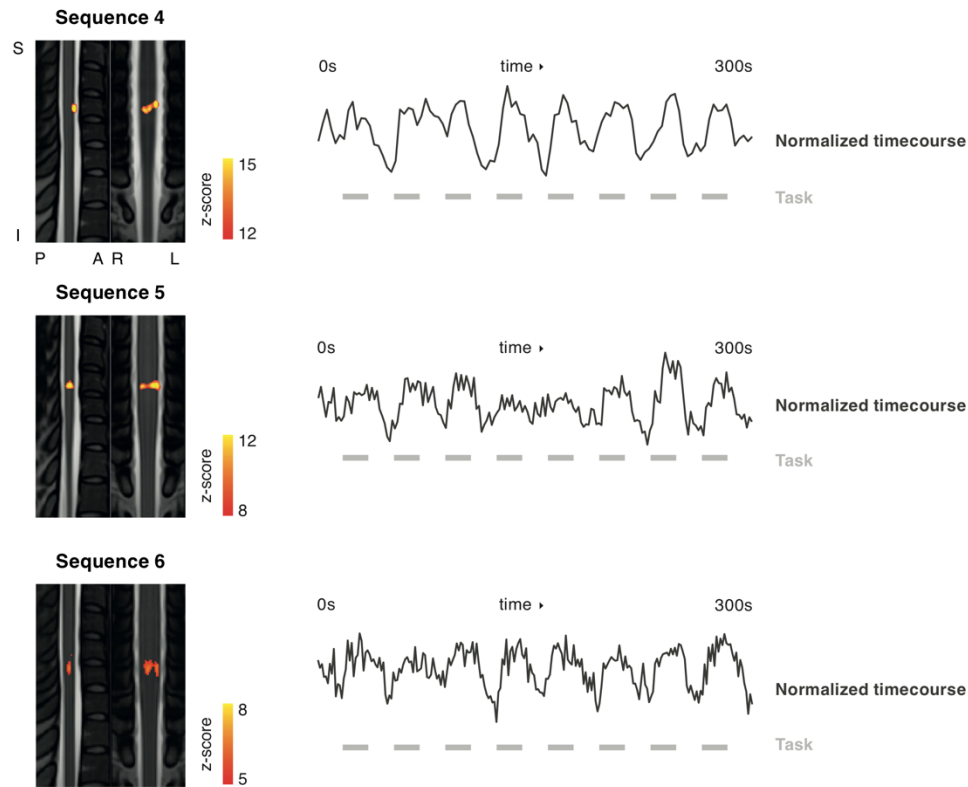


Figure 4.2 – Data-driven recovery of task dynamics (Experiment A, S01). Using FSL’s MELODIC tool, an ICA was performed on the datasets acquired using the six different sequences. The temporal and spatial properties of the recovered components were inspected to probe their potential task-related nature. Sequences 4, 5 and 6 all had one component reflecting task activity. Spatial maps (normalized to the PAM50 template (De Leener *et al.*, 2018)) are presented along with their associated temporal modes (task timing indicated as a reference). Representative coronal and sagittal views are presented for each sequence. S = superior, I = inferior, L = left, R = right, A = anterior, P = posterior.

Based upon these results, we opted for ZOOMit sequences (4 and 5) in further analyses, as they allowed detection of strong and localized activity along with an extensive coverage (i.e., from C5 to C8, see Figure 4.1B). Sequence 4 offered the best spatial resolution (1 x 1 x 3 mm), a feature that is particularly appealing in the context of spinal cord fMRI, as it enables to appreciate small regions in more detail. In a re-test scan using this sequence (Experiment B, S01), activity patterns were found to be in agreement with those acquired in Experiment A (i.e., 88% of the active voxels in C6, 12% in C7) (Figure 4.1F).

4.3.2 Z-shimmed sequence shows improved signal quality but limited BOLD sensitivity (Experiment C)

While the six sequences employed in Experiment A were built upon standard acquisition schemes provided by the scanner manufacturer, dedicated approaches have also been proposed to address specific limitations inherent to spinal cord imaging. In particular, improvements to the shimming procedure can help reduce the impact of field inhomogeneities. Here, we evaluated a custom approach based on the work of Finsterbusch *et al.* (Finsterbusch *et al.*, 2012), which enables slice-

specific shimming. Results were compared with a standard ZOOMit sequence of the same resolution (i.e., 1 x 1 x 5 mm).

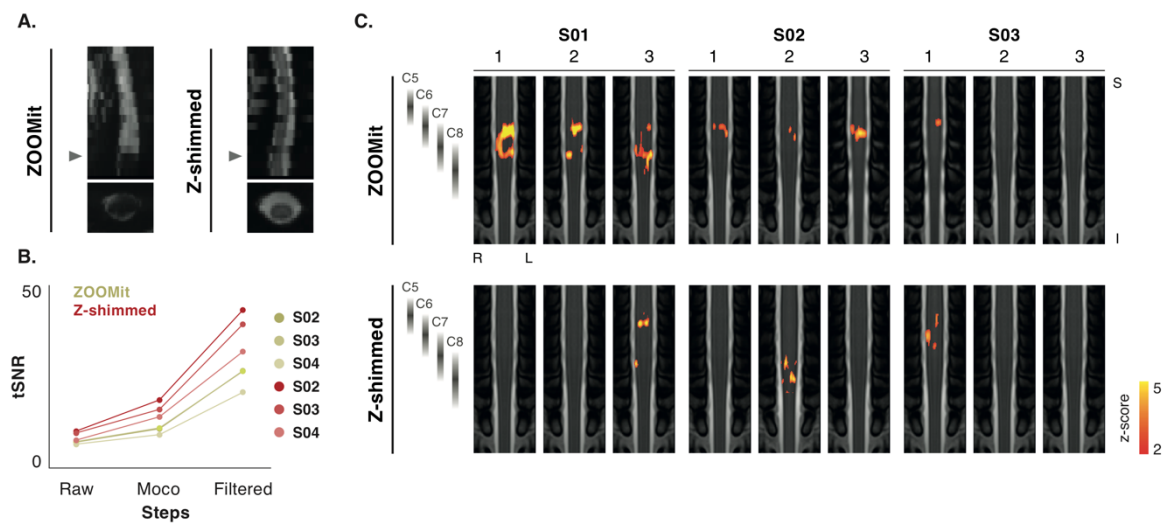


Figure 4.3 – Comparison of ZOOMit and Z-shimmed sequences (Experiment C). **A.** Mean motion corrected image for the two sequences. A central sagittal slice is presented, as well as one example axial slice (position indicated by a grey arrow). **B.** Temporal signal-to-noise ratio (tSNR) was computed for (i) the raw signals (Raw), (ii) following motion correction (Moco), and (iii) following spatial and temporal filtering (Filtered). Values associated with ZOOMit and Z-shimmed sequences are presented in green and in red, respectively. For each subject, the mean tSNR over runs are shown. **C.** Activation maps for the contrast task VS baseline are presented for both sequences, independently for each subject (S01, S02 and S03) and run (1, 2, 3). Maps are thresholded at a Z-score > 2 (cluster-defining threshold of $p < 0.01$ to account for multiple comparisons) and normalized to the PAM50 template (De Leener *et al.*, 2018). Representative coronal views are presented. Probabilistic spinal levels are provided as a reference (Cadotte *et al.*, 2015). S = superior, I = inferior, L = left, R = right, A = anterior, P = posterior.

In line with the findings from Finsterbusch *et al.* (Finsterbusch *et al.*, 2012), signal losses were more pronounced for the acquisitions with no dynamic shimming. Indeed, signals from lower slices displayed very low intensities, as opposed to the satisfying performance of the Z-shimmed approach in this region (Figure 4.3A). It should be noted that lower slices of the ZOOMit acquisitions that contained insufficient signals were removed for later stages of the analysis, to prevent issues when realigning volumes. The tSNR was also consistently higher for Z-shimmed acquisitions (range 32.19 - 43.58, mean over runs for each subject, using filtered signals) than for the standard sequence (range 21.07 - 26.91) (Figure 4.3B). Interestingly, these differences in terms of signal quality were not reflected in the fMRI correlates of task performance (Figure 4.3C). Seven of the nine runs performed with the ZOOMit sequence showed significant activations, in contrast to the Z-shimmed sequence, for which detection of task-related activity was limited to three runs. More importantly, the location of the activity was more stable in the ZOOMit results. For these runs, on average 92% of the voxels were found rostrally, in the C6 and C7 spinal levels (mean over runs, range 65 - 100 %). The patterns detected using the Z-shimmed approach were, instead, more variable. For S01 and S03, the activity was similarly located in rostral spinal levels (respectively, 49% and 84 % of the voxels in C6 - C7), although S01 also displayed activity in C5 (45% of the active voxels). On the other hand, the activation of S02 appeared to be more caudal (84% of the voxels in C8). In summary, these findings emphasized the efficiency of ZOOMit sequences to image task-related activity, while suggesting a limited BOLD sensitivity of the Z-shimmed approach despite improvements in signal quality.

4.3.3 ZOOMit sequence can image motor-related activity in the lumbosacral spine (Experiment D)

Experiments A to C emphasized the potential of a ZOOMit acquisition scheme to image cervical functional activity. Yet, extending this technique to the lumbosacral segments of the spinal cord could pave the way for studies investigating motor or sensory stimulation involving the lower limbs. Here, we evaluated whether a ZOOMit sequence could be employed for this purpose. Using a GLM approach, activity associated with ankle extension was detected in the S1 spinal level (Figure 4.4), which innervates the gastrocnemius (Schirmer *et al.*, 2011), the main muscle involved in this movement. Furthermore, the activation map was clearly circumscribed to the right anterior quadrant, as expected from the nature of the task, which involved a unilateral and isometric movement (i.e., limited sensory and tactile feedback). This suggests that fMRI correlates of lower limb movements can be observed using a ZOOMit sequence.

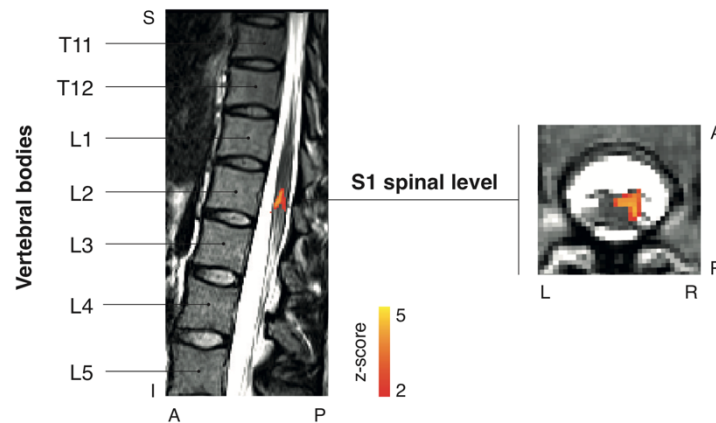


Figure 4.4 – Detection of lumbosacral activity using a ZOOMit sequence (Experiment D, S04). The activation map for the contrast task VS baseline (S04, Experiment C) is thresholded at a Z-score > 2 (cluster-defining threshold of $p < 0.01$ to account for multiple comparisons) and registered to the subject's T2 anatomical image. Representative sagittal and axial views are shown, and vertebral bodies are indicated. S = superior, I = inferior, L = left, R = right, A = anterior, P = posterior.

4.4 Discussion

Spinal cord fMRI is a promising approach to shed light on spinal mechanisms in vivo, but the progression of the field has been relatively limited, with many technical difficulties hindering its deployment. Nevertheless, as MRI-based technology advances (e.g., higher field strength, innovative pulse sequences or improved processing methodologies), new tools that can potentially promote the development of spinal cord imaging are now made available. Here, we conducted a pilot study to evaluate different acquisition protocols based upon recent literature. Our findings highlighted the potential of the ZOOMit acquisition scheme to image spinal functional activity in the cervical and lumbosacral segments.

4.4.1 Reduced field-of-view imaging for spinal cord fMRI

To characterize the ability of different acquisition protocols to detect spinal cord activity, functional images were acquired during simple motor tasks (finger tapping and ankle extension). Performances were compared in terms of signal quality and coverage, and task-related activity was used as a measure of BOLD sensitivity. The results from the different experiments suggested that neural

activity could be detected using spinal cord fMRI, with disparate efficiencies depending on the acquisition parameters. In particular, ZOOMit sequences allowed to efficiently detect BOLD activity in the cervical (Experiments A, B and C) and lumbosacral regions (Experiment D), as emphasized using a combination of model-based (GLM) and data-driven (ICA) approaches to recover task-related activations. The locations of the activations were robust across different runs and consistent with anatomical expectations (i.e., activity localized in C6-C7 for finger tapping, and in S1 for ankle extension). Interestingly, tSNR appeared to be higher for other sequences (e.g., Z-Shimmed sequences, Experiment C), but this disparity did not seem to be associated with an enhanced BOLD detection. This parallels previous results in resting-state spinal cord fMRI, where the tSNR was shown to be a poor predictor of network fidelity (Barry *et al.*, 2018a). While two implementations of the ZOOMit sequences were successfully tested, we finally opted for the version offering the highest spatial resolution (1 x 1 x 3 mm), in order to potentially capture smaller structures and to limit partial volume effects.

Interestingly, the main feature of the ZOOMit approach lies in its ability to perform reduced field-of-view (FOV) imaging, which is achieved thanks to dynamic pulses specifically exciting a region-of-interest in the phase-encoding direction (Siemens, 2012). As a result, signals from external tissues (e.g., muscles, vessels, etc.) are not acquired, thus limiting noise and aliasing artifacts. Since encoding is limited to the targeted region, selective FOV imaging can offer reduced acquisition time without affecting the spatial resolution. This is particularly suited to the geometry of the spinal cord (i.e., small cross-sectional dimensions and long rostro-caudal extent), as many axial slices matching the region-of-interest can be acquired in a short time. In fact, the applicability of reduced FOV approaches has been widely demonstrated for diffusion weighted imaging of the spinal cord (Wheeler-Kingshott *et al.*, 2002; Saritas *et al.*, 2008; Zaharchuk *et al.*, 2011; Finsterbusch, 2012; Samson *et al.*, 2016; Alizadeh *et al.*, 2017). The observations reported in this chapter suggest that functional MRI can also benefit from such imaging protocols. Although we used the ZOOMit sequence (Siemens), it should be noted that similar implementations are also provided by other manufacturers (e.g., FOCUS for GE and iZOOM for Philips), thus facilitating the deployment of this approach in different research and clinical centers.

4.4.2 Methodological considerations and limitations

Another contribution of this pilot work was to establish a processing pipeline tailored to spinal cord fMRI. To this end, we reviewed literature regarding physiological noise removal (Brooks *et al.*, 2008; Kong *et al.*, 2012; Brooks, 2014; Fratini *et al.*, 2014; Eippert *et al.*, 2017a), motion correction (Cohen-Adad *et al.*, 2007, 2009; Summers *et al.*, 2014; Eippert *et al.*, 2017a), normalization to a common template (Fonov *et al.*, 2014; De Leener *et al.*, 2018) and spatial smoothing (Weber *et al.*, 2017). In addition, we benefitted from recent efforts aiming to develop automatic and standardized methods to analyze spinal cord images. Specifically, the proposed pipeline is largely built upon the Spinal Cord Toolbox (SCT) (De Leener *et al.*, 2017), an open-source comprehensive software package offering tools dedicated to the processing of MRI data of the spinal cord.

The main limitation of this study comes from the low number of subjects. Nevertheless, the fact that consistent activations could be detected at the subject-level (with correction for multiple comparison) using the ZOOMit sequences points to the potential of this approach and supports our conclusions. Notwithstanding this limitation, the aim of this pilot study was mainly to provide a reliable ground for future studies. As such, the selected approach was extensively validated in Chapter 5. In addition, this potential was also confirmed in several studies including larger sample sizes (Weber *et al.*, 2016a, 2016b, 2018, 2020).

4.5 Conclusion

In this pilot study, we showed that ZOOMit sequences were promising candidates to perform spinal cord fMRI. In particular, we used simple motor tasks (finger tapping and ankle extension) to demonstrate its ability to capture spinal cord activity. These auspicious results indicated an accurate correspondence with anatomical expectations, both in the cervical and lumbosacral segments. This exploration brings valuable knowledge to build a robust pipeline for spinal cord fMRI.

Chapter 5

Motor output and spinal activity

Functional imaging of rostrocaudal spinal activity during upper limb motor tasks

Nawal Kinany^{1,2,3}, Elvira Pirondini^{2,3}, Roberto Martuzzi⁴, Loan Mattera⁴, Silvestro Micera^{1,5*}, Dimitri Van de Ville^{2,3*}

¹ Bertarelli Foundation Chair in Translational Neuroengineering, Center for Neuroprosthetics, Institute of Bioengineering, School of Engineering, École Polytechnique Fédérale de Lausanne (EPFL), Lausanne, 1015, Switzerland; ² Medical Image Processing Laboratory, Center for Neuroprosthetics, Institute of Bioengineering, École Polytechnique Fédérale de Lausanne (EPFL), Lausanne, 1015, Switzerland; ³ Department of Radiology and Medical Informatics, University of Geneva, Geneva, 1211, Switzerland; ⁴ Fondation Campus Biotech Genève, 1202, Geneva, Switzerland; ⁵ Translational Neural Engineering Area, The Biorobotics Institute, Scuola Superiore Sant'Anna, Pisa, 56025, Italy.

** Equally contributing authors*

Abstract – The spinal cord is the main interface between the brain and the periphery. It notably plays a central role in motor control, as spinal motoneurons activate skeletal muscles involved in voluntary movements. Yet, the spinal mechanisms underlying human movement generation have not been completely elucidated. In this regard, functional magnetic resonance imaging (fMRI) represents a potential tool to probe spinal cord function non-invasively and with high spatial resolution. Nonetheless, a thorough characterization of this approach is still lacking, currently limiting its impact. Here, we aimed at systematically quantifying to which extent fMRI can reveal spinal cord activity along the rostrocaudal direction. We investigated changes in the blood oxygenation level dependent signal of the human cervical spinal cord during bimanual upper limb movements (wrist extension, wrist adduction and finger abduction) in nineteen healthy volunteers. Prior to scanning, we recorded the muscle activity associated with these movements in order to reconstruct the theoretical motor-pool output pattern using an anatomy-based mapping of the electromyographic (EMG) waveforms. EMG-derived spinal maps were characterized by distinct rostrocaudal patterns of activation, thus confirming the task-specific features of the different movements. Analogous activation patterns were captured using spinal cord fMRI. Finally, an additional fMRI dataset was acquired from a subset of the participants (n = 6) to deploy a multivoxel pattern analysis, which allowed successful decoding of movements. These combined results suggest that spinal cord fMRI can be used to image rostrocaudal activation patterns reflecting the underlying activity of the motoneuron pools innervating the task-related muscles. Spinal cord fMRI offers the prospect of a novel tool to study motor processes and potentially their modification following neurological motor disorders.

5.1 Introduction

More than a simple relay, the spinal cord plays a crucial role in movement generation and control (Alstermark and Isa, 2012; Giszter *et al.*, 2012; Vahdat *et al.*, 2015) and can be functionally affected in neurological motor disorders, such as spinal cord injury or multiple sclerosis. Yet, tools to directly and non-invasively investigate the nature and function of the underlying spinal mechanisms in humans are still lacking.

To date, studies assessing spinal cord function in humans have mainly relied on indirect peripheral measurements (muscle activity or force, reflexes, sensory tests, etc.). Notably, muscle recordings have been used to indirectly infer spinal activity during movements by reconstructing theoretical spatiotemporal motoneural activation maps (i.e., ‘spinal maps’), using a combination of the acquired electromyographic (EMG) signals with anatomical knowledge of muscle innervation (Yakovenko *et al.*, 2002). These spinal maps have been extensively used to explore spinal motor output in healthy humans (Ivanenko *et al.*, 2006, 2013; Cappellini *et al.*, 2010; Pirondini *et al.*, 2016), or also to illustrate disrupted motor pathways (e.g., Grasso *et al.*, 2004, in spinal cord injured patients, Coscia *et al.*, 2015, in stroke patients). Nevertheless, this technique relies solely on anatomy-based mapping of muscle outputs. For that reason, it is merely an indirect estimation of the spinal cord activity and it does not fully elucidate the underlying mechanisms.

In this context, functional magnetic resonance imaging (fMRI) of the spinal cord stands as a promising tool to directly and non-invasively investigate spinal processes involved in voluntary movements (Wheeler-Kingshott *et al.*, 2014). In the brain, this technique is already widely deployed, to understand motor control as well as to capture neural signatures of clinical conditions. Relying on the same principle (i.e., the blood oxygenation level dependent – BOLD – signal), spinal cord fMRI measures signal changes reflecting spinal neural activity, in spite of additional technical difficulties inherent to the region of interest (e.g., small structure, field inhomogeneities, physiological noise) (Giove *et al.*, 2004). Since the seminal work of Yoshizawa in 1996 (Yoshizawa *et al.*, 1996), several studies have indeed confirmed the potential of spinal cord fMRI to monitor task-related activity, mainly with tasks involving the upper extremities (Backes *et al.*, 2001; Madi *et al.*, 2001; Stroman and Ryner, 2001; Govers *et al.*, 2007; Maieron *et al.*, 2007; Bouwman *et al.*, 2008; Ng *et al.*, 2008), but also during active and passive ankle movements (Kornelsen and Stroman, 2004, 2007).

However, technological limitations in the formerly available acquisition and processing methods (e.g., low field strength, no correction of physiological noise, no registration to a common template) have initially hindered the development of this approach. As a matter of fact, most early studies were mainly qualitative reports, hence limiting their potential applications, notably to clinical investigations (Kornelsen and Mackey, 2010). In comparison, a few recent works have leveraged novel advanced acquisition and processing paradigms to systematically assess spinal cord activity recorded with fMRI. For instance, these advances allowed confirmation of the robust lateralization of the cervical signal during unimanual isometric contractions (Weber *et al.*, 2016b).

Here, we aim at further investigating the organization of spinal cord activity during voluntary movements, so as to better apprehend the potentials and limitations of the current spinal cord fMRI techniques. We believe that these evaluations represent a pivotal step to further develop spinal cord fMRI and potentially extend it to clinical investigations. Specifically, we want to systematically analyze cervical activations during different movements as regards to their distribution in the rostrocaudal direction. Indeed, during movement generation, spinal motoneurons (i.e., lower motoneurons), which are distributed over different spinal levels, act as an interface between upper

motoneurons located in the motor cortex and skeletal muscles (Marieb and Hoehn, 2014). Thus, movements requiring activations of different muscles should be characterized by distinct spinal activation patterns.

So far, only one early study has investigated the potential of fMRI to reveal these distinct rostrocaudal activation patterns associated with different movements (Madi *et al.*, 2001). In their study, Madi *et al.* probed BOLD signal changes, in three to six subjects, during three upper limb movements (elbow flexion, wrist extension and finger abduction, thus involving different myotomes) and observed activity at the site of muscle innervation, despite unexpected signal in other spinal segments. Notwithstanding the qualitative nature of the obtained results, this study provided a valuable insight into the potential of fMRI to capture the complexity of spinal cord functional activity in humans.

In our study, we extended this preliminary investigation to a more systematic analysis of rostrocaudal functional activity, in a larger cohort of subjects, during distal upper limb movements (wrist extension, wrist adduction and finger abduction). Those movements were selected to include different myotomes, whose rostro-caudal locations vary from C5 to T1. To systematically explore these activation patterns, we capitalized on advances in fMRI acquisition (e.g., higher field strength and selective field-of-view imaging (Finsterbusch, 2013)) and processing (e.g., slice-wise motion correction (Cohen-Adad *et al.*, 2009; De Leener *et al.*, 2017), physiological noise correction (Eippert *et al.*, 2017a) and normalization to a common template (De Leener *et al.*, 2018)). Prior to fMRI acquisitions, muscular activity was also recorded to characterize the motoneuron output by means of EMG-derived spinal maps, so as to obtain theoretical estimations of the rostrocaudal activations, further compared to the acquired fMRI-derived spinal maps. Finally, we complemented our analysis pipeline with a multivariate statistical approach (i.e., multivoxel pattern analysis – MVPA), so as to fully exploit the information content of distributed patterns of spinal activity as well as to probe their precision and stability (Pereira *et al.*, 2009).

Our results show that BOLD activity presented a distinct rostrocaudal cervical organization associated to the different upper limb movements, similar to the one inferred by anatomy-based mapping. Moreover, the subject-specific maps allowed decoding of performed motor tasks with high accuracy, confirming the task-specificity of BOLD spinal signals. These combined results allow highlighting the potential of spinal cord fMRI, and pave the way towards localized observation of human spinal cord function during disparate motor actions. We foresee that such straight measures of spinal neural activity could shed light on mechanisms disrupting motor pathways in neurological conditions. This could eventually lead to the development of new spinal biomarkers, hence complementing current peripheral and anatomical approaches.

5.2 Methods

5.2.1 Participants

Nineteen right-handed healthy subjects (11 females, 26.9 ± 3.4 years old) were enrolled in the study. Two participants had to be excluded from further analyses (see 5.3.1). All participants gave their written informed consent to participate, and the study had been approved by the Commission Cantonale d’Ethique de la Recherche Genève (CCER, Geneva, Switzerland, 2016-01566). All volunteers had normal or corrected-to-normal vision and no history of neurological disorders.

5.2.2 Experimental protocols

EMG and fMRI data were acquired during the same experimental session, which was divided into two phases (Figure 5.1A): (1) Phase 1, in the mock scanner, serving both as training and to record EMG activity; (2) Phase 2, in the MRI scanner, to record spinal functional activity using fMRI.

Six of the subjects (3 females, 28 ± 1.7 years old) participated in an additional experimental session (i.e., Phase 3), during which only fMRI was performed, with a protocol adapted for Multivoxel Pattern Analysis (MVPA) (Coutanche and Thompson-Schill, 2012).

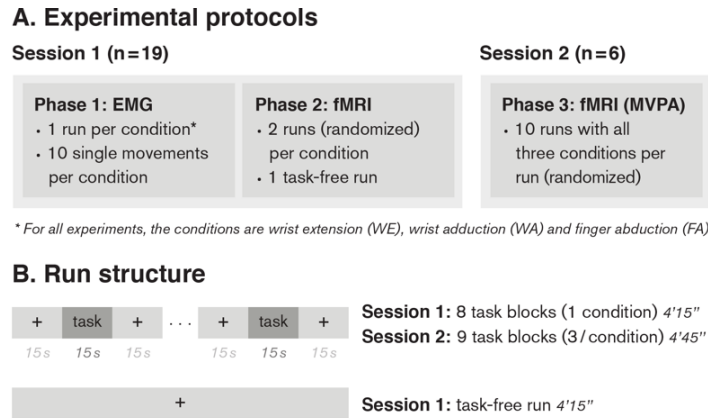


Figure 5.1 – A. Overview of the experimental recordings. **B.** Schematic presentation of the structure of the runs.

Phase 1: EMG experiment

At the beginning of the first experimental session, the different bilateral movements were presented to the participants: wrist extension (i.e., wrist towards the top), wrist adduction (i.e., wrist towards the outside, with an ulnar deviation) and finger abduction (i.e., fingers spreading with thumb adducted). These movements were selected to include different myotomes, in order to potentially elicit activations in different spinal segments (Kendall *et al.*, 2005). Subjects were asked to keep their fingers as relaxed as possible during the wrist movements, and to focus on their muscle activations throughout the experiment.

After appropriate training (i.e., when all movements were performed consistently by the subjects), subjects were installed in a mock scanner (a realistic magnet-free model of the actual MRI scanner) in supine position, with their hands relaxed on their thighs and the palm facing downwards. Phase 1 was subdivided into two parts during which the subjects were asked to perform the movements bilaterally following two paradigms (Figure 5.1A – Phase 1). The first paradigm was designed as a *block experiment* with 8 blocks of movement alternated with 9 blocks of rest (Figure 5.1B). Each block lasted 15 seconds, with an entire run lasting 4 minutes and 15 seconds. Instructions were displayed on a screen (fixation cross ‘+’ during the rest blocks and text indicating ‘movement repetitions’ during the task blocks). Auditory cues were provided to inform the subjects of the different blocks. During the task blocks, subjects executed dynamic repetitions of the movements, prompted by the auditory cues (i.e., tones at a rate of ~ 0.5 Hz, so that 8 movements were performed per task block). Subjects were instructed to remain as still as possible during the rest blocks. One run was done for each movement type (i.e., three runs in total, with only one movement type performed during each run) and the order of the runs was randomized across participants. The second paradigm, instead, was a *single movement experiment* where movements were executed with only one

repetition at a time (e.g., one bilateral wrist extension and back to the resting position) lasting approximately two seconds. For each repetition (i.e., each single movement), an auditory instruction was given by the experimenter to indicate the movement type to be performed. In total, each movement was repeated ten times, in a pseudo-randomized manner. This second paradigm was specific to the EMG experiment and not used in the MRI scanner (see 5.2.2).

Phase 2: fMRI characterization experiment

During functional acquisitions, the participants were installed in the MRI scanner in supine position. The experimental setup was identical to the one used in the mock scanner (visual and auditory cues) and the paradigm was the same as the block experiment in Phase 1. Each subject executed two runs of each movement, in a randomized manner (i.e., six runs in total, with only one movement type performed during each run, in blocks, see Figure 5.1A – Phase 2). A task-free run (i.e., without any overt task) of the same duration as a task run was acquired at the beginning of the experiment (Figure 5.1B). All runs (task and task-free) lasted 4 minutes and 15 seconds. Throughout the recordings, subjects were instructed to relax, breathe normally and minimize motion of the neck, head and shoulders. Movement execution was monitored using a camera. The goal of this monitoring was to ensure that subjects were performing the requested movement type for each run or block. In the event of an error, the fMRI acquisition was stopped and started again with the right movement type.

Phase 3: fMRI multivoxel pattern analysis experiment

In order to confirm the reliability of the fMRI activations elicited during Phase 2 and to further emphasize the task-specific characteristics of the spinal activation maps, an additional dataset was obtained (Figure 5.1A – Phase 3). The experimental design was optimized for MVPA (i.e., many short runs including all three movements (Coutanche and Thompson-Schill, 2012)). Six of the initial subjects participated in this additional phase in the MRI scanner, where the same three movements had to be performed. The experiment was divided into ten runs, each including nine blocks alternated with rest, with each movement repeated three times in a randomized manner (Figure 5.1B). Similarly to the previous session, movements were performed in blocks of 15 seconds and with 8 movement repetitions within each block (i.e., ~0.5 Hz). Each run lasted 4 minutes and 45 seconds.

5.2.3 EMG acquisition and preprocessing

During Phase 1, EMG recordings were performed on 15 arm and hand muscles (biceps brachii long head, BICL, triceps brachii long head, TRIC, brachialis, BRA, brachioradialis, BRAD, pronator teres, PRO, extensor carpi radialis, EXCR, extensor carpi ulnaris, EXCU, extensor digitorum communis, EXDC, flexor carpi radialis, FLCR, flexor carpi ulnaris, FLCU, flexor digitorum superficialis, FLDS, abductor digiti minimi, ABDM, extensor pollicis brevis, EXPB, adductor pollicis transversus, ADPT, abductor pollicis brevis, ABPB). EMG signals were acquired using a Noraxon Desktop DTS wireless system and superficial Ag-AgCl electrodes (Kendall H124SG, ECG electrodes 30 x 24 mm) placed on the above-mentioned muscles of the right upper limb, after appropriate skin preparation. EMG signals were sampled at 1500 Hz. The quality of the EMG signals was visually assessed throughout the recordings (e.g., noise, cross-talk between muscles, etc.). Before the beginning of the experiment, a Maximum Voluntary Contraction (MVC) test was performed for each muscle. This test consists in isometric contractions against resistance, repeated three times for each muscle and alternated with breaks to prevent muscle fatigue.

All raw EMG signals were first detrended and high-pass filtered at a frequency of 50 Hz (Butterworth filter, 7th order). Signals were then rectified and low-pass filtered at a frequency of 10 Hz (Butterworth filter, 7th order). Finally, they were normalized to the MVC value of each muscle (obtained after preprocessing of the related EMG signals), to allow comparison between subjects and movements. All processing steps were performed using Matlab (versions 2016a and 2017b, MathWorks, Natick MA).

5.2.4 EMG analysis

EMG-based estimation of spinal activity

EMG-derived spinal maps provide an anatomy-based estimation of the spatiotemporal activation of lower motoneurons in the spinal cord (Yakovenko *et al.*, 2002). They are based on a combination of EMG recordings with knowledge of the rostrocaudal location of motoneurons pools innervating different muscles, hence providing the theoretical spinal cord output, without relying on direct imaging. For each spinal segment, we used a weighted summation of the preprocessed EMG envelopes (Figure 5.2A), based on the weight coefficients summarized by Kendall *et al.*, (2005), derived from empirical human studies, for the spinal levels C5 to T1 (Table C1). For the block experiment, EMG data were first segmented into individual repetitions (i.e., 8 repetitions for each block, thus 64 repetitions per movement type). For each movement, EMG-derived spinal maps were then computed for each repetition and averaged. Group spinal maps were obtained for each movement type by averaging over participants. In addition, the stability of the EMG-derived spinal maps across movements was estimated for each participant by computing the average Pearson's correlation coefficients between the 64 repetitions. In order to relate EMG-derived and fMRI-derived activation maps, the group-level EMG-derived spinal maps obtained from the block experiment were averaged over time and interpolated (spline interpolation) to generate one-dimensional projections along the z dimension (i.e., spinal levels). These projections were then compared to the fMRI-derived projections using Pearson's correlation coefficients.

Subject-wise classification of estimated spinal maps

In order to confirm the task-specific characteristics of the rostrocaudal activations patterns derived using EMG, a classifier (Linear Discriminant Analysis, LDA) was designed for each subject to discriminate across the three movements using the EMG-derived spinal maps from the *single movement experiment* (i.e., ten repetitions). For the *single movement experiment*, EMG-derived spinal maps were computed as above, independently for each repetition. We used as features the activity of the EMG-derived spinal maps from C5 to T1 averaged over time. The average discards the temporal component of the EMG-derived spinal maps, but allows comparison with the fMRI-MVPA results, where beta images are used as inputs. A three-class LDA classifier was employed (same covariance matrix for each class), with leave-one-movement-out cross validation, within each subject (for the sake of comparison, only the six subjects who performed the MVPA experiment were considered). Confusion matrices were computed considering all cross validation folds, to summarize the accuracy of the classification. In order to assess the statistical significance of those results, we performed non-parametric permutation tests. Specifically, we built 1000 classifiers for each subject, with randomly assigned labels at each permutation fold (i.e., same labels for all subjects within the same permutation), and computed confusion matrices for each permutation and subject. For each permutation, the mean overall accuracy over subjects was calculated and the 99th percentile of this null distribution was defined to obtain the threshold for significance ($p = 0.01$).

5.2.5 fMRI acquisition and preprocessing

Imaging protocol

Imaging data were acquired with a 3.0 Tesla Siemens Prisma scanner (Erlangen, Germany), equipped with a 64-channel head (only inferior element, HC7, was used) and neck coil (both anterior and posterior elements, NC1 and NC2, were used – i.e., 24 channels). For the MVPA recordings, a soft cervical collar was employed to stabilize the neck. All functional acquisitions were performed with a gradient-echo echo-planar sequence, with ZOOMit selective field-of-view imaging (Repetition Time (TR) = 2.5 s, Echo Time (TE) = 34 ms, FOV = 48 x 144 mm, flip angle = 80°, in-plane resolution = 1 x 1 mm, slice thickness = 3 mm). A similar sequence was used by Weber and colleagues (Weber et al., 2016b) and allowed to efficiently observe spinal activation during isometric wrist movements. 32 axial slices were acquired for each volume, covering the cervical enlargement. Before acquisition, shimming adjustments focused on the spinal cord were carried out to optimize the magnetic field homogeneity. In Session 1, 102 volumes were acquired (scan duration of 4 minutes and 15 seconds), while 114 volumes were acquired for Session 2 (scan duration of 4 minutes and 45 seconds). A high-resolution T2-weighted anatomical image, covering C1 to T6 vertebra, was also acquired with a SPACE sequence (single slab 3D turbo spin echo sequence with a slab selective, variable excitation pulse, TR = 1500 ms, TE = 135 ms, echo train length = 74, flip angle = 140°, resolution = 0.4 x 0.4 x 0.8 mm, sagittal orientation).

All preprocessing steps were performed using the Oxford Center for fMRI of the Brain's (FMRIB) Software Library (FSL, version 5.0) (Jenkinson *et al.*, 2012) and the Spinal Cord Toolbox (SCT, version 3.2.1) (De Leener *et al.*, 2017).

Motion correction

As the spinal cord is a very small structure, motion correction is a crucial step to increase the temporal signal-to-noise ratio (tSNR). Motion correction was performed in two steps: i) slice-wise realignment, to account for the articulated structure of the spine (Cohen-Adad et al., 2009; De Leener et al., 2017); and ii) motion scrubbing (Power et al., 2014). For the slice realignment, all images were visually inspected to rule out the presence of artifacts and cropped to remove bottom slices with insufficient signal (the number of removed slices ranges from 3 to 8 across subjects and runs). Then, the volumes of each functional run were averaged and the centerline of the spinal cord was automatically extracted from the resulting image. A cylindrical mask with a diameter of 30 mm along this centerline was drawn and further used to exclude regions outside the spinal cord from the motion correction procedure, as those regions may move independently from the cord. Slice-wise realignment was performed using the mean functional image as the target image. The amount of motion was assessed by computing the average absolute value of the framewise displacement (FD), as well as the Pearson's correlation coefficients between the movement parameters and the task paradigm. Finally, all runs were aligned to the task-free run with FLIRT (FMRIB's Linear Image Registration Tool), using six degrees-of-freedom rigid-body transformations with spline interpolation and a normalized correlation cost function (Jenkinson et al., 2002). Motion scrubbing was subsequently performed by including outlier volumes as noise regressors during the GLM analysis (see 5.2.6). Outliers were detected with FSL's dedicated tool and using DVARS (i.e., the root mean square intensity difference of volume N to volume N+1) with a box-plot cutoff (75th percentile + 1.5 x the interquartile range) (Power et al., 2014). This metric was computed within the spinal cord mask. On average, two volumes per run were considered as outliers.

Physiological noise correction

The close proximity of the lungs, the heart and other visceral organs is an important source of motion when performing spinal cord fMRI (Brooks *et al.*, 2008; Piché *et al.*, 2009; Eippert *et al.*, 2017a). Moreover, cardiac activity generates a pulsatile flow in the cerebrospinal fluid (CSF) around the spinal cord, hence urging the need for physiological noise correction. Therefore, we recorded physiological signals during the functional acquisitions using a photoplethysmograph and a respiratory belt (Biopac MP150 system, California, USA). In order to ensure proper synchronization, the scanner triggers were simultaneously recorded. The physiological recordings were used to build slice-wise nuisance regressors, with a model-based approach derived from the RETROspective Image CORrection (RETROICOR) procedure (Glover *et al.*, 2000a). This method assumes the physiological processes to be quasi-periodic, which means that cardiac and respiratory phases can be uniquely assigned for each image. The signals are then modeled using a low-order Fourier expansion subsampled at the time of image acquisition. This technique has been shown to be efficient for brainstem (Harvey *et al.*, 2008) and spinal cord imaging (Brooks *et al.*, 2008; Kong *et al.*, 2012), where the inclusion of higher order terms was found to be beneficial. Note that 32 regressors are most commonly used to correct for physiological noise in the spinal cord (Kong *et al.*, 2012). Considering the relatively low number of volumes of each run (102 volumes), a solution requiring less regressors was favored, so as to limit the number of degrees-of-freedom, while still accounting for respiratory and cardiac terms as well as for the interaction between those processes, which was demonstrated to be a significant source of noise (Brooks *et al.*, 2008). As such, we used the optimized model presented by Harvey *et al.* (Harvey *et al.*, 2008) and previously employed in the spinal cord by Tinnermann *et al.* (Tinnermann *et al.*, 2017). Specifically, the physiological noise modeling (PNM) tool from FSL was used to yield 18 voxelwise noise regressors. Finally, the signal from the CSF (mean signal in the 10% of CSF voxels whose signal varies the most) was also included as an additional physiological noise regressor, as recommended by Kong *et al.* (2012).

Normalization

To allow comparison between the different movements and subjects, a two-step registration procedure was used to register the images to a template space (i.e., PAM50 template, De Leener *et al.*, 2018), using the Spinal Cord Toolbox (De Leener *et al.*, 2017); i) Anatomical-to-template: a binary mask of the spinal cord was automatically created based on the T2-weighted anatomical image. Subsequently, vertebrae were automatically labelled after manual initialization of the C2-C3 vertebral disk. The spinal cord was straightened along its centerline using the anatomical labels and non-rigid registration to the PAM50 template was performed. This step generates an anatomical image warped into the template space, a template image warped into the anatomical space, as well as the corresponding warping fields; ii) Functional-to-anatomical: the functional images were registered to the template in anatomical space with non-rigid transformations, generating the corresponding warping fields. The warping fields from steps i) and ii) were finally concatenated to obtain the functional-to-template transformation. Mean normalized anatomical and functional images are presented in Figure 5.2B.

Segmentation

Segmentation of the T2-weighted anatomical image was automatically performed using the Spinal Cord Toolbox (De Leener *et al.*, 2017), generating binary masks of the spinal cord and CSF. As for functional images, binary masks of the spinal cord and CSF were manually drawn.

5.2.6 fMRI analysis

fMRI-based estimation of spinal activity

fMRI data analysis was carried out using FSL's fMRI Expert Analysis Tool (FEAT). At the subject-level, the preprocessed images of each run (in the native space, after motion correction) were spatially smoothed and highpass temporal filtering ($\sigma = 45.0$ s) was applied. In order to preserve anatomical consistency, spatial smoothing was performed along the centerline of the spinal cord, using a 3D Gaussian kernel with a full width half maximum (FWHM) of $2 \times 2 \times 6$ mm³. Using these preprocessed time-series, a first-level statistical analysis (intra-subject – within run) was carried out using FMRIB's Improved Linear Model (FILM) with local autocorrelation correction (Woolrich *et al.*, 2001). The design matrix included the explanatory variables, the physiological noise regressors as well as the outlier volumes for motion scrubbing. Specifically, the explanatory variables were defined based on the temporal dynamics of the task (block design), which was convolved with three optimal basis functions using FMRIB's Linear Optimal Basis Set (FLOBS) (Woolrich *et al.*, 2004), in order to account for differences of hemodynamic response function (HRF) between regions and subjects. The second and third waveforms (i.e., the temporal and dispersion derivatives, respectively) were orthogonalized to the first waveform. For each subject and movement, the parameter estimates corresponding to the first FLOBS waveform (i.e., task against rest), obtained independently for the two runs, were combined by passing them up to a second level analysis (intra-subject – across runs), in which task-specific subject level activation maps were obtained using a fixed-effects model.

Parameter estimates obtained during the second level analyses (i.e., subject-level) were then normalized to the PAM50 template (i.e., functional-to-template transformation) and passed up to a third level analysis (inter-subjects) to obtain average group activation maps using FMRIB's Local Analysis of Mixed Effects (FLAME) stages 1 and 2 with outlier detection (Woolrich *et al.* 2004, 2008). Z statistic images were thresholded using clusters determined by $Z > 2$ and a cluster-defining threshold of $p < 0.01$ to account for multiple comparisons. Recent discussions have highlighted concerns regarding the use of parametric testing with a cluster-defining threshold larger than $p = 0.001$ for whole brain fMRI (Eklund *et al.*, 2016). However, our approach is in agreement with recent spinal cord literature (e.g., Tinnermann *et al.*, 2017; Weber *et al.*, 2016a), where the smaller number of voxels curtails the impact of the multiple comparison problem. Furthermore, the use of FSL's FILM to correct for autocorrelation minimizes inflation in the false positive rate (Faull *et al.*, 2015). Besides, we also assessed the presence of false positives using a control analysis. Dice coefficients (Dice, 1945) between the individual movement-related activation patterns were also computed (values ranging from 0 – no similarity – to 1 – equal), so as to assess to what extent the thresholded maps were spatially similar for the different movement types.

In order to relate EMG- and fMRI-derived activation maps, the group-level parameter estimates (i.e., beta maps from the third-level analysis) were masked in order to isolate the motor and sensory components of the signal (i.e., the anterior or posterior hemicords) and summed over the x and y dimensions to generate one-dimensional projections along the z dimension. These projections were smoothed (moving average filter, window length of about one spinal level) to summarize the trends of the distributions and compared to the EMG-derived projections using Pearson's correlation coefficients.

Control analysis

In order to evaluate the presence of false positives, an additional control analysis was performed, similarly to Weber et al (Weber *et al.*, 2016a, 2016b). The preprocessed timeseries of the task-free run recorded at the beginning of the experiment were analyzed following the same procedure as the task runs (i.e., GLM where the explanatory variable was computed using the temporal dynamics – onsets and durations – of an actual task run). Equivalently to the task runs, we computed a group average activation map (thresholded using clusters determined by $Z > 2$ and a cluster-defining threshold of $p < 0.01$). For each subject independently, we also calculated the percentage of spatial extent (number of active voxels divided by the number of voxels in the region of interest; i.e., the C5 to C8 spinal levels) and the average Z-score of the active voxels. This was done in the template space to allow comparison between subjects. Z statistic images were thresholded at $Z > 2$ ($p = 0.01$, uncorrected). In order to compare task-free runs with task runs, we also computed those metrics for all runs of the experiment and averaged results over movement type, independently for each subject. Task-free and task results across subjects were then compared using two-tailed paired t-tests.

Multivoxel pattern analysis

For each subject, MVPA was performed to confirm the task-specific characteristics of the rostrocaudal activations patterns derived using fMRI activity. Images were processed as presented in 5.2.5. Due to the small number of subjects, group activation maps were obtained using a fixed-effects model. Z statistic images were thresholded using clusters determined by $Z > 2$ and a cluster-defining threshold of $p < 0.001$ to account for multiple comparisons. In order to preserve the information content before deploying MVPA, the dataset was also smoothed using a 3D Gaussian kernel with a full width half maximum (FWHM) of $1 \times 1 \times 3 \text{ mm}^3$. Parameter estimates were obtained for each run using the same GLM as presented above but where the explanatory variables were the task dynamics of the three movements. We defined three contrasts, one for each movement type against rest. The resulting parameter estimates (in the native space) were masked to include the C5 to T1 spinal levels. All voxels were used as inputs (no feature selection) and a three-class LDA classifier similar to the EMG-classifier was employed, with leave-one-run-out cross validation. In order to compare the information content of different regions-of-interest, classification was also performed within specific masks (superior and inferior levels, as well as anterior and posterior hemicords). Confusion matrices were computed considering all cross validation folds, to summarize the accuracy of the classification. Statistical significance was computed following the same procedure as the EMG-based classification (see 5.2.4). Finally, we also assessed the stability of the LDA weight maps, by computing the Pearson's correlation coefficients between the LDA weights of each fold.

5.3 Results

5.3.1 Data quality assessment

All subjects completed Phase 1 (EMG experiment) and Phase 2 (fMRI experiment), and 6 of them completed Phase 3 (MVPA experiment). Subjects' performance was monitored during each phase and the quality of the preprocessing steps was visually assessed. As for EMG, data were inspected to rule out the presence of movement artifacts. The assessment of the fMRI data prompted the exclusion of two subjects from further analyses (fMRI and related EMG), as their functional scans did not include the C8 spinal level. A region spanning C5 to C8 spinal levels was imaged in all the

remaining subjects (Figure 5.3A). In order to assess the impact of the different processing steps, we computed the tSNR on the task-free time-series, by dividing the average signal over time by the standard deviation. The efficiency of the motion correction procedure was confirmed by a significant increase ($p < 0.001$, two-tailed paired t-test) of the average tSNR (\pm SE) from 5.15 ± 0.16 before motion correction to 7.92 ± 0.15 after motion correction (Figure C2A). The tSNR further increased to 28.22 ± 0.67 ($p < 0.001$) thanks to temporal filtering and spatial smoothing. Overall, the motion of the spinal cord was limited, as highlighted by the average absolute value of the framewise displacement (\pm SE) ($FD_x = 0.106 \pm 0.002$ mm and $FD_y = 0.143 \pm 0.002$ mm), and only weakly correlated with the task ($\rho_x = 0.063 \pm 0.005$ and $\rho_y = 0.124 \pm 0.004$).

5.3.2 Rostrocaudal activation patterns captured using EMG and fMRI

EMG-derived spinal maps

In order to estimate task-related spinal activity, we first computed EMG-derived spinal maps. These maps are based on anatomical mapping (Figure 5.2A) and they, therefore, represent the theoretical spinal activation patterns. As hypothesized, the spinal activation patterns elicited by the three motor tasks (wrist extension or WE, wrist adduction or WA and finger abduction or FA) exhibited distinct rostrocaudal organizations (Figure 5.2B). Notably, the activity shifted from higher cervical segments during wrist extension to lower spinal regions during wrist adduction and finger abduction. Specifically, the activity elicited by wrist extension was relatively spread out and mainly distributed over the C5-C7 spinal levels. This pattern is associated with EMG activity in the wrist extensor muscles as well as in more proximal muscles, such as the brachioradialis (Figure C3, Table C1). For the wrist adduction, instead, the activity was mainly focused in C7 and C8, coinciding with EMG activity in the flexor and extensor carpi ulnaris. Finally, finger abduction presented an activation pattern similar to the one of wrist adduction, but with an activity peak more focalized over C8, explained by EMG activity in the finger extensor muscles, as well as in distal muscles such as the abductor digiti minimi (Figure C3). We evaluated the stability of the rostrocaudal patterns over repetitions (Figure 5.2C), which highlighted more variability for the maps related to wrist extension ($r = 0.78 \pm 0.07$, mean over subjects \pm SE) compared to the patterns of wrist adduction ($r = 0.92 \pm 0.04$) and finger abduction ($r = 0.97 \pm 0.01$).

This characterization of the estimated spinal activity confirmed that the selected movements required distinct rostrocaudal cervical activations, and they were, thus, apt to explore the potential of fMRI in capturing the complexity of human spinal cord functional activity.

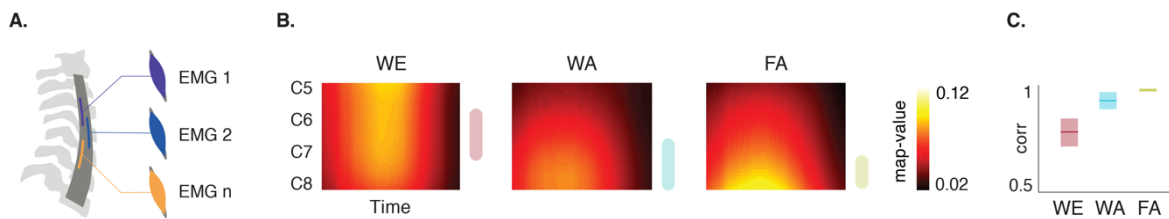


Figure 5.2 – Characterization of rostrocaudal spinal activation patterns (EMG). **A.** EMG-derived spinal maps are used to estimate the spatiotemporal activation of lower motoneurons in the spinal cord (Yakovenko *et al.*, 2002). The motor-pool output patterns are computed using a weighted summation of the EMG signals from the 15 recorded muscles, based on knowledge about the rostrocaudal locations of the motoneuron pools innervating those muscles (see Table C1). **B.** Group EMG-derived spinal maps for the different movements (WE = wrist extension, WA = wrist adduction, FA = finger abduction). Spinal maps were averaged over subjects and repetitions (64 repetitions of each movement for each subject). The color bars, displayed at the right

of each map, represent the a priori expected peaks of activation. Spinal levels are displayed on the y-axis, and x-axis corresponds to the duration of the movement (~ 2 seconds). **C.** Correlation between the time-averaged EMG-derived spinal maps of the different movement repetitions. Data are presented as mean over subjects \pm SE.

fMRI-derived spinal maps

In order to elucidate whether spinal cord BOLD activity also displayed a similar task-specific rostrocaudal organization, we computed fMRI-derived spinal maps. After preprocessing, we assessed group level spinal activity using a GLM with mixed-effects modelling. For all movements, a larger portion of the active voxels was observed in the anterior (i.e., motor) part of the spinal cord ($56.44 \pm 2\%$, mean over movements \pm SD, see sagittal slices in Figure C4), while the activity was roughly distributed evenly between left and right hemicords ($47.65 \pm 17.8\%$ in the right hemicord), as expected for bimanual motor tasks. Activity was also spread out between the grey and white matter ($33.84 \pm 8.5\%$ in the grey matter), in accordance with reports from Weber and colleagues (Weber et al., 2017). Similarly to the EMG-derived spinal maps, wrist extension resulted in more rostral activity than wrist adduction and finger abduction (Figure 5.3B-C, Table C2). Specifically, the activity related to wrist extension was mainly located in the C6 spinal level (81.8% of the active voxels), while it was also the only movement eliciting activity in the C5 spinal level (12.9% of the active voxels). The main activity peak during wrist adduction and finger abduction, instead, was focused in C8 (respectively 68.7 % and 55.4 % of the active voxels), while the remaining activations were only found in the C7 spinal level. The difference between these activation patterns was also illustrated by the low Dice coefficients between them ($D = 0$ between WE and WA, $D = 0.04$ between WE and FA and $D = 0.36$ between WA and FA).

These results highlight that the BOLD activity reveals a distinct rostrocaudal cervical organization associated with different upper limb movements, consistent with the one inferred using anatomy-based mapping.

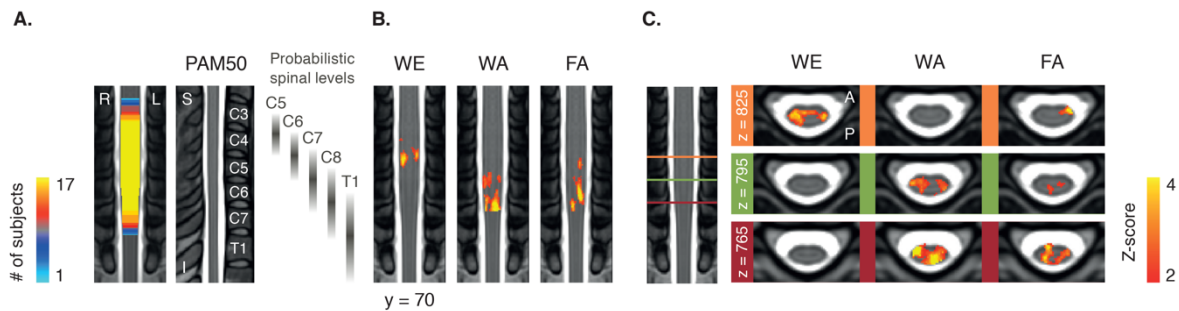


Figure 5.3 – Characterization of rostrocaudal spinal activation patterns (fMRI). **A.** Imaged regions map, normalized to the PAM50 template (De Leener *et al.*, 2018). The color bar indicates the number of subjects with the corresponding region included in the functional maps. A sagittal view of the PAM50 template is presented for reference. The vertebral bodies are labeled, as well as the corresponding probabilistic spinal levels (Cadotte *et al.*, 2015). **B.** Group activation maps (mixed-effects modelling) for the contrast task VS baseline (WE = wrist extension, WA = wrist adduction, FA = finger abduction). Maps are thresholded at a Z-score > 2 (cluster-defining threshold of $p < 0.01$) and normalized to the PAM50 template. Only a region from C5 to C8 is considered (imaged in all subjects). Central coronal views are presented, with the same slice ($y = 70$) shown for all movements. **C.** Three axial slices ($z = 765$, $z = 795$ and $z = 825$, see left panel) are presented (right panel), overlaid on the PAM50 template. For sagittal slices, see Figure C4. S = superior, I = inferior, L = left, R = right, A = anterior, P = posterior.

The activation patterns are specific to task runs

In order to control for false positives, we employed a control analysis in which the same procedure as the one used to detect task-related activity was applied to task-free runs. At the group level, no voxel exceeded the significance threshold when combining the task-free activation maps from all subjects (Figure 5.4A), emphasizing that task-free activity was not localized in a particular spinal level.

We then further assessed the significance of fMRI activation during task runs by comparing both the extent and amplitude of the activity linked to task and task-free runs at the subject-level, similarly to Weber *et al.* (Weber *et al.*, 2016b, 2016a). The spatial extent of the activity (i.e., percentage of activated spinal cord) identified during the task runs (Figure 5.4B, $8.44 \pm 1.16\%$, mean over subjects \pm SE) was significantly larger ($p < 0.001$) than during the task-free runs ($2.97 \pm 0.47\%$). Similarly, the intensity of the activity, as illustrated by the average Z-score over the active voxels, was significantly higher ($p < 0.01$) during the task runs (Figure 5.4B, 2.56 ± 0.04) than during the task-free runs (2.38 ± 0.03).

These combined results indicate that the cervical rostrocaudal activation patterns imaged during task runs are likely not artefactual and reflect motoneuron activity.

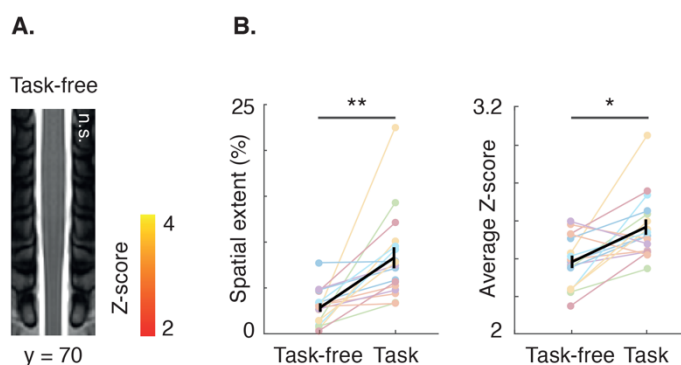


Figure 5.4 – Control analyses. **A.** Group activation maps (mixed-effects modelling) for the control analysis (task-free runs). Maps are thresholded at a Z-score > 2 (cluster-defining threshold of $p < 0.01$) and normalized to the PAM50 template (coronal view). n.s. indicates that no significant activity was detected. **B.** Comparison of the percentage spatial extent of the activity, relative to the C5 to C8 region of the spinal cord (left panel), and average Z-score (right panel) during the task-free and task runs. Each colored line corresponds to one subject. The black line corresponds to the mean \pm SE. * corresponds to $p < 0.01$ and ** to $p < 0.001$ (two-tailed paired t-test).

EMG- and fMRI-derived spinal maps present similar rostrocaudal distributions

To further examine the similarities between the rostrocaudal distributions of spinal activity extracted using EMG and fMRI and, thus, to confirm the specificity of spinal BOLD signal, we compared the obtained activation patterns using their respective projections along the z direction. When focusing on the anterior (i.e., motor) profiles (Figure 5.5), similar distributions were observed for both modalities, with task-related profiles shifted towards rostral or caudal spinal levels, depending on the motor task. During wrist extension, the spread of activity was stronger at the rostral part of the cord, while the activity during wrist adduction and finger abduction was more localized in the caudal region. The projections of activity derived from the two modalities were significantly correlated ($p < 0.001$), as stressed by the correlation coefficients ρ between the EMG- and fMRI-

derived trends: 0.32 for wrist extension, 0.90 for wrist adduction, and 0.70 for finger abduction. These moderate to high correlations indicate similar rostrocaudal distributions, inferred either peripherally from the EMG activity or directly from functional imaging of the spinal activity, and it supports the use of fMRI to directly image spinal cord involvement during upper limb movements. In addition, the profiles of WA and FA, both shifted towards the caudal side of the cord, also exhibited a high correlation between their related EMG- and fMRI- derived profiles (e.g., $\rho = 0.96$ between the fMRI-derived profile of WA and the EMG-derived profile of FA, see full correlation matrix in Figure C5A). This is, however, in accordance with the high correlation of 0.98 between the EMG-derived profiles of those two movement types (see Figure C5C). Interestingly, the fMRI-derived projections, when considering only the posterior (i.e., sensory) component of the spinal activity, were also highly correlated ($p < 0.001$) with the EMG-derived projections ($\rho_{WE} = 0.73$, $\rho_{WA} = 0.87$ and $\rho_{FA} = 0.43$) (Figure C5B).

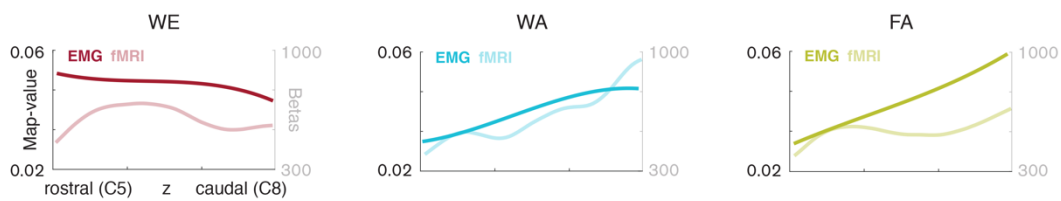


Figure 5.5 – Rostrocaudal distributions of activations. For each movement type (WE = wrist extension, WA= wrist adduction, FA= finger abduction), distributions of the EMG- (dark line) and fMRI- (light line) derived spinal maps along the z direction are presented. Time-averaged-map values are used for the projections of EMG-derived spinal map while group parameter estimates (anterior, or motor, hemicord), summed over the x and y dimensions, are used for the projection of fMRI-derived spinal maps. Spinal levels are displayed on the x-axis, and y-axis corresponds to the projected map-values (EMG) or betas (fMRI). Pearson's correlation coefficients between the two modalities are respectively 0.32 ($p < 0.001$), 0.90 ($p < 0.001$) and 0.70 ($p < 0.001$).

5.3.3 Imaged rostrocaudal organization is task-specific

Both EMG- and fMRI-derived spinal maps suggest task-specific rostrocaudal distributions of the cervical spinal cord activity. In order to verify this hypothesis, we used a machine learning approach that exploits the information content of each motor task in the spinal maps derived from both modalities.

When using EMG-derived projections (i.e., time-averaged) of the estimated spinal activity as features (i.e., one feature for each spinal level), the classifier was able to differentiate the three classes with a high accuracy, as emphasized by the diagonal confusion matrix (Figure 5.6A). The overall accuracy (95%) was significantly higher than chance ($p < 0.01$, permutation testing, chance level at ~33%), highlighting the specificity of the estimated spinal activation patterns.

Furthermore, we deployed MVPA to decode the executed task based on the voxelwise spinal BOLD activity. When using information from the whole spinal cord, rostrocaudal activation patterns allowed to decode movements for all three classes with an overall accuracy of 54.5% (Figure 5.6B), significantly better than chance ($p < 0.01$). The stability of the LDA weight maps over cross-validation folds was also assessed by computing their average Pearson's correlation coefficients. This analysis showed a high correlation between folds (0.87 ± 0.01 , mean over subjects \pm SE).

In order to investigate the relative contribution of different sub-regions of the cord, we performed the classification independently: i) for inferior and superior spinal levels and ii) for each hemicord (i.e., anterior and posterior) (Figure C6). Although wrist adduction and finger abduction could still be decoded using both rostral and caudal segments, wrist extension failed to be detected using the inferior region of the cord (38.4%), emphasizing the rostral character of the related activation. Interestingly, movements could be classified efficiently using both anterior and posterior hemicords (average classifications of 48.4% and 51.1%, respectively), highlighting the shared influence of motor and sensory processes.

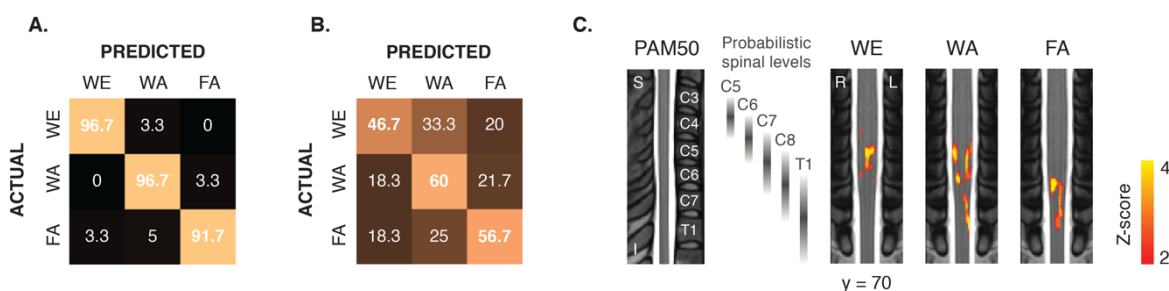


Figure 5.6 – Average decoding accuracy. **A.** Each subject performed 10 repetitions of each movement. EMG-derived spinal maps were computed for each repetition and averaged over time to keep only the spatial information (i.e., five features per sample, corresponding to the mean activity over time in the spinal levels from C5 to T1). Classification was performed in each subject using an LDA classifier (leave-one-movement-out cross validation). Confusion matrices were then averaged over subjects (here, only the six subjects who participated in the MVPA experiment were considered). The average accuracy over subjects and conditions was 95% and significantly above the chance level ($p < 0.01$, permutation testing, chance level at ~33%). All values are reported in percentage. **B.** Multivoxel pattern analysis (MVPA) was performed in each subject, using data from the C5 to T1 spinal levels and a LDA classifier (leave-one-run-out cross validation). Confusion matrices were averaged over subjects. The average accuracy over subjects and conditions was 54.5% and significantly above the chance level ($p < 0.01$, permutation testing). **C.** Group activation maps (of the six subjects who participated in the MVPA experiment) for the contrast task VS baseline. Maps represent the mean activity over the group (fixed-effects analysis) and are thresholded at a Z-score > 2 (cluster-defining threshold of $p < 0.001$). All maps are normalized to the PAM50 template (De Leener *et al.*, 2018). Coronal views are presented, with the same slice shown for all movements. A sagittal view of the PAM50 template is shown as a reference, with the corresponding probabilistic spinal level. WE = wrist extension, WA = wrist adduction, FA = finger abduction. S = superior, I = inferior, L = left, R = right.

Finally, to validate the rostrocaudal cervical patterns presented in 5.3.2, we assessed the group level activity elicited by the three movements during the MVPA experiment (Figure 5.6C, Table C3). This analysis uncovered activation maps consistent with those imaged during the first experimental session (Figure 5.3B). Similarly, the three different task-related patterns presented distinct spatial distributions ($D = 0.33$ between WE and WA, $D = 0.15$ between WE and FA and $D = 0.19$ between WA and FA). More specifically, activation patterns related to wrist extension were located in higher spinal levels (8.3% of the active voxels in C6, and 65.4% in C7) than the ones elicited by wrist adduction (45.1% in C7, 29.4% in C8 and 23.4% in T1) or finger abduction (50% in C8 and 50% in T1). These results further demonstrate the robustness of the task-specific rostrocaudal organization.

These combined results corroborate the hypothesis that the measured BOLD signal actually reflects the spinal processes underlying movement. They, therefore, support the potential of fMRI to image task-specific rostrocaudal organization, offering as such the prospect of a novel tool to study spinal function and its disruption in neurological conditions.

5.4 Discussion

Here, we hypothesized that spinal cord fMRI could be used to reliably image task-specific activity in different cervical segments during distinct upper limb movements. To address this question, we combined spinal functional imaging with EMG recordings, as advised in previous studies (Madi *et al.*, 2001; Weber *et al.*, 2016b). Specifically, we exploited anatomical knowledge of muscle innervation to infer the contribution of each muscle to the spinal activity in the different segments. Notwithstanding the limitations inherent to the imaging of spinal cord function, we acquired distinct task-specific rostrocaudal activation patterns using fMRI, consistent with the theoretical maps derived from the muscular recordings. These task-specific spinal maps allowed for a successful decoding of motor tasks. Here we discuss our results with an emphasis on acquisition and processing precautions for reliable spinal fMRI BOLD signal.

5.4.1 Imaged cervical activation patterns have a task-specific rostrocaudal organization

To characterize the specificity of the activation in the rostrocaudal direction, we selected movements that allowed capitalizing on the different locations of the motoneuron pools innervating the employed muscles. Wrist extension, if performed with no radial or ulnar deviation, should mainly be linked to motoneuron activity in the C6-C7 spinal levels, while wrist adduction and finger abduction were expected to elicit lower activity, in the C7-C8 and C8-T1 segments, respectively (Table C1). These task-specific rostrocaudal activations were first confirmed using EMG recordings (Figure 5.2). Muscular activity was mapped back onto the spinal cord using anatomical knowledge of muscle innervation. As expected, the activity shifted from rostral levels for wrist extension to caudal regions for wrist adduction and finger abduction. However, these maps, derived from indirect peripheral recordings, are solely based on anatomical considerations and, thus, do not fully inform on the actual spinal cord function. Conversely, fMRI enables localized observation of spinal cord activity. Using this technique, we showed that spinal BOLD signal also reflected these task-specific activations patterns (Figure 5.3). In line with the findings of Madi *et al.* (2001), we observed higher activations for wrist extension than for finger abduction. Nonetheless, the detected activity was more focal in our study, possibly due to the increased field strength, the choice of sequence (selective field-of-view imaging), and to the ad hoc noise correction steps applied to the signal. Wrist adduction, which was not performed in the study of Madi *et al.*, also elicited the expected activity, with an activation profile shifted towards caudal segments. For the three movements, the activity was equally distributed between the left and right hemicords and mainly located in the anterior (i.e., ventral) hemicord. This is in agreement with anatomical knowledge, as movements were performed bilaterally and motoneurons are found in the ventral horns. Despite the larger anterior activity, significant activity was also found in the posterior (i.e., dorsal) hemicord. As the task consisted in performing dynamic repetitions of the movements, this is likely resulting from sensory processes and proprioception. In parallel, a control analysis where we applied our analysis pipeline to task-free runs emphasized that the imaged cervical patterns were likely not of artefactual origin (Figure 5.4).

In a subsequent step, we quantified the relationship between the EMG- and fMRI-derived spinal maps by using their respective projections on the z dimension (i.e., spinal levels) and demonstrated analogous rostrocaudal distributions of activity between the two modalities (Figure 5.5). This suggests that both activation maps stem from the same motor-related spinal processes, hence supporting the use of fMRI to reliably and directly image task-related rostrocaudal cervical activity.

In order to further confirm the identified task-specific activation patterns, we employed a machine learning paradigm on a subset of participants, so as to decode motor tasks based on spinal activation maps. fMRI-derived patterns presented significant decoding performances (54.5%), highlighting the task-specific information contained in the acquired BOLD signal. Wrist extension, however, presented a lower classification accuracy (46.7%), potentially related to higher movement variability when executing this task. This hypothesis is supported by the theoretical EMG-derived spinal maps, where a lower correlation was observed between the activation patterns of the different repetitions of this movement (Figure 5.2), possibly indicating that the wrist was not consistently moved in the expected neutral ulnar deviation. Nevertheless, it should be emphasized that wrist extension and adduction, although involving the same joint, could be distinguished with a significant accuracy. Interestingly, when using only the inferior portion of the spinal cord, wrist extension tended to be mistaken for wrist adduction (Figure C6A), further supporting the rostral character of the underlying activation.

Another compelling finding concerned the high decoding performances obtained when using the anterior or posterior hemicord only (48.4% and 51.1%, respectively, see Figure C6C-D). This suggests that both motor and sensory processes were reliably captured by spinal cord fMRI and were both task-specific. The task-specificity of sensory information parallels recent findings from Yeganegi *et al.* (2018). In that study, the authors showed for the first time that electrophysiological recordings of dorsal gray matter activity in anesthetized cats allowed for successful decoding of hind limb movements. Indeed, movements not only elicit efferent signals travelling from the ventral horns of the spinal cord to the muscles, they also involve afferent feedback provided by sensory receptors (e.g., muscles spindles, tendons or mechanoreceptors) and going to the central nervous system, through the dorsal horns of the spinal cord (Enoka, 2008). Consequently, observing task-specific sensory activity is not unexpected, as also reflected by the significant correlations obtained between the EMG- and fMRI-derived profiles, when considering the sensory component only.

Importantly, the group activation maps resulting from this additional imaging session presented similar rostrocaudal patterns as the ones derived from the initial experiment, confirming the robustness of the captured rostrocaudal activation patterns. Altogether, these results underscore the broad potential of spinal cord fMRI, not only to image spinal motoneuron activity, but also to explore sensory and proprioceptive mechanisms, one aspect that cannot be probed with peripheral recordings, such as EMG acquisitions. To our knowledge, our study is the first report of MVPA in the spinal cord during different types of movements (note, however, that Weber and colleagues previously used MVPA to decode left and right wrist flexions (Weber *et al.*, 2016b)).

5.4.2 Methodological challenges of spinal cord fMRI and possible solutions

Although spinal cord fMRI relies on the same principles as brain fMRI, it presents additional challenges (Giove *et al.*, 2004) and has therefore not yet received as much interest. First, the small cross-sectional dimensions of the spinal cord prompt the need for high resolution imaging to avoid partial volume effects and to unravel the details of the structure of interest. Second, the spinal cord is surrounded by different tissue types, whose disparate magnetic susceptibilities affect the static magnetic field. This can lead to image artifacts, such as distortions or signal dropouts, when standard T2*-weighted fMRI protocols are employed. Advancements in terms of hardware (Cohen-Adad *et al.*, 2011) and sequences (Finsterbusch *et al.*, 2012) are currently being proposed in order to obviate these constraints. Finally, another prominent issue is related to the close proximity of the lungs, the heart and other visceral organs, which are important sources of motion (Piché *et al.*, 2009).

Notably, cardiac activity generates a pulsatile flow in the cerebrospinal fluid (CSF) around the spinal cord.

In our study, we employed different approaches, from data acquisition to (pre-)processing, to overcome these limitations and get a reliable signal. Specifically, prior to acquisition, shimming adjustments focused on the cervical spinal cord were carried out to optimize the field homogeneity in the region of interest. The acquisition was performed using selective field-of-view imaging, hence increasing imaging speed while allowing for high spatial resolution (1 x 1 x 3 mm). In order to curtail the detrimental effect of motion, we applied several processing steps. Realignment was first conducted using a slice-wise procedure, accounting for the articulated structure of the spinal cord (Cohen-Adad *et al.*, 2009; De Leener *et al.*, 2017). Outlier volumes were then identified and included as confounds during the GLM analysis. Finally, we used the physiological recordings acquired throughout the experiment to model additional nuisance regressors, based on the RETROICOR procedure (Glover *et al.*, 2000a), and a CSF regressor was also included. Both approaches have been demonstrated to improve activation statistics (Brooks *et al.*, 2008), and their impact was reflected by the increase in tSNR observed consecutive to these processing steps (see 5.3.1 and Figure C2). In addition, the GLM analysis was also adapted to account for potential variations of the HRF, compared to the canonical HRF commonly employed. Indeed, the temporal properties of the spinal HRF are still unclear (Giulietti *et al.*, 2008) and no solution to tackle this limitation has so far been proposed in the context of spinal cord fMRI. Therefore, we opted for an approach previously used in brainstem fMRI (e.g., Faull *et al.*, 2015), a field facing similar challenges in this regard (Devonshire *et al.*, 2012) and employed a FLOBS-generated basis set instead of the canonical HRF (Woolrich *et al.*, 2004), so as to be less sensitive to hemodynamic variability (e.g., dispersion, delay or shape).

Following this advanced pipeline, we were able to image robust rostrocaudal patterns. Nevertheless, some limitations need to be acknowledged. Regardless of the consistent sequence of motoneuron pools across subjects (e.g., distal arm muscles innervated by lower spinal levels than proximal muscles), individual differences in the location of spinal levels with respect to the corresponding vertebral bodies have previously been reported (Cadotte *et al.*, 2015). When registering subject data to a common template, these differences are not taken into account with current normalization algorithms, an issue which was already raised by Weber *et al.* (2016a, 2016b). This could hinder our ability to detect activation patterns along the rostrocaudal direction, due to potential mismatches between subjects. Although less prevalent, similar issues exist in brain fMRI (Dubois and Adolphs, 2016) and progresses in both fields (e.g., advanced algorithms or functionally-informed alignment) could gradually overcome these difficulties.

5.4.3 Experimental limitations and considerations

Our paper aimed to relate EMG and fMRI activity in order to highlight the neural origin of the signal recorded with spinal cord fMRI. This represents a first step in showing that this technique can shed light on spinal motor responses. We believe that future studies could deploy similar motor-based paradigms, to infer general principles regarding human spinal cord functional organization. We propose hereafter a number of experimental and technical recommendations. While the structure of our experiment (i.e., two complementary sessions to record EMG and fMRI) imposed certain timing constraints to prevent subjects' fatigue, future studies focusing solely on fMRI recordings could potentially limit the number of conditions, so as to increase the scan duration, or the number of runs, to further explore the properties of the underlying spinal signals. An additional aspect that may be of interest is the variability of movement execution. Indeed, as muscle activations were not performed at a specific percentage of the Maximum Voluntary Contraction, the exact output of the

muscles during the fMRI scans was not controlled. Performing isometric tasks could help in this regard, although it may require the use of custom splints, which need to be adapted to the movements of interest. Finally, we recommend the use of a soft cervical collar for the functional recordings, as this helps stabilize and straighten the neck, hence participating to improve image quality.

5.5 Conclusion

Despite technological challenges, we captured variations in spinal activity and revealed task-specific rostrocaudal patterns in agreement with the anatomical arrangement of motoneuron pools. These results contribute to advance our understanding of the potential of spinal cord fMRI. They demonstrate its prospects as a reliable tool to investigate spinal cord function and to further understand mechanisms involved in motor control and neurological motor disorders, such as spinal cord injury or multiple sclerosis. For instance, spinal cord fMRI could allow exploiting information on spinal sensorimotor function, rather than theoretical estimations such as EMG-based maps. Eventually, we foresee that such advances in our knowledge of the spinal cord could support clinical decision-process and help inform intervention procedures.

Chapter 6

Spinal cord's functional architecture

Dynamic functional connectivity of resting-state spinal cord fMRI reveals fine-grained intrinsic architecture

Nawal Kinany^{1,2}, Elvira Pirondini³, Silvestro Micera^{2,4,6*}, Dimitri Van De Ville^{1,3,5,6*}

¹ Medical Image Processing Laboratory, Center for Neuroprosthetics, Institute of Bioengineering, Ecole Polytechnique Fédérale de Lausanne (EPFL), 1202 Geneva, Switzerland; ² Bertarelli Foundation Chair in Translational Neuroengineering, Center for Neuroprosthetics, Institute of Bioengineering, Ecole Polytechnique Fédérale de Lausanne (EPFL), 1202 Geneva, Switzerland; ³ Department of Radiology and Medical Informatics, University of Geneva, 1211 Geneva, Switzerland; ⁴ The BioRobotics Institute and Department of Excellence in Robotics and AI, Scuola Superiore Sant'Anna, 56025 Pontedera, Italy

** Equally contributing authors*

Abstract – The neuroimaging community has shown tremendous interest in exploring the brain's spontaneous activity using fMRI. On the contrary, the spinal cord has been largely overlooked despite its pivotal role in processing sensorimotor signals. Only a handful of studies have probed the organization of spinal resting-state fluctuations, always using static measures of connectivity. Many innovative approaches have emerged to analyze dynamics of brain fMRI but they have not yet been applied to the spinal cord, although they could help disentangle its functional architecture. Here, we leveraged a dynamic connectivity method based on the clustering of hemodynamic-informed transients to unravel the rich dynamic organization of spinal resting-state signals. We tested this approach in 19 healthy subjects, uncovering fine-grained spinal components and highlighting their neuroanatomical and physiological nature. We provide a versatile tool, SpiCiCAP, to characterize spinal circuits during rest and task, as well as their disruption in neurological disorders.

6.1 Introduction

Since its early days in the 90s, functional Magnetic Resonance Imaging (fMRI) has had a tremendous impact on the field of neuroscience, substantially advancing our understanding of the central nervous system (CNS). Relying on non-invasive detection of blood-oxygen-level dependent (BOLD) signal changes, this imaging technique offers meaningful insights into the underlying neuronal activity (Logothetis *et al.*, 2001). As such, it has been widely deployed to investigate systems-level brain function, not only during tasks, but also at rest, with fMRI studies focusing on the spontaneous fluctuations of the BOLD signals (Van Den Heuvel and Hulshoff Pol, 2010). In this context, resting-state networks (RSNs) are conventionally extracted using functional connectivity (FC) measures based on the coherent activation (e.g., Pearson's correlation) of distinct brain regions. These intrinsic

networks have emerged as the building blocks of human brain function (Damoiseaux *et al.*, 2006) and their activity has been shown to encode a wide array of behavioral traits, from emotion to intellectual performances (Greicius *et al.*, 2003; Liégeois *et al.*, 2019). Besides, their widespread alteration in neurological diseases also support their clinical relevance and their potential as biomarkers of functional integrity (Castellanos *et al.*, 2013; Allali *et al.*, 2018). Unfortunately, this exploration of the functional architecture of the human CNS *in vivo* has been essentially focused on the brain. In contrast, the spinal cord, another component of the CNS, has been mostly overlooked, even though this structure plays a crucial role in sensorimotor processing, for instance in proprioception, pain processing, or during movement generation and control (Darby and Frysztak, 2013). As such, insights into the intrinsic functional organization of human spinal circuits appear as pivotal contributions to fundamental and clinical neurosciences.

This limited amount of research may partly stem from the inaccessibility of the spinal cord, a small structure deeply encapsulated in the vertebral column (Marieb, E. N, Hoehn, 2014; Powers *et al.*, 2018). Imaging this region is indeed particularly challenging, as the adjacent bones and organs make it prone to field inhomogeneities and physiological noise (Giove *et al.*, 2004; Stroman *et al.*, 2014). This may explain why functional activity of the spinal cord was, at first, mainly explored using indirect peripheral measurements (e.g., muscle activity, force, reflexes or sensory tests) (Yakovenko *et al.*, 2002; Greenberg, 2003; Knikou, 2008). Yet, developments in spinal cord fMRI acquisition (Finsterbusch, 2013) and processing protocols (De Leener *et al.*, 2017; Eippert *et al.*, 2017a) have worked toward circumventing these constraints and a growing body of research highlighted the feasibility of this approach (Wheeler-Kingshott *et al.*, 2014). Moreover, the validity of BOLD signals as a hemodynamic proxy of spinal neural activity was recently confirmed in non-human primates, as signal variations were shown to be in agreement with electrophysiological activity (i.e., local field potentials) (Wu *et al.*, 2019).

Spinal cord fMRI studies have primarily focused on task-evoked activity, offering an unparalleled opportunity to examine the human spinal cord *in action* (Wheeler-Kingshott *et al.*, 2014). Spontaneous signal fluctuations, on the other hand, were only explored in recent years. Sensory and motor RSNs were first reported using different approaches, such as seed-based FC (at 3T, Eippert *et al.*, 2017b, and at 7T, Barry *et al.*, 2014, 2016) or independent component analysis (ICA) (at 3T, Kong *et al.*, 2014). Similar components were also identified at ultra-high field (9.4T) in rats (Wu *et al.*, 2018) and non-human primates (Chen *et al.*, 2015). Although these studies demonstrated the existence of functional circuits in the spinal cord at rest, their neurophysiological underpinnings remained unclear (Eippert and Tracey, 2014).

A critical factor that hindered thorough characterization of the nature of spinal networks was the use of *static* measures of FC, as all earlier studies assumed temporal stationarity over the scanning session. As a result, they did not account for the dynamic evolution of interactions over time and they could not fully capture the properties of functional networks (Calhoun *et al.*, 2001). In the brain, however, it has been highlighted that FC fluctuates at the time scale of seconds, and numerous *dynamic* functional connectivity (dFC) approaches have been proposed to delve into these time-varying properties (Preti *et al.*, 2016). This has provided new insights into the properties of resting-state (RS) signals, as well as informed on the disrupted dynamic interplay of distinct brain regions in various neurological disorders.

Here, we posit that dynamic methods could enable disentangling the ongoing sustained spinal activity, possibly revealing new attributes of spinal RSNs. To this end, we leveraged a promising approach to extract dynamic RS components, termed *innovation-driven co-activation patterns*, or

iCAPs. In this context, the term *innovation* refers to transient activity, recovered using robust hemodynamic-informed deconvolution (Karahanoğlu *et al.*, 2013). Patterns obtained using transients constitute the building blocks of time-resolved activity and offer a unique way to dissect temporally overlapping signals. Of note, this has previously enabled the separation of known brain RSNs (e.g., the default mode network) into multiple subsystems (Karahanoğlu and Van De Ville, 2015). Capitalizing on this potential to unfold ongoing functional activity, we combined this method with a dedicated spinal cord fMRI pipeline into the spinal iCAP framework – SpiCiCAP. Using this framework, we assessed spatial and temporal properties of cervical RS activity in healthy participants and uncovered precise features of the spinal cord functional architecture. To the best of our knowledge, this is the first time that fine-grained RS components are revealed in the spinal cord. This unparalleled level of detail allowed us to shed new light on their neuroanatomical nature as well as to further characterize their physiological roles, hence emphasizing their involvement in distributed neural pathways supporting ascending sensory feedback (e.g., for proprioception), and descending communication from supraspinal structures (e.g., for motor control). The SpiCiCAP framework could foster relevant advances in our understanding of spinal cord function, not only at rest, but also when dynamically modulated in sensory and motor tasks. Finally, this opens an avenue to map spinal circuits in neurological conditions and to investigate the mechanisms associated with dysfunction and recovery.

6.2 Methods

6.2.1 Data and Code Availability

Codes generated in this study, as well as raw and analyzed MRI data, are available on Mendeley Data (<http://dx.doi.org/10.17632/n2k7zz2xyt.1>).

6.2.2 Experimental model and subject details

Twenty-two right-handed healthy subjects (11 females, 28.5 ± 3.5 years old) were enrolled in the study. All participants gave their written informed consent to participate, and the study had been approved by the Commission Cantonale d'Éthique de la Recherche Genève (CCER, study 2019-00203). All volunteers had normal or corrected-to-normal vision and no history of neurological disorders.

6.2.3 Method details

Data acquisition

The imaging protocol was the same as the one used in our previous study in which we imaged the rostrocaudal patterns of activity elicited by upper limb movements (Kinany *et al.*, 2019). Imaging data were acquired with a 3.0 Tesla Siemens Prisma scanner (Erlangen, Germany), equipped with a 64-channel head (only inferior element, HC7, was used) and neck coil (both anterior and posterior elements, NC1 and NC2, were used – i.e., 24 channels). For 14 subjects, the upper element of the spine coil (SP1) was also used (optimal coil combination defined by the scanner). All functional acquisitions were performed with a gradient-echo echo-planar sequence, with ZOOMit selective field-of-view imaging (Repetition Time (TR) = 2.5 s, Echo Time (TE) = 34 ms, FOV = 48 x 144 mm, flip angle = 80°, in-plane resolution = 1 x 1 mm, slice thickness = 3 mm). The cervical enlargement was covered using 32 axial slices. Particular care was taken in placing slices perpendicularly to the spinal cord, in order to maximize the alignment with the intervertebral discs and limit signal

dropouts due to field inhomogeneities (Finsterbusch *et al.*, 2012). Before acquisition, the magnetic field homogeneity was optimized using shimming adjustments focused on the spinal cord. For each participant, 360 volumes (i.e., 15 minutes) were acquired, during rest (i.e., no explicit task), with eyes open (an empty screen was shown). A high-resolution T2-weighted anatomical image, covering a region from C1 to the upper part of the thoracic spine, was also acquired with a SPACE sequence (single slab 3D turbo spin echo sequence with a slab selective, variable excitation pulse, TR = 1500 ms, TE = 135 ms, echo train length = 74, flip angle = 140°, resolution = 0.4 x 0.4 x 0.8 mm, sagittal orientation). Throughout the recordings, subjects were instructed to relax, breathe normally and minimize motion. A soft cervical collar was used in order to stabilize the neck.

6.2.4 Quantification and statistical analysis

Data processing

All preprocessing steps were performed using the Oxford Center for fMRI of the Brain's (FMRIB) Software Library (FSL, version 5.0) (Jenkinson *et al.*, 2012) and the Spinal Cord Toolbox (SCT, version 3.2.7) (De Leener *et al.*, 2017). The pipeline is based on the one used in our previous study (Kinany *et al.*, 2019).

1) *Motion correction*

All functional and anatomical images were inspected for potential artifacts. For each participant, the bottom slices whose signal was insufficient to accurately detect the spinal cord were removed. The mean functional image was then used to automatically detect the centerline of the spinal cord. A cylindrical mask (diameter of 30 mm) along the centerline was generated to prevent the inclusion of regions moving independently from the spinal cord and slice-wise realignment was performed with the mean functional image as reference. This procedure allows to account for the articulated structure of the spinal cord (De Leener *et al.*, 2017). Motion parameters were extracted and used to compute the mean (i.e., average over slices and volumes) framewise displacement along the x and y directions (FD_x and FD_y). A stringent threshold on the framewise displacement (i.e., mean FD_x or $FD_y > 0.2$ mm) was applied to detect subjects with excessive motion. This led to the exclusion of three subjects. All the other subjects ($n = 19$) were included in further analyses. The overall level of motion of these remaining subjects was minimal (mean \pm SE along x and y: $FD_x = 0.10 \pm 0.04$ mm, and $FD_y = 0.10 \pm 0.03$ mm).

Following slice-wise realignment, outliers volumes were detected for motion scrubbing (i.e., to be included as noise regressors during the time courses denoising, see 2) *Denoising time courses*). Variations in image intensity were assessed to identify potential outliers with FSL, using DVARS (i.e., the root mean square intensity difference of volume N to volume N+1) within the spinal cord, and a box-plot cutoff (75th percentile + 1.5 x the interquartile range) (Power *et al.*, 2014). On average, five volumes per run were considered as outliers.

2) *Denoising time courses*

Due to the proximity of respiratory tracts and visceral organs, the spinal cord is particularly prone to physiological motion (Brooks *et al.*, 2008; Piché *et al.*, 2009; Eippert *et al.*, 2017a). It is, therefore, essential to limit the detrimental impact of those fluctuations on BOLD time courses. For this purpose, physiological signals (i.e., heart rate and respiration) and scanner triggers were acquired throughout the functional scans, using a photoplethysmograph and a respiratory belt (Biopac

MP150 system, California, USA). These recordings were used to generate noise regressors, with a procedure based on RETROspective Image CORrection (RETROICOR) (Glover *et al.*, 2000b). Briefly, this approach assigns cardiac and respiratory phases to each functional volume, considering their acquisition timings with respect to the physiological traces. Then, a low-order Fourier expansion is typically used to model physiological noise. In the spinal cord, however, recommendations suggest to include higher order Fourier terms as well as the noise related to the cerebrospinal fluid (CSF) (Brooks *et al.*, 2008; Kong *et al.*, 2012). Accordingly, we generated 32 voxelwise noise regressors using the physiological noise modeling (PNM) tool from FSL, along with an additional regressor corresponding to the CSF signal (mean signal in the 10% of CSF voxels whose signal varies the most).

These 33 physiological noise regressors (PNM and CSF) were combined with motion correction parameters (i.e., two slice-wise regressors, for the motion in x and y) and motion outliers (see 1) *Motion correction*), and regressed from the fMRI time-series using FSL's fMRI Expert Analysis Tool (FEAT). The resulting residuals were then spatially smoothed using a 3D Gaussian kernel with a full width half maximum (FWHM) of $2 \times 2 \times 6 \text{ mm}^3$. Smoothing was performed along the centerline of the spinal cord, so as to preserve anatomical consistency.

3) *Estimating warping fields for normalization*

The PAM50 template (spatial resolution of $0.5 \times 0.5 \times 0.5 \text{ mm}^3$) was employed as a common space (De Leener *et al.*, 2018). Using the Spinal Cord Toolbox (De Leener *et al.*, 2017), a two-step registration procedure was performed for each subject: i) *Anatomical-to-template*: automatic spinal cord segmentation and vertebrae labelling was performed, based on the T2-weighted image. The spinal cord was then straightened along its centerline and registered to the PAM50 template, using the labels (specifically for the vertebral bodies C4 and C7) and non-rigid transformations; ii) *Functional-to-anatomical*: functional images were registered to the T2-weighted image, using non-rigid transformations. The warping fields from steps i) and ii) were finally concatenated to obtain the *functional-to-template* transformation. Accurate spatial registration to a common space is a crucial step to allow meaningful inter-subject comparison. Nevertheless, the normalization procedure in the spinal cord is notoriously challenging, partly because of its small size, combined with non-uniform signal quality (Giove *et al.*, 2004). To validate the precision of our registration to the PAM50 template, we show the results of this procedure in Figure D1, which illustrates the accurate correspondence between the normalized anatomical and functional images and the template. Importantly, the delineation between grey and white matter can be clearly observed in the normalized fMRI runs.

Data analysis

1) *Extracting innovation-driven coactivation patterns (iCAPs)*

The innovation-driven co-activation patterns (iCAPs) pipeline was performed using the iCAP toolbox (Matlab code openly available on <https://c4science.ch/source/iCAPs/>, Karahanoğlu and Van De Ville, 2015). The different steps of the pipeline are illustrated in Figure 6.1. In detail, the measured fMRI time course is assumed to reflect the underlying activity-inducing signal, temporally smoothed by the effect of the hemodynamic response function (HRF). As a result, we first used the denoised images (native space) and deployed a regularized deconvolution, using the Total Activation framework (TA, Karahanoğlu *et al.*, 2013), to reliably retrieve these activity-inducing signals. Transients (i.e., the so-called innovation signals) were computed as the temporal derivative of

these activity-inducing time courses. It is worth highlighting that innovation frames present spatial patterns that are much cleaner than the related fMRI frames because they have been undone from hemodynamic blur, but also noise that is not compatible with the hemodynamic properties. In order to select significant innovations (i.e., frames with significant transitioning activities), a two-step thresholding procedure was used: i) temporal thresholding: for each voxel, a surrogate distribution was obtained by applying TA on phase randomized data and a 5% confidence interval was used to select significant voxels, ii) spatial thresholding: only the innovation frames with at least 5% of active voxels were considered to be significant. Significant innovation frames were normalized to the PAM50 and used to identify resting-state components, the iCAPs, using temporal K-means clustering. Two levels of granularity were chosen: i) $K = 4$ (low granularity) and ii) $K = 40$ (high granularity). The iCAPs spatial maps were then thresholded ($Z > 1.6$ for $K = 4$ and $Z > 5$ for $K = 40$) and binarized, and their spatial similarity evaluated by means of Dice coefficients (i.e., twice the overlapping area, divided by the total number of voxels in both maps).

It should be pointed out that *a priori* estimating data dimensionality is a long standing issue in network analyses (Xu and Wunsch, 2005). In order to ensure that selecting 4 low-granularity and 40 high-granularity components provided reliable partitions of the data, we systematically evaluated the reproducibility of the clustering for different values of K (see supplementary materials, Figure D3). Specifically, we used a subsampling scheme where clustering was repeated using random subsets of the data (100 subsets of 10 subjects). For each repetition, K-means clustering was performed using different values of K and each clustering solution was compared to the global clustering obtained with the 19 subjects, using the adjusted mutual information (AMI) (Vinh *et al.*, 2010) which estimates the similarity of two discrete assignments (i.e., by comparing the assignments of the significant innovation frames to the different clusters). Of note, this metric is corrected for the effect of chance in order to avoid biasing results in favor of a large number of clusters. Values range from 0 (chance level) to 1 (equal partitions). In order to explore low-granularity values, K values corresponding to multiples of four (i.e., number of spinal levels in the imaged regions) were probed. Moreover, we investigated higher values of K , ranging from 20 to 90 in steps of 10, hence covering a wide range of potential fine-grained subdivisions. Details of this analysis are presented in Figure D3.

2) *Linking iCAPs with spinal levels and atlas regions*

To validate the relevance of the iCAP spatial patterns, we assessed whether they were related to the underlying neuroanatomy of the spinal cord. In order to do so, we relied on probabilistic atlas maps provided by the Spinal Cord Toolbox (De Leener *et al.*, 2017), including both spinal levels (Cadotte *et al.*, 2015) and atlas regions (Lévy *et al.*, 2015) (see Figure D2). To investigate the spatial distribution of the low- and high-granularity iCAPs, we used binarized versions of the probabilistic atlas maps and computed, for each iCAP, the proportion of voxels found in the different levels and regions. As the aim was to precisely localize spatial maps with respect to the atlas regions, atlas maps were thresholded at a probability of 0.5 before binarization, to ensure that only the highest probabilities were taken into account for the assignment. Based on these distributions, low- and high-granularity iCAPs were then uniquely matched to individual spinal levels or atlas regions, respectively, using a hard assignment based on the maximum number of voxels. Dice coefficients were used to confirm the accuracy of the matching. To this end, the full extent of the corresponding atlas maps was considered (i.e., non-zero probability), so as to assess the correspondence between borders. Finally, fine-grained iCAPs were grouped based on their neuroanatomical identity. For presentation purposes, iCAPs were ordered rostral-caudally based on the location of their center-of-gravity, unless indicated otherwise.

3) *Assessing iCAP stability*

We assessed iCAPs stability within and between subjects. In order to investigate the temporal stability over all subjects (i.e., stability within subjects), we assessed the *intra-subject* similarity. For each subject, the functional run was split into two equal parts of 7.5 minutes (i.e., 180 volumes). The procedure to obtain iCAP maps was performed independently for these two parts and using both levels of granularity ($K = 4$ or 40). Dice coefficients were computed to assess the similarity between the spatial maps of the two parts. To ensure that the spatial organization of iCAPs was stable across subjects on the entire dataset (i.e., stability between subjects), we computed the *inter-subject* similarity, as the mean Dice coefficients over each pair of subjects, for a particular iCAP pair. For each subject, subject-wise iCAP maps were computed as the mean over the frames of this subject assigned to each iCAP and binarized ($Z > 3$).

4) *Extracting temporal dynamics*

Finally, subject-specific time courses were obtained by regional averaging of the activity-inducing signals within the binarized iCAP maps. In order to extract their temporal properties, the subject-level iCAPs time courses were Z-scored and thresholded ($|Z| > 1$) to highlight active and de-active time points. The total and average durations of each iCAP were computed, as well as couplings and anti-couplings between pairs of iCAPs, based on the number of time points with same signs or different signs simultaneous coactivations, expressed as Jaccard indices (i.e., percent joint activation time). To evaluate the statistical significance of these (anti-)couplings, we performed non-parametric permutation tests. At each permutation ($n = 5000$), we randomly assigned iCAP labels, for each subject and computed (anti-)couplings using Jaccard indices. The mean overall couplings (or anti-couplings) matrix over subjects was then calculated. The upper triangular matrices resulting from each permutation were finally used to build a null distribution on which thresholds for significance were obtained. Bonferroni correction ($n = 2$) was applied to account for the presence of both couplings and anti-couplings. Mean durations and couplings were compared using paired t-tests (Bonferroni corrected).

5) *Investigating neural interplays*

In order to investigate whether interplays were functionally relevant, we studied interactions inside (between iCAPs of one pathway) and across (between iCAPs of different pathways) neural pathways (as defined based on the neuroanatomical identity of iCAPs, see 2) *Linking iCAPs with spinal levels and atlas regions*). Interactions were described using four features (couplings and anti-couplings, both within and between levels). Values were Z-scored for each subject and feature and scatter plots were used to capture potential interaction signatures. To further assess whether these signatures were pathway-specific, three-class QDA classifiers were employed, with leave-one-subject-out cross validation. Confusion matrices were computed considering all cross validation folds to summarize the accuracy of the classification. Statistical significance of accuracy was verified by performing non-parametric permutation testing. Specifically, classification was performed using the same procedure, but with randomly assigned labels. For each permutation ($n = 5000$), the three diagonal elements of the resulting confusion matrix were retrieved and used to build a null distribution on which thresholds for significance were obtained. As both interactions inside and across pathways were considered, Bonferroni correction was applied to account for the two comparisons.

6.3 Results

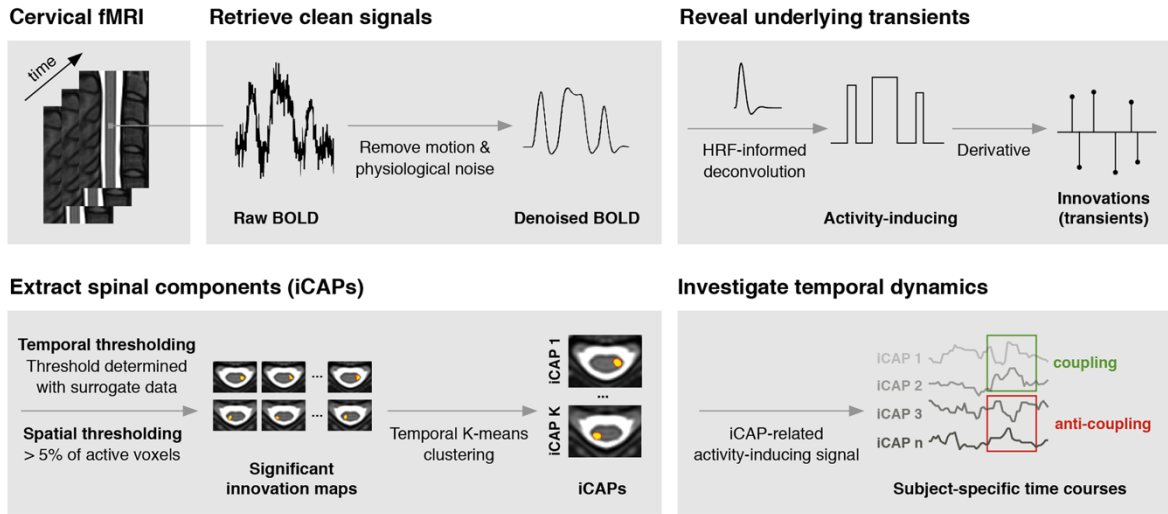


Figure 6.1 – SpiCiCAP framework. Cervical functional images are processed to circumvent the effect of various sources of noise. Hemodynamic blur is removed using hemodynamic-informed deconvolution, to reveal activity-inducing signals. Innovation signals (i.e., transients) are then obtained by temporal derivation. A two-step thresholding is applied to select significant innovation frames, which undergo K-means temporal clustering to obtain stable iCAPs (K = number of iCAPs). Recovered iCAPs can be used as regions of interest to extract subject-specific time courses from activity-inducing signals. Finally, interaction measures (e.g., Jaccard index for couplings and anti-couplings) can be computed. Inspired by Karahanoğlu *et al.*, 2013.

6.3.1 The SpiCiCAP framework

Our goal was to achieve a deeper understanding of spinal cord’s functional architecture. To this end, we reasoned that exploring the time-varying content of spinal spontaneous fluctuations would bring new light on their neurophysiological nature. The SpiCiCAP framework, whose approach is outlined in Figure 6.1, integrates tailored spinal cord fMRI protocols with a state-of-the-art method to extract dynamic RSNs using clustering of hemodynamic-informed transients. It enables to decompose spinal circuits and to investigate their spatio-temporal properties.

6.3.2 Spatial maps of spinal iCAPs specifically match spinal cord neuroanatomy

Using the SpiCiCAP framework, we extracted spinal iCAPs for two levels of granularity (i.e., temporal clustering done independently for two different parameters K , to recover 4 or 40 iCAPs, see Figure 6.1). The choice of these two levels of granularity was supported by a systematic evaluation of clustering reproducibility for different K s (details presented in Figure D3). Visual inspection of the recovered iCAPs confirmed the absence of noisy spatial patterns (Figure 6.2). Components displayed high spatial segregation, as underlined by the limited overlap between iCAP maps (Figure D5). In line with previous studies (Kong *et al.*, 2014; Weber *et al.*, 2018), spinal iCAPs spanned a limited rostro-caudal extent, likely reflecting the segmental structure of the spinal cord. Specifically, low-level granularity iCAPs corresponded to spinal levels C5 to C8 (Figure 6.2B), with on average 91% of their voxels in a single spinal level (Figure D5). The specificity of the matching between iCAPs and segmental borders was confirmed using Dice coefficients (mean \pm SD = 0.71 ± 0.03). For this low-level granularity, all iCAPs were bilateral and included dorsal and ventral components (Figure D4).

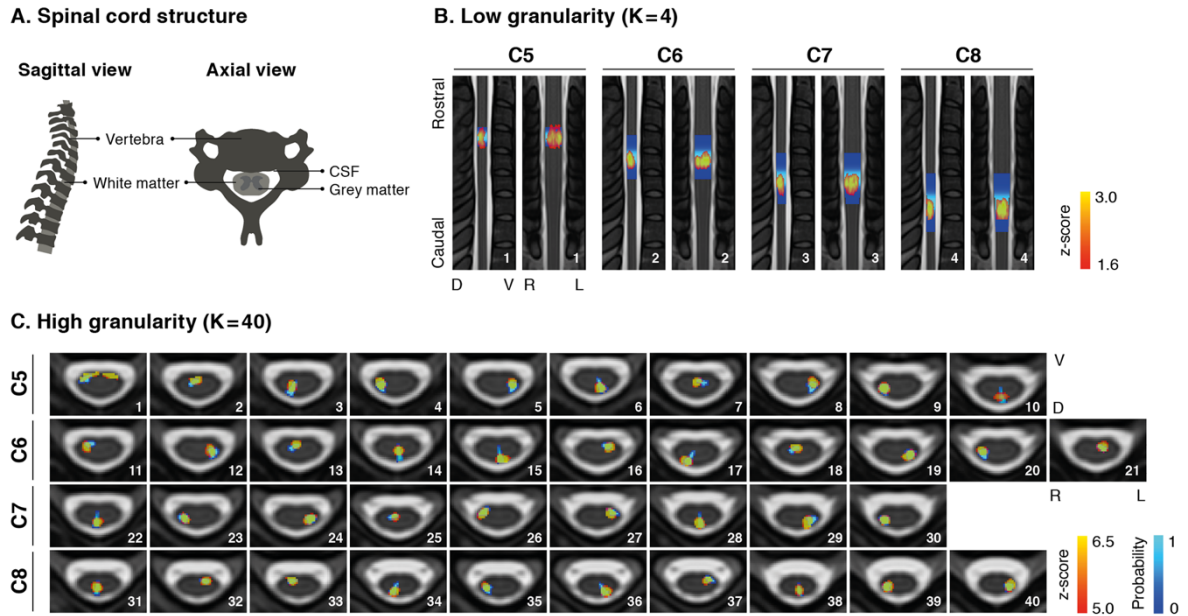


Figure 6.2 – iCAPs spatial patterns. **A.** Schematic representation of the structure of the spinal cord. CSF = cerebrospinal fluid. **B.** Each low-granularity iCAP spans a limited rostro-caudal extent, in line with the segmental structure of the spinal cord (one iCAP corresponds to one spinal level, mean Dice coefficient \pm SD = 0.71 ± 0.03). Axial views are presented in Figure D4. **C.** When extracting 40 spinal iCAPs (presented from rostral to caudal components), spatial maps get divided within the axial plane and lined up with known subdivisions of the spinal cord, reflecting meaningful neuroanatomical structures (Figure D2), such as white matter tracts or grey matter horns (mean Dice coefficient \pm SD = 0.61 ± 0.11). Coronal and sagittal views are presented in Figure D4. Thresholded iCAP maps, in red, are overlaid on the corresponding spinal level or atlas region probabilistic maps, in blue (De Leener *et al.*, 2017). The PAM50 template is used as a background (De Leener *et al.*, 2018). iCAPs numbers are indicated in the bottom right corners. L = left, R = right, D = dorsal, V = ventral.

When increasing the granularity to 40 iCAPs, we observed that components got further subdivided within the axial plane (Figure 6.2C), with high-granularity iCAPs that were predominantly unilateral and strictly confined to either the dorsal or ventral side. In order to achieve a comprehensive description of this axial organization, we harnessed a detailed atlas of the spinal cord (Figure D2) to precisely quantify the axial voxel distribution. For each of these fine-grained iCAPs, voxels were distributed over a restricted number of atlas regions (on average, two regions per iCAP included 68% of its voxels, Figure D5), emphasizing that the activity patterns were highly localized and structured. Each spinal component was, thus, matched to a specific atlas region (mean Dice coefficient \pm SD = 0.61 ± 0.11). Overall, these results illustrated the high correspondence between the components extracted using the SpiCiCAP framework and the underlying neuroanatomy of the spinal cord.

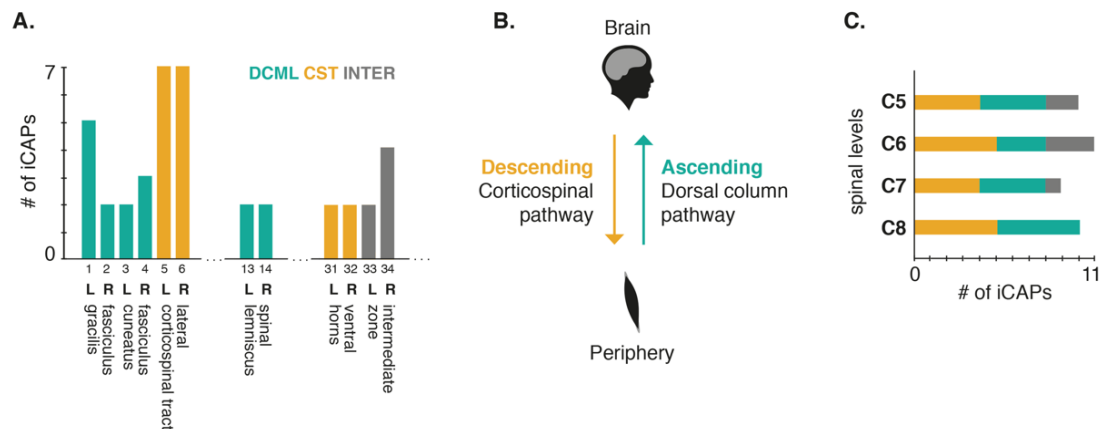


Figure 6.3 – Neural pathways. **A.** Each fine-grained iCAPs was matched to one of the 36 atlas regions (hard assignment based on the maximum number of voxels, see Figure D2 for the details of the atlas regions and Figure D5 for the voxel distributions). The number of iCAPs per atlas region is presented, omitting regions with no assigned iCAP. Atlas regions from 1 to 30 correspond to the white matter and regions from 31 to 36 are found in the grey matter. ICAPs cluster into spinal neural pathways involved in transmitting and processing information from and to the brain (DCML: Dorsal Column Medial Lemniscus pathway and CST: Cortico-Spinal Tract pathway). Intermediate regions (INTER) are also present. **B.** Schematic representation of the spinal neural pathways. **C.** ICAP distribution in the different spinal levels. Colors refer to neural pathways.

6.3.3 Spinal iCAPs assemble into neural pathways

To further inspect the neuroanatomical identity of the 40 spinal iCAPs, we used the hard assignment proposed above (i.e., each iCAP uniquely matched with an atlas region) and computed the number of iCAPs found in each of the atlas regions, so as to seek whether an organized topographical distribution could be highlighted (Figure 2.2). We observed that iCAPs fell into a limited number of regions, i.e., 12 of the 36 atlas regions (see Figure D2 for the exhaustive list), which corresponded to six distinct neuroanatomical zones comprising both grey (i.e., ventral horns and intermediate regions) and white matter (i.e., the dorsal column, formed by the fasciculus gracilis and fasciculus cuneatus, the cortico-spinal tract and the medial lemniscus). For each of them, iCAPs were present in both left and right lateralization. We then investigated whether this apparent sparsity, driven by fMRI activity, had a functional meaning. An examination of the different roles of these regions (Figure D2, Darby and Frysztak, 2013) revealed that iCAPs were essentially organized following two neural pathways of the spinal cord: 18 iCAPs relied on the cortico-spinal tract pathway (CST), while 16 iCAPs corresponded to the dorsal column-medial lemniscus pathway (DCML) (Figure 6.3A). These pathways fulfill distinct functional contributions (Figure 6.3B), as they are involved in conveying and processing signals from (e.g., for motor control) and to (e.g., for proprioception) the brain, respectively (Darby and Frysztak, 2013). The former is a *descending* pathway that goes from the motor cortex to the ventral horns (regions 31-32), through the cortico-spinal tract (regions 5-6). The latter is an *ascending* pathway, sending proprioceptive and sensory information from the periphery to the somatosensory cortex, by travelling through the dorsal column (regions 1-4) and the medial lemniscus (regions 13-14). Finally, 6 iCAPs were found in the *intermediate* zone (regions 33-34), at the interface between these ascending and descending pathways. The rostro-caudal distribution of the iCAPs underlined a uniform presence of ascending and descending pathways from C5 to C8, while no intermediate regions were found in C8 (Figure 6.3C). To evaluate the distance between iCAPs along the two pathways, we computed the mean rostro-caudal position of the associated iCAPs, in each spinal level. The average spatial gaps along the CST and DCML pathway were, respectively, 17.88 ± 1.70 mm and 18.43 ± 0.6 mm (mean \pm SD over spinal levels), in line

with the anatomical distance between spinal levels (Cadotte *et al.*, 2015). In sum, these results suggested that the recovered spinal iCAPs were functionally relevant. This hints at the potential of the proposed framework to non-invasively monitor the neural mechanisms underlying information flow and processing, both locally in the spinal cord and in relation to inputs from the brain and the periphery.

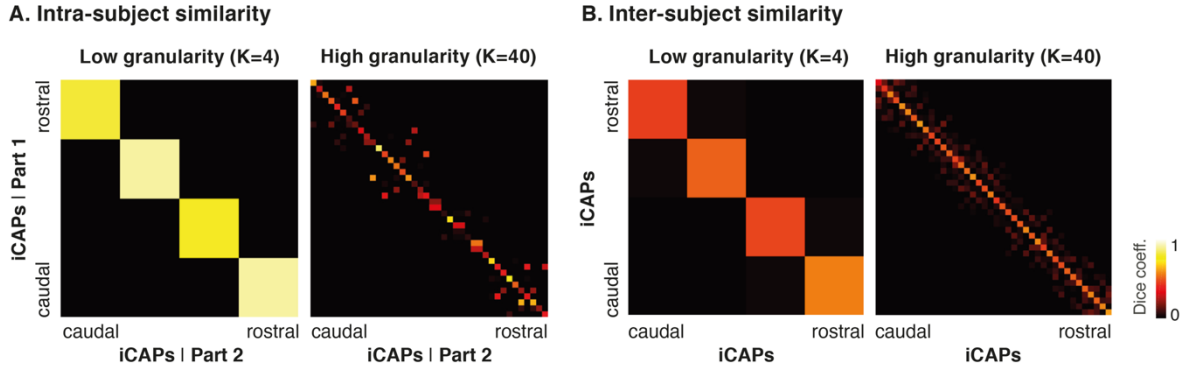


Figure 6.4 – Stability of spatial patterns. **A.** In order to evaluate the intra-subject stability of the iCAPs spatial maps, the dataset was split into two equal parts (180 volumes each, i.e., 7.5 minutes), and iCAPs were then computed independently for each part. The matrices show the Dice coefficients between both sets of iCAPs, for the two granularity levels ($K = 4$, low granularity, and $K = 40$, high granularity). **B.** The inter-subject stability was computed as the mean Dice coefficients over each pair of subjects, for a particular iCAP pair. In all matrices, iCAPs are ordered rostral-caudally.

6.3.4 Spinal functional organization is stable within and between subjects

We evaluated the consistency of the observed iCAPs both within and between subjects. First, we assessed the *intra-subject* stability by splitting each subject's dataset into two equal parts (180 volumes each, i.e., 7.5 minutes) in which we recomputed iCAPs independently (Figure 6.4A). The intra-subject stability was particularly high for the low-granularity iCAPs (mean Dice coefficient \pm SD of 0.83 ± 0.08), indicating that the coarse functional organization was stable over time within the same subjects. Conversely, the stability of fine-grained spatial patterns was more variable (mean Dice coefficient \pm SD of 0.38 ± 0.20), with 12 iCAPs displaying Dice coefficients superior to 0.5 (maximum value of 0.84), while 7 iCAPs exhibited coefficients lower than 0.2 (minimum value of 0.06). ICAPs with low and high Dice coefficients were distributed over the different pathways, with no specific pattern. Despite this variability, both sets of iCAPs were in line with the underlying neuroanatomy (mean Dice coefficient with atlas regions \pm SD of 0.63 ± 0.10 for part 1 and 0.61 ± 0.10 for part 2). Moreover, they carried similar functional relevance, as atlas regions of the two parts could still be clustered into the same pathways (ascending DCML, descending CST and intermediate INTER) (Figure D6). We then probed *inter-subject* stability by comparing the iCAPs maps of all subjects for each iCAP pair of the full dataset. The spatial patterns were similar across subjects (Figure 6.4B), as highlighted by the diagonal matrices obtained for low- and high-granularity iCAPs (mean Dice coefficient \pm SD of 0.49 ± 0.05 and 0.51 ± 0.06 for the different levels of granularity, respectively). Altogether, these findings underlined the stability of the spinal cord's functional organization, along with the potential of iCAPs to represent its underlying building blocks.

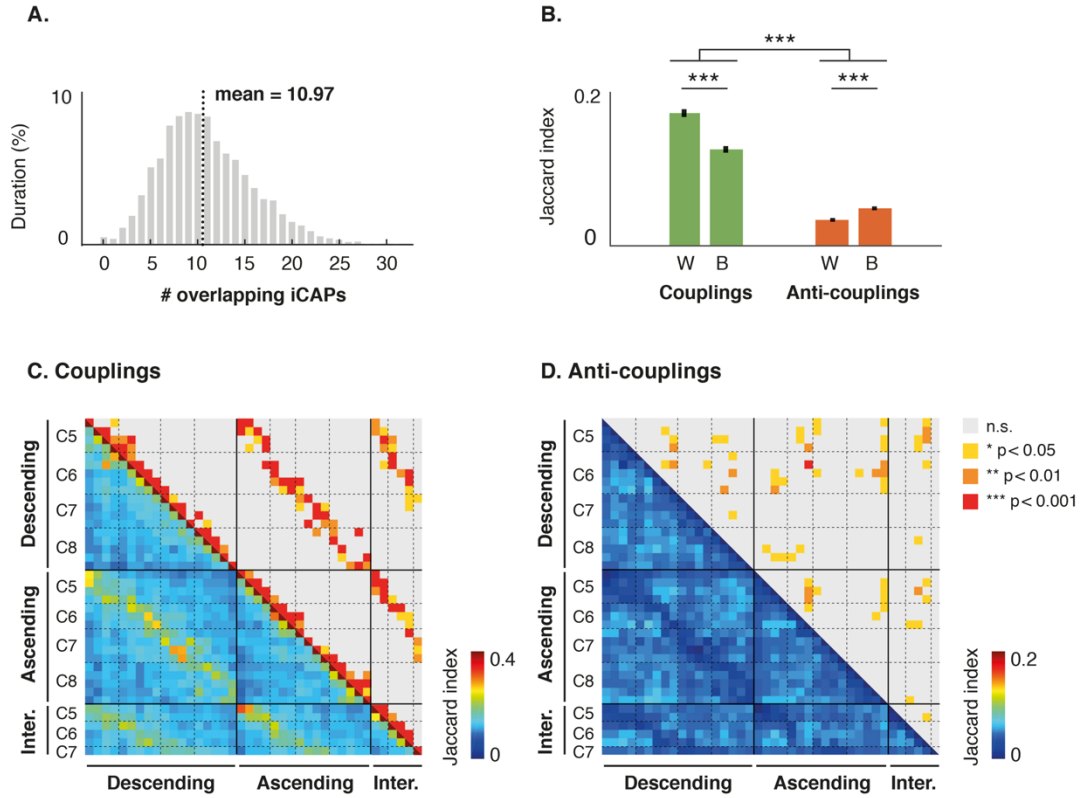


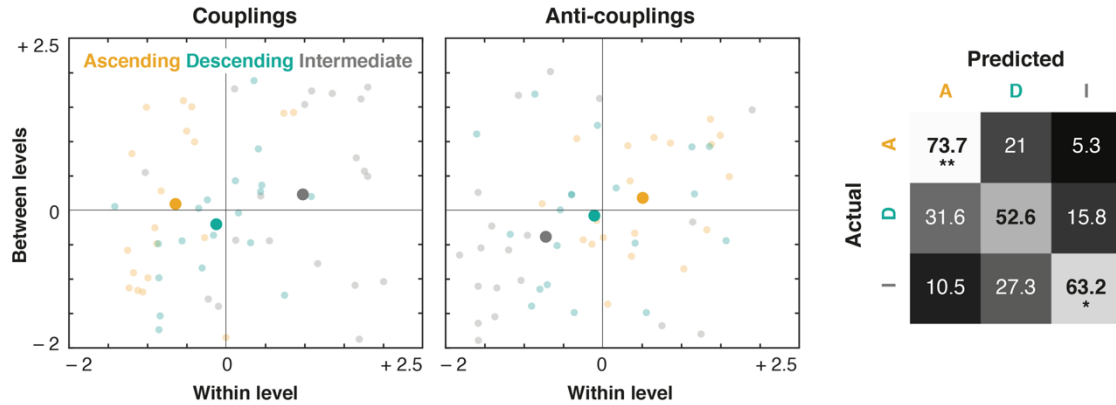
Figure 6.5 – Investigating temporal overlap between iCAPs. **A.** Percent duration of different degrees of co-activation (i.e., number of overlapping iCAPs), with respect to the total run duration. The dotted line indicates the mean over subjects. **B.** After extraction of the subject-specific time courses, interactions between iCAPs were assessed using Jaccard index (both for couplings, see panel **C.**, and anti-couplings, see panel **D.**) Strong couplings were found between the different regions, mainly at the same spinal levels. Anti-couplings are weaker and mostly observed between spinal levels. Means over subjects \pm SE are presented. W = within, B = between. *** $p < 0.001$, paired t-test, Bonferroni corrected. **C-D.** For each matrix, iCAPs are grouped into ascending, descending and intermediate regions, and ordered rostro-caudally for each category (dashed lines indicate the different spinal levels). The mean over subjects is presented. Lower triangular matrices show Jaccard index for each pair of iCAPs, while upper triangular matrices highlight significant interactions (non-parametric permutation testing, corrected for multiple comparisons).

6.3.5 Dynamic temporal interactions are observed between iCAPs

Capitalizing on this stable spatial organization, we probed the temporal features of the 40 fine-grained spinal iCAPs. Each iCAP occurrence lasted on average 2.71 ± 0.15 volumes (mean over iCAPs \pm SD, no significant difference between iCAPs), for a total duration of activation (positive and negative occurrences) of 27.42 ± 1.82 % (mean over iCAPs \pm SD, percentage of run length, no significant difference between iCAPs). A substantial amount of temporal overlap was observed between iCAPs, with an average of 10.97 ± 0.17 co-active iCAPs at each timepoint (mean over subjects \pm SE, Figure 6.5A). To better understand the features of this large temporal overlap, we explored the (anti-)couplings between the 40 iCAPs (Figure 6.5B-D). Overall, couplings (mean Jaccard index over subjects \pm SE = 0.15 ± 0.007) were significantly stronger than anti-couplings (0.04 ± 0.003 , $p < 0.001$) and they exhibited distinct behaviors. Specifically, larger couplings were observed within level (0.17 ± 0.005) than between levels (0.13 ± 0.004 , $p < 0.001$). Conversely, anti-couplings were more prominent between levels (0.05 ± 0.002) than within level (0.03 ± 0.002 , $p < 0.001$). This notable interplay between spinal iCAPs was stable across subjects, both for couplings (mean cosine

similarity over subjects \pm SE of 0.88 ± 0.01) and anti-couplings (0.76 ± 0.01). These results corroborated the hypothesis that spinal cord spontaneous fluctuations are highly entwined, prompting the need for dynamic approaches to dissect this activity.

A. Inside neural pathways



B. Across neural pathways

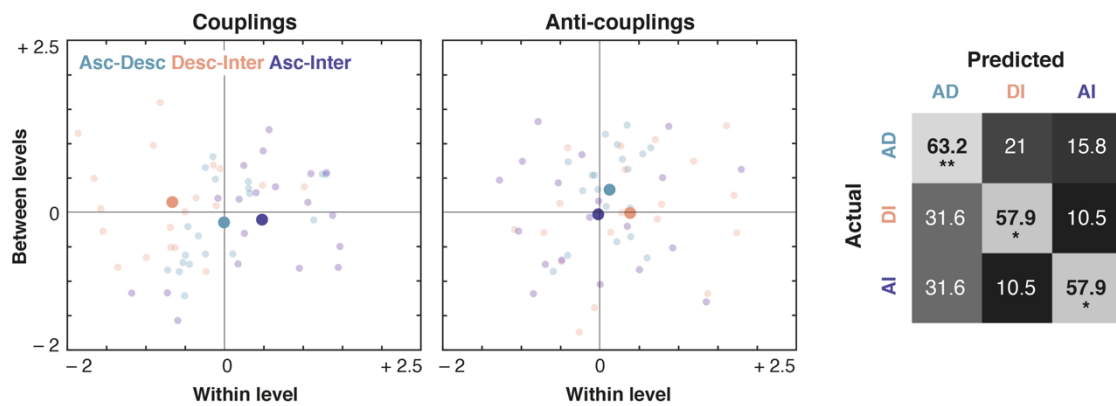


Figure 6.6 – Interaction signatures of neural pathways. In order to highlight whether couplings had a specific organization pertaining to neural pathways, we studied interactions inside (A.) or across them (B.). Patterns were highlighted based on four features: couplings and anti-couplings, both within level and between levels. Left panels present interactions in this feature space. Scatter plots show the relationship of within level and between levels couplings and anti-couplings. Values are presented separately for the different interaction types, represented by distinct colors. The light dots correspond to the values of individual subjects, while the bold dots indicate the means over subjects. The distinct distributions of these values for each interaction type suggested that specific interaction signatures exist for the different neural pathways. In order to confirm these signatures, a QDA classifier (leave-one-subject-out cross validation) was used to distinguish them. The average confusion matrices are displayed on the right panels. * $p < 0.05$, ** $p < 0.01$ (non-parametric permutation testing, corrected for multiple comparisons). Asc/A = Ascending, Desc/D = Descending, Inter/I = Intermediate.

6.3.6 iCAPs of different neural pathways exhibit distinct interplays

Finally, we examined the interactions between iCAPs grouped according to their neural relevance (ascending, descending or intermediate), to potentially uncover distinctions regarding their coupling properties. This highlighted interaction profiles specific to each pathway (i.e., between the iCAPs belonging to the same pathway, Figure 6.6A), in particular in terms of within level interactions. Couplings appeared larger inside the intermediate zone, while they were smaller in the ascending and descending pathways, especially for the former. Anti-couplings followed an opposite

trend. The strong coupling inside the intermediate zone might be attributed to commissural interneurons, whose axons cross the midline to link the two hemicords. When assessing the interactions shared across pathways (i.e., between the iCAPs belonging to different pathways, Figure 6.6B), we found that the intermediate zone was differently coupled with the two others pathways, with stronger couplings occurring with the ascending regions. Anti-couplings, however, did not display any clear tendency. To further investigate whether these distinctions were inherent properties of connectivity inside and across neural pathways, we attempted to classify them using the aforementioned features (couplings and anti-couplings, within and between levels). This allowed to distinguish interactions occurring inside the ascending and intermediate pathways, as they could be discriminated with high accuracy (respectively 73.7%, $p < 0.01$ and 63.2%, $p < 0.05$, non-parametric permutation testing against chance level, i.e., $\sim 33.3\%$), confirming their distinct behaviors. Internal couplings within the descending pathways exhibited a more hybrid profile, resulting in a lower classification accuracy (52.6%, not significant). When looking at the interactions across neural pathways, the highest accuracy was found for the relationship between the ascending and descending pathways (63.3%, $p < 0.01$), although the interactions across the intermediate zones and the two other pathways could also be classified (57.9%, $p < 0.05$). This suggests that peculiar interactions exist between pathways, as they are engaged to support disparate sensorimotor functions.

6.4 Discussion

In previous work, RSNs were shown to be a feature of the entire CNS, with the spinal cord demonstrating an intrinsic functional organization akin to the recognized brain's functional architecture (Van Den Heuvel and Hulshoff Pol, 2010). Although this organization has been presumed to support sensory, motor, or autonomic functions, its neurophysiological purpose has so far remained elusive. Former studies had solely focused on static FC, which merely reflects the average organization over the course of a functional run. In this regard, exploiting the dynamic features of spinal spontaneous activity could promote new insights into its physiological nature. In this study, we leveraged state-of-the-art spinal cord fMRI protocols, combined with a dFC method (Karahanoğlu and Van De Ville, 2015), and deployed the SpiCiCAP framework to unweave spinal RS fluctuations. We showed that these fluctuations were highly structured and could be precisely delineated into neuroanatomically relevant components. To the best of our knowledge, this is the first time that such fine-grained subdivisions of the spinal cord are extracted using fMRI measures and, in particular, RS activity. Thanks to this unprecedented level of detail, our results shed new light on the functional relevance of spinal fluctuations, underscoring their association with the main spinal neural pathways. Hereafter, we discuss these findings with an emphasis on their clinical potential.

6.4.1 Methodological aspects

In this work, we deployed a dFC approach to exploit the richness of spontaneous spinal activity. Specifically, the SpiCiCAP framework first employs a tailored processing pipeline on spinal cord fMRI data. Regularized deconvolution of denoised time courses is then applied to retrieve the underlying activity-inducing signals, subsequently used to reveal robust transient activity (see Figure 6.1 for a summary of the different steps) (Karahanoğlu *et al.*, 2013; Karahanoğlu and Van De Ville, 2015). Transients encode changes in the BOLD time courses (i.e., activations and de-activations) and can be used to determine components reflecting consistent patterns of co-activation, the so-called iCAPs. A unique feature of this method is its ability to disentangle spatially and temporally overlapping signals. In this study, fine-grained components could be revealed, suggesting that spinal activity manifests complex and non-stationary temporal properties that are better unraveled

using a dynamic approach over conventional static methods. In order to thoroughly characterize iCAPs, we relied on maps of spinal levels and atlas regions (Cadotte *et al.*, 2015; Lévy *et al.*, 2015; De Leener *et al.*, 2017), which enabled systematic assessment of each component's physiological relevance (Figure D2). Of note, inter-subject variability is not represented in the atlas, but differences were assumed not to be critical at this spatial resolution. While the SpiCiCAP framework offers unique advantages, certain drawbacks should be highlighted. First, this clustering-based approach implies that the number of clusters K should be *a priori* defined. Here, we selected K based on anatomical knowledge and reproducibility analyses, although this selection is not exclusive. Another aspect that should be considered pertains to the estimation of the HRF. Indeed, the deconvolution step, which is deployed to recover activity-inducing signals (Figure 6.1), uses a single canonical HRF. Yet, the HRF is known to vary across subjects and regions (Handwerker *et al.*, 2004). Although these differences have not been closely investigated in the spinal cord, one study highlighted that the HRF may be slower than in the brain (Giulietti *et al.*, 2008). Besides, variations of the hemodynamic response between grey and white matter could also be probed, as differences in this regard have been demonstrated in the brain (Li *et al.*, 2019). This warrants further investigations, and potential improvements to the SpiCiCAP framework could include a variable HRF model or integrate HRF identification within the deconvolution step. Finally, future research could examine the impact of changes in the processing pipeline (e.g., physiological noise removal, smoothing, etc.) on the reproducibility of spinal iCAPs, similar to how Eippert *et al.* (2017b) investigated static connectivity.

To foster the emergence of new research characterizing spinal functional pathways, we are providing our dataset and analysis pipeline as resources for the neuroscientific community. Spinal cord fMRI is still an emerging field and, currently, no such open dataset is publicly available. Despite significant improvements in the last years, spinal cord fMRI remains challenging and some limitations should be acknowledged, notably in terms of image quality. For instance, field inhomogeneities can lead to distortion and signal dropouts, although the extent of these signal variations was limited (Figure D1). It should also be noted that the low temporal resolution ($TR = 2.5s$) might impede the detection of fast transients.

6.4.2 Spinal resting-state components are highly structured and robust

The SpiCiCAP framework was used to explore spinal RS fluctuations using two separate levels of granularity (i.e., either 4 low-granularity or 40 high-granularity iCAPs were extracted). All iCAPs presented spatially segregated patterns (Figure D5) and a limited rostro-caudal extent (Figure 6.2 and Figure D4), corroborating previous results reporting that ICA-derived components did not span more than one vertebra (Kong *et al.*, 2014). Here, we could further confirm that each low-granularity iCAP coincided with a single spinal level, from C5 to C8 (Figure 6.2B). A most striking observation was that increasing the granularity to 40 iCAPs allowed to uncover fine-grained spinal components extending beyond the commonly reported dorso-ventral division (Figure 6.2C). These components were in close agreement with the underlying neuroanatomy and could be matched with a specific grey or white matter region. In line with previous studies, we observed components corresponding to the ventral (i.e., motor) horns (Barry *et al.*, 2014; Kong *et al.*, 2014; Liu *et al.*, 2016b; Weber *et al.*, 2018). No iCAPs were, instead, assigned to the dorsal (i.e., sensory) horns, although few voxels were indeed present in these regions (Figure D5, regions 35 and 36). FC in the dorsal horns was previously reported as weaker and harder to reliably detect (Barry *et al.*, 2016, 2018a; Eippert *et al.*, 2017b), possibly because of their narrow geometry (see Figure D2). An unexpected observation was the presence of clearly defined iCAPs in the white matter, as FC is conventionally

studied for the grey matter only. Despite the surprising character of these findings, there is compelling evidence that white matter has the vascular capacity to support hemodynamic changes and that the initial lack of interest in these signals was probably due to a limited sensitivity (lower field strength), rather than linked to a fundamental property that would impede their detection (Gawryluk et al., 2014; Gore et al., 2019). Indeed, recent studies reliably captured functionally relevant information in cerebral white matter (e.g., Ding et al., 2018; Huang et al., 2018; Peer et al., 2017; Wu et al., 2017). In the spinal cord, specifically, weaker BOLD signals in the white matter might be compensated by its large volume (i.e., more than three times the grey matter volume, see Figure D2). Coherent activity has previously been reported in spinal white matter at rest, as Barry et al. observed correlations between white matter regions using a seed-based analysis (Barry et al., 2014). Besides, the ICA components presented by Kong et al. did not allow an accurate delineation between grey and white matter and seemingly contained both structures (Kong et al., 2014). Altogether, our findings illustrate the potential of a dFC framework to resolve functional activity with high precision, down to the level of individual grey and white matter regions. Importantly, this may offer valuable insight into neurological conditions principally affecting the white matter, such as multiple sclerosis. To evaluate the reliability of our approach, we probed the robustness of spinal iCAPs intra-subject, by extracting components on split-half datasets (Figure 6.4A). The low-granularity architecture was particularly stable and high-granularity iCAPs of both sets coincided with atlas regions. The latter indicated that short acquisitions already allowed to recover meaningful fine-grained components and could be foreseen in the context of clinical applications, where time is often a limiting factor. By evaluating inter-subject similarity (Figure 6.4B), we then showed that low- and high-granularity iCAPs were stable across subjects, hence supporting the idea that they represent consistent features of spinal cord functional organization. It is noteworthy that low-granularity iCAPs were more stable within than between subjects. This could pertain to individual differences regarding the location of spinal levels, as anatomical variability was, indeed, previously acknowledged (Cadotte et al., 2015). In contrast, high-granularity iCAPs were more similar between than within subjects. We hypothesized that fine-grained maps, as they capture regions involved in specific functions (e.g. proprioception or muscle tone control), were more likely to vary over time depending on external variations (e.g., fatigue, stress or muscle relaxation). Spinal FC was previously reported to be state-dependent, for instance following thermal stimulation (Weber et al., 2018). Further studies with physiology-based measures of cognitive states (e.g., electroencephalography, blood pressure, skin conductance, pupillometry) (Lohani et al., 2019) could help validate this conjecture.

6.4.3 The “restless” spinal cord is organized according to neural pathways

To date, the mechanisms at the core of spinal RS fluctuations are still speculative. Three main processes have been hypothesized (Eippert and Tracey, 2014; Kong *et al.*, 2014; Eippert *et al.*, 2017b): *i)* RS signals could be driven by the continuous processing of inputs from the periphery (e.g., proprioception, touch or vibration); *ii)* Alternatively, they potentially stem from the ongoing communication between the brain and the spinal cord, through ascending (sensory) and descending (motor) signals; *iii)* Finally, they could be generated locally from intrinsic features of spinal activity, for instance linked to coordinated movements (e.g., bilateral coordination (Jankowska, 2008; Soteropoulos *et al.*, 2013), breathing (Sandhu *et al.*, 2015), or central pattern generators (Guertin and Steuer, 2009)). To further shed light on these three hypotheses, we inspected the functional roles of the fine-grained iCAPs. First of all, we found that, similarly to the brain (Fox and Raichle, 2007; Smith *et al.*, 2009), RS spinal components were distributed in networks corresponding to distinct neural pathways, usually active and modulated during task. This suggests that, at the level

of the spinal cord, the same neural substrates likely support active and passive behaviors. Specifically, networks were mainly involved in descending and ascending processes associated with two spinal neural pathways: the cortico-spinal pathway (CST) and the dorsal column-medial lemniscus pathway (DCML) (Figure 6.3). By conveying and processing signals from (e.g., for motor control) and to (e.g., for proprioception) the brain, respectively, these pathways subserve distinct functions (Darby and Frysztak, 2013). The CST is the major pathway supporting voluntary motor function and it connects motor cortical regions to the ventral horns of the spinal cord. Conversely, the DCML is related to proprioception, fine touch and vibration sensation. Peripheral signals originating from receptors involved in tactile sensation and conscious proprioception travel through the dorsal column and the medial lemniscus, before reaching the primary somatosensory cortex. Although other spinal pathways exist, they were not detected here, possibly due to their secondary role at rest. One such example is the reticulospinal tract, mainly involved in postural control (Figure D2). The absence of these pathways could also pertain to their small size, as the spatial resolution (1 x 1 x 3 mm) could have hindered their identification. A few components were observed in the intermediate region of the spinal cord and can be engaged in different mechanisms, such as commissural interneuronal connections between contralateral horns, for instance to coordinate movement (Jankowska, 2008; Soteropoulos *et al.*, 2013). At the interface between ascending and descending pathways, they may also support interaction between sensory and motor components, notably for reflexes (Pierrot-Desseilligny and Burke, 2005; Koch, 2019). From these findings, we could infer that the aforementioned mechanisms likely coexist and generate *restless* spinal cord activity.

To help further clarify the organizational principles of this dynamic architecture, we then considered the temporal characteristics of spinal iCAPs, which displayed a significant overlap (Figure 6.5A). While strong couplings occurred mostly within the same spinal level, in line with earlier studies (Barry *et al.*, 2014; Kong *et al.*, 2014; Liu *et al.*, 2016b; Eippert *et al.*, 2017b; Weber *et al.*, 2018), anti-couplings were weaker and identified between spinal levels (Figure 6.5B-D). Weak negative correlations between spinal segments were previously reported by Kong *et al.* (Kong *et al.*, 2014) and may be reminiscent of mechanisms involved in intersegmental inhibition (Friesen and Cang, 2001; McBain *et al.*, 2016). Patterns of interactions specific to each neural pathway also emerged from this analysis (Figure 6.6). Successful classification of these pathway-dependent signatures further confirmed their specificity, highlighting that distinct pathways might rely on different dynamic interactions to achieve their functional contributions. The strongest level of couplings was found for iCAPs located in the intermediate zone, not only among them, but also with regions of the ascending pathway. This suggests that ongoing communication between hemicords may occur through interneuronal connections, while pointing to a potential role of the intermediate pathway in bridging sensory networks. Conversely, ascending and descending pathways appeared to be more loosely connected, maybe due to the absence of active task. This initial disentanglement of spinal neural pathways *in vivo* could help understand the impact of task-related modulations on their interactions, for instance during the complex integration of sensory feedback and motor commands involved in voluntary movements. In this context, collecting behavioral data will be pivotal to further assess the relevance of these networks.

6.4.4 Clinical potential

In addition to these findings, the versatility of our framework could enable to explore the disruption of spinal functional architecture in impaired individuals. Studies assessing spinal functional integrity may be especially valuable when structural damages are minimal and do not allow to fully characterize the patient's status. Multiple sclerosis could particularly benefit from this approach, as its

pathological hallmark is the formation of demyelinating lesions in the brain and spinal cord (Filippi *et al.*, 2018). Recent work from Conrad *et al.* has already initiated this effort, with promising results (Conrad *et al.*, 2018). Using a region of interest correlation analysis in a cohort of multiple sclerosis patients, they showed that the presence of lesions was concomitant to local alterations of FC. They speculated that different mechanisms could explain these changes, such as a compensatory effect of white matter damage or a disruption of inhibitory spinal interneurons. Our data-driven approach could help distinguish between these hypotheses, by granting access to fine-grained features of spinal cord FC in the white and grey matter. In addition, studying functional integrity could also bring valuable knowledge in the context of spinal cord injuries. To this end, RS scans are particularly attractive, as even severely affected patients can undergo such recordings (Krakauer, 2007). No such study has so far been performed in humans, but the clinical relevance of RS fluctuations was investigated in non-human primates at ultra-high field (Chen *et al.*, 2015), by longitudinally monitoring the effect of a unilateral spinal cord injury. This emphasized that disruptions in FC within and between spinal levels were related to the recovery process, thus underscoring the potential of intrinsic RSNs as imaging biomarkers of spinal cord functional integrity. The framework proposed in our study offers the prospect of identifying such functional biomarkers in the human spinal cord with a remarkable level of detail. This can have major translational implications, as they could potentially be used for diagnosis and prognosis, to quantify disease progression or to investigate the effect of different interventions. Ultimately, a thorough understanding of spinal functional circuitry could help steer the development of innovative therapies, notably in the context of neurotechnological solutions that are able to deliver precise and knowledge-based treatment (Micera *et al.*, 2020). For instance, electrical epidural stimulation has been used to restore locomotion following a spinal cord injury, with very promising results (Wagner *et al.*, 2018). Patient-specific maps of spinal pathways could be used to fine-tune these protocols, so as to optimally engage the spared connections and networks to further improve patients' clinical outcome.

6.5 Conclusion

So far, studies have only inspected spinal RS fluctuations using static FC, showing that signals were organized into networks, but without demonstrating their physiological origin. Here, we deployed the SpiCiCAP framework to exploit the rich dynamic features of spontaneous spinal activity and recovered fine-grained components. Capitalizing on this unprecedented level of detail, we showed that these components were related to the underlying neuroanatomical organization and that they were functionally relevant. We provide a powerful tool to delineate stable spinal circuits *in vivo*, thus enabling access to the building blocks of spinal functional activity. This approach provides a ground for future work to elucidate how spinal networks can be flexibly combined to support particular functions, both at rest or when specifically modulated by a task. We believe that the versatility of this methodological framework opens new avenues to tackle fundamental and clinical neuroscientific questions related to the function of the spinal cord.

Chapter 7

Cerebro-spinal dynamics of motor learning

Dynamics of cerebral and spinal networks during acquisition and consolidation of motor skills

Nawal Kinany ^{1,2,3}, Ali Khatibi ^{4,5}, Ovidiu Lungu ⁶, Silvestro Micera ^{1,7}, Dimitri Van de Ville ^{2,3},
Véronique Marchant-Pauvert⁸, Julien Doyon⁶

¹ Bertarelli Foundation Chair in Translational Neuroengineering, Center for Neuroprosthetics, Institute of Bioengineering, School of Engineering, École Polytechnique Fédérale de Lausanne (EPFL), Lausanne, 1015, Switzerland; ² Medical Image Processing Laboratory, Center for Neuroprosthetics, Institute of Bioengineering, École Polytechnique Fédérale de Lausanne (EPFL), Lausanne, 1015, Switzerland; ³ Department of Radiology and Medical Informatics, University of Geneva, Geneva, 1211, Switzerland; ⁴ Centre of Precision Rehabilitation for Spinal Pain, School of Sport, Exercise and Rehabilitation Sciences, University of Birmingham, Birmingham, UK; ⁵ Centre for Human Brain Health, University of Birmingham, Birmingham, UK; ⁶ McConnell Brain Imaging Center, Montreal Neurological Institute, McGill University, Montreal, Canada; ⁷ Translational Neural Engineering Area, The Biorobotics Institute, Scuola Superiore Sant'Anna, Pisa, 56025, Italy; ⁸ Sorbonne Université, Inserm, CNRS, Laboratoire d'Imagerie Biomédicale, Paris, France;

7.1 Introduction

The vast majority of human behaviors is associated with motor function, making the acquisition and retention of new motor skills essential to our daily lives. In this context, motor skill learning refers to all processes leading to effortless movements through repeated practice (Doyon and Benali, 2005). Considering their multifaceted nature, unveiling these mechanisms is a complex endeavor. Neuroimaging studies have thus been instrumental to explore their neural underpinnings, notably to demonstrate how functional plasticity in distinct brain regions underlies learning processes (Dayan and Cohen, 2011; Doyon *et al.*, 2018). Traditionally, learning has been largely attributed to such cerebral functional changes, while the spinal cord, on the other hand, has merely been viewed as a hardwired relay for cortical commands transiting towards muscles. Nonetheless, evidence challenging the concept of the spinal cord as a passive relay has accumulated over the years (Wolpaw and Tennissen, 2001; Grau, 2014). Already in early physiological experiments, its ability to generate and learn semi-autonomous behaviors without supraspinal inputs was highlighted (Reggie Edgerton *et al.*, 1997). Later, animal and human studies provided support for learning-dependent plasticity in the spinal cord, notably with respect to changes observed in reflexes (e.g., Hoffmann reflex) (Nielsen *et al.*, 1993; Meunier *et al.*, 2007; Wolpaw, 2007; Nielsen, 2016; Christiansen *et al.*, 2017), which were then shown to be engaged in controlling hand postures (Weiler *et al.*, 2019). While these observations hinted at a more sophisticated role of the spinal cord than initially assumed, its precise involvement in motor control and learning remains elusive.

In this context, non-invasive imaging of spinal cord functions can shed new light on spinal processes linked to skilled movements. In particular, simultaneous brain and spinal cord fMRI could offer a more comprehensive characterization of these mechanisms through the entire central nervous system (CNS). Yet to date, only one study capitalized on this potential to unravel the cerebro-spinal mechanisms involved in motor control and learning. In their pioneering work, Vahdat *et al.* deployed simultaneous brain-cervical cord fMRI during a finger-tapping motor sequence learning (MSL) task (Vahdat *et al.*, 2015) and observed learning-related modulation of activity in the spinal cord, independently from the modulation of supraspinal structures. Using static functional connectivity analyses, they also demonstrated an effect of task practice on cerebro-spinal interactions. As such, these results offered unprecedented insights into the role of the spinal cord in the initial stages of motor learning. However, electrophysiological experiments have also provided indirect evidence of an involvement of the spinal in the subsequent phases of learning (Nielsen *et al.*, 1993), when skills get consolidated (Dayan and Cohen, 2011; Diedrichsen and Kornysheva, 2015; Doyon *et al.*, 2018). Non-invasive imaging could, therefore, offer a unique opportunity to probe the nature of these long-term spinal changes, as well as their ties with cerebral plasticity.

In the current study, we took advantage of a novel fMRI dataset acquired by Doyon and colleagues, in which they built upon their pioneering work (Vahdat *et al.*, 2015) and acquired simultaneous brain and spinal cord fMRI, this time using a MSL paradigm involving wrist-controlled reaching movements. In addition, they evaluated MSL not only during a single session (early learning), but also following a week-long motor training regimen (late learning). To leverage this dataset and unravel the cerebro-spinal correlates of skilled movements, we combined the dynamic connectivity framework introduced in Chapter 6 (Kinany *et al.*, 2020) with a multivariate classification technique. Using these data-driven methodological approaches, we highlighted specific learning-related neural networks associated with the acquisition and the consolidation of a new motor skill, and motor sequence learning in particular. Furthermore, we probed the dynamic interplay occurring between spinal and supraspinal brain regions. Taken together, our results suggest that the short- and long-term stages of MSL are characterized by distinct functional fingerprints distributed throughout the CNS, hence underscoring again the importance of the spinal cord in this form of memory.

7.2 Methods

7.2.1 Participants

Thirty young healthy participants were enrolled in the study. All participants were right-handed and had no history of neurological or psychiatric disease, no motor-system complications, nor were they using neurological medications. Individuals who previously participated in motor-learning experiments, as well as those with previous training in playing an instrument for more than three consecutive years in the last five years, could not be included in the study. Of these thirty participants, five subjects were subsequently excluded (two drop-outs, one for excessive motion, and two for incomplete functional scans). Finally, 25 subjects were included in the analyses (13 females, 24.8 ± 3 years old). All participants gave their written informed consent to participate, and the study was approved by the Ethics Committee at the Centre de Recherche de l'Institut Universitaire de Gériatrie de Montréal (CRIUGM).

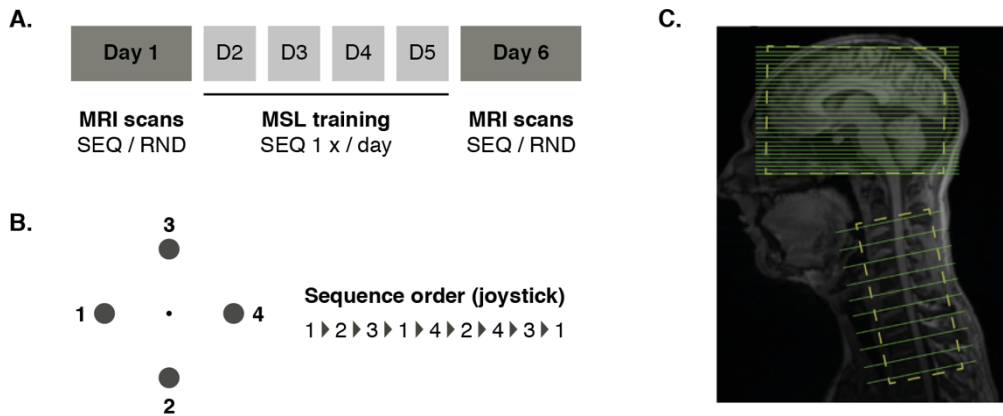


Figure 7.1 – Experimental protocols. **A.** Overview of the different experimental sessions. **B.** Display of the motor sequence learning task as well as the specific sequence subjects had to practice during the SEQ runs, while using an MRI compatible joystick controlled with the right (dominant) hand. **C.** A novel fMRI acquisition scheme (Finsterbusch *et al.*, 2013) was employed to perform simultaneous cerebro-spinal fMRI with region-specific shimming and scan parameters. The two subvolumes are highlighted by the yellow boxes, while slices are shown in green (30-33 slices for the brain and 8-10 slices for the spinal cord).

7.2.2 Experimental protocols

General procedure

Each participant participated in six experimental sessions, distributed over six consecutive days (Figure 7.1A). These sessions comprised two MRI scans: at the beginning (Day 1) and at the end (Day 6) of the study. At the beginning of the first experimental session, subjects were familiarized with the set-up by practicing a motor sequence learning (MSL) task in a mock scanner, using a different sequence than the one used during the actual experiment. Participants were then installed in the MRI scanner, where functional acquisitions were obtained during the performance of two different motor tasks (Sequence or Random, see below for details). During Day 2 to Day 5, participants performed a daily training of the sequential task while lying supine in the mock scanner.

Motor sequence learning paradigm

The motor task was performed using a joystick manipulated with the dominant (right) hand. At the beginning of the task, the cursor representing the joystick position was positioned in the center of the screen (i.e., neutral position) and indicated by a black circle. Four static targets, represented as circles, were positioned at equal distance from the center (3, 6, 9 and 12 o'clock, Figure 7.1B). Participants were instructed to move the cursor towards a target as soon as the corresponding circle was filled. Once the target was reached, it disappeared and the circle corresponding to the following target was highlighted. The sequence was not known in advance by the participants, who were simply asked to reach targets as quickly as possible. The sequence was repeated ten times in each block, with 15 blocks in total, interleaved with rest periods of 20 seconds. Two different conditions were used: (i) an 8-item Sequence Learning condition (SEQ) in which the order of the targets was sequential and repeated every 8 reaching movements (Figure 7.1B), and (ii) a Random condition (RND) where targets appeared in a pseudo-random non-sequential order. During each scanning session (Day 1 and Day 6), functional MRI acquisitions were acquired during both experimental conditions on two separate runs (SEQ and RND) and the order of the two runs was counterbalanced between subjects.

Data acquisition

Imaging data were acquired with a 3.0 Tesla Siemens Prisma scanner (Erlangen, Germany), equipped with a 12-channel head coil paired with a 4-channel neck coil (both receive only). Extra foam pads were installed around the subjects' head and neck in order to minimize motion. The isocenter of the magnet was aligned to the lower edge of the head coil (i.e., approximately at the vertebral level C2/C3).

In order to investigate the cerebro-spinal correlates of motor learning, functional images were acquired using a custom fMRI protocol enabling combined brain and spinal cord imaging (Finsterbusch *et al.*, 2013). Briefly, this approach allows to perform simultaneous functional measurements in two subvolumes (brain, spinal cord) with different geometric properties (Figure 7.1C). As such, each subvolume was tailored to the region-of-interest (i.e., brain or cervical spinal cord). Optimal acquisition parameters (shim properties and resonance frequencies) were selected for the two subvolumes at the beginning of each scanning session, using five sample volumes acquired before the actual experiment. Then, parameters were dynamically updated during the functional acquisitions. Details regarding shimming procedure are discussed in Tinnermann *et al.*, 2017. Based on the prescan acquisitions, a specific z-shim slice-specific approach was also used to maximize the signal intensity within the spinal cord (Finsterbusch *et al.*, 2012). Forty to 43 slices (depending on the participant size) were acquired for both subvolumes. Specifically, the brain subvolume contained 30 to 33 axial slices (FOV = 220 x 220 mm², in-plane resolution = 2 x 2 mm², slice thickness = 5 mm, 10% gap between slices, flip angle = 90°, GRAPPA factor 2, TE = 30 ms). This was sufficient to cover the whole-brain of most participants, except for a few subjects for whom the box was tilted upward of approximately 10 degrees (around the x axis), which cut a small part of the upper motor cortex. As for the spinal subvolume, 8 to 10 slices were acquired (FOV = 132 x 132 mm², in-plane resolution = 1.2 x 1.2 mm², slice thickness = 5 mm, 15% gap between slices, flip angle = 90°, GRAPPA factor 2, TE = 33 ms). The imaged region extended from C4 to C8 vertebrae. The Repetition Time (TR) was 3140 ms for S01, 3200 ms for S02 to S04 and 3050 ms for the other subjects, as the TR was slightly optimized in the first acquisitions. Importantly, the same TR was always used within the same subject. To limit noise, only signal from the head coil was used for the brain images, while only signal from the neck coil was used for the spinal cord images. A 3D-MPRAGE T1-weighted anatomical image was also acquired (175 sagittal slices, head to upper thoracic spine, TR = 2300 ms, TE = 3.45 ms, flip angle = 9°, TI = 1.1s, FOV = 192 x 240 x 320 mm³, resolution 1 x 1 x 1 mm³).

Data processing

All preprocessing steps were performed independently for the brain and the spinal cord using the Oxford Center for fMRI of the Brain's (FMRIB) Software Library (FSL) (Jenkinson *et al.*, 2012) and the Spinal Cord Toolbox (SCT) (De Leener *et al.*, 2017).

1) Motion correction

Brain: Following removal of the first two volumes to allow for T1 equilibration effects, non-brain regions were removed using BET (Smith, 2002) and motion correction was applied using MCFLIRT (Jenkinson *et al.*, 2002).

Spinal cord: Similarly to the brain, the first two fMRI volumes were discarded and slice-wise motion correction was performed with the mean image as reference, using the SCT (De Leener *et al.*, 2017). The corrected time series were visually inspected and parameters were adapted if needed.

2) *Image denoising*

Brain: FSL's FEAT tool was used to regress out signals of no interest from fMRI time series. The following noise regressors were included: six motion correction parameters (translations and rotations), CSF and white matter signals. Residuals were spatially smoothed using an isotropic Gaussian kernel with a FWHM of 4 mm

Spinal cord: Noise regression was also performed in the spinal cord using the following confounds: PNM regressors (Brooks *et al.*, 2008), slice-wise motion correlation parameters (x and y), CSF signal and mean global signal outside the spinal cord. The resulting residuals were then spatially smoothed using a 3D Gaussian kernel with a full width half maximum (FWHM) of $2 \times 2 \times 4 \text{ mm}^3$, along the spinal cord.

3) *Estimating warping fields for normalization*

Brain: Functional-to-anatomical and anatomical-to-template transformations were carried out using FLIRT (Jenkinson *et al.*, 2002). Registration from high resolution structural to standard space (3mm resolution) was then further refined using FNIRT nonlinear registration (Andersson *et al.*, 2007).

Spinal cord: Spinal cord segmentation was performed automatically on the T1 anatomical images using a two-step process: the spinal centerline was extracted using a first segmentation and subsequently used to yield a smoothed image on which a second segmentation was obtained. Segmentations were visually inspected and manual adjustments were performed when necessary. Landmarks were placed at the C4 and C7 vertebrae and used to normalize the structural scans to the MNI-Poly-AMU template (Fonov *et al.*, 2014). The spinal cord was semi-automatically segmented (i.e., with manual corrections) on the mean motion-corrected fMRI volume. All segmentations were performed by one rater and inspected by a second examiner, in order to optimize segmentation quality. This segmentation was used to support the registration of the mean motion-corrected to the T1 anatomical scan. Functional-to-template warping fields were obtained by concatenating the functional-to-anatomical and anatomical-to-template transformations.

Data analysis

1) *Task performance*

Subject's performance during each block of practice of the two experimental conditions (Sequence and Random) was evaluated by measuring the movement's jerkiness. Briefly, the jerk was computed as the third-time derivative of the pointer displacement, for each time point. Values were then integrated to obtain an Integrated Absolute Jerk (IAJ) index (Goldvasser *et al.*, 2001) for each task block. A repeated measures ANOVA with Blocks (1:7 vs 9:15) \times Day (1 vs 6) \times Condition (SEQ vs RND) as within-subject factors was conducted to assess improvement in performance. Performances across days and conditions were then evaluated using paired t-tests (Bonferroni corrected for multiple comparisons). As for within-session learning, a similar analysis was conducted to compare the jerk in the first seven blocks against the last seven blocks, for both days and conditions.

2) *Extracting innovation-driven coactivation patterns (iCAPs)*

We deployed the (SpiC)iCAP frameworks to extract spinal and brain iCAPs (Karahanoğlu and Van De Ville, 2015; Kinany *et al.*, 2020), whose different steps have been described in detail in Chapter

6. Briefly, the raw BOLD signals were denoised, and a regularized HRF deconvolution was employed to recover the activity-inducing signals thanks to the Total Activation framework (Karahanoğlu *et al.*, 2013). Transient activity (i.e., the so-called innovation signal) was obtained as the temporal derivative of the activity-inducing timecourses. A two-step thresholding process was then used to select significant innovation frames: (i) temporal thresholding: a surrogate distribution was generated by applying TA to phase randomized data and a 5% confidence interval was used to pick significant voxels; (ii) spatial thresholding: only the frames containing more than 5% of active voxels were kept. This procedure was applied to each run independently, for both the spinal cord and the brain. Significant innovation frames were normalized to the MNI-Poly-AMU and MNI template, respectively. Of note, a mask, shown in Figure E1, was used to constrain brain analyses to regions relevant to the study of motor control and learning, as defined based on previous literature (Doyon and Benali, 2005; Dayan and Cohen, 2011; Hardwick *et al.*, 2013; Vahdat *et al.*, 2015). As for the spinal cord, a region extending from C5 to T1 spinal levels was used. The spatially normalized maps were masked and concatenated (i.e., both days and conditions, for all subjects, independently for the brain and the spinal cord) and temporal K-means clustering was conducted to obtain group level iCAP maps. Similarly to Zöller *et al.* (2018, 2019), the optimal number of clusters was determined by means of consensus clustering (Monti *et al.*, 2003), which uses a subsampling scheme to estimate clustering stability. Specifically, K-means clustering was applied to multiple subsets of the data to generate a consensus matrix indicating the fraction of subsets for which two frames were clustered together. Ideally, two frames should either (i) always be clustered together (i.e., fraction value of 1) or (ii) never be clustered together (i.e., fraction value of 0). This procedure was repeated for different values of K, yielding a consensus matrix for each K of the selected range. The average consensus (i.e., mean consensus per cluster) and the cumulative distribution function of values in the consensus matrices were then probed to select the best clustering solution. In the brain, 17 iCAPs were recently reported to describe resting-state activity (Zöller *et al.*, 2019). In order to obtain a similar level of details, we applied consensus clustering for $K_{BR} \in [14, 20]$ (i.e., range of ± 3 compared to this previous study). Results are presented in Figure E2 and prompted the selection of $K_{BR} = 15$ for further analyses. As for the spinal cord, we relied on a priori knowledge on anatomy and explored a range corresponding to the potential number of dorsal and ventral components, expected to be around 10, as 5 spinal levels were imaged. Specifically, consensus clustering was evaluated for $K_{SC} \in [7, 13]$ (i.e., range of ± 3 compared to anatomical expectations) and we opted for $K_{SC} = 11$ based on the consensus clustering quality measures. In order to ensure that the spatial organization of iCAPs was stable across conditions (i.e., for both days and both tasks), we computed condition-specific iCAPs maps (i.e., mean of the frames of one condition, assigned to a particular iCAP). Stability was evaluated using cosine similarity and Dice coefficients (maps binarized with a threshold $Z > 2$). Finally, subject-specific timecourses were obtained for all iCAPs (brain and spinal cord) using spatio-temporal transient-informed regression (Zöller *et al.*, 2018). As both the RND and SEQ tasks were self-paced, timecourses were averaged per task / rest block to allow comparisons between subjects.

3) *Classification of cerebro-spinal correlates of MSL*

A multivariate data-driven approach was employed to highlight brain and spinal correlates of MSL. Specifically, we used Linear Discriminant Analysis (LDA) to investigate whether distinct neural activity patterns were associated with the execution of RND or SEQ tasks, in Day 1 and Day 6. Features were defined as the mean difference of activity during task and rest blocks for each iCAP (i.e., 11 spinal cord features and 15 brain features). Values were Z-scored and fed to a two-class LDA classifier, with leave-one-subject-out cross validation. Confusion matrices were computed using all

cross-validation folds and statistical significance was assessed using non-parametric permutation tests. Specifically, 1000 classifications were performed with randomly assigned labels and used to build a null distribution on which significance threshold were calculated. The significance of the LDA weights was evaluated with the same procedure. A similar procedure was employed to compare MSL (i.e., SEQ > RND) between sessions.

4) *Investigating iCAP-informed correlations*

In order to explore whether distinct cerebro-spinal interactions were associated with MSL, we performed a series of correlation analyses between the brain and the spinal cord. In particular, we examined task-dependent functional connectivity by leveraging the ability of the iCAP framework to retrieve activity-inducing signals unblurred from the hemodynamic lag. Specifically, functional connectivity estimates were performed using iCAPs as seeds and timecourses from each spinal iCAP were correlated with whole-brain activity-inducing signals from the brain. In order to rule out that connectivity merely reflected shared task input (i.e., correlation with task timings), timecourses were constrained to eroded task blocks (i.e., one TR removed at both ends of each block) (Cole *et al.*, 2019). Pearson's correlation coefficients were computed between these task-only timecourses, for all subjects, days and conditions. Values were then Fisher Z-transformed and MSL-related correlation maps were obtained by contrasting the SEQ and RND conditions within each subject. Finally, we assessed whether there were significant differences in learning-induced connectivity between the two sessions. Voxel-wise differences were evaluated using non-parametric paired t-tests with 5000 permutations, as implemented in FSL's randomize tool (Anderson and Robinson, 2001). Threshold-free cluster enhancement (TFCE) was conducted to correct for multiple comparison, and p values < 0.05 were considered significant.

7.3 Results

7.3.1 Motor sequence learning leads to smoother task execution

First, we probed participant's performance, as evaluated using movement jerkiness (IAJ), over time and conditions (Figure 7.2A). Distinct learning curves were observed, as emphasized by a significant three-way interaction between block, day and condition (repeated measures ANOVA, $F(1,24) = 812.99$, $p < 0.001$). In particular, learning effects were present across days (significant interaction between day and condition, $F(1,24) = 823.26$, $p < 0.001$) as well as within the same day (significant interaction between block and condition ($F(1,24) = 976.73$, $p < 0.001$). Paired t-tests were used to further analyse these learning dynamics and confirmed an improvement between sessions ($p < 0.05$, Figure 7.2B) and within session ($p < 0.001$, Figure 7.2C), for the sequential (SEQ) task, but not for the random (RND) condition. These observations suggested that repeated practice of the SEQ task, as opposed to non-specific effect of random motor practice, led to smoother movements. In order to disentangle learning effects from motor practice, MSL was thus defined as SEQ > RND in further analyses.

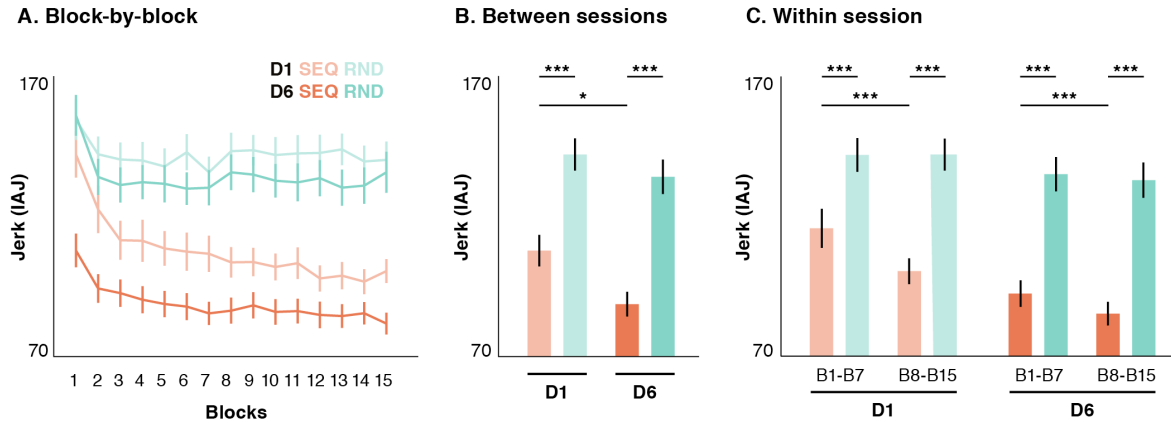


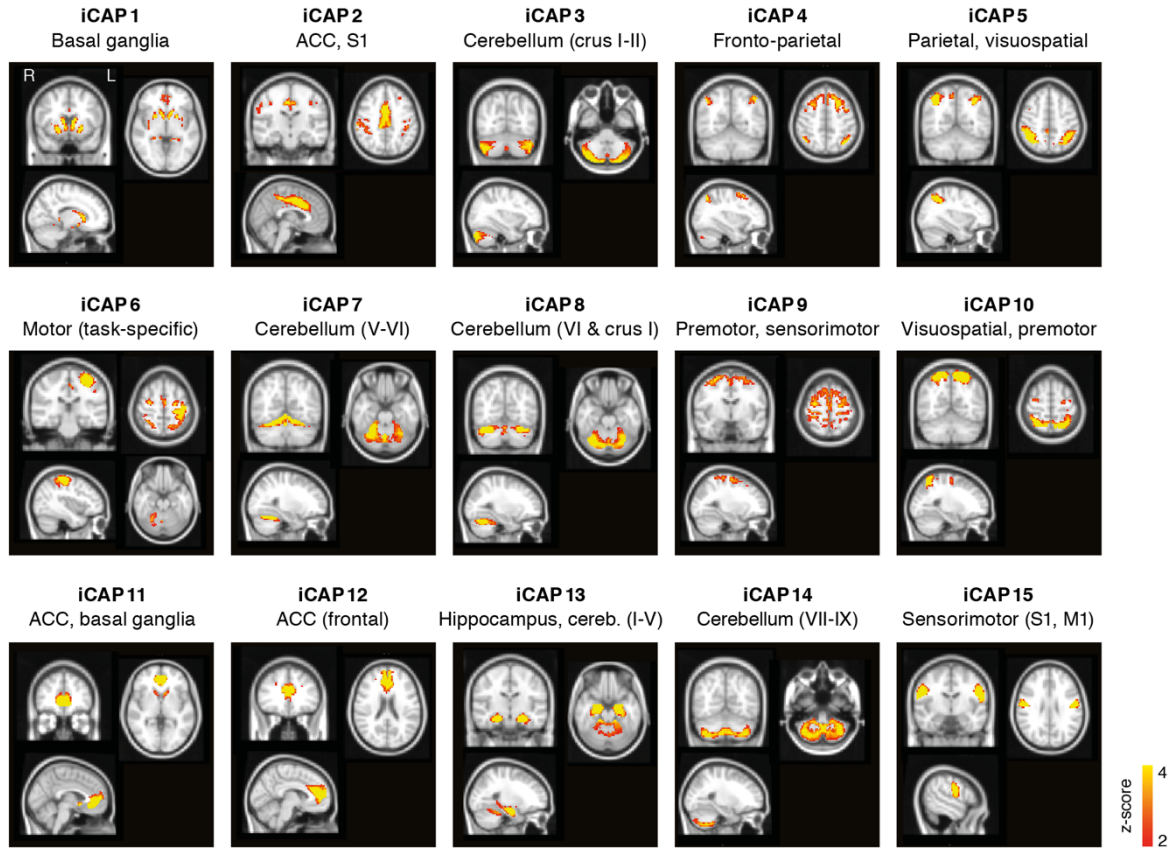
Figure 7.2 – Behavioral performance. Performance was assessed using the Integrated Absolute Jerk (IAJ), which characterizes the smoothness of movement trajectories (i.e., a decrease in IAJ values reflects an increase in smoothness). **A.** IAJ averaged across all subjects for each block, illustrating learning curves for both days and conditions. **B.** Comparison of subjects' performance (i.e., mean IAJ values) between days for both conditions. **C.** Comparison of the performance between the early (first seven blocks: B1-B7) and late (last seven blocks: B9-B15) phases of learning, for both days and both conditions. Values are presented as mean \pm SE. * corresponds to $p < 0.05$ and *** to $p < 0.001$ (paired t-tests corrected for multiple comparisons).

7.3.2 Brain and spinal activity can be decomposed into meaningful networks

We applied the iCAP framework in the brain and the spinal cord independently, so as to retrieve regional iCAPs across all subjects and conditions. 15 brain iCAPs were extracted and corresponded to well delineated cortical and subcortical regions known to be involved in various aspects of motor learning and practice (Figure 7.3A, see Table E1 for details of the regions). Notably, a task-specific network was recovered (iCAP 6) and included contralateral sensorimotor cortices, the secondary motor areas bilaterally and the ipsilateral cerebellum. Of note, there were several additional iCAPs displaying subparts of the cerebellum (iCAPs_{BR} 3, 7, 8, 13 and 14). Moreover, multiple areas known to be involved in various aspects of motor control and learning were found, such as striatal regions of the basal ganglia (iCAPs_{BR} 1 and 11), premotor cortex (iCAPs_{BR} 9 and 10) or areas supporting visuospatial perception (iCAPs_{BR} 5 and 10). The anterior cingulate cortex (ACC) was also well represented (iCAPs_{BR} 2, 11 and 12). Other regions comprised the somatosensory areas (iCAPs_{BR} 2, 9 and 15), fronto-parietal networks (iCAP_{BR} 4) and hippocampus (iCAPs_{BR} 1 and 13). At the level of the spinal cord, 11 iCAPs were identified (Figure 7.3B), covering a region extending between C5 to T1 spinal levels. As previously reported (Kong *et al.*, 2014; Kinany *et al.*, 2020), all maps spanned a limited rostro-caudal extent. ICAPs appeared to be divided into dorsal and ventral components, likely reflecting sensory and motor mechanisms, and all patterns were bilateral.

To ensure that these networks could reliably be used to characterize cerebro-spinal activity under different conditions, we assessed their spatial similarity across days and tasks. Spatial patterns were highly stable, both in the brain (cosine similarity = 0.97 ± 0.01 , Dice coefficient = 0.72 ± 0.20 , mean over iCAPs \pm SE) and the spinal cord (cosine similarity = 0.99 ± 0.002 , Dice coefficient = 0.86 ± 0.03). Given the spatial robustness of the functional organization as described using iCAPs, we then probed the temporal expression of these building blocks in each subject. Task-related changes in activity were observed in the brain and the spinal cord Figure 7.4, hence suggesting the ability of the iCAP framework to capture learning dynamics.

A. Brain iCAPs



B. Spinal iCAPs

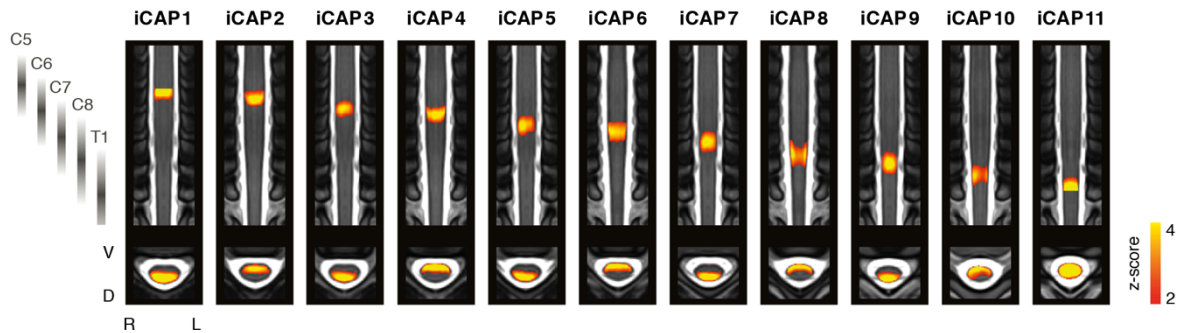


Figure 7.3 – iCAPs spatial maps. The iCAP framework was employed to identify cerebral and spinal networks for all subjects (both days and both conditions included). **A.** Spatial patterns for the 15 iCAPs that were extracted at the level of the brain. Networks correspond to regions with distinct functional & anatomical relevance. Maps are overlaid on the MNI template. ACC = Anterior Cingulate Cortex. **B.** Spatial patterns for the 11 spinal iCAPs. Networks are clearly segregated in the rostrocaudal direction, reflecting the segmental anatomy of the spinal cord. Dorsal (i.e., sensory) and ventral (i.e., motor) iCAPs are present. Maps are overlaid on the MNI-Poly-AMU template (Fonov *et al.*, 2014) and spinal levels are provided as reference (Cadotte *et al.*, 2015). L = left, R = right, D = dorsal, V = ventral

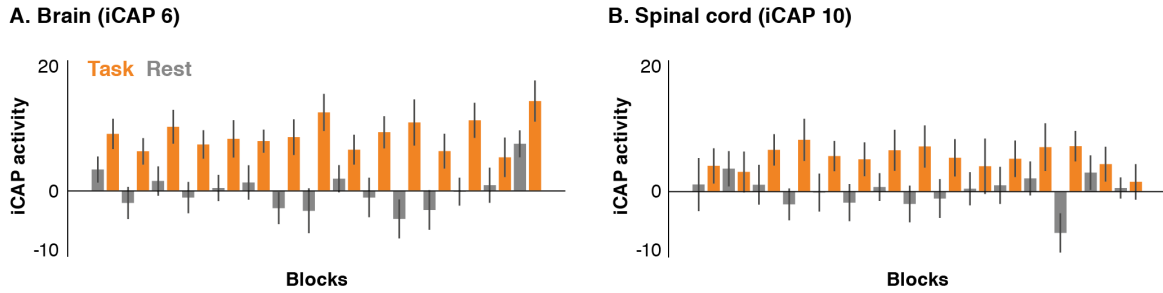
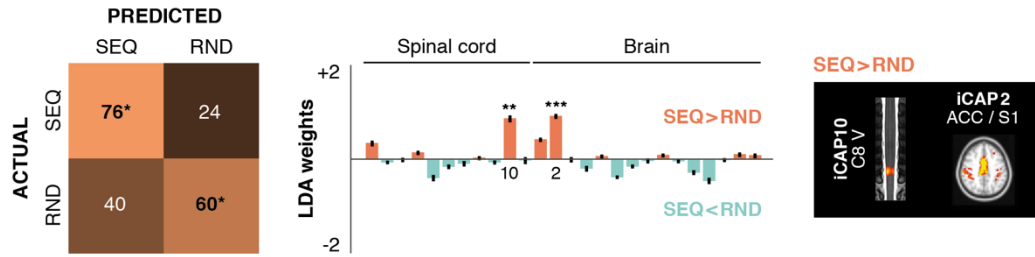


Figure 7.4 – iCAP temporal dynamics. Examples of timecourses for one brain iCAP (A.) and one spinal cord iCAP (B.), corresponding to practice of the SEQ task, on Day 1. Timecourses are normalized by the mean value during rest for this particular iCAP. Each bar corresponds to the mean activity in one block (task in orange and rest in grey). Values are presented as mean over subjects \pm SE.

7.3.3 Cerebro-spinal dynamics are predictive of short- and long-term motor learning

In order to further explore the relevance of these dynamics, we conducted a multivariate classification analysis to determine whether specific activity profiles were associated with different learning stages. Using mean iCAP task activities as features, we first aimed to quantify changes in cerebro-spinal activity pertaining to within-session MSL, as reflected by the difference between SEQ and RND task practice. On both days, the task could be decoded with a high accuracy, as emphasized by diagonal confusion matrices (Figure 7.5). On Day 1, the average accuracy was 68% ($p < 0.05$ against chance level, non-parametric permutation testing) (Figure 7.5A), while it reached 86% on Day 6 ($p < 0.001$) (Figure 7.5B). LDA weights were stable across cross-validation folds (cosine similarity = 0.98 ± 0.01 on Day 1 and 0.99 ± 0.02 on Day 6, mean \pm SD over folds) and they revealed distinct activity patterns linked to short- (Day 1, Figure 7.5A) and long- (Day 6, Figure 7.5B) term MSL. On Day 1, iCAP_{SC} 10 and iCAP_{BR} 2 were consistently engaged in classifying MSL (i.e., SEQ > RND), as highlighted by a high discriminative power. These iCAPs correspond, respectively, to the ventral side of C8 and to ACC and somatosensory regions (Figure 7.5a). On Day 6, numerous features carried discriminant power, with significant weights found for six iCAPs (Figure 7.5B). In particular, two spinal iCAPs (iCAP_{SC} 4 and 6, corresponding to ventral networks at the C6 and C7 spinal levels) and two brain iCAPs (iCAP_{BR} 1 and 15, corresponding to striatal regions of the basal ganglia and to sensorimotor regions) were positively associated with MSL. On the other hand, iCAP_{BR} 6 and 10, which mainly include motor and visuospatial regions, appeared to be less prominent during MSL.

A. Day 1, SEQ vs RND



B. Day 6, SEQ vs RND

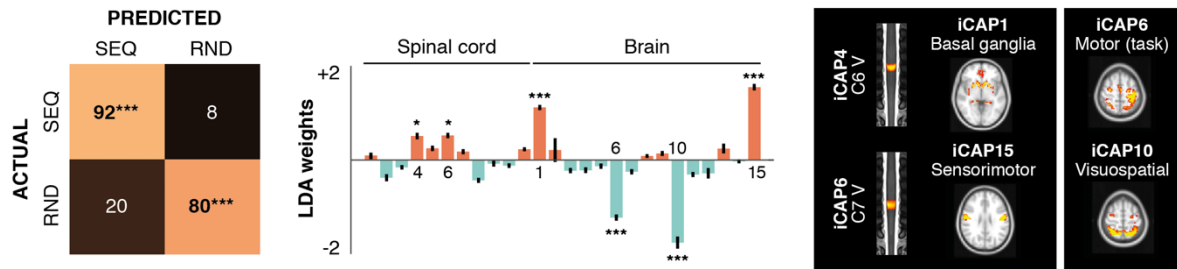


Figure 7.5 – Within-session classification. Independently on Day 1 (A.) and Day 6 (B.), two-class LDA classifiers (leave-one-subject-out cross validation) were employed to discriminate between SEQ and RND task practice using iCAP activities as features. Confusion matrices are displayed in the left panels. On Day 1, the average accuracy was 68%, while it reached 86% on Day 6. The middle panels show the LDA weights (mean over cross-validation folds \pm SD). Significant values are indicated and the corresponding iCAPs are presented in the right panels. * corresponds to $p < 0.05$, ** to $p < 0.01$ and *** to $p < 0.001$ (non-parametric permutation testing)

To better characterize the temporal evolution of learning-specific neural correlates, we then aimed to classify MSL activity patterns between sessions (Figure 7.6). For that purpose, the differences in iCAP activity during the SEQ and RND task practice, on both days, were taken as features. Again, the high classification accuracy (on average 72%, $p < 0.01$ against chance level, non-parametric permutation testing) underlined that cerebro-spinal iCAPs were differentially activated during short- and long-term MSL. LDA weights were stable across cross-validation folds (cosine similarity = 0.98 ± 0.004) and indicated that iCAPs_{SC} 5 and 6 (spinal level C7) along with iCAPs_{BR} 1 and 15 (basal ganglia and sensorimotor) were involved in long-term motor learning (MSL D6 > MSL D1), in line with within-session observations. In contrast, short-term motor learning (MSL D1 > MSL D6) displayed a functional pattern including iCAP_{SC} 10 (ventral side of C8) as well as iCAPs_{BR} 6 and 10 (motor and visuospatial).

In summary, these findings highlighted the fact that there are robust changes in neural dynamics during learning, entailing a high discriminability between short- and long-term MSL. In particular, spinal cord involvement shifted from caudal (i.e., C8 spinal level) to rostral cervical levels (i.e., C6-C7 spinal levels), while distinct cortical and subcortical areas participated in the different learning phases.

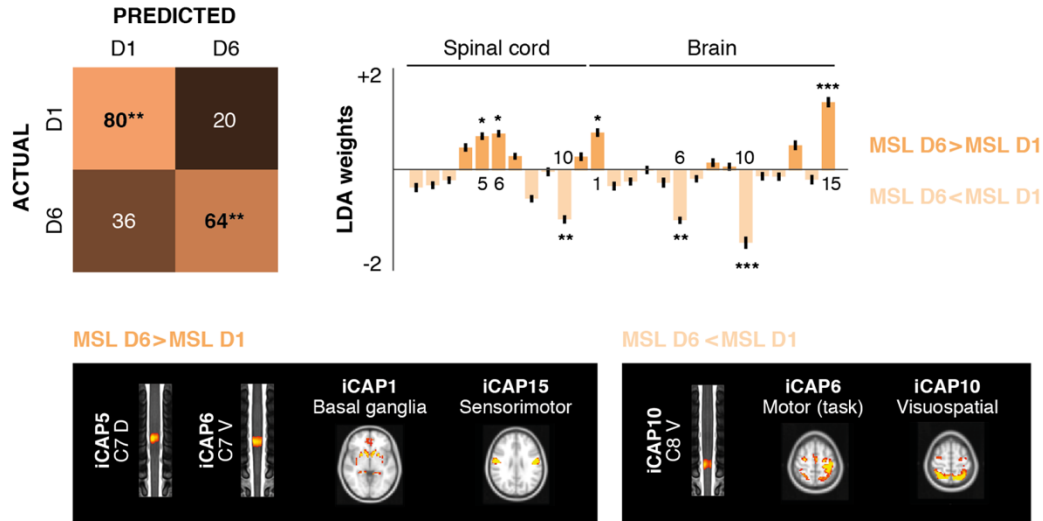


Figure 7.6 – Between-session classification. A two-class LDA classifier (leave-one-subject-out cross validation) was used to discriminate between activity patterns associated with MSL (defined as the contrast SEQ > RND) between the two sessions (i.e., Day 1 and Day 6). The resulting confusion matrix is displayed in the upper left panel and shows an average accuracy of 72%. LDA weights are reported in the upper right panel (mean over cross-validation folds \pm SD) and the iCAPs corresponding to significant weights are presented in the lower panel. * corresponds to $p < 0.05$, ** to $p < 0.01$ and *** to $p < 0.001$ (non-parametric permutation testing)

7.3.4 Long-term motor learning changes brain-spinal cord interactions

To better understand the mechanisms through which the brain and the spinal cord support MSL, we then investigated whether their relationship exhibited learning-dependent characteristics. To this end, we used the spinal iCAP networks as seeds and examined their functional connectivity with supraspinal regions for the different days and conditions. Specifically, we compared the connectivity patterns related to short- (MSL on Day 1) and long- (MSL on Day 6) term motor learning (Figure 7.7). This analysis revealed significant learning-dependent connectivity changes between sessions, as two spinal iCAPs showed an increase in correlation with brain regions during MSL in Day 6 compared to Day 1 (Figure 7.7A). In particular, we observed an increased interaction between iCAP_{SC} 3 (i.e., dorsal side of C6) and brain regions encompassing areas in the left dorsal ACC and left cerebellum, along with a stronger correlation between ICAP_{SC} 8 (i.e., ventral side of C8) and a cluster located in the sensorimotor cortex. In order to gain additional insights into learning-induced changes of connectivity, we finally assessed the mean correlation between the three cerebral clusters and the associated spinal iCAPs, for the different days and conditions (Figure 7.7B). As for the SEQ task practice, a negative synchronization with brain regions was found on Day 1. Spinal iCAPs then became less correlated with the ACC and the sensorimotor cortex following the week of training, while the a positive synchronization with the cerebellum emerged. During the RND practice, instead, an opposite pattern was highlighted. In particular, the coupling between ICAP_{SC} 8 (C8) and the sensorimotor cortex shifted towards a negative correlation on Day 6.

Altogether, these results emphasized that specific brain-spinal cord functional interactions arose during the acquisition and consolidation of motor skills.

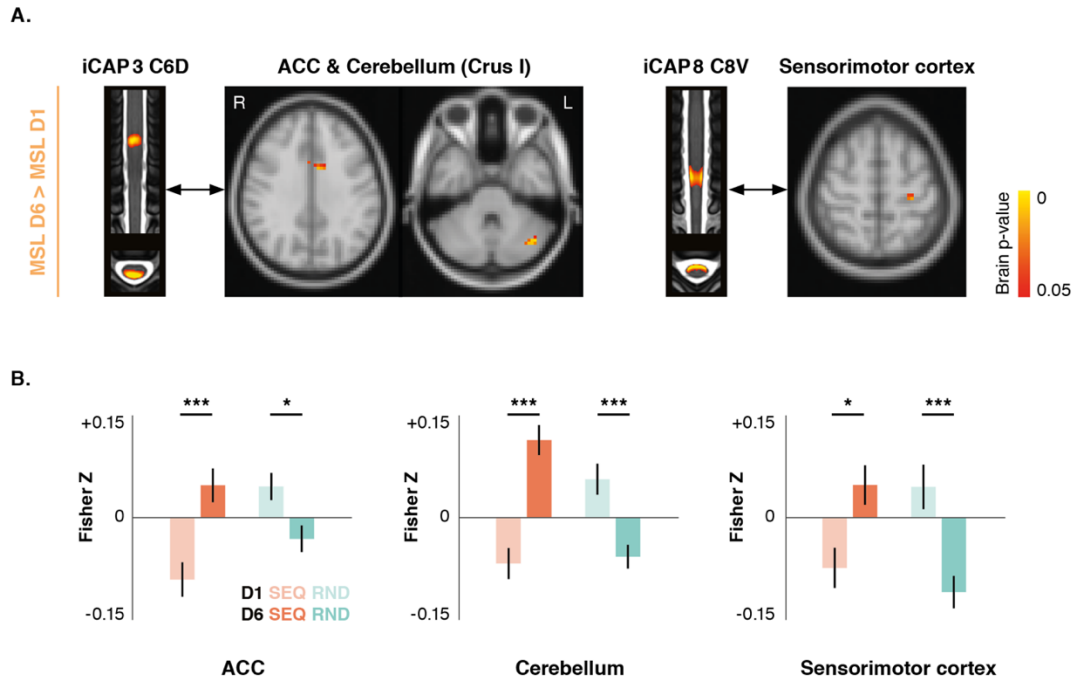


Figure 7.7– Cerebro-spinal interactions during motor learning. **A.** An iCAP-informed correlation analysis (i.e., correlating spinal iCAPs timecourses with brain activity inducing signals) was used. Specifically, we aimed to inspect differences in learning-induced cerebro-spinal connectivity between the two sessions (i.e. MSL on Day 1 against MSL on Day 6). Two spinal iCAPs changed their connectivity with supraspinal structures, which are presented in the adjacent brain maps (non-parametric permutation testing, TFCE corrected). For both iCAPs, correlation levels increased following the week of training, with clusters in the left ACC and cerebellum for ICAP_{sc} 3, and with a cluster in the sensorimotor cortex for ICAP_{sc} 8. **B.** For each cerebro-spinal coupling highlighting in A., we present bar plots showing the mean Fisher Z-transformed correlations values independently for the different days and conditions. Values are presented as mean \pm SE. * corresponds to $p < 0.05$ and *** to $p < 0.001$ (paired t-tests corrected for multiple comparisons).

7.4 Discussion

In this work, we leveraged a novel simultaneous brain and spinal cord fMRI dataset, in which functional activity was monitored in the early and late phases of motor sequence learning (MSL). To examine the neural correlates of MSL, we extracted brain and spinal cord networks, the so-called iCAPs (Karahanoğlu and Van De Ville, 2015; Kinany *et al.*, 2020), and showed that they exhibited functionally relevant spatio-temporal properties. A multivariate classification approach confirmed that specific patterns of functional activities were associated with short- and long-term MSL. Importantly, these patterns were stable across subjects and distributed throughout the motor neural hierarchy, from the brain to the spinal cord. In particular, spinal activity displayed a shift from caudal to rostral levels following extended training. In addition, functional connectivity analyses uncovered learning-induced changes in neural synchronization between the cervical cord and brain regions, notably with the anterior cingulate cortex, the cerebellum and the sensorimotor cortex.

7.4.1 Brain and spinal networks correspond to functionally relevant CNS structures

To disentangle the building blocks of cerebral and spinal activities, we deployed a dynamic connectivity approach based on hemodynamic-informed deconvolution of BOLD time courses (Karahanoğlu and Van De Ville, 2015; Kinany *et al.*, 2020) (see Chapter 6 for details). Even though

this framework has previously been used in resting-state studies (Kinany et al. 2020 in the spinal cord; Zöller et al. 2019 in the brain), this is the first time that this methodology is extended to probe task-related signals. Unsurprisingly, the 15 brain networks did not correspond to commonly observed resting-state patterns, but rather exhibited motor- and learning-relevant features (Figure 7.3). Notably, iCAP_{BR} 6 included contralateral sensorimotor cortices, bilateral premotor cortices and superior parietal lobules, as well as ipsilateral cerebellum. These regions correspond to well-known structures involved in movement generation (Miall, 2013), and their lateralization advocates for the task-specific nature of this network. Importantly, the neural substrates mediating motor skill learning are known to rely on distributed cortical and subcortical regions (Dayan and Cohen, 2011; Doyon et al., 2018). In particular, the role of cortico-striatal and cortico-cerebellar circuits have been suggested to play a critical role in this form of procedural memory. In this context, the delineation of two iCAPs comprising striatal regions of the basal ganglia, such as the putamen, caudate and accumbens, may provide insights into their learning-dependent mechanisms. Furthermore, the cerebellum was also dissected into anatomically and functionally meaningful sub-regions. Several networks included parietal regions involved in representation of the hands and in visuospatial guidance (Hardwick et al., 2013), an expected result owing to the nature of the motor task (visual presentation of targets to be reached using a joystick). These regions were combined with the premotor cortex, also implicated in spatial planning of movement (Tanji, 2001). Finally, the anterior cingulate cortex (ACC), known to participate to movement coordination (Wenderoth et al., 2005) and error processing (Seidler et al., 2013), was also recovered in several networks. Of note, the fact that a single region, such as the ACC, could be present in multiple networks was rendered possible by the unique ability of the iCAP method to identify spatially overlapping components (Karahanoğlu and Van De Ville, 2015). Regarding the 11 spinal iCAPs, we could also isolate networks corresponding to spinal levels and displaying dorsal (i.e., sensory) and ventral (i.e., motor) components, in line with resting-state studies (Barry et al., 2014; Kong et al., 2014; Kinany et al., 2020). Interestingly, all networks were bilateral, despite the unilaterality of the task. Although finer components have been previously reported (Kinany et al., 2020), as well as unilateral networks (Kong et al., 2014), the coarse organization detected in this study may pertain to the low spatial resolution ($1.2 \times 1.2 \times 5 \text{ mm}^3$), which prevented a detailed observation of spinal structures. Nevertheless, our findings suggest that we could access simple building blocks of spinal cord's functional architecture. Capitalizing on the time-varying feature of the iCAP method, we then explored the temporal dynamics of these functionally-relevant cerebro-spinal modules and confirmed that they manifested task-related activity fluctuations underlying MSL.

7.4.2 Distinct neural structures support short- and long-term motor learning

Behavioral studies have underlined that sequence learning occurs in distinct stages (Doyon and Benali, 2005; Diedrichsen and Kornysheva, 2015; Doyon et al., 2018). Short-term motor learning is characterized by rapid improvements in performance in the early stage of skill acquisition (i.e., within a single training session), while skills are then slowly consolidated and optimized as long-term practice continues over several sessions. A large body of evidence has demonstrated that multiple cortical and subcortical regions positively and negatively modulate their activity at different timescales, to support the acquisition and retention of novel skills (Tanji, 2001; Doyon and Benali, 2005; Floyer-Lea and Matthews, 2005; Dayan and Cohen, 2011; Wymbs and Grafton, 2015; Doyon et al., 2018). In addition to these experiments examining cerebral correlates of MSL, several studies suggested changes at the level of the spinal cord (Nielsen et al., 1993; Meunier et al., 2007; Wolpaw, 2007; Lungu et al., 2010; Vahdat et al., 2015). Mostly, knowledge on this topic was gathered thanks to electrophysiological recordings, for instance using the H-reflex as a proxy for spinal excitability.

While this pointed to an active role of the spinal cord in skill acquisition, the precise underpinnings of this involvement, as well as its temporal properties, are yet to be characterized.

Capitalizing on the two acquisition sessions provided in the dataset, we addressed this question by probing time-dependent learning effects. fMRI time series were acquired during RND and SEQ tasks, in the early (day 1) and late (day 6) stages of learning, to distinguish skill learning from mere motoric output. As anticipated, behavioral results (Figure 7.2) confirmed within- and between-session improvements that were specific to the SEQ task, while performances remained stable during RND practice. Given these observations, we hypothesized that cerebro-spinal functional activity, as described using iCAPs, would exhibit differential patterns reflecting MSL at different timescales. A multivariate classification approach was employed and showed that activity patterns associated with the SEQ and RND tasks in each session could be classified with high accuracies (Figure 7.5). Specifically, performance increased from Day 1 (68%) to Day 6 (86%), suggesting a stabilization of the underlying neural structures as the skills got consolidated and more and more automatic (Diedrichsen and Kornysheva, 2015). To further appreciate the specificities of short- and long-term skill acquisition, classification was also performed between sessions and enabled to discriminate between the neural activity patterns associated with early and late MSL (mean accuracy of 72%) (Figure 7.6).

Interestingly, distinct cerebro-spinal structures were involved in discriminating between tasks. On Day 1, one cortical iCAP (regions in ACC and S1) was found to be associated with SEQ practice and may have contributed to the initial learning of the sequence through processes supporting sensory feedback and error correction (Hardwick *et al.*, 2013). When comparing MSL-related patterns on both days, we found that four brain iCAPs showed significant discriminative power, with concomitant increase and decrease of activity, as reported in earlier studies (Steele and Penhune, 2010). Networks encompassing premotor areas were tied to early learning, in line with evidence suggesting a dominant contribution of these regions during the formation of sequence-specific knowledge (Penhune and Steele, 2012; Lohse *et al.*, 2014; Wymbs and Grafton, 2015). Following training, a global decrease was observed in task-specific sensorimotor areas, along with visuospatial regions, potentially indicating that sequential movements were done effortlessly after several days of practice, with minimal reliance on visual information. These diminutions occurring with long-term learning were accompanied by an increase of activity in other cortical and subcortical domains, in particular in a network comprising striatal and hippocampal regions, and in an iCAP including bilateral sensorimotor regions. Importantly, cortico-striatal systems are presumed to mediate MSL consolidation (Doyon *et al.*, 2003, 2018; Doyon and Benali, 2005; Lohse *et al.*, 2014), notably by means of interactions with the hippocampus (Albouy *et al.*, 2013). Furthermore, our findings are in agreement with a reported shift from a task-specific cortical network in short-term learning, to a bihemispheric cortical and subcortical network in long-term learning (Floyer-Lea and Matthews, 2005).

At the spinal level, within-session classification emphasized that several networks were positively associated with MSL, with a shift from caudal (C8) to rostral (C6-C7) spinal levels from Day 1 to Day 6. It should be noted that these levels coincide, respectively, with innervation sites of fingers and wrist muscles (Kendall *et al.*, 2005; Kinany *et al.*, 2019) (see Chapter 5). In addition, these networks were located on the ventral side, thus pointing to their motor essence. This may indicate a temporal evolution of the motor strategies employed by the participants to achieve smooth sequential motion. We hypothesized that accurate movements may initially rely on distal muscles, as finger grip enabled precise control of the joystick and allowed prompt trajectory correction in the event of errors. In contrast, a more optimal muscle control scheme may have arisen following practice,

entailing a decrease of finger activations, coupled with the emergence of synergistic strategies involving more proximal muscles, such as wrist actuators. It is noteworthy that the learning-related regions reported on Day 1 are in agreement with results from Vahdat *et al.*, 2015, despite differences in the nature of the task. Finally, classification between sessions confirmed that early and late learning intervals were dominated by disparate spinal regions, with a rostro-caudal shift, from C8 to C7, following extended practice of the sequential task.

In conclusion, we showed that distributed networks of cortical, subcortical and spinal structures contribute selectively to short- and long-term motor learning. These observations suggest that functional reorganization occurs in the whole CNS to subserve the acquisition and retention of novel skills.

7.4.3 Integrated brain-spinal cord networks may support synergistic control

A further aim of this study was to investigate how dynamic interactions between brain and spinal cord regions may foster the establishment of new motor skills. To this end, we conducted an iCAP-informed correlation analysis and showed that several cerebro-spinal networks emerged following long-term practice (Figure 7.7). Significant connectivity changes were found between the dorsal side of the C6 spinal level and clusters in the left ACC and cerebellum. Moreover, a network comprising the ventral side of the C8 spinal level and a cluster in the left sensorimotor cortex was also found. Interestingly, cerebro-spinal networks have been formerly highlighted, during task (Vahdat *et al.*, 2015) and at rest (Vahdat *et al.*, 2020).

In particular, Vahdat *et al.* (Vahdat *et al.*, 2015) demonstrated learning-induced modulations of connectivity between the spinal cord and the brain during short-term learning. In particular, the relationship with the sensorimotor decreased with practice, while it got stronger with the cerebellum. Our results indicated a similar decoupling between the spinal cord and the sensorimotor cortex as learning proceeds. Of note, the sensorimotor cluster overlapped with the posterior area of M1 (BA4p), which contains corticomotoneuronal (CM) cells that make direct monosynaptic with spinal motoneurons (Rathelot and Strick, 2006, 2009). CM projections are presumed to be involved in precision grip, notably to subserve voluntary control of independent finger movements (Lemon, 2008). Therefore, desynchronization between the spinal cord and the sensorimotor cortex during practice of a learnt sequence may indicate that subjects part ways from an error-focused strategy relying on fine finger movements.

We posit that this decrease in finger use may appear concomitantly to the emergence of a more synergistic control, likely implying a transition towards the use of wrist muscles. In non-human primates, evidence underscored the interaction of fractionated and synergistic control to support the versatility of hand movements (Takei and Seki, 2010; Takei *et al.*, 2017). In general, synergies have been proposed as a way to simplify complex motor control, by simultaneously recruiting muscles (i.e., muscle synergies, Mussa-Ivaldi *et al.*, 1994; D'Avella *et al.*, 2003) or joints (i.e., postural synergies, Santello *et al.*, 1998) in a coordinated fashion. The neural underpinnings of these synergies remain unclear, but an interplay between spinal and supraspinal regions have been argued (Bizzi and Cheung, 2013; Santello *et al.*, 2013; Giszter, 2015). On one hand, an involvement of motor cortical areas have been demonstrated (Overduin *et al.*, 2012, 2015; Rana *et al.*, 2015; Leo *et al.*, 2016). On the other hand, findings derived from intraspinal stimulation in animals have highlighted the ability of the spinal cord to generate functional modular movements (Saltiel *et al.*, 2001; Moritz *et al.*, 2007; Zimmermann *et al.*, 2011). Accordingly, synergies may be embedded in the spinal circuitry, for instance through interneurons, and orchestrated by supraspinal regions. In this context,

these mechanisms have been proposed to rely on spino-cerebellar interactions (Jörntell, 2016). According to this hypothesis, the spinal cord adapts to the most optimal muscle coordination patterns, based on the kinematic and biomechanical constraints of the task, and the cerebellum can then time the use of these synergistic components. Besides, cerebellar damage was recently shown to impact the spatiotemporal structure of muscle synergies (Berger *et al.*, 2020), thus providing support for its role in timing coordinated movements. Here, we hypothesized that the strengthening of synchronization between the cerebellum (Crus I) and the C6 spinal level may pertain to the emergence of muscular synergies relying on wrist muscles. In line with this hypothesis, primate and human studies have highlighted that cells in Crus I are linked to forelimb movements (Lu *et al.*, 2007; Mottolese *et al.*, 2012). Besides, it is likely that synergistic control relies on peripheral feedback from muscles, joints and skin (Santello *et al.*, 2013; Ting *et al.*, 2015), which would explain the dorsal lateralization of C6 in this spino-cerebellar network. Importantly, it should be emphasized that this coupling was only detected following long-term practice, while a weak negative connectivity was observed in the early phase, in agreement with Vahdat *et al.*, 2015. The shift to a synchronized spino-cerebellar network suggests that distinct mechanisms are in place when skills get consolidated. While these conclusions remain conjectural, future studies could explicitly compare synergistic and non-synergistic hand movements, similarly to previous work in the brain (Ehrsson *et al.*, 2002).

Finally, a negative functional connectivity between C6 and the dorsal ACC was found in short-term learning. Considering the role of the ACC in error detection and online monitoring of performance (Seidler *et al.*, 2013), such an observation is not unexpected during the acquisition of sequence-specific skills through visual feedback. In these circumstances, the negative corticospinal correlation may imply an inverse relationship between erroneous behavior and synergistic control. Alternatively, increased activity in the dorsal ACC may indicate performance anxiety and result in a deterioration of sequential motor performance (Ganesh *et al.*, 2019), possibly occurring through a decrease in the recruitment of rostral spinal levels. The self-initiated nature of the task used by Vahdat *et al.*, 2015, which implied less reliance on external error monitoring, may explain why such a network was not revealed in their study.

7.4.4 Outlook and clinical potential

In this work, we combined neural networks extracted using dynamic functional connectivity with a multivariate classification approach, to achieve a synthetic view of the cerebrospinal correlates of MSL at multiple timescales. While this study focused on task-related data, it should be noted that the data-driven character of this methodology makes it readily adaptable to resting-state recordings, in contrast to activation-based studies requiring a task paradigm (e.g., general linear model). As such, it offers an inroad into investigating intrinsic changes in the brain-spinal cord functional architecture following MSL. Indeed, resting-state studies can provide insights into motor learning whilst limiting confounds from task practice (Krakauer, 2007; Doyon *et al.*, 2018), and learning-induced modulations in resting-state connectivity have been demonstrated at the brain level (Vahdat *et al.*, 2011; Sami *et al.*, 2014).

Analogous approaches could be deployed to investigate the impact of neurological disorders on motor learning. As a matter of fact, the acquisition and consolidation of motor skills, both in healthy and impaired individuals, rely on plastic changes at multiple sites throughout the CNS (Wolpaw and Tennissen, 2001; Cramer *et al.*, 2011; Dayan and Cohen, 2011). It has not only been argued that principles derived from motor learning could help guide future interventions (Krakauer, 2006; Zeiler and Krakauer, 2013; Maier *et al.*, 2019), but also that efficient rehabilitation strategies should

capitalize on plasticity in spinal reflex pathways (Wolpaw, 2012). Therefore, an integrative view of MSL could provide a tool to gain valuable knowledge on the dynamics of spinal and supraspinal mechanisms mediating learning.

7.5 Conclusion

Our study uncovered neural correlates of motor sequence learning, distributed throughout the entire neural axis. In particular, we showed that short- and long-term learning were characterized by specific patterns of cortical, subcortical and spinal activity. A compelling observation was a shift from caudal to rostral spinal levels following extended sequential practice. We hypothesized that this may reflect the neural substrates supporting a transition towards a synergistic motor control strategy. This claim was also supported by the dynamic interactions observed between the brain and the spinal, suggesting a decrease in coupling with sensorimotor regions, concomitant with an increased synchronization with cerebellar regions likely involved in timing coordinated motor routines. To conclude, this work provides a potential starting point to investigate the widespread neural networks underlying motor memory and learning in the healthy and impaired nervous system.

Chapter 8

Clinical applications of spinal cord fMRI

8.1 Introduction

Owing to its key position in the motor hierarchy, the spinal cord could offer promising avenues to enhance functional recovery (Wolpaw, 2012; Baker *et al.*, 2015). As such, investigating how its structure and function underpin sensorimotor behavior is crucial, not only in health, but also in disease. In this perspective, imaging methods aiming at probing spinal cord structure have been widely deployed, for instance to evaluate spinal cord integrity following a cerebral (Ward *et al.*, 2006; Zhu *et al.*, 2011; Puig *et al.*, 2013; Maraka *et al.*, 2014; Karbasforoushan *et al.*, 2019) or spinal cord injury (Martin *et al.*, 2016; Cadotte *et al.*, 2018). Although these approaches can provide meaningful information regarding the progression of an injury and its potential recovery, they only offer a partial comprehension of the complex events taking place in the spinal cord. In particular, they do not inform about residual neural function. Therefore, extending these assessments to spinal cord function could give new insights into the processes mediating spinal neural plasticity. This could help gear therapies toward knowledge-based strategies harnessing neurological function to promote recovery.

Throughout the last chapters, we have emphasized the potential of spinal cord fMRI to explore these functional mechanisms. While we focused on the normal functioning of spinal circuits, it stands to reason that it may also be a powerful tool to probe their alterations. In this chapter, we present two prospective applications of spinal cord fMRI in a clinical context. In particular, we introduce preliminary results in a stroke population (study 1), as well as a case study in a spinal cord injured (SCI) patient (study 2).

Adaptive and maladaptive plasticity in stroke: Spinal circuits are not immutable. Instead, they evolve throughout our lifetime, as they experience dynamic changes shaped by supraspinal and peripheral inputs (Christiansen *et al.*, 2017). While this can occur during learning or normal aging, plastic reorganization can also result from damages to sensorimotor pathways (Wolpaw and Tennissen, 2001). In this context, plasticity can help compensate for a loss of function, as axonal or synaptic rearrangements can foster the emergence of alternative pathways to recovery (Fouad and Tse, 2008; Wolpaw, 2012). Nevertheless, plastic adaptation is not always beneficial. One such example is the case of spasticity, an increased velocity-dependent resistance to muscle stretch, a common symptom following CNS lesions (Nielsen *et al.*, 2007). This increased excitability of the stretch reflex is thought to rely on changes in spinal neurons. Although the exact mechanisms of action remain unclear (Li and Francisco, 2015; Li, 2017), imbalances between spinal excitatory and inhibitory inputs may putatively arise from perturbations in supraspinal signals. In more general terms, several studies in humans have emphasized that multiple descending motor pathways likely contribute to adaptive and maladaptive plasticity at the spinal level (McPherson *et al.*, 2018; Karbasforoushan *et al.*, 2019; Sangari *et al.*, 2019). Capitalizing on the potential of the SpiCiCAP framework to disentangle spinal pathways *in vivo* (see details in Chapter 6) (Kinany *et al.*, 2020),

we posit that spinal cord fMRI could shed new light on these mechanisms. To this end, we deployed this approach in a small cohort of stroke patients ($n = 9$) and attempted to relate changes in cervical functional organization to clinical assessments of spasticity.

Personalized mapping of the lumbosacral spinal cord following SCI: In addition to its potential for understanding plasticity mechanisms, spinal cord fMRI can also be employed to assess subject-specific spinal properties, for instance to support personalized rehabilitation strategies. Here, we discuss one such assessment in the context of SCI. As they disrupt the flow of descending and ascending information between the brain and the periphery, SCI are among the most incapacitating neurological conditions, often leaving survivors with severe paralysis (Ahuja *et al.*, 2017). In this context, electrical epidural stimulation (EES) in the lumbosacral spine has emerged as a potential treatment to restore locomotion, with promising results in humans (Wagner *et al.*, 2018). Given that EES operates by activating proprioceptive circuits through the dorsal horns (Capogrosso *et al.*, 2013), precise spatiotemporal neuromodulation is required to maximize clinical outcome (Wenger *et al.*, 2016). While afferents from a single muscle innervate only a few spinal levels, a substantial intersubject variability in the innervation pattern has been reported (Sharrard, 1964; Schirmer *et al.*, 2011). Consequently, mapping innervation patterns in a personalized manner could help optimize EES protocols. For that purpose, we conducted a spinal cord fMRI experiment in one spinal cord injured patient to achieve a personalized mapping of innervation patterns. Specifically, the patient underwent passive mobilization of his leg joints (hip, knee and ankle) so as to produce sensory activation in the dorsal horns, expected to be in distinct rostrocaudal locations depending on the muscles in movement (Schirmer *et al.*, 2011).

8.2 Methods

8.2.1 Participants

Study 1

Nine stroke patients (2 females, 69.5 ± 13.2 years old) were recruited in collaboration with the Clinique Romande de Réadaptation (Sion, Switzerland), as part of a longitudinal multimodal study (TiMeS project – Towards individualized Medicine in Stroke). Spinal MRI acquisitions were performed 3 months after the stroke. Detailed subject demographics are provided in Table F1. Spasticity was evaluated using the Modified Ashworth Scale (upper limb muscles, on a scale of 48). In order to probe its evolution, we considered this assessment at two timepoints (3 weeks and 3 months post-stroke). The nineteen healthy subjects analyzed in Chapter 6 (Kinany *et al.*, 2020) were used as a control group (10 females, 28.5 ± 3.1 years old).

Study 2

One SCI patient (male, 33 years old) was recruited in collaboration with the Centre Hospitalier Universitaire Vaudois (Lausanne, Switzerland), before implantation of an epidural stimulator, as part of a collaboration with the G-lab (EPFL). The participant was classified as AIS-A using the American Spinal Cord Injury Association Impairment Scale (AIS).

8.2.2 Image acquisition

All imaging was performed using a 3.0 Tesla Siemens Prisma scanner. Cervical images were acquired using the parameters we previously employed to characterize spinal activity during upper

limb movements (Kinany *et al.*, 2019) and rest (Kinany *et al.*, 2020) (i.e., ZOOMit sequence, resolution of $1 \times 1 \times 3 \text{ mm}^3$, TR = 2.5 s, TE = 34 ms). Lumbosacral acquisitions followed the protocols introduced in Chapter 4 (i.e., ZOOMit sequence, resolution of $1.1 \times 1.1 \times 3 \text{ mm}^3$, TR = 2.5 s, TE = 34 ms). High-resolution T2-weighted anatomical images from the region-of-interest were also obtained (SPACE sequence, resolution of $0.4 \times 0.4 \times 0.8 \text{ mm}^3$, TR = 1.5 s, TE = 135 ms).

Study 1

For each participant, 240 volumes (i.e., 10 minutes) were acquired during rest. Subjects were simply asked to relax, breathe normally and minimize motion. Physiological monitoring was performed using a photoplethysmograph and a respiratory belt (Biopac MP150 system, California, USA).

Study 2

The patient was installed in supine position while his right leg was passively mobilized by a trained therapist, so as to stretch different muscles of interest using (i) ankle extension (expected muscle activation: tibialis anterior), (ii) ankle flexion (soleus and gastrocnemius), (iii) knee flexion (vastus lateralis and rectus femoris), and (iv) hip flexion (iliopsoas). Two runs were acquired for each condition (order not randomized, as each condition required the limb to be specifically positioned and stabilized using foam paddings). Movements were performed in blocks of 15 seconds (13 blocks of rest alternated with 12 blocks of movements) and an entire run lasted 6 min and 15 s. Auditory cues were provided using headphones to inform the therapist of the different phases. Although physiological signals could not be acquired with the available setup, it should be noted that physiological motion is most prominent in the spinal cord and decreases significantly toward the lumbosacral regions (Figley *et al.*, 2008; Cadotte *et al.*, 2018).

8.2.3 Data processing and analysis

Study 1

Processing was the same for all participants and followed the pipeline described in Chapter 6 (Kinany *et al.*, 2020). Briefly, it included motion correction, timecourse denoising (regression of motion, physiological noise and CSF signal) and smoothing along the cord (Gaussian kernel with a FWHM of $2 \times 2 \times 6 \text{ mm}^3$). Volumes of the patients who had a lesion in the left hemisphere were flipped so that all lesions were on the right hemisphere for group analysis. The SpiCiCAP framework introduced in Chapter 6 (Kinany *et al.*, 2020) was then applied to recover 40 fine-grained spinal iCAPs, whose temporal properties were extracted. As two subjects had functional scans that did not include the C8 spinal level, iCAP extraction was constrained to a region extending from C5 to C7. The SpiCiCAP framework was also run in the control group. In order to enable comparison with the patients, functional scans of healthy subjects (Kinany *et al.*, 2020) were cropped temporally (to keep the first 240 volumes, out of 360) and spatially (to only include regions from C5 to C7). For both groups, the neuroanatomical relevance of each fine-grained components was evaluated using an atlas of grey and white matter regions (Lévy *et al.*, 2015).

Study 2

Processing and analysis were based on our previous study assessing the cervical correlates of upper limb movements (Kinany *et al.*, 2019). First, timecourses were motion corrected, smoothed along the cord (Gaussian kernel with a FWHM of $2 \times 2 \times 6 \text{ mm}^3$) and highpass filtered (sigma = 45s). A

first-level statistical analysis (within run) was carried out using FSL's fMRI Expert Analysis Tool (FEAT). Explanatory variables were defined using the timings of task blocks, convolved with three optimal basis functions using FLOBS (FMRI's Linear Optimal Basis Set) (Woolrich *et al.*, 2004b) to model potential temporal and dispersion shifts. Slice-wise CSF signal and motion parameters were included as noise regressors, along with motion outliers. For each movement, the parameter estimates (i.e., task against rest) obtained for the two runs were combined using a second-level statistical analysis (across runs) using a fixed-effects model to obtain movement-specific activation maps. Finally, these maps were used to map the rostro-caudal locations of activations. To ensure that activity was related to the passive movements, this analysis was constrained to the right dorsal quadrant.

8.3 Results

8.3.1 Patient-derived spinal iCAPs line up with neuroanatomy (Study 1)

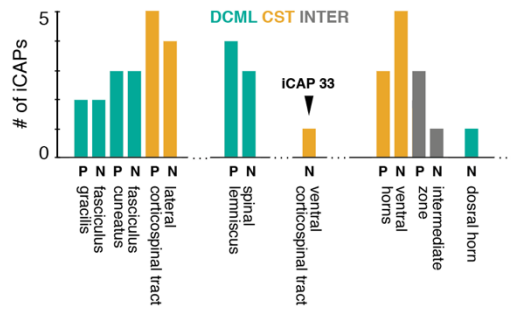
Data quality was evaluated prior to iCAP extraction. In the x direction, patients displayed slightly higher motion (framewise displacement, $FD_x = 0.07 \pm 0.03\text{mm}$, mean over subjects \pm SD) than healthy subjects ($0.04 \pm 0.01\text{ mm}$, $p < 0.001$), while no significant difference was observed in the y direction ($FD_y = 0.11 \pm 0.06\text{ mm}$ for patients and $0.10 \pm 0.04\text{ mm}$ for healthy subjects, $p = 0.24$). Regardless of these differences, participants from both groups had average FD inferior to 0.3 mm in the x and y directions and all subjects were included in the analysis.

40 fine-grained components were uncovered in patients using the SpiCiCAP framework. Spontaneous spinal activity was highly structured and could be delineated into precise axial subdivisions (Figure 8.1A). Following the approach introduced in Chapter 6 (Kinany *et al.*, 2020), each component was matched to an atlas region (Lévy *et al.*, 2015) based on its voxel distribution. Dice coefficients (0.56 ± 0.09 , mean over iCAPs \pm SD) confirmed the accuracy of the assignment. To probe the functional relevance of the revealed components, we then evaluated the nature of the corresponding atlas regions (Figure 8.1B). As a comparison, we performed the same analysis in the control group (Figure 8.1C). For both groups, iCAPs were organized according to spinal neural pathways (i.e., the corticospinal tract pathway, CST, and the dorsal column medial lemniscus pathway, DCML). Despite this general agreement, two atlas regions (referred to as *patient-specific* hereafter) were only observed in stroke patients. Specifically, they corresponded to a region in the ventral corticospinal tract (iCAP 33) and to a dorsal horn (iCAP 12). While iCAP 33 was matched with the ventral corticospinal tract using an hard assignment procedure (i.e., maximum number of voxels), we observed that it extended beyond the boundaries of this atlas region. In particular, it covered regions in the tectospinal and medial reticulospinal tracts (Figure 8.2A). it should be noted that these smaller tracts are known to be less neatly defined than their larger counterparts, such as the CST (Nathan *et al.*, 1996), and that they tend to be intermingled with other pathways.

A. Spatial maps (patients)



B. Distribution in atlas regions (patients)



C. Distribution in atlas regions (healthy)

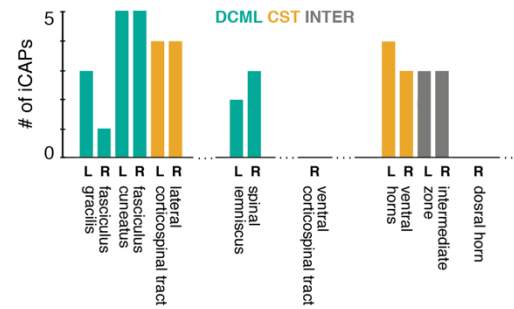


Figure 8.1– iCAPs spatial characteristics (Study 1). **A.** 40 spinal iCAPs were extracted in stroke patients. In line with our previous findings (see Chapter 6) (Kinany et al., 2020), the fine-grained components correspond to meaningful neuroanatomical structures. Each iCAP was matched to an atlas region (Lévy et al., 2015) (mean Dice coefficient \pm SD = 0.56 ± 0.09). ICAPs are presented in rostral-caudal order. Thresholded iCAP maps, in red, are overlaid on the corresponding atlas region probabilistic maps, in blue. The PAM50 template is used as a background (De Leener et al., 2018). ICAPs numbers are indicated in the bottom right corners. N = non-paretic, P = paretic, D = dorsal, V = ventral. **B.** The nature of the atlas regions associated with the 40 patient-specific iCAPs was probed. The number of iCAPs per atlas region is presented, omitting regions with no assigned iCAP. ICAPs cluster into spinal neural pathways (DCML: Dorsal Column Medial Lemniscus pathway and CST: Cortico-Spinal Tract pathway) and intermediate regions (INTER). ICAP 33, corresponding to a patient-specific descending region, is indicated. **C.** Distribution of iCAPs in the control group is provided as a reference.

8.3.2 Overall dynamics are preserved in stroke patients (Study 1)

We then evaluated temporal features of iCAP expression, in order to probe potential alterations in global dynamics following stroke. The overall level of activity (i.e., total iCAP activation time, including positive and negative occurrences) was similar ($p = 0.54$) between patient (27.87 ± 0.41 %, mean over subjects \pm SE, expressed as a percentage of run duration) and control (27.30 ± 0.60 %) groups. Likewise, no significant difference was observed between the average iCAP durations ($p =$

0.28, 2.70 ± 0.05 volumes in patients, against 2.77 ± 0.02 in healthy participants). Finally, the levels of coactivation were comparable ($p = 0.54$), with on average 11 iCAPs present at each time point. In sum, these observations suggest a correspondence between the overall dynamics of spinal resting-state fluctuations in healthy and stroke subjects.

8.3.3 Patient-specific descending iCAP is correlated with spasticity (Study 1)

To address the specific hypothesis of this exploratory study, namely the influence of descending tracts on spasticity following stroke, we focused on the patient-specific component corresponding to such regions, iCAP 33 (Figure 8.2). To better understand its functional relevance, we first assessed its rostrocaudal properties, which indicated its localization in the C7 spinal level (Figure 8.2B), mostly innervating elbow and forearm muscles (Kendall *et al.*, 2005). To investigate the behavioral relevance of this iCAP, we then tested for an association between its total duration and spasticity, as measured using the MAS. While no correlation was observed with spasticity at 3 months following stroke (Figure F1), we found that the total duration of iCAP 33 was positively correlated with the development of spasticity from 3 weeks to 3 months post-lesion ($\rho = 0.76$, $p = 0.0178$) (Figure 8.2C). In other words, regions associated with multiple descending pathways appeared to be more expressed in patients for which spastic symptoms increased over time.

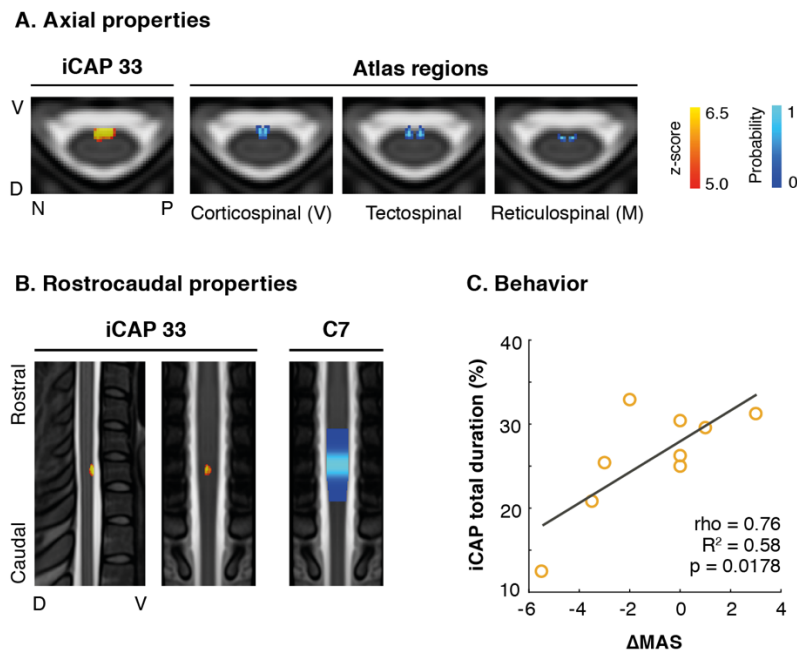


Figure 8.2 – Properties of iCAP 33 (Study 1). Given its patient-specific nature, as well as its location in descending pathways, we evaluated the spatial properties of iCAP 33 and investigated its behavioral relevance. **A.** In spite of its hard assignment to a ventral (V) corticospinal region, the spatial extent of iCAP 33 also covered smaller pathways, such as the tectospinal or medial (M) reticulospinal tracts (Lévy *et al.*, 2015). An axial view of iCAP 33 is presented (in red) in the left panel, and the three mentioned atlas regions are displayed (in blue) in the right panels. All maps are overlaid on the PAM50 template (De Leener *et al.*, 2018). N = non-paretic, P = paretic, D = dorsal, V = ventral. **B.** Sagittal and coronal views of iCAP 33 are shown to evaluate its rostrocaudal position. A map of the corresponding spinal level is provided as a reference. **C.** To probe the potential behavioral relevance of iCAP 33, we correlated its total duration in the nine subjects with the change of spasticity from 3 weeks to 3 months following the stroke, as measured using the Modified Ashworth Scale ($\Delta MAS = MAS_{3months} - MAS_{3weeks}$).

8.3.4 Passive joint mobilization enabled mapping of lower limb muscles (Study 2)

The aforementioned results suggest the potential of fMRI to explore spinal changes following a CNS lesion. Nevertheless, other applications can be foreseen and spinal cord imaging can, alternatively, be used as an assessment tool. To explore this direction, we conducted a case study in an SCI patient with the purpose of obtaining a personalized mapping of the afferent innervation of lower limb muscles involved in locomotion. Motion was assessed for each individual run, highlighting acceptable average FD_x (range 0.06 - 0.27 mm) and FD_y (range 0.05 - 0.30 mm). Of note, motion was higher when passively mobilizing the knee and hip joints. Lumbosacral activity was then mapped using a GLM approach, which pointed to specific innervation sites for the different muscles (Figure 8.3B). The iliopsoas (involved in hip flexion), the vastus lateralis and the rectus femoris (knee flexion) were related to rostral spinal levels (L1 to L3), while stretching the tibialis anterior (ankle extension), the gastrocnemius and the soleus (ankle flexion) elicited activation patterns located in caudal levels (respectively L5, S1 and S2). These rostrocaudal distributions were in line with population innervation patterns reported in previous literature (Schirmer *et al.*, 2011) and, in addition, they allowed to identify individualized features.

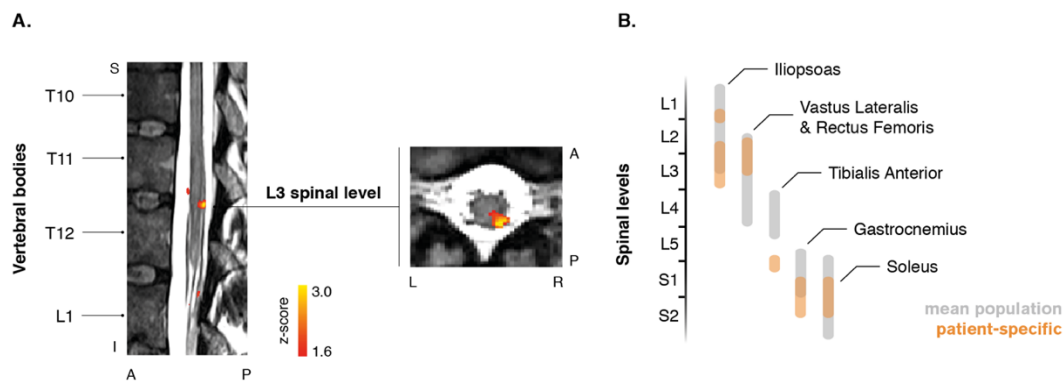


Figure 8.3 – Personalized mapping of lumbosacral activity (Study 2). **A.** Mean activation map during passive knee flexion (uncorrected), registered to the subject T2 anatomical image. Representative sagittal and axial views are shown, and vertebral bodies are labeled. **B.** Summary of the right dorsal activation patterns for the different muscles stretched during passive lower limb mobilization. Activations obtained in the patient are displayed in orange and overlaid from average innervation maps derived from previous literature (Schirmer *et al.*, 2011).

8.4 Discussion

In this work, we extended the methodologies introduced in the previous chapters in order to probe spinal cord functional activity in impaired individuals. Notwithstanding the preliminary nature of these two studies, they provide auspicious indications of the potentialities of spinal cord fMRI in clinical settings. In particular, this exploration highlighted a spinal network seemingly associated with spasticity in stroke patients. In addition, personalized innervation maps could be obtained in a SCI patient. Hereafter, we discuss these results independently, with an emphasis on the efforts that could further foster translational development.

8.4.1 Changes in descending pathways may contribute to development of spasticity

Even though spatial and temporal properties of spinal cord's functional architecture appeared to be mostly preserved following stroke, patient-specific components emerged. In particular, we

uncovered an iCAP associated with alternative descending pathways (Figure 8.2), such as the ventral corticospinal (vCST). In contrast to its lateral counterpart, the vCST is linked to the control of proximal musculature (Darby and Frysztak, 2013). As such, its presence in patients, but not in controls, could potentially be explained by the development of compensatory strategies involving the trunk and shoulders (Cirstea and Levin, 2000). It is noteworthy that the precise neuroanatomical identity of this patient-specific iCAP warrants further investigation, as it overlapped not only with the vCST, but also the tectospinal (TST) and medial reticulospinal (mRST) tracts. Accurate identification is, moreover, hindered by the fact that fibers of the RST can be relatively scattered through the ventral side of the spinal cord (Nathan *et al.*, 1996). Regardless of these considerations, alterations in white matter integrity were recently reported in these regions in chronic stroke patients (Karbasforoushan *et al.*, 2019). With respect to functional changes, it is commonly thought that brainstem descending pathways, such as the TST and the mRST, are hyperactivated post-stroke to compensate for disrupted cortical input (Trompetto *et al.*, 2014). Given the excitatory effect of mRST on spinal stretch reflex, imbalances in its activity are presumed to play an important role in spasticity (Li and Francisco, 2015). Using indirect measurements (motor evoked potentials and electromyographic measurements), increased RST output was previously shown following stroke (McPherson *et al.*, 2018; Choudhury *et al.*, 2019) and SCI (Sangari and Perez, 2019) and associated with poorer motor function. Our imaging results in a small stroke subpopulation hint, indeed, at a positive relationship between hyperactive descending pathways and the development of spasticity (i.e., from 3 weeks to 3 months) (Figure 8.2). On the other hand, we did not detect an association with the spasticity at 3 months. Considering that spasticity likely results from a combination of (i) weak extension (due to decreased cortical input) and (ii) strengthened flexion (due to hyperexcitable RST) (Li and Francisco, 2015), it may indicate that these two processes evolve on different timescales. In particular, the initial level of spasticity may pertain to (i), while maladaptive plasticity progressively leads to (ii). This association remains speculative and should be validated in a larger patient population, compared to an age-matched control group. Finally, it is noteworthy that the granularity (i.e., 40 iCAPs) was selected based on our previous study (see Chapter 6) (Kinany *et al.*, 2020). Exploring distinct levels of detail could ensure that robust iCAP components are extracted, possibly disentangling the influence of coalescent descending pathways (Nathan *et al.*, 1996). In summary, we posit that spinal cord fMRI could help investigate the role of distinct neural circuits in motor function following stroke. Future work could include longitudinal evaluation of spinal cord function, for instance before and after a botulinum toxin therapy, a common treatment for upper limb spasticity (Bensmail *et al.*, 2009). This knowledge could be employed to develop personalized rehabilitation strategies harnessing the abilities of spared connections while avoiding maladaptive plasticity.

8.4.2 Towards individualized EES therapy

In order to maximize efficiency of EES therapy, neurostimulation should reproduce the natural dynamics of motoneurons involved in locomotion (Wenger *et al.*, 2016). To this end, structural imaging can be combined with modeling protocols to identify posterior roots projecting to distinct motoneuron pools (Wagner *et al.*, 2018). Nevertheless, this does not account for inter-subject differences in the innervation patterns, even though substantial variability has been reported (Schirmer *et al.*, 2011). To address this, we performed spinal cord fMRI during passive limb mobilization and obtained personalized myotomal maps. The spatial distribution of lumbosacral activity was in agreement with anatomical knowledge, while outlining individual characteristics (see Figure 8.3). Considering the absence of statistical correction for multiple comparison, these preliminary results should, however, be taken with caution and merely represent a proof of principle. Yet, it should be

noted that direct root stimulation, using EES, corroborated these findings. In that regard, our findings allude to the potential of fMRI-derived knowledge to inform stimulation protocols. Nevertheless, experimental limitations should be acknowledged. Indeed, performing passive movements in a reproducible manner is challenging, for a number of reasons (motion, spasticity, etc.). Besides, certain muscles, for instance the ones involved in hip extension, cannot readily be stretched. Future work should consider alternative approaches, such as tendon vibration (Kavounoudias *et al.*, 2008), to possibly circumvent these drawbacks.

8.5 Conclusion

In this chapter, we provide novel evidence, though preliminary, for the clinical relevance and applicability of spinal cord fMRI. Further investigations in a larger population should complement these initial observations, so as to thoroughly characterize possibilities and limitations.

Summary and outlook

In this section, we parted ways from established assessment methods in order to bridge the gap between the brain and the periphery. In particular, we went beyond the encephalo-centered view of the CNS and resorted to spinal cord fMRI to capture spinal functional activity *in vivo* in humans. Considering the relative novelty of this approach, **Chapter 4** was dedicated to an initial comparison of acquisition protocols. This evaluation pointed to the superiority of reduced field-of-view imaging, such as ZOOMit sequences, over conventional protocols. Using a tailored acquisition and processing pipeline, we notably detected task-related activations in the cervical and lumbosacral spinal cord. Building on these results, we carried out a multimodal study including spinal cord fMRI and muscular activity to identify rostrocaudal correlates of upper limb movements (**Chapter 5**). With a combination of univariate and multivariate methods, we revealed activation patterns associated with distinct muscles, in line with anatomical knowledge. On top of outlining the association between motor output and fMRI-derived activity, this systematic evaluation provided compelling evidence of the potential of the selected pipeline. From task-evoked activity, we then extended our analyses to spontaneous fluctuations of spinal activity and conducted a resting-state fMRI study to explore the spinal cord's functional architecture (**Chapter 6**). Instead of relying on static functional connectivity, in which time-varying signal properties are not considered, we turned to dynamic approaches to further unravel the restless nature of spinal functional organization. In particular, we introduced the SpiCiCAP framework, which uses transient activity to retrieve subtle patterns of co-activation. Owing to the ability of this framework to disentangle temporally overlapping signals, we revealed robust fine-grained spinal components structured according to neuroanatomy. Besides, we underscored their physiological relevance, as they organized into networks based on ascending and descending spinal neural pathways. Capitalizing on its potential to delineate spinal circuits, we translated this framework to probe the dynamics of CNS networks during motor sequence learning, thanks to a simultaneous brain-spinal cord fMRI dataset (**Chapter 7**). Specifically, we combined this system-level network view with a multivariate classification approach, thus demonstrating that specific cerebral and spinal neural structures contributed to short- and long-term motor learning. At the spinal level, this entailed a shift from rostral to caudal levels following extended practice, possibly linked to a transition towards synergistic movements. Remarkably, we could also highlight specific patterns of cerebro-spinal interactions, which dynamically evolved with the emergence of motor routines. In light of these promising results, an exciting prospect for spinal cord fMRI is its extension to clinical applications. Therefore, we considered the clinical relevance of this approach in two preliminary experiments (**Chapter 8**). We deployed the SpiCiCAP framework in stroke patients, thus enabling the investigation of spinal dynamics following a CNS lesion. While the overall dynamics was preserved in patients compared to healthy participants, we detected localized changes in activity pertaining to descending motor pathways. Importantly, these changes were seemingly tied to motor deficits, as higher expression in these descending structures was positively associated with the development of spasticity. Aside from this exploration of spinal plasticity post-

stroke, we utilized a task-based fMRI paradigm to achieve a personalized mapping of lumbosacral innervation patterns in an SCI patient. Further analyses, notably in larger populations, should confirm these initial explorations, but they provide auspicious insights into the clinical applicability of spinal cord fMRI.

In conclusion, we argue that spinal cord fMRI is a promising tool to investigate spinal functional circuits. Our findings show how it can be deployed to scrutinize normal and aberrant spinal dynamics. Besides, they also advocate for its amenability to clinical settings.

Chapter 9 General conclusion

In this thesis, we aimed to achieve a comprehensive and multimodal view of central and peripheral mechanisms underpinning human motor function, with a particular focus on the pivotal position occupied by the spinal cord. We argued that a thorough understanding of these processes is crucial to improve neurorehabilitative treatments. Our contributions encompass methodological developments and application studies in healthy and impaired individuals. In what follows, we discuss our main achievements, inserting them in a broader context and suggesting potential directions for future research.

9.1 Summary and discussion

Nervous system disorders can considerably impact motor function, with long-term health consequences affecting the quality of life of millions of individuals. Current strategies to restore motor function are increasingly integrating technology to enhance recovery and help patients regain autonomy (Micera *et al.*, 2020). Despite the promises of these approaches, full recovery remains, in practice, rarely achieved. In this context, adapting treatments on a patient-specific basis has been suggested as the cornerstone of future improvements (Borton *et al.*, 2013; Raffin and Hummel, 2018; Coscia *et al.*, 2019). The motivation that initiated this thesis was, thus, to investigate the potential of paradigms for personalized technology-assisted neurorehabilitation. Arising from this was the need to understand the machinery subtending recovery, a condition *sine qua non* to optimally steer treatments.

Capturing dynamics of recovery In Part I of this thesis, we started tackling this problem from a technical viewpoint and evaluated methodologies to quantify individual dynamics of recovery in post-stroke patients. In that regard, the concept of recovery is manifold and ranges from rapid adaptive responses (Panarese *et al.*, 2012b) to durable plastic changes (Langhorne *et al.*, 2009; Buma *et al.*, 2013). These different facets have numerous implications for rehabilitation, which should not only be adapted to the immediate abilities of the patient, but also maximize the prospect of long-term effects based on his/her residual function. To obtain insights into the former, the most straightforward way to monitor motor improvements is to rely on kinematic measurements, such as movement speed or smoothness (Panarese *et al.*, 2016). In our first study (**Chapter 2**), this was achieved using an exoskeleton that enabled continuous three-dimensional tracking of limb position (Pirondini *et al.*, 2016; Giang *et al.*, 2020). We introduced a model-based personalization routine that uses this information to adjust training in real-time and validated its applicability in healthy subjects during a visual adaptation task, as well as in subacute stroke patients undergoing a rehabilitative training. On top of providing a task tailored to the patient's skills, this paradigm has the potential to sustain motivation and engagement, a pivotal factor influencing the effectiveness of therapy (Nielsen *et al.*, 2015; Rapolienė *et al.*, 2018). Owing to its simplicity and versatility, this

approach is well suited for a systematic use in clinical practice (Lambercy *et al.*, 2016). Nevertheless, kinematics is just one part of the picture and complementary knowledge can be gained from other levels of the neuromusculoskeletal hierarchy (Belfatto *et al.*, 2018). To this end, **Chapter 3** was dedicated to the establishment of a multimodal approach integrating kinematics along with muscular and neural variables (Pierella *et al.*, 2020). These variables were combined into a set of neuro-biomechanical features, whose relationship with recovery was outlined in longitudinal data from stroke patients. In particular, the multimodal analysis could capture the multifaceted nature of post-stroke recovery, with disparate dynamics through the neuromusculoskeletal system, something that cannot be rendered using standard clinical evaluations. From a practical standpoint, this approach also addresses a common criticism from therapists, against abstract technology-based outcome measures that lack functional applicability (Maggioni *et al.*, 2016), by distilling multimodal assessments into a few clinically relevant parameters. To ensure its clinical validation, however, further work should deploy this approach in a larger sample size to assess its reliability. Together, these results emphasize the potential of neurotechnology to pinpoint markers of recovery and track their evolution.

Exploring spinal cord function In Part I, we highlighted the pressing need to integrate multimodal knowledge so as to fully characterize the complexity of each individual patient's neuro-biomechanical state. This characterization of central and peripheral motor mechanisms should, subsequently, pave the way to knowledge-based neurorehabilitative treatments. Given the rising evidence of the involvement of the spinal cord in the recovery process (Fouad and Tse, 2008; Wolpaw, 2012; Baker *et al.*, 2015; Christiansen *et al.*, 2017; Li, 2017), we argued that acknowledging its role is necessary to develop a comprehensive description of healthy and impaired motor function. Contrarily to the long-held belief that the spinal cord merely serves the brain's interest, it should be recognized as an active and plastic part of the CNS. Nevertheless, in comparison to the wealth of research into cerebral plasticity, much less interest has been devoted to the spinal cord (Tennant, 2014). Certain insights have been gained through animal studies, notably using rodents to elucidate principles of spinal plasticity following CNS damage (Lilja *et al.*, 2006; LaPash Daniels *et al.*, 2009; Sist *et al.*, 2014). Yet, significant distinctions exist between motor systems of different species and these findings cannot simply be transferred to humans (Baker *et al.*, 2015). There is thus a strong incentive to develop protocols enabling non-invasive assessment of spinal cord function *in vivo* in humans. In this perspective, fMRI holds great potential to image endogenous spinal activity (Harel and Strittmatter, 2008; Wheeler-Kingshott *et al.*, 2014), though technological hurdles, primarily linked to the spinal cord's location and anatomy, have impeded the development of this field. Consequently, Part II of this thesis was first focused on introducing and evaluating methodological approaches to circumvent these limitations. In **Chapter 4**, we performed a pilot study primarily targeting issues and possibilities related to acquisition. Our conclusions pointed out robust activations, both in the cervical and lumbosacral regions, when using reduced field-of-view sequences. Interestingly, several studies in recent years corroborated these observations (Weber *et al.*, 2016a, 2016b, 2020; Dehghani *et al.*, 2020). In line with these findings, we were able to successfully deploy this pipeline to image the rostrocaudal correlates of upper limb movements, as presented in **Chapter 5** (Kinany *et al.*, 2019). Notwithstanding these achievements, it should be noted that spinal cord fMRI still suffers from a number of drawbacks that can impact data quality, as well as subsequent results. In that regard, further improvements regarding the acquisition procedure could be foreseen, for instance to ensure homogeneous signal quality with tailored shimming protocols (Finsterbusch, 2014; Vannesjo *et al.*, 2018) or to increase temporal resolution using multiband imaging (Moeller *et al.*, 2010; Barth *et al.*, 2016). As for the processing of functional images, efforts are also required to benchmark the potential of different approaches. Recent studies have undertaken

this endeavor and evaluated aspects such as motion correction (Dehghani *et al.*, 2020), smoothing (Weber *et al.*, 2017), or denoising (Kong *et al.*, 2012; Eippert *et al.*, 2017a). Needless to say that the availability of the Spinal Cord Toolbox (De Leener *et al.*, 2017) represents an important stepping stone towards establishing generalized guidelines. Finally, inter-subject variability in spinal activation patterns remains to be investigated, to better understand to which extent it arises from genuine anatomical differences (Schirmer *et al.*, 2011; Cadotte *et al.*, 2015), or rather reflects technical constraints.

Dynamics of the restless spinal cord While the aforementioned studies deployed paradigms probing spinal cord's response to a particular task, there is also much to grasp in baseline activity. Reflexes, proprioception or cerebro-spinal communication are among the processes that could drive spontaneous fluctuations (Eippert and Tracey, 2014). The study of resting-state spinal activity is of utmost interest, for a number of reasons. First, it can shed light on the spinal mechanisms supporting our body's physiological needs, from basic autonomic activity to more sophisticated proprioceptive processes. Second, understanding the intrinsic architecture of the spinal cord can reveal its functional backbone, which, possibly, represents the substrate for task-evoked activity. Indeed, the correspondence between rest and task functional organizations has been underscored in the brain, suggesting that they are two sides of the same coin (Smith *et al.*, 2009; Cole *et al.*, 2014). Finally, the simplicity of resting-state recordings places them as ideal candidates for clinical applications (Fox and Greicius, 2010; Lee *et al.*, 2013). In sum, these considerations led to research reporting coordinated spontaneous fluctuations in the spinal cord, that manifested in the form of sensory and motor networks, using static functional connectivity (see Barry *et al.*, 2014; Kong *et al.*, 2014 for seminal works). In this thesis, we aimed to go beyond conventional static methods, in order to further exploit the time-varying content of spinal cord resting-state signals. To this end, the SpiCiCAP framework was introduced in **Chapter 6** and demonstrated for the first time the potential of a dynamic functional connectivity approach to disentangle spinal activity (Kinany *et al.*, 2020). We revealed its fine-grained functional architecture, dissecting spinal circuits in components lining up with neuroanatomical and physiological principles. In particular, we provided compelling evidence that resting-state networks organized according to neural pathways involved in proprioception and motor control. Altogether, our findings shed new light on the restless nature of the spinal cord, emphasizing a substantial synchrony. From a more broader viewpoint, dynamic features have provided precious insights into the cerebral underpinnings of behavior (Liégeois *et al.*, 2019; Bolton *et al.*, 2020). One can envision a spectrum of possibilities in the spinal cord as well, for instance to investigate the temporal dynamics subtending reflexes or bilateral coordination. Interestingly, the fact that spinal dynamics seem better disentangled when using a dynamic approach leveraging transient activity suggests that synchrony occurring at multiple time scales may generate dynamic fluctuations in spinal resting-state activity (Hutchison *et al.*, 2013). Animal experiments using electrophysiological recordings (e.g., local field potentials, similarly to Wu *et al.*, 2019) could provide a more direct view on neural activity, to better understand the underlying processes.

Cerebro-spinal correlates of motor learning In light of these prospects, we went on to probe the dynamics of spinal and cerebral processes underlying short- and long-term motor sequence learning. It is widely held that neuroplasticity contributes distinctly to skill acquisition and consolidation but, to date, most studies had only focused on the brain (Doyon *et al.*, 2018). In **Chapter 7**, we explored whether these plastic changes were a general trait of the CNS, by deploying our dynamic functional connectivity framework in a simultaneous brain and spinal cord fMRI dataset acquired during motor sequence learning. Owing to the longitudinal nature of this data, we provided evidence that distinct patterns of cortical, subcortical and spinal networks were associated with the

different stages of learning. Besides, we highlighted a dynamic interplay between these structures, as the spinal cord synchronized over time with the cerebellum while parting ways from sensorimotor regions, thus extending on similar results obtained in a single session (Vahdat *et al.*, 2015). While this remains conjectural, we hypothesized that these neural changes may form a substrate for motor synergies (D'Avella *et al.*, 2003; Ting *et al.*, 2015). All in all, our findings endorse the differential role of the spinal cord throughout early and late motor learning. They also lend credence to the use of fMRI, combined with advanced analyses methods, to unravel these mechanisms, as well as their interactions with supraspinal structures. Considering its relationship with motor training (Zeiler and Krakauer, 2013), understanding motor learning and skill retention could open new avenues of investigation for neurorehabilitation, targeting experience-dependent plasticity (Dancause and Nudo, 2011) and optimizing the processes of motor (re-)learning (Winstein *et al.*, 2014).

Translational potential of spinal cord fMRI Spurred by these considerations, and in line with the advent of brain fMRI in patients (Matthews *et al.*, 2006; Fox and Greicius, 2010), our final focus (**Chapter 8**) was to glimpse into the clinical potential of the approaches discussed in the second part of this thesis. Using the SpiCiCAP framework, we first explored changes in spinal activation patterns following stroke. Our preliminary results alluded to a link between the development of spasticity and hyperactive descending pathways, notably including reticulospinal (RST) regions. Further work on a larger population is required to thoroughly characterize the nature of this interaction. Of note, the relationship between RST and spasticity had been suggested in previous research (Trompetto *et al.*, 2014; Li, 2017), and formerly inferred using indirect measurements, such as reflexes (McPherson *et al.*, 2018; Choudhury *et al.*, 2019). Spinal cord fMRI could thus provide a way to directly scrutinize these mechanisms. On top of this exploratory analysis, we resorted to a basic task-based paradigm to successfully map innervation patterns of lower limb afferents in an SCI patient. Such a personalized mapping can help inform therapies relying on spinal neuromodulation, where accurate spatio-temporal stimulation is critical to maximize clinical outcome (Wenger *et al.*, 2016; Wagner *et al.*, 2018). Interestingly, this endeavor resembles fMRI assessments conducted in the context of presurgical mapping, routinely used in clinical praxis (Specht, 2020).

9.2 Perspectives

The strategies introduced in this thesis constitute a valuable contribution towards understanding central and peripheral principles of the motor hierarchy. Most notably, they provide insights into human spinal processes, which have long remained impenetrable. As evidence indicates the pressing need for science-based neurorehabilitation (Nielsen *et al.*, 2015; Micera *et al.*, 2020), we argue that an extensive view of motor function can help apprehend and manipulate the underlying mechanisms.

Investigating the neural underpinnings of motor synergies In Chapter 3, we used muscle synergies in order to inform on muscle coordination patterns following a stroke. This alluded to the importance of motor synergies, notably as potential biomarkers of cortical injury (Cheung *et al.*, 2012). Despite the interest around synergies, both from a clinical viewpoint and to answer fundamental questions regarding the control of skilled movements, their neural substrates are poorly understood (Bizzi and Cheung, 2013; Ting *et al.*, 2015). In Chapter 7, we suggested that changes in cerebro-spinal interactions reflected the emergence of a synergistic motor strategy. However, these conclusions remain largely conjectural and future studies could build on these initial observations using dedicated experiments. For instance, simultaneous fMRI of the brain and the spinal cord could

be performed to compare the neural correlates of synergistic and non-synergistic movements, as previously done at the cerebral level (Ehrsson *et al.*, 2002). Alternatively, a comparison of upper limb movements relying on distinct muscle and joint configurations (e.g., different grasps) could also be foreseen (Leo *et al.*, 2016). In all instances, fMRI acquisitions should be complemented by kinematic and EMG recordings, so as to compute muscle and postural synergies and assess their cerebral and/or spinal encoding, as well as the role of cerebro-spinal interactions in their orchestration.

Understanding and harnessing plasticity The tools introduced in this thesis can be particularly relevant in the context of plasticity. As a matter of fact, neuromotor conditions affecting the CNS lead to plastic changes occurring at many levels of the motor architecture, from the muscles to the brain (Wolpaw and Carp, 2006). While the neuroplasticity of the spinal cord has been recognized (Wolpaw and Tennissen, 2001; Wolpaw, 2007), its mechanisms, as well as its interaction with peripheral and cerebral changes, remain elusive. Furthermore, plasticity can be seen as a two-edged sword (Allred and Jones, 2008; Ferguson *et al.*, 2012): on one hand, adaptive processes can help regain function, but on the other hand, maladaptive processes can compromise recovery. In future work, spinal cord fMRI could bring new light on the development of beneficial and detrimental plasticity. Eventually, these explorations should be performed along with simultaneous recordings of cerebral or muscular activity, so as to achieve a system-level view of plasticity. This new knowledge can set the ground for targeted rehabilitative therapies aiming to guide plastic processes (Cramer *et al.*, 2011; Dancause and Nudo, 2011; Wolpaw, 2012; Nielsen *et al.*, 2015). In practical terms, one can envision treatments focused on shaping activity-dependent plasticity, for instance through tailored constraint-induced robotic training (Coscia *et al.*, 2019) or using neuromodulatory interventions (Hummel and Cohen, 2006; Bradnam *et al.*, 2013; Raffin and Hummel, 2018).

Comprehensive multimodal assessments In Chapter 3, we proposed a multimodal framework to characterize patient's neuro-biomechanical state (Pierella *et al.*, 2020). A major advantage of this approach lies in its versatility, as variables stemming from multiple domains can readily be combined. Future studies could capitalize on this ability, by integrating measurements obtained using additional approaches, such as brain or spinal cord fMRI. This comprehensive view would enable the exploration of the complex and interleaved functional changes linked, for instance, with stroke, and to correlate them with behavioral and clinical indicators. Furthermore, this can help pinpoint particular interactions between central and peripheral mechanisms, that could be relevant in a clinical context. On top of expanding our understanding of the mechanisms involved in impaired motor control, the information gleaned from this analysis could help highlight biomarkers informing on recovery. Eventually, this effort could be facilitated by computational models (Reinkensmeyer *et al.*, 2016), to make accurate predictions at the individual level, regarding optimal intervention, timing or intensity.

Extension to other neurological disorders In Chapter 8, we touched upon the clinical potential of spinal cord fMRI, in the context of stroke and SCI. Nonetheless, the proposed methodologies undoubtedly hold great potential to study motor dysfunction resulting from other conditions (Kornelsen and Mackey, 2010). Of note, a few studies started initiated this effort, by investigating changes in spinal processes associated with multiple sclerosis (Conrad *et al.*, 2018), cervical spondylotic myelopathy (Liu *et al.*, 2016a) or fibromyalgia (Martucci *et al.*, 2019). Considering the primary role of the spinal cord in sensory processing, studies targeting the pathogenesis of neuropathic pain can also be foreseen (Dou and Yang, 2019). Future research should leverage the dynamic content of spinal signals, for instance using the SpiCiCAP framework introduced in Chapter 6 (Kinany *et al.*, 2020), to further characterize their nature. Understanding the mechanisms

underlying pathological alterations, as well as probing residual function, could have implications as regards diagnosis and prognosis. Relevant developments may also include imaging along the entire central neural axis. Finally, particular attention should be devoted to ensure robustness and reproducibility of fMRI-derived clinical measures (O'Connor and Zeffiro, 2019). Advances could entail the creation of multi-center databases, generalized acquisition and analysis routines, test-retest studies in individual subjects, in line with initiatives emerging in brain fMRI (Zuo and Xing, 2014; Choe *et al.*, 2017). Progresses in that regard will be instrumental to push spinal cord fMRI towards a clinically useful tool, notably in the context of personalized neurorehabilitative applications.

A. Supplementary material for Chapter 2

Additional analysis of performance measures

In order to demonstrate the capability of the proposed model to capture varying performance measures dynamics, we simulated different rehabilitation scenarios under varying conditions (Figure A1a). Specifically, data were generated for the three variables MV, SAL, and p_k using an exponential equation:

$$r_{j,k} = r_{j,end} - r_{j,start} \exp\left(-\frac{k}{\tau_j}\right) \quad (1)$$

where $j = 1, 2, 3$ are the different performance measures and $k = 1, \dots, 25$ are the different repetitions of a movement. $r_{j,end}$ and $r_{j,start}$ are parameters used to set the desired initial and final values of each performance measure. τ_j is the individual time constant for each performance measure. The equation was used to simulate the data of MV, SAL, and p_k for 25 repetitions of the movement towards the same target. The values for SUCC were deduced by using the values of p_k and a Bernoulli distribution model. We ran the simulations under four conditions: in the first three conditions, the time constant of one performance measure was reduced to $\tau = 5$, while the other two were kept at $\tau = 15$. In the fourth condition, the time constants for all three measures were reduced to $\tau = 5$. For all conditions, we obtained approximations of the simulated data by inserting the estimates of the unknown model parameters into the observation equations. Moreover, we calculated the 95% confidence intervals of the approximations and the corresponding motor improvement estimates. The results of the simulations illustrate the capability of the proposed model to capture varying dynamics of the performance measures properly. The simulated data lie within the 95% confidence intervals of the approximations for the most part. Moreover, the only condition where the requirement for a replacement is met is the one where all performance measures are simulated with low time constants and quickly reach a plateau, highlighting the fact that a replacement is only suggested by the algorithm when no further improvement is expected.

Moreover, we simulated MI estimation for lower number of data points (Figure A1b). The simulations presented in Figure A1b were run with varying amount of data (4, 8 and 12 data points) from the same data set. We observed that the simulated data were mostly in the 95% confidence interval of the model estimates for MV, SAL and p_k when 8 or 12 data points were used for the estimation. However, this was not the case when only 4 data points were considered for calculating the estimates. Based on this analysis, we have set the minimum number of data points necessary for MI estimation to 8.

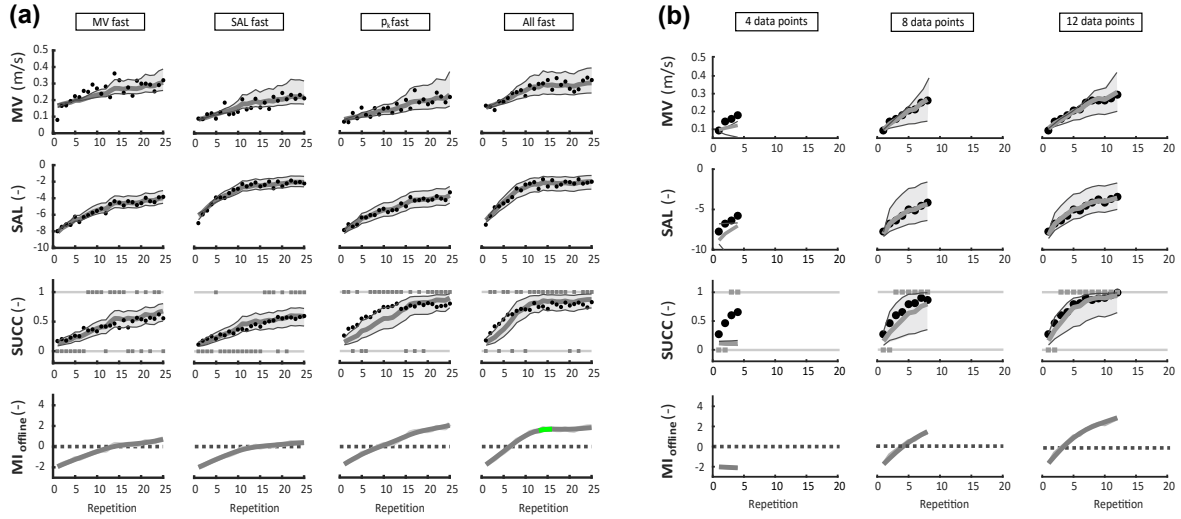


Figure A1 – Simulated data for motor improvement estimation under varying conditions. **(a)** Data shows the simulated performance measures and the corresponding motor improvement estimates under four different conditions for 25 repetitions of the same movement. In the first column, the time constant for the mean velocity (MV) was reduced to $\tau = 5$ repetitions ($\tau = 15$ repetitions for the remaining two measures), in the second column the time constant of the spectral arch length (SAL) was reduced to $\tau = 5$ repetitions and in the third column the time constant reduced to $\tau = 5$ repetitions was the one of the probability of success (p_k). In the last column, the time constant for all performance measures was set to $\tau = 5$ repetitions. The first two rows show simulated data (black dots) for MV and SAL. The third row depicts the simulated data for p_k (black dots) and the corresponding discrete performance measures SUCC (grey squares) deduced from p_k using a Bernoulli distribution model. Grey lines show approximations of the performance measures using the estimated parameters resulting from the algorithm. Shaded area depicts 95% confidence interval of the approximations. The last row shows the resulting offline motor improvement estimates (M_{offline}) using an offline implementation of the model. Dotted lines depict necessary condition (M_{offline} > 0) for target replacement. Green area indicates the time span where the algorithm detects a performance plateau and suggests a target replacement. **(b)** Simulated motor improvement estimates provided by the model based on 4, 8 and 12 data points of the same data set. The first two rows show simulated data (black dots) for MV and SAL. The third row depicts the simulated data for p_k (black dots) and the corresponding discrete performance measures SUCC (grey squares) deduced from p_k using a Bernoulli distribution model. Grey lines show approximations of the performance measures using the estimated parameters resulting from the algorithm. Shaded area depicts 95% confidence interval of the approximations. The last row shows the resulting offline motor improvement estimates (M_{offline}) using an offline implementation of the model. Dotted lines depict necessary condition (M_{offline} > 0) for target replacement.

Preliminary experiments with healthy participants

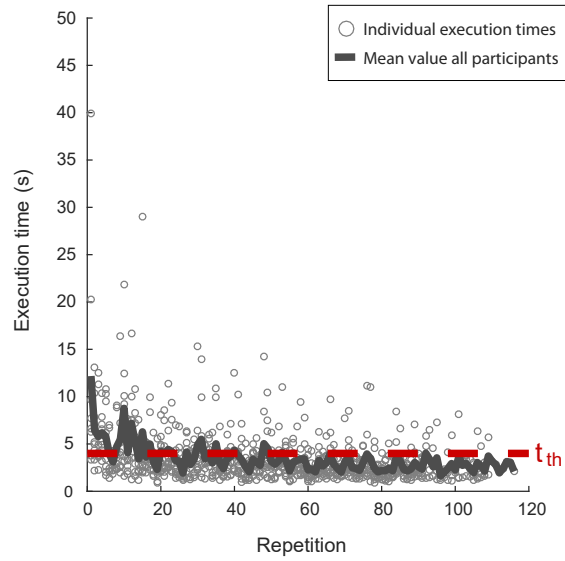


Figure A2 – Execution time of eight healthy participants (seven females, a male, 54.8 ± 13.8 years old) performing the regular point-to-point reaching task. Data for each participant is pooled for all movement directions (i.e., for all targets) and presented in chronological order (grey circles). Solid grey line shows evolution of execution time averaged over all eight participants. Red dashed line depicts the time threshold ($t_{th} = 4s$) used to determine the discrete performance measure SUCC in the visually manipulated reaching task. t_{th} was selected as the upper bound for the average execution time after the 50th repetition.

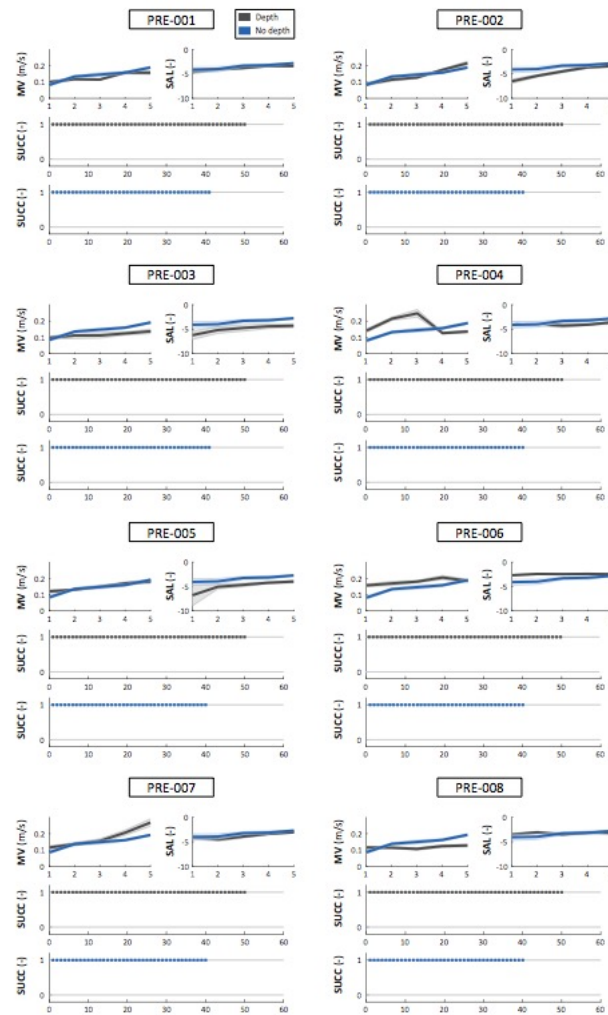


Figure A3 – Performance measures of eight healthy participants (seven females, a male, 54.8 ± 13.8 years old) performing the regular point-to-point reaching task (same data reported in Figure A2). First row shows the mean values and standard error of the mean of MV and SAL for five repetitions of no-depth targets (blue, targets 1-8) and depth targets (grey, targets 9-18). Data for each repetition is averaged for all targets of a class. Second and third row show the data of SUCC for no-depth (blue) and depth targets (grey). The data for each class of targets is presented chronologically for each repetition of the movements. SUCC was defined by the usage of the robot assistance (i.e., SUCC = 1 if the participant performed the movement without robotic assistance, SUCC = 0 otherwise). Overall, performances were not different for depth and no-depth targets, confirming that the participants could properly perceive the depth.

Additional analysis of model parameters

We have performed additional analyses to illustrate the temporal dynamics of the model parameters for both fast and slow adapters (Figure A). With increasing number of repetitions, all model parameters converged towards final values, indicating that the recorded data fit well the model. Interestingly, the model parameters for the fast adapters seemed to converge faster, probably because in this group participants showed faster improvements in the performance measures, which would fit the chosen observation models. When looking at the final mean values of the model parameters for both groups we did not observe notable differences, indicating that on average, motor improvement models were similar for both groups and that improvement could be observed only in changes of the MI estimates. The only remarkable difference was found for σ_{ϵ} which appeared to be higher for the fast adapters, reflecting the improvements in MI values for this group. Finally, values for σ_{δ_j} remained bounded in a range of reasonable values, indicating a limited influence of the gaussian noise terms δ_j on the motor improvement estimates.

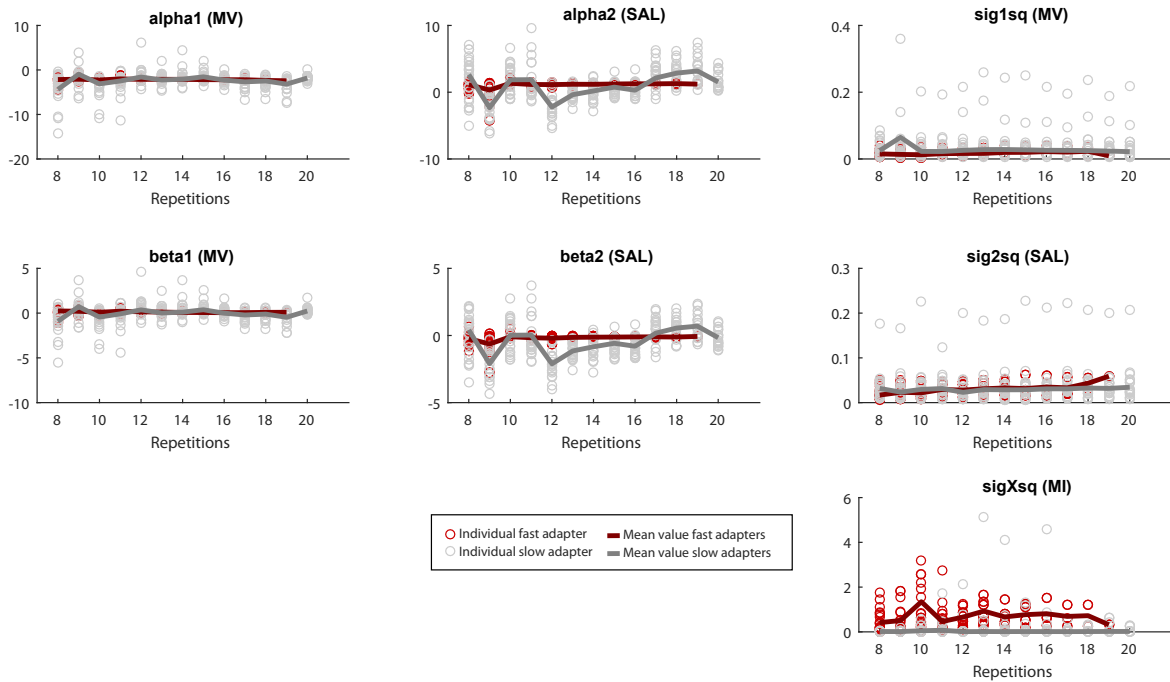


Figure A4 – Model parameters estimated for participants doing the visually inverted reaching task (n = 17). For each new set of data points, parameters were estimated using Bayesian Monte Carlo Markov Chain methods with three independent estimation chains and different initial guesses. Each chain was iterated for 5000 steps to determine the model parameters. The median of the three chains were taken as the final estimation values for the parameters. Data is presented for movements towards all targets for all subjects of the fast adapter (red circles) and slow adapter (grey circles) groups. Red and grey lines indicate average parameter values for both groups. Parameters were calculated for each number of repetitions towards a target (minimum 8 repetitions, maximum 20 repetitions).

Moreover, we calculated overall MI estimates for the two subjects presented as examples in Figure 2.3. Therefore, we merged the data from movements towards all training targets and calculated the MI estimates based on these combined data sets. Although an increase in MI can be observed in both subjects, we observed that the overall MI estimates for both subjects appeared to be noisier

and less descriptive, since now data of movements towards easy and difficult targets are pooled together. Indeed, basing the analysis on the overall MI estimates, the recoveries of the movements presented in Figure 2.3, are obscured by the inferior performances recorded for the difficult targets. Moreover, the detection of performance plateaus would not correspond to the actual performances for each subtask. As a result, some subtasks would be kept too long, while others would be replaced too early, potentially leading to a less efficient training schedule. For instance, the overall MI estimate for the slow adapter suggest a performance plateau already after 39 repetitions (corresponds to approximately 5 repetitions for each subtask). However, when looking at the performance measures of this subject for target 13 separately, it is clear that a replacement of this target after 5 repetitions would have been too soon. We therefore believe that this analysis further supports our approach to specifically consider MI estimation at subtask level.

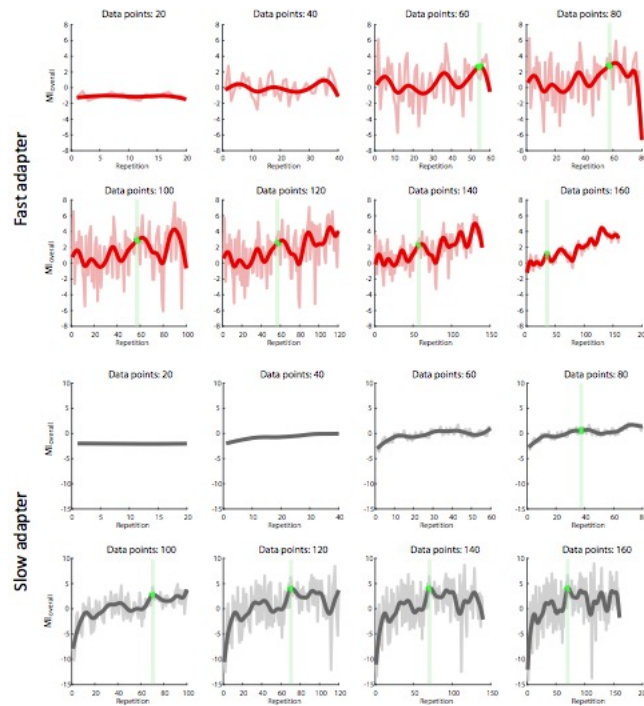


Figure A5 – Overall MI estimates for fast (red) and slow adapter (grey) presented as examples in Figure 2.3. Overall MI estimated were based on data chronologically merged from all training targets and were calculated for the first 20, 40, 60, 80, 100, 120, 140 and 160 data points. Data for MI estimates were low-pass filtered for visualization purposes (raw data shown in light red/grey). Green area indicates the time span where the algorithm detects a performance plateau and suggests a target replacement.

B. Supplementary material for Chapter 3

Patients division in training groups

The stroke participants were enrolled one at a time on a continuous basis. The subjects were randomly divided in the three different groups of experimental training. Specifically, subjects S1 and S2 were assigned to treatment group 1 (additional dose of conventional therapy), subjects S3 and S4 to treatment group 2 (additional standard robotic therapy), and subjects S5 and S6 to treatment group 3 (additional automatic personalized robotic therapy (Giang *et al.*, 2020)).

Muscle innervation from the spinal segments

Table B1 – Muscle innervated by each spinal cord segment. X correspond to a weight coefficient equal 1

	C2	C3	C4	C5	C6	C7	C8	T1
TRAPS	X	X	X					
TRAPM	X	X	X					
DANT				X	X			
DMED				X	X			
DPOS				X	X			
PECM				X	X	X		
LAT					X	X	X	
INFRA			X	X	X			
RHO			X	X				
BICL				X	X			
BICS				X	X			
BRAD				X	X			
TRILA					X	X	X	X
TRILO					X	X	X	X
PRO					X	X		

Details on muscle synergies similarities

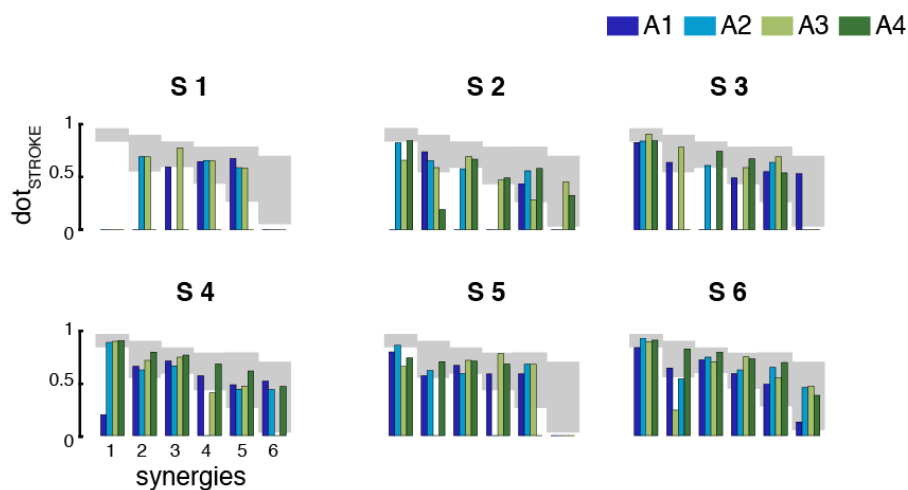


Figure B1 – Muscle synergies similarity. Results of the comparison between each muscle synergy of the stroke subjects with the ones of the healthy population at different time points, before (shades of blue) and after (shades of green) the rehabilitative intervention. The shaded area reports the mean and standard error for the healthy population and the bar plot the mean value of the stroke one.

Subject- and session-specific SVD maps

In order to demonstrate that all subjects had similar spatial map per component, we performed SVD decomposition of the EEG signal of each subject and session. We then matched the spatial map obtained for each participant and session (i.e., individual EEG-SVD maps) to the spatial maps obtained concatenating all subjects and sessions (i.e., group-level EEG-SVD maps) using Hungarian algorithm (Munkres, 1957). We computed correlation values between the individual spatial maps and the group-level EEG-SVD maps. The correlation was high for all top-five components (mean and standard deviation across components: 0.88 ± 0.02 – see Supplementary Figure B2) highlighting that all the subjects had similar spatial maps.

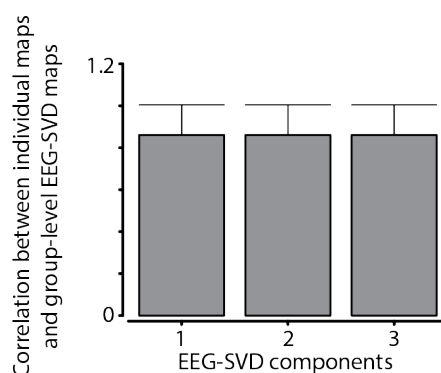


Figure B2 – Individual maps. Correlation between individual maps and group-level EEG-SVD maps for the first five components. Error bars represent mean \pm standard error of the mean across participants

C. Supplementary material for Chapter 5

Anatomy of muscle innervation

Table C1 – Mapping of the muscle activity on the spinal cord segments (from Kendall *et al.*, 2005) | BICL = biceps brachii long head, TRIC = triceps brachii long head, BRA = brachialis, BRAD = brachioradialis, PRO = pronator teres, EXCR = extensor carpi radialis, EXCU = extensor carpi ulnaris, EXDC = extensor digitorum communis, FLCR = flexor carpi radialis, FLCU = flexor carpi ulnaris, FLDS = flexor digitorum superficialis, ABDM = abductor digiti minimi, EXPB = extensor pollicis brevis, ADPT = adductor pollicis transversus, ABPB = abductor pollicis brevis.

	BICL	TRI	BRA	BRAD	PRO	EXCR	EXCU	EXDC	FLCR	FLCU	FLDS	ABDM	EXPB	ADPT	ABPB
C5	1	0	1	1	0	0.5	0	0	0	0	0	0	0	0	0
C6	1	0.5	1	1	1	1	0.5	1	1	0	0	0	0.5	0	0.5
C7	0	1	0	0	1	1	1	1	1	0.5	1	0.25	1	0	0.5
C8	0	1	0	0	0	0.5	1	1	0.5	1	1	1	1	1	0.5
T1	0	0.5	0	0	0	0	0	0	0	0.5	1	1	0	1	0.5

Results

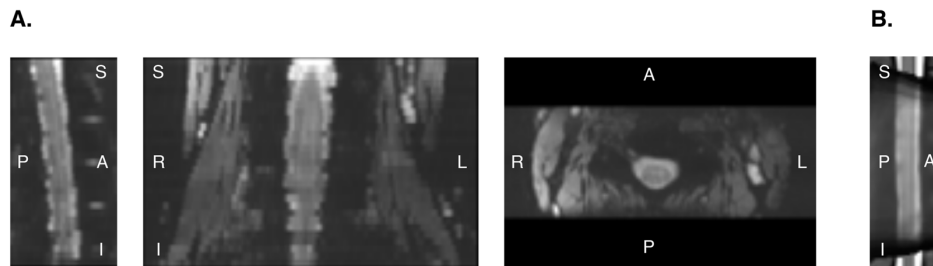


Figure C1 – Functional images. **A.** Mean functional image (after motion correction) for an example subject. Sagittal, coronal and axial views are presented. **B.** Group-average mean functional image (sagittal view) normalized to the PAM50 template (De Leener *et al.*, 2017). A = anterior, P = posterior, S = superior, I = inferior, L = left, R = right.

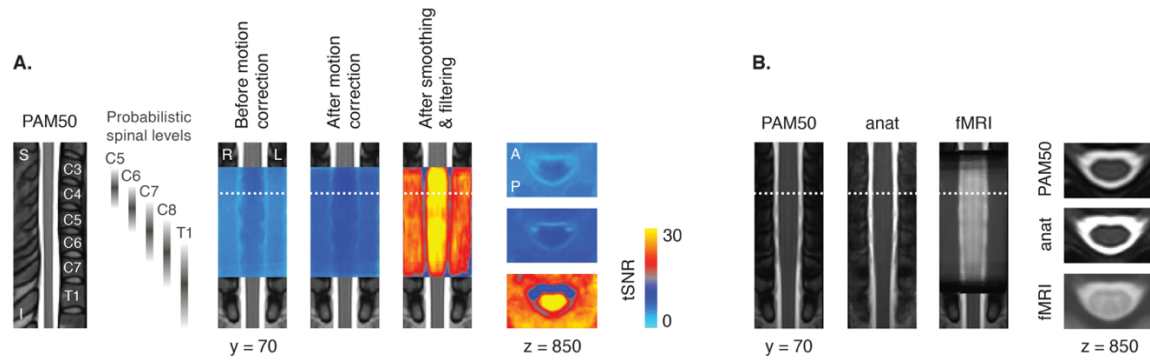


Figure C2 – Temporal signal-to-noise ratio and normalization. **A.** Temporal signal-to-noise ratio (tSNR) before and after motion correction, and after the filtering steps. Group maps, normalized to the PAM50 template (De Leener *et al.*, 2018), are presented, with one coronal slice and one axial slice per condition. **B.** Assessment of the normalization quality. The left panel (coronal views) presents representative slices of the PAM50 template, the mean normalized anatomical image and the mean normalized functional image. Example axial slices are shown on the right panel. A = anterior, P = posterior, S = superior, I = inferior, L = left, R = right.

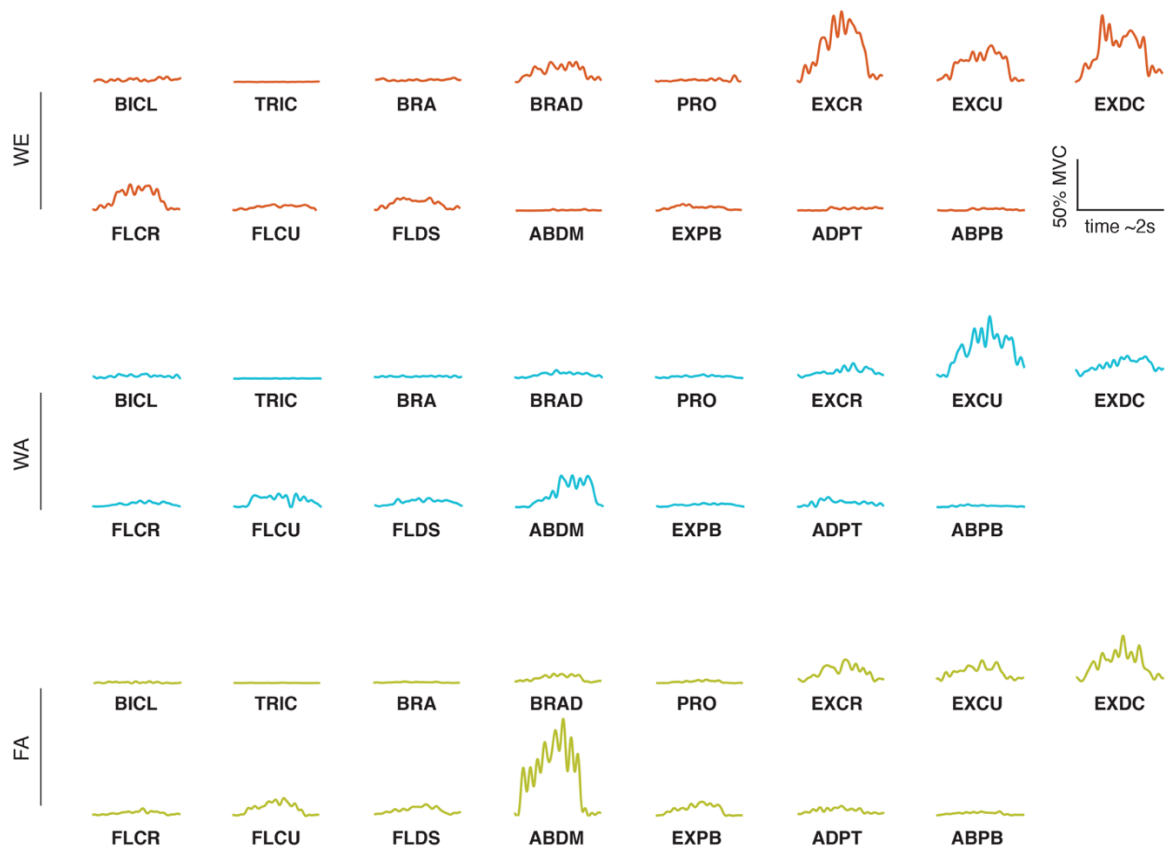


Figure C3 – EMG waveforms. Examples of muscular activations during one repetition of the three movements (WE = wrist extension, WA = wrist adduction, FA = finger abduction). Each waveform represents the activity of one muscle (EMG activity is displayed on the y-axis in percentage of the Maximum Voluntary Contraction, and x-axis corresponds to the duration of the movement, i.e., two seconds). BICL = biceps brachii long head, TRIC = triceps brachii long head, BRA = brachialis, BRAD = brachioradialis, PRO = pronator teres, EXCR = extensor carpi radialis, EXCU = extensor carpi ulnaris, EXDC = extensor digitorum communis, FLCR = flexor carpi radialis, FLCU = flexor carpi ulnaris, FLDS = flexor digitorum superficialis, ABDM = abductor digiti minimi, EXPB = extensor pollicis brevis, ADPT = adductor pollicis transversus, ABPB = abductor pollicis brevis.

Table C2 – Summary of group activity (Phase 2). Reported coordinates are in the PAM50 template space

	# voxels	p	COG (x)	COG (y)	COG (z)
WE	2719	0.00235	67.7	70.7	828
WA	5133	3.81e-05	69.5	70.6	773
FA	3827	0.000339	73.1	70.8	785

Table C3 – Summary of group activity (Phase 3 - MVPA). Reported coordinates are in the PAM50 template space

	# voxels	p	COG (x)	COG (y)	COG (z)
WE	5270	6.56e-07	70.8	69.8	797
WA	5767	5.96e-08	71.5	70.2	773
FA	4777	1.01e-06	70.2	70.5	740

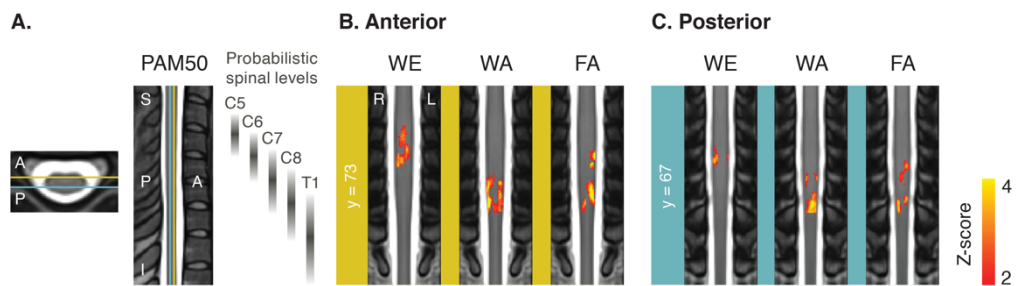


Figure C4 – Group activation maps. **A.** PAM50 template (De Leener *et al.*, 2018), where selected anterior and posterior slices are indicated. **B.** Group maps (anterior hemicord) for the contrast task VS baseline (WE = wrist extension, WA = wrist adduction, FA = finger abduction). Maps are thresholded at a Z-score > 2 (cluster-defining threshold of $p < 0.01$) and normalized to the PAM50 template (De Leener *et al.*, 2018). Only a region from C5 to C8 is considered (imaged in all subjects). Sagittal views are presented, with the same slice shown for all movements. **C.** Group maps (posterior hemicord). S = superior, I = inferior, L = left, R = right, A = anterior, P = posterior.

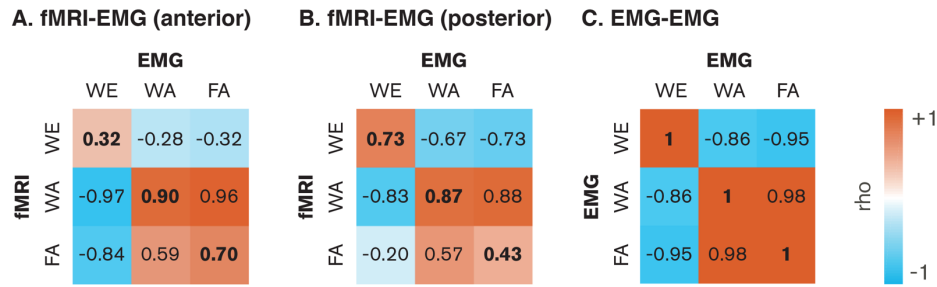


Figure C5 – Similarity of rostrocaudal profiles. Pearson's correlation coefficients between the rostrocaudal profiles related to the three different movements (WE = wrist extension, WA = wrist adduction, FA = finger abduction), for the following conditions: **A.** Between the EMG-derived profiles and the fMRI-derived profiles (anterior, or motor, side of the spinal cord only), **B.** Between the EMG-derived profiles and the fMRI-derived profiles (posterior, or sensory, side of the spinal cord only), **C.** Between the EMG-derived profiles.

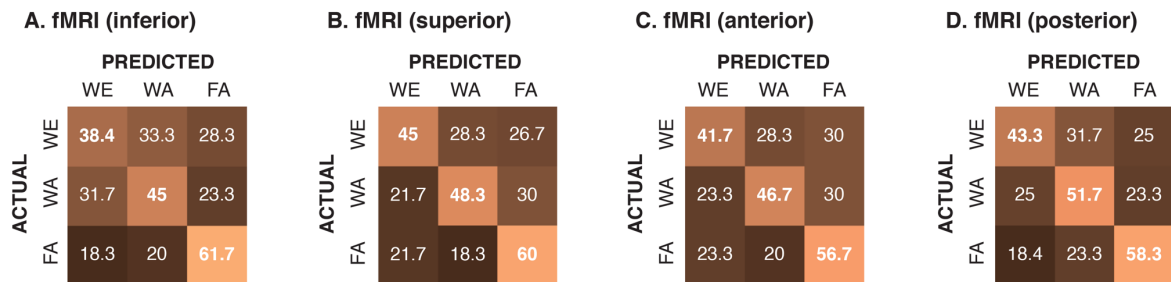


Figure C6 – Average decoding accuracy. Each subject performed 10 repetitions of each movement. EMG-derived spinal maps were computed for each repetition and averaged over time to keep only the spatial information (i.e., five features per sample, corresponding to the mean activity over time in the spinal levels from C5 to T1). Classification was performed in each subject using an LDA classifier (leave-one-movement-out cross validation), using only the voxels included in specific masks: **A.** Inferior region of the spinal cord **B.** Superior region of the spinal cord. **C.** Anterior (motor) hemicord **D.** Posterior (sensory) hemicord. All values are reported in percentage. WE = wrist extension, WA = wrist adduction, FA = finger abduction.

D. Supplementary material for Chapter 6

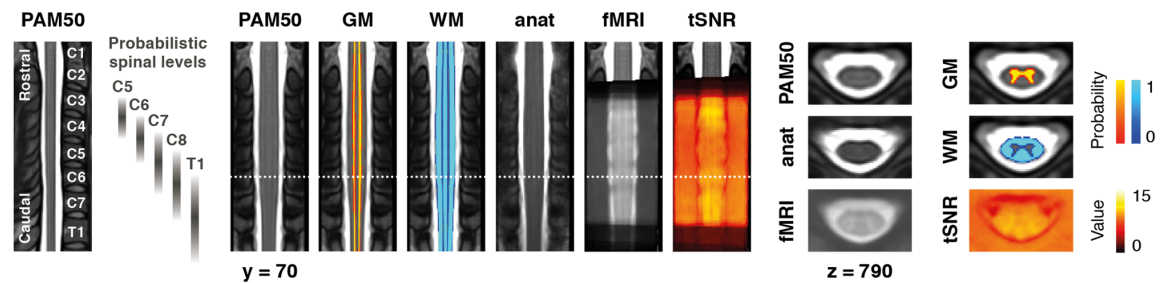
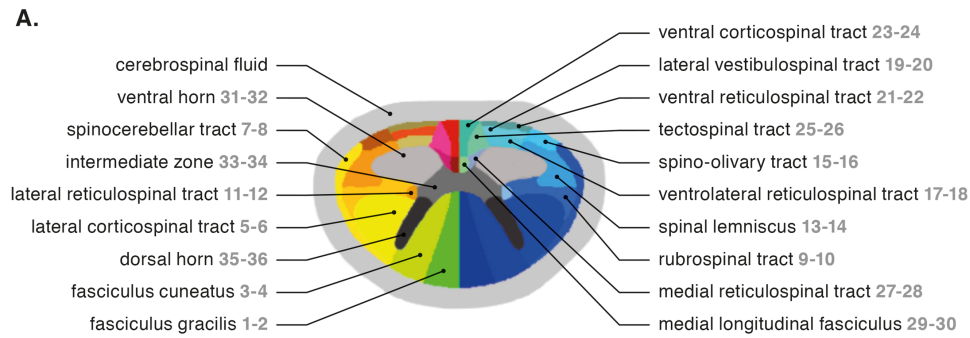


Figure D1 – Assessment of the normalization quality. Coronal views of the PAM50 template (De Leener *et al.*, 2018), the mean normalized anatomical image, the mean normalized functional image and the mean normalized temporal signal-to-noise ratio (tSNR, following motion correction) map are presented, along with example axial slices. The probabilistic maps of the grey matter (GM) and the white matter (WM) are also provided as references.

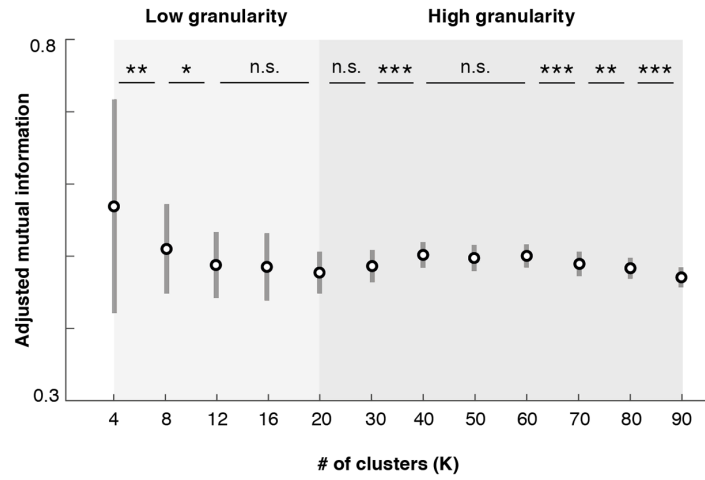


B.

#	ATLAS REGION	FUNCTION
1-2	fasciculus gracilis	touch, pressure, vibration, proprioception (lower body)
3-4	fasciculus cuneatus	touch, pressure, vibration, proprioception (upper body)
5-6	lateral corticospinal tract	descending motor pathway (distal muscles – e.g., limbs)
7-8	spinocerebellar tract	proprioception (posture and limb movement)
9-10	rubrospinal tract	facilitates flexor and inhibits extensor muscle groups
11-12	lateral reticulospinal tract	facilitates antigravity muscles
13-14	spinal lemniscus	touch, pressure, vibration, proprioception
15-16	spino-olivary tract	proprioception, balance
17-18	ventrolateral reticulospinal tract	facilitates/inhibits muscle groups (locomotion, posture)
19-20	lateral vestibulospinal tract	facilitates antigravity muscles
21-22	ventral reticulospinal tract	facilitates/inhibits muscle groups (locomotion, posture)
23-24	ventral corticospinal tract	descending motor pathway (proximal muscles – e.g., trunk)
25-26	tectospinal tract	reflex postural movements (e.g., if visual or auditory stimuli)
27-28	medial reticulospinal tract	facilitates/inhibits muscle groups (locomotion, posture)
29-30	medial longitudinal fasciculus	head position relative to eye movement
31-32	ventral horns	muscle control
33-34	intermediate zone	various
35-36	dorsal horns	sensory input

Figure D2 – Atlas regions. **A.** Schematic representation of the spinal cord (axial view) with the different regions of interest indicated (adapted with permission from Lévy *et al.*, 2015). The numbers correspond to the ones used in Figure D5 (note that odd numbers refer to regions on the left side, while even numbers are found on the right side). **B.** Main functional roles of each atlas region (Darby and Frysztak, 2013).

A. Clustering stability



B. Correspondence with atlas

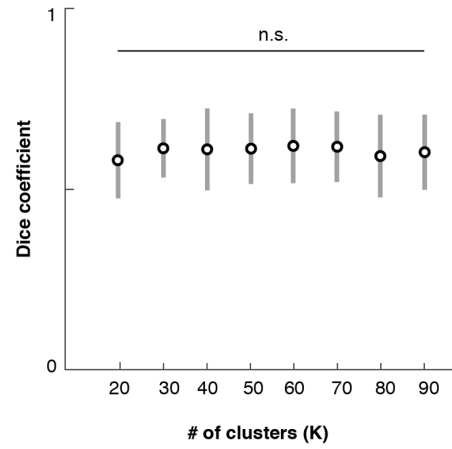
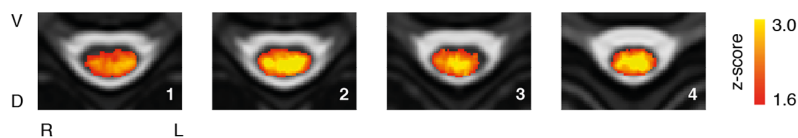


Figure D3 – Selection of the number of iCAPs. **A.** In order to assess the reproducibility of the clustering for different values of K (i.e., different numbers of iCAPs), we employed a subsampling scheme, where the clustering was repeated 100 times using random subsets of the data (10 subjects in each repetition). For each repetition, clustering of the significant innovation frames was performed for (i) low granularity K values, from 4 to 20, using multiple of the number of spinal levels (i.e., four); and (ii) high granularity K values, ranging from 20 to 90, in steps of 10, in order to cover a wide range of potential fine-grained subdivisions. The stability of the clustering solutions was then evaluated using the adjusted mutual information (AMI) (Vinh *et al.*, 2010) between the assignments in each subset and the assignments obtained for the full dataset (i.e., for the 19 subjects). Using repeated measures ANOVA, we confirmed that reproducibility was significantly different between K values, both within the low granularity ($F(4,396) = 25.57$, $p < 0.001$) and the high granularity ($F(7,693) = 47.50$, $p < 0.001$) ranges. Post-hoc Tukey tests highlighted a maximum for low K values, at $K = 4$ (AMI of 0.57, significantly different from subsequent Ks, $p < 0.01$). Furthermore, reproducibility increased again from $K = 30$ and reached a high-granularity maximum at $K = 40$ (AMI of 0.50, no significant difference with $K = 50$ or 60), to subsequently decrease from $K = 70$ ($p < 0.001$). $K = 40$ was selected for fine-grained analyses, as this value was the most parsimonious and stable in the explored range. Mean \pm SD over the 100 repetitions of the clustering are presented. **B.** The correspondence with the atlas was evaluated by means of Dice coefficients, for the high-granularity clustering solutions obtained using the full dataset. An ANOVA indicated that there was no significant difference between K values ($F(7,432) = 0.5$, $p = 0.84$). These findings corroborated the stability of the observed organization, highlighting that the correspondence with the atlas was preserved for different iCAP choices and not coincidental to the selected K value. This provided additional support in favor of the robustness of our approach, underlining its potential to reliably uncover meaningful neuroanatomical structures. Mean \pm SD over iCAPs are presented. n.s. = not significant, * $p < 0.05$, ** $p < 0.01$, *** $p < 0.001$

A. Low granularity (K=4)



B. High granularity (K=40)

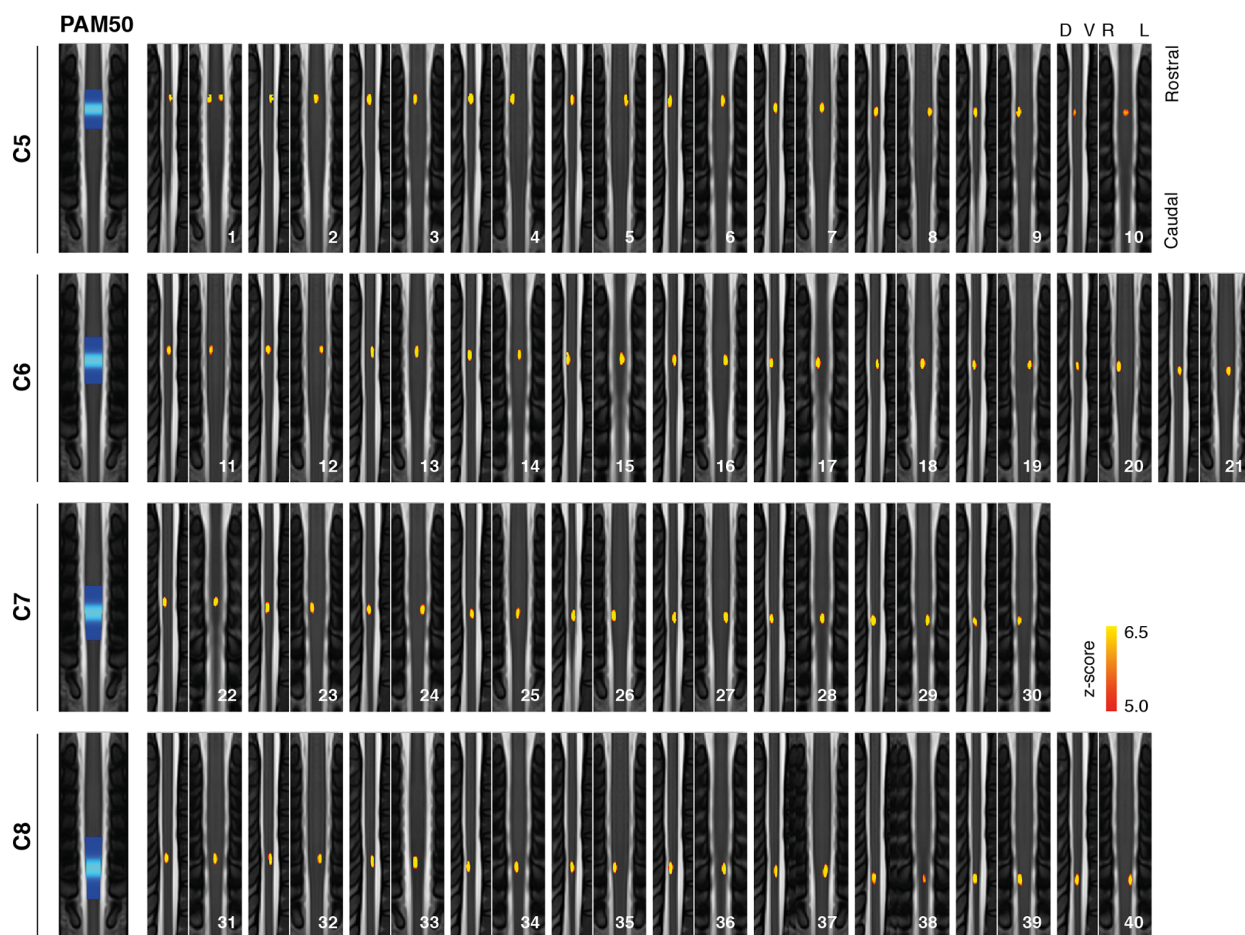
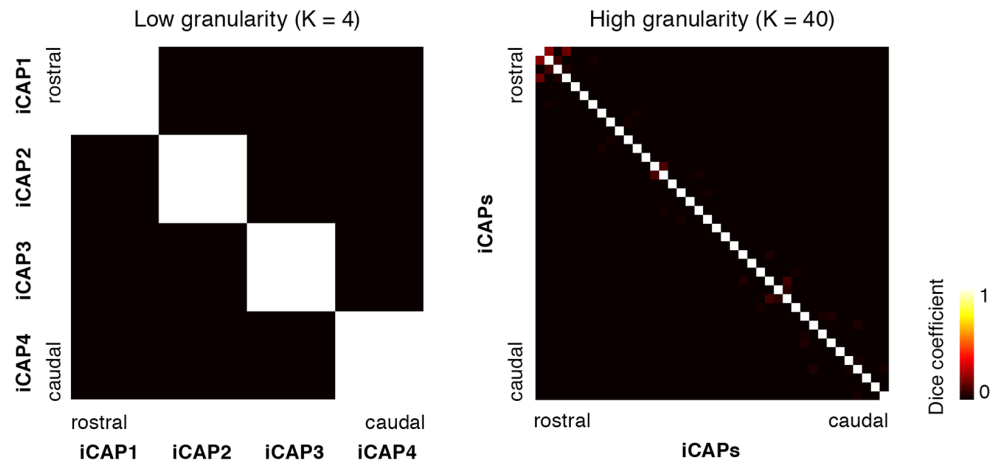


Figure D4 – iCAPs spatial patterns. **A.** Axial views of the four low-granularity iCAPs. Coronal and sagittal views are presented in Figure 6.2. **B.** Coronal and sagittal views of the 40 high-granularity iCAPs. Spinal levels are provided as a reference (blue maps in the left panel) (De Leener *et al.*, 2017). Thresholded iCAP maps are overlaid onto the PAM50 template (De Leener *et al.*, 2018). ICAPs numbers are indicated in the bottom right corners. L = left, R = right, D = dorsal, V = ventral.

A. Spatial overlap between iCAPs



B. Distribution of voxels in spinal levels and atlas regions

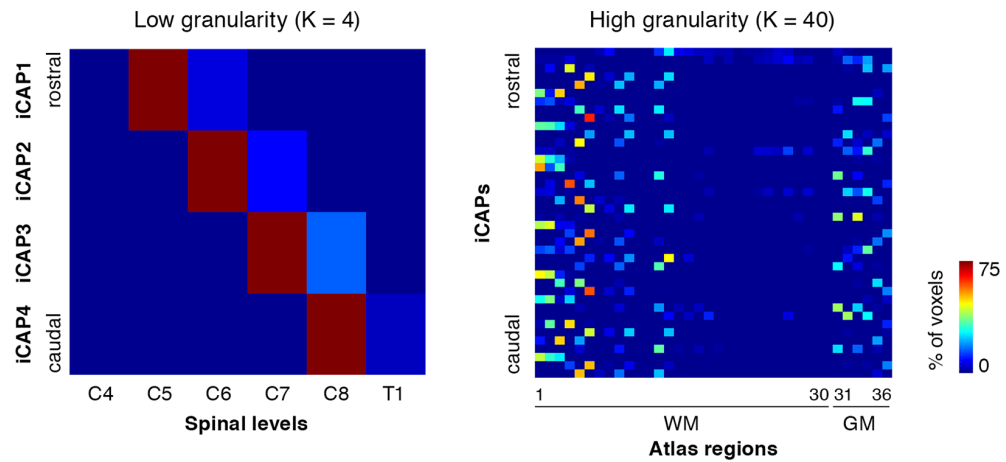
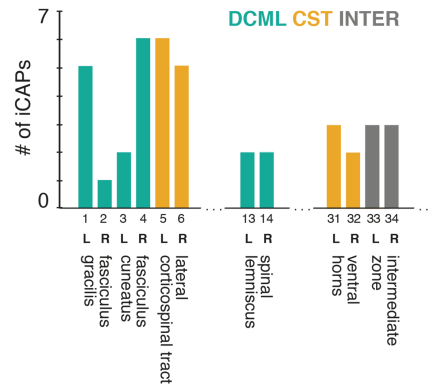


Figure D5 – iCAPs spatial properties. **A. Spatial overlap between iCAPs.** We computed the Dice coefficients between iCAP maps, thus highlighting a very limited spatial overlap between the different components. **B. iCAPs voxel distribution.** We computed the distributions of the voxel content of each iCAP into each spinal level (low granularity) or atlas region (high granularity) (i.e., percentage of voxels in each region, as defined by the Spinal Cord Toolbox (De Leener *et al.*, 2017)). The numbers of the atlas regions correspond to the ones presented in Figure D2. WM = white matter, GM = grey matter. These analyses are done for both levels of granularity (K = 4, low granularity, and K = 40, high granularity).

A. Part 1



B. Part 2

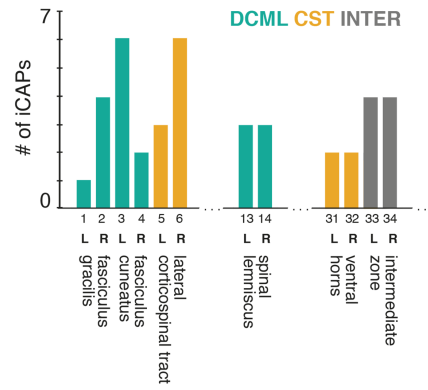


Figure D6 – Consistency of neural pathways. In order to evaluate the stability of the iCAPs spatial maps, the dataset was split into two equal parts, in which iCAPs were computed independently. The neuroanatomic identities of the iCAPs from both sets were then investigated (see Figure D2). The same atlas regions are found in Part 1 (A.) and Part 2 (B.), indicating that the same neural pathways (DCML, CST and INTER) are present throughout the experiment.

E. Supplementary material for Chapter 7

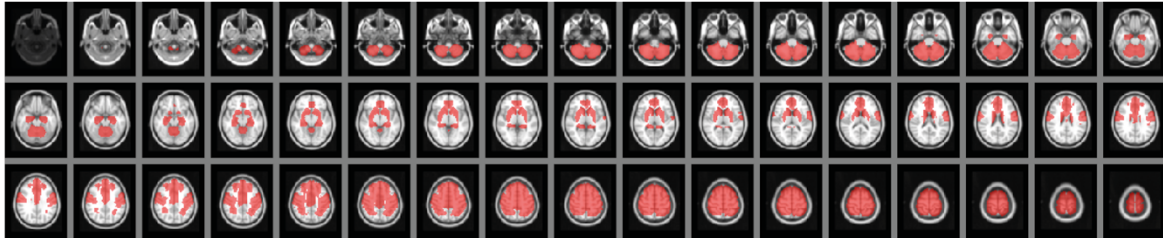


Figure E1 - Regions included in the brain mask. In order to limit the analysis to regions known to be involved in motor control and motor learning, the following regions were selected for the analysis at the level of the brain: accumbens, anterior cingulate cortex, caudate, cerebellum, hippocampus, primary motor cortex, premotor cortex, putamen, primary somatosensory cortex, superior frontal gyrus and superior parietal lobule. They are highlighted in red on the MNI template.

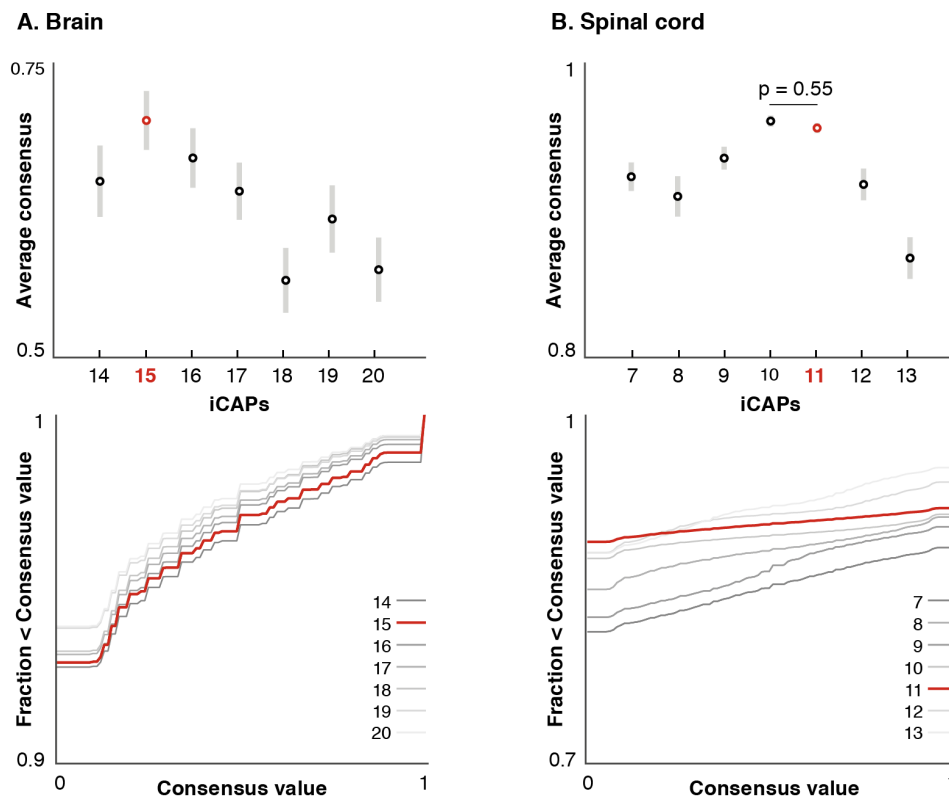


Figure E2 – Consensus clustering. The selection of the number of iCAPs was based on consensus clustering measures, as introduced in (Monti *et al.*, 2003), and performed independently for the brain and the spinal cord. The upper panels show the mean consensus values per cluster, which should be equal to 1 in case of perfect consensus. The lower panels correspond to the cumulative distribution function (CDF) of values in the consensus matrices obtained for different number of iCAPs (i.e., different K values). In an ideal clustering

scenario, the CSF should display an horizontal line, with values only distributed between 0 (two frames never clustered together) or 1 (two frames always clustered together). **A.** Previously, 17 iCAPs were used to decompose brain activity using iCAPs (Zöller *et al.*, 2019). In order to obtain a similar level of details, we assessed the clustering consensus around this value (± 3 , from 14 to 20). This supported the choice of $K_{BR} = 15$ for our analyses. **B.** Considering that the region imaged in spinal cord covered five spinal levels, we explored a range going from 7 to 13 (10 ± 3), in order to possibly look at dorsal and ventral components. Both $K_{SC} = 10$ and $K_{SC} = 11$ appeared as reasonable options (no significant difference). The latter was selected after visual inspection of the components (better subdivision of spinal levels into dorsal and ventral components).

Table E1 – Regions present in brain iCAPs. Based on FSL atlases. Structures are observed bilaterally, unless otherwise specified.

iCAP	Regions
1	Basal ganglia (putamen, caudate, accumbens), ACC, hippocampus
2	ACC, S1, Middle frontal gyrus
3	Cerebellum Crus I, II, Vermis VIIIa
4	Inferior / Superior parietal lobule, Middle / Superior frontal gyrus
5	Anterior intraparietal sulcus, Superior parietal lobule
6	M1 (L), S1 (L), PMC, Superior parietal lobule, Cerebellum (R) V, VI, Vermis VIIIa
7	Cerebellum V, VI, Vermis VIIb
8	Cerebellum VI, Crus I, Vermis Crus II, Vermis VI
9	PMC, M1, S1
10	Superior parietal lobule, PMC
11	ACC, Paracingulate gyrus, Caudate, Accumbens
12	ACC, Paracingulate gyrus
13	Hippocampus, Cerebellum I-V
14	Cerebellum VII-IX, Crus II, Vermis VIII, IX
15	M1, S1

F. Supplementary material for Chapter 8

Table F1 – Demographics of stroke patients (study 1), MAS = Modified Ashworth Scale (upper limb muscles)

Subject	Age	Gender	Affected hemisphere	MAS /48 (3 weeks)	MAS /48 (3 months)
P01	74	Male	Right	5	1.5
P02	68	Male	Left	5	8
P03	82	Male	Left	8	2.5
P04	69	Male	Right	0	0
P05	72	Male	Left	2	0
P06	87	Female	Right	2	2
P07	40	Male	Left	0	0
P08	70	Female	Right	5	2
P09	64	Male	Right	5	6

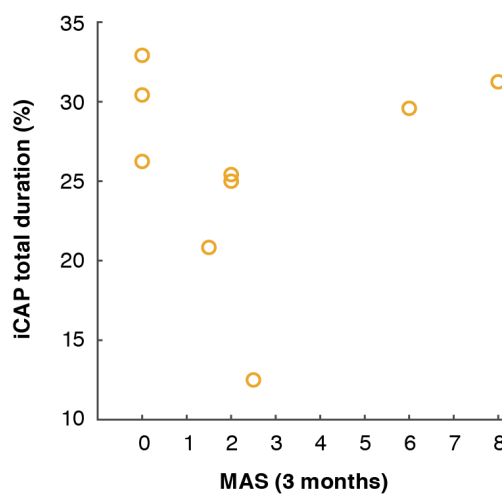


Figure F1 – We attempted to correlate the total duration of iCAP 33 with spasticity at 3 months following stroke (Study 1). No significant correlation was reported ($\rho = 0.13$, $p = 0.74$).

References

- Ahuja, C. S., Wilson, J. R., Nori, S., Kotter, M. R. N., Druschel, C., Curt, A. and Fehlings, M. G. (2017) 'Traumatic spinal cord injury', *Nature Reviews Disease Primers*, 3. doi: 10.1038/nrdp.2017.18.
- Albouy, G., King, B. R., Maquet, P. and Doyon, J. (2013) 'Hippocampus and striatum: Dynamics and interaction during acquisition and sleep-related motor sequence memory consolidation', *Hippocampus*, 23(11), pp. 985–1004. doi: 10.1002/hipo.22183.
- Alizadeh, M., Intintolo, A., Middleton, D. M., Conklin, C. J., Faro, S. H., Mulcahey, M. J. and Mohamed, F. B. (2017) 'Reduced FOV diffusion tensor MR imaging and fiber tractography of pediatric cervical spinal cord injury', *Spinal Cord*, 55(3), pp. 314–320. doi: 10.1038/sc.2016.121.
- Allali, G., Blumen, H. M., Devanne, H., Pirondini, E., Delval, A. and Van De Ville, D. (2018) 'Brain imaging of locomotion in neurological conditions', *Neurophysiologie Clinique*, 48(6), pp. 337–359. doi: 10.1016/j.neucli.2018.10.004.
- Allred, R. P. and Jones, T. A. (2008) 'Experience--a double edged sword for restorative neural plasticity after brain damage', *Future neurology*, 3(2), pp. 189–198. doi: 10.2217/14796708.3.2.189.
- Alstermark, B. and Isa, T. (2012) 'Circuits for Skilled Reaching and Grasping', *Annual Review of Neuroscience*, 35(1), pp. 559–578. doi: 10.1146/annurev-neuro-062111-150527.
- Anderson, M. J. and Robinson, J. (2001) 'Permutation Tests for Linear Models', *Australian & New Zealand Journal of Statistics*, 43(1), pp. 75–88. doi: 10.1111/1467-842X.00156.
- Andersson, J., Jenkinson, M. and Smith, S. (2007) 'Non-linear registration, aka spatial normalisation.', *fMRIB technical report TR07JA2*.
- Anne, S., M., K. C., Olivier, L., R., L. A. and M., V. J. (2019) 'Systematic Review on Kinematic Assessments of Upper Limb Movements After Stroke', *Stroke*, 50(3), pp. 718–727. doi: 10.1161/STROKEAHA.118.023531.
- Arber, S. and Costa, R. M. (2018) 'Connecting neuronal circuits for movement', *Science*, 360(6396), pp. 1403–1404. doi: 10.1126/science.aat5994.
- Arthurs, O. J. and Boniface, S. (2002) 'How well do we understand the neural origins of the fMRI BOLD signal?', 25(1), pp. 27–31.
- Attwell, D., Buchan, A. M., Charpak, S., Lauritzen, M., Macvicar, B. a and Newman, E. a (2010) 'Glial and neuronal control of brain blood flow.', *Nature*, 468(7321), pp. 232–43. doi: 10.1038/nature09613.
- Backes, W. H., Mess, W. H. and Wilmink, J. T. (2001) 'Functional MR Imaging of the Cervical Spinal Cord by Use of Median Nerve Stimulation and Fist Clenching', *American Journal of Neuroradiology*, 22(December), pp. 1854–1859.
- Badesa, F. J., Morales, R., Garcia-Aracil, N. M., Sabater, J. M., Zollo, L., Papaleo, E. and Guglielmelli, E. (2016)

'Dynamic Adaptive System for Robot-Assisted Motion Rehabilitation', *IEEE Systems Journal*, 10(3), pp. 984–991. doi: 10.1109/JSYST.2014.2318594.

Baker, S. N., Zaaïmi, B., Fisher, K. M., Edgley, S. A. and Soteropoulos, D. S. (2015) *Pathways mediating functional recovery*, *Progress in Brain Research*. doi: 10.1016/bs.pbr.2014.12.010.

Balasubramanian, S., Melendez-Calderon, A. and Burdet, E. (2012) 'A robust and sensitive metric for quantifying movement smoothness', *IEEE Transactions on Biomedical Engineering*, 59(8), pp. 2126–2136. doi: 10.1109/TBME.2011.2179545.

Barbara, J. G. and Clarac, F. (2011) 'Historical concepts on the relations between nerves and muscles', *Brain Research*, 1409, pp. 3–22. doi: 10.1016/j.brainres.2011.06.009.

Barra, B., Roux, C., Kaeser, M., Schiavone, G., Lacour, S. P., Bloch, J., Courtine, G., Rouiller, E. M., Schmidlin, E. and Capogrosso, M. (2018) 'Selective Recruitment of Arm Motoneurons in Nonhuman Primates Using Epidural Electrical Stimulation of the Cervical Spinal Cord', in *2018 40th Annual International Conference of the IEEE Engineering in Medicine and Biology Society (EMBC)*, pp. 1424–1427. doi: 10.1109/EMBC.2018.8512554.

Barry, R. L., Conrad, B. N., Smith, S. A. and Gore, J. C. (2018a) 'A practical protocol for measurements of spinal cord functional connectivity', *Scientific Reports*, 8(1), pp. 1–10. doi: 10.1038/s41598-018-34841-6.

Barry, R. L., Rogers, B. P., Conrad, B. N., Smith, S. a and Gore, J. C. (2016) 'Reproducibility of resting state spinal cord networks in healthy volunteers at 7 Tesla.', *NeuroImage*, 133, pp. 31–40. doi: 10.1016/j.neuroimage.2016.02.058.

Barry, R. L., Smith, S. A., Dula, A. N. and Gore, J. C. (2014) 'Resting state functional connectivity in the human spinal cord', *eLIFE*, pp. 1–15. doi: 10.7554/eLife.02812.

Barry, R. L., Vannesjo, S. J., By, S., Gore, J. C. and Smith, S. A. (2018b) 'Spinal cord MRI at 7T', *NeuroImage*, 168, pp. 437–451. doi: <https://doi.org/10.1016/j.neuroimage.2017.07.003>.

Barth, M., Breuer, F., Koopmans, P. J., Norris, D. G. and Poser, B. A. (2016) 'Simultaneous multislice (SMS) imaging techniques', *Magnetic Resonance in Medicine*, 75(1), pp. 63–81. doi: 10.1002/mrm.25897.

Beckmann, C. F., DeLuca, M., Devlin, J. T. and Smith, S. M. (2005) 'Investigations into resting-state connectivity using independent component analysis.', *Philosophical transactions of the Royal Society of London. Series B, Biological sciences*, 360(1457), pp. 1001–13. doi: 10.1098/rstb.2005.1634.

Beckmann, C. F. and Smith, S. M. (2004) 'Probabilistic independent component analysis for functional magnetic resonance imaging', *IEEE Transactions on Medical Imaging*, 23(2), pp. 137–152. doi: 10.1109/TMI.2003.822821.

Behzadi, Y., Restom, K., Liau, J. and Liu, T. T. (2007) 'A component based noise correction method (CompCor) for BOLD and perfusion based fMRI.', *NeuroImage*, 37(1), pp. 90–101. doi: 10.1016/j.neuroimage.2007.04.042.

Belfatto, A., Scano, A., Chiavenna, A., Mastropietro, A., Mrakic-Sposta, S., Pittaccio, S., Tosatti, L. M., Molteni, F. and Rizzo, G. (2018) 'A multiparameter approach to evaluate post-stroke patients: An application on robotic rehabilitation', *Applied Sciences*, 8(11). doi: 10.3390/app8112248.

Bensmail, D., Robertson, J., Fermanian, C. and Roby-Brami, A. (2009) 'Botulinum Toxin to Treat Upper-Limb Spasticity in Hemiparetic Patients: Grasp Strategies and Kinematics of Reach-to-Grasp Movements', *Neurorehabilitation and Neural Repair*, 24(2), pp. 141–151. doi: 10.1177/1545968309347683.

Bergamasco, M., Salsedo, F. and Lenzo, B. (2013) 'An exoskeleton structure for physical interaction with

a human being’.

Berger, D. J., Masciullo, M., Molinari, M., Lacquaniti, F. and d’Avella, A. (2020) ‘Does the cerebellum shape the spatiotemporal organization of muscle patterns? Insights from subjects with cerebellar ataxias’, *Journal of Neurophysiology*, 123(5), pp. 1691–1710. doi: 10.1152/jn.00657.2018.

Bertrand, A. M., Fournier, K., Wick Brasey, M.-G., Kaiser, M.-L., Frischknecht, R. and Diserens, K. (2015) ‘Reliability of maximal grip strength measurements and grip strength recovery following a stroke’, *Journal of Hand Therapy*, 28(4), pp. 356–363. doi: <https://doi.org/10.1016/j.jht.2015.04.004>.

Biernaskie, J. (2004) ‘Efficacy of Rehabilitative Experience Declines with Time after Focal Ischemic Brain Injury’, *Journal of Neuroscience*, 24(5), pp. 1245–1254. doi: 10.1523/JNEUROSCI.3834-03.2004.

Biswal, B. B. (2012) ‘Resting state fMRI: a personal history.’, *NeuroImage*, 62(2), pp. 938–44. doi: 10.1016/j.neuroimage.2012.01.090.

Bizzi, E. and Cheung, V. C. K. (2013) ‘The neural origin of muscle synergies ’, *Frontiers in Computational Neuroscience* , p. 51. Available at: <https://www.frontiersin.org/article/10.3389/fncom.2013.00051>.

Bolton, T. A. W., Morgenroth, E., Preti, M. G. and Van De Ville, D. (2020) ‘Tapping into Multi-Faceted Human Behavior and Psychopathology Using fMRI Brain Dynamics’, *Trends in Neurosciences*. doi: <https://doi.org/10.1016/j.tins.2020.06.005>.

Borton, D., Micera, S., Del R. Millán, J. and Courtine, G. (2013) ‘Personalized neuroprosthetics’, *Science Translational Medicine*, 5(210). doi: 10.1126/scitranslmed.3005968.

Bosecker, C., Dipietro, L., Volpe, B. and Igo Krebs, H. (2010) ‘Kinematic Robot-Based Evaluation Scales and Clinical Counterparts to Measure Upper Limb Motor Performance in Patients With Chronic Stroke’, *Neurorehabilitation and Neural Repair*, 24(1), pp. 62–69. doi: 10.1177/1545968309343214.

Bourbonnais, D., Vanden Noven, S., Carey, K. M. and Rymer, W. Z. (1989) ‘Abnormal spatial patterns of elbow muscle activation in hemiparetic human subjects’, *Brain*, 112(1), pp. 85–102. doi: 10.1093/brain/112.1.85.

Bouwman, C. J. C., Wilmink, J. T., Mess, W. H. and Backes, W. H. (2008) ‘Spinal cord functional MRI at 3 T: gradient echo echo-planar imaging versus turbo spin echo.’, *NeuroImage*, 43(2), pp. 288–96. doi: 10.1016/j.neuroimage.2008.07.024.

Bradnam, L., Stinear, C. and Byblow, W. (2013) ‘Ipsilateral Motor Pathways after Stroke: Implications for Non-Invasive Brain Stimulation’, *Frontiers in Human Neuroscience*, p. 184.

Britz, J., Van De Ville, D. and Michel, C. M. (2010) ‘BOLD correlates of EEG topography reveal rapid resting-state network dynamics’, *NeuroImage*, 52(4), pp. 1162–1170. doi: <https://doi.org/10.1016/j.neuroimage.2010.02.052>.

Brooks, J. C. W. (2014) ‘Chapter 4.2 - Physiological Noise Modeling and Analysis for Spinal Cord fMRI’, in Cohen-Adad, J. and Wheeler-Kingshott, C. (eds) *Quantitative imaging of the spinal cord*, pp. 240–257.

Brooks, J. C. W., Beckmann, C. F., Miller, K. L., Wise, R. G., Porro, C. A., Tracey, I. and Jenkinson, M. (2008) ‘Physiological noise modelling for spinal functional magnetic resonance imaging studies’, *Neuroimage*, 39, pp. 680–692. doi: 10.1016/j.neuroimage.2007.09.018.

Brunet, D., Murray, M. M. and Michel, C. M. (2011) ‘Spatiotemporal Analysis of Multichannel EEG: CARTOOL’, *Computational Intelligence and Neuroscience*, 2011, p. 813870. doi: 10.1155/2011/813870.

Brunnström, S. (1970) ‘Movement therapy in hemiplegia: a neurophysiological approach’, *Facts and comparisons*.

-
- Bulea, T. C., Kilicarslan, A., Ozdemir, R., Paloski, W. H. and Contreras-Vidal, J. L. (2013) 'Simultaneous Scalp Electroencephalography (EEG), Electromyography (EMG), and Whole-body Segmental Inertial Recording for Multi-modal Neural Decoding', *JoVE*, (77). doi: doi:10.3791/50602.
- Bullmore, E. T. and Bassett, D. S. (2011) 'Brain Graphs: Graphical Models of the Human Brain Connectome', *Annual Review of Clinical Psychology*, 7(1), pp. 113–140. doi: 10.1146/annurev-clinpsy-040510-143934.
- Buma, F., Kwakkel, G. and Ramsey, N. (2013) 'Understanding upper limb recovery after stroke.', *Restorative neurology and neuroscience*, 31(6), pp. 707–22. doi: 10.3233/RNN-130332.
- Burle, B., Spieser, L., Roger, C., Casini, L., Hasbroucq, T. and Vidal, F. (2015) 'Spatial and temporal resolutions of EEG: Is it really black and white? A scalp current density view', *International journal of psychophysiology : official journal of the International Organization of Psychophysiology*, 97(3), pp. 210–220. doi: 10.1016/j.ijpsycho.2015.05.004.
- Caballero-Gaudes, C. and Reynolds, R. C. (2017) 'Methods for cleaning the BOLD fMRI signal', *NeuroImage*, 154, pp. 128–149. doi: https://doi.org/10.1016/j.neuroimage.2016.12.018.
- Cadotte, D. W., Akbar, M. A., Fehlings, M. G., Stroman, P. W. and Cohen-Adad, J. (2018) 'What Has Been Learned from Magnetic Resonance Imaging Examination of the Injured Human Spinal Cord: A Canadian Perspective', *Journal of Neurotrauma*, 35(16), pp. 1942–1957. doi: 10.1089/neu.2018.5903.
- Cadotte, D. W., Cadotte, A., Cohen-Adad, J., Fleet, D., Livne, M., Wilson, J. R., Mikulis, D., Nugaeva, N. and Fehlings, M. G. (2015) 'Characterizing the location of spinal and vertebral levels in the human cervical spinal cord', *American Journal of Neuroradiology*, 36(4), pp. 803–810. doi: 10.3174/ajnr.A4192.
- Calhoun, V. D., Adali, T., Pearlson, G. D. and Pekar, J. J. (2001) 'A Method for Making Group Inferences from Functional MRI Data Using Independent Component Analysis', *Human Brain Mapping*, 14, pp. 140–151. doi: 10.1002/hbm.
- Capogrosso, M., Wenger, N., Raspopovic, S., Musienko, P., Beauparlant, J., Bassi Luciani, L., Courtine, G. and Micera, S. (2013) 'A Computational Model for Epidural Electrical Stimulation of Spinal Sensorimotor Circuits', *The Journal of Neuroscience*, 33(49). doi: 10.1523/JNEUROSCI.1688-13.2013.
- Cappellini, G., Ivanenko, Y. P., Dominici, N., Poppele, R. E. and Lacquaniti, F. (2010) 'Migration of Motor Pool Activity in the Spinal Cord Reflects Body Mechanics in Human Locomotion', *Journal of Neurophysiology*, 104(6), pp. 3064–3073.
- Di Carlo, A. (2009) 'Human and economic burden of stroke', *Oxford University Press*.
- Carod-Artal, J., Egido, J. A., Gonzalez, J. L. and Varela de Seijas, E. (2000) 'Quality of Life Among Stroke Survivors Evaluated 1 Year After Stroke : Experience of a Stroke Unit', *Stroke*, 31(12), pp. 2995–3000. doi: 10.1161/01.STR.31.12.2995.
- Carrera, E. and Tononi, G. (2014) 'Diaschisis: past, present, future', *Brain*, 137(9), pp. 2408–2422. doi: 10.1093/brain/awu101.
- Carter, A. R., Astafiev, S. V., Lang, C. E., Connor, L. T., Rengachary, J., Strube, M. J., Pope, D. L. W., Shulman, G. L. and Corbetta, M. (2010) 'Resting Interhemispheric Functional Magnetic Resonance Imaging Connectivity Predicts Performance after Stroke', *ANNALS of Neurology*, 67(3), pp. 365–375. doi: 10.1002/ana.21905.
- Castellanos, F. X., Di Martino, A., Craddock, R. C., Mehta, A. D. and Milham, M. P. (2013) 'Clinical applications of the functional connectome', *NeuroImage*, 80, pp. 527–540. doi: 10.1016/j.neuroimage.2013.04.083.
- Chen, L. M., Mishra, A., Yang, P.-F., Wang, F. and Gore, J. C. (2015) 'Injury alters intrinsic functional

- connectivity within the primate spinal cord.', *Proceedings of the National Academy of Sciences of the United States of America*, 112(19), pp. 5991–6. doi: 10.1073/pnas.1424106112.
- Cheung, V. C. K., Piron, L., Agostini, M., Silvoni, S., Turolla, A. and Bizzi, E. (2009) 'Stability of muscle synergies for voluntary actions after cortical stroke in humans', *Proceedings of the National Academy of Sciences of the United States of America*, 106(46), p. 19563–19568 NEUROSCIENCE.
- Cheung, V. C. K., Turolla, A., Agostini, M., Silvoni, S., Bennis, C. and Kasi, P. (2012) 'Muscle synergy patterns as physiological markers of motor cortical damage', *Proceedings of the International Society for Magnetic Resonance in Medicine*, 109(36), pp. 14652–14656. doi: 10.1073/pnas.1212056109/-/DCSupplemental.www.pnas.org/cgi/doi/10.1073/pnas.1212056109.
- Choe, A. S., Nebel, M. B., Barber, A. D., Cohen, J. R., Xu, Y., Pekar, J. J., Caffo, B. and Lindquist, M. A. (2017) 'Comparing test-retest reliability of dynamic functional connectivity methods', *NeuroImage*, 158, pp. 155–175. doi: <https://doi.org/10.1016/j.neuroimage.2017.07.005>.
- Choudhury, S., Shobhana, A., Singh, R., Sen, D., Anand, S. S., Shubham, S., Baker, M. R., Kumar, H. and Baker, S. N. (2019) 'The Relationship Between Enhanced Reticulospinal Outflow and Upper Limb Function in Chronic Stroke Patients', *Neurorehabilitation and Neural Repair*, 33(5), pp. 375–383. doi: 10.1177/1545968319836233.
- Christiansen, L., Lundbye-Jensen, J., Perez, M. A. and Nielsen, J. B. (2017) 'How plastic are human spinal cord motor circuitries?', *Experimental Brain Research*, 235(11), pp. 3243–3249. doi: 10.1007/s00221-017-5037-x.
- Cirstea, M. C. and Levin, M. F. (2000) 'Compensatory strategies for reaching in stroke', *Brain*, 123(5), pp. 940–953. doi: 10.1093/brain/123.5.940.
- Cirstea, M. C., Mitnitski, A. B., Feldman, A. G. and Levin, M. F. (2003) 'Interjoint coordination dynamics during reaching in stroke', *Experimental Brain Research*, 151(3), pp. 289–300. doi: 10.1007/s00221-003-1438-0.
- Clarke, P., Marshall, V., Black, S. E. and Colantonio, A. (2002) 'Findings From the Canadian Study of Health and Aging', *Stroke*, 33(4), pp. 1016–1021.
- Cohen-Adad, J. (2008) *PhD Thesis - Anatomic-functional magnetic resonance imaging of the spinal cord and its application to the characterization of spinal lesions in cats, Université de Montréal, Ecole Centrale de Paris*.
- Cohen-Adad, J., Mareyam, A., Keil, B., Polimeni, J. R. and Wald, L. L. (2011) '32-Channel RF coil optimized for brain and cervical spinal cord at 3 T', *Magnetic Resonance in Medicine*, 66(4), pp. 1198–1208.
- Cohen-Adad, J., Piché, M., Rainville, P., Benali, H. and Rossignol, S. (2007) 'Impact of realignment on spinal functional MRI time series', *Proceedings of the 29th Annual International Conference of the IEEE EMBS*, pp. 2126–2129.
- Cohen-Adad, J., Rossignol, S. and Hoge, R. D. (2009) 'Slice-by-slice motion correction in spinal cord fMRI: SliceCorr', in *Proceedings of the 17th Annual Meeting of the International Society for Magnetic Resonance in Medicine*.
- Cole, M. W., Bassett, D. S., Power, J. D., Braver, T. S. and Petersen, S. E. (2014) 'Intrinsic and task-evoked network architectures of the human brain', *Neuron*, 83(1), pp. 238–251. doi: 10.1016/j.neuron.2014.05.014.
- Cole, M. W., Ito, T., Schultz, D., Mill, R., Chen, R. and Cocuzza, C. (2019) 'Task activations produce spurious but systematic inflation of task functional connectivity estimates', *NeuroImage*, 189, pp. 1–18. doi: <https://doi.org/10.1016/j.neuroimage.2018.12.054>.

Colombo, R., Pisano, F., Delconte, C., Mazzone, A., Grioni, G., Castagna, M., Bazzini, G., Imarisio, C., Maggioni, G. and Pistarini, C. (2017) 'Comparison of exercise training effect with different robotic devices for upper limb rehabilitation: a retrospective study', *European journal of physical and rehabilitation medicine*, 53(2), p. 240—248. doi: 10.23736/s1973-9087.16.04297-0.

Colombo, R., Pisano, F., Mazzone, A., Delconte, C., Micera, S., Carrozza, M. C., Dario, P. and Minuco, G. (2007) 'Design strategies to improve patient motivation during robot-aided rehabilitation.', *Journal of neuroengineering and rehabilitation*, 4, p. 3. doi: 10.1186/1743-0003-4-3.

Colombo, R., Pisano, F., Micera, S., Mazzone, A., Delconte, C., Carrozza, M. C., Dario, P. and Minuco, G. (2008) 'Assessing mechanisms of recovery during robot-aided neurorehabilitation of the upper limb', *Neurorehabilitation and Neural Repair*, 22(1), pp. 50–63. doi: 10.1177/1545968307303401.

Colombo, R., Sterpi, I., Mazzone, A., Delconte, C., Minuco, G. and Pisano, F. (2010) 'Measuring changes of movement dynamics during robot-aided neurorehabilitation of stroke patients', *IEEE Transactions on Neural Systems and Rehabilitation Engineering*, 18(1), pp. 75–85. doi: 10.1109/TNSRE.2009.2028831.

Conrad, B. N., Barry, R. L., Rogers, B. P., Maki, S., Mishra, A., Thukral, S., Sriram, S., Bhatia, A., Pawate, S., Gore, J. C. and Smith, S. A. (2018) 'Multiple sclerosis lesions affect intrinsic functional connectivity of the spinal cord', *Brain*, 141(6), pp. 1650–1664. doi: 10.1093/brain/awy083.

Cooke, F. J., Blamire, A. M., Manners, D. N., Styles, P. and Rajagopalan, B. (2004) 'Quantitative proton magnetic resonance spectroscopy of the cervical spinal cord', *Magnetic Resonance in Medicine*, 51(6), pp. 1122–1128. doi: 10.1002/mrm.20084.

Coscia, M. (2011) 'Computational aspects of MN activity estimation : a case study with post-stroke subjects', *IEEE International Conference on Rehabilitation Robotics*, pp. 0–4.

Coscia, M., Monaco, V., Martelloni, C., Rossi, B., Chisari, C. and Micera, S. (2015) 'Muscle synergies and spinal maps are sensitive to the asymmetry induced by a unilateral stroke.', *Journal of neuroengineering and rehabilitation*, 12(39). doi: 10.1186/s12984-015-0031-7.

Coscia, M., Wessel, M. J., Chaudary, U., Millán, J. del R., Micera, S., Guggisberg, A., Vuadens, P., Donoghue, J., Birbaumer, N. and Hummel, F. C. (2019) 'Neurotechnology-aided interventions for upper limb motor rehabilitation in severe chronic stroke', *Brain*, 142(8), pp. 2182–2197. doi: 10.1093/brain/awz181.

Coutanche, M. N. and Thompson-Schill, S. L. (2012) 'The advantage of brief fMRI acquisition runs for multi-voxel pattern detection across runs', *NeuroImage*, 61(4), pp. 1113–1119. doi: 10.1016/j.neuroimage.2012.03.076.

Cramer, G. D. and Darby, S. A. (2014) *Clinical Anatomy of the Spine, Spinal Cord, and ANS*. doi: <https://doi.org/10.1016/B978-0-323-07954-9.02001-6>.

Cramer, S. C. (2008) 'Repairing the human brain after stroke: I. Mechanisms of spontaneous recovery', *Annals of Neurology*, 63(3), pp. 272–287. doi: 10.1002/ana.21393.

Cramer, S. C., Sur, M., Dobkin, B. H., O'Brien, C., Sanger, T. D., Trojanowski, J. Q., Rumsey, J. M., Hicks, R., Cameron, J., Chen, D., Chen, W. G., Cohen, L. G., deCharms, C., Duffy, C. J., Eden, G. F., Fetz, E. E., Filart, R., Freund, M., Grant, S. J., Haber, S., Kalivas, P. W., Kolb, B., Kramer, A. F., Lynch, M., Mayberg, H. S., McQuillen, P. S., Nitkin, R., Pascual-Leone, A., Reuter-Lorenz, P., Schiff, N., Sharma, A., Shekim, L., Stryker, M., Sullivan, E. V and Vinogradov, S. (2011) 'Harnessing neuroplasticity for clinical applications', *Brain*, 134(6), pp. 1591–1609. doi: 10.1093/brain/awr039.

Cunningham, H. A. and Pavel, M. (1991) 'Target axis effects under transformed visual-motor mappings', *Pictorial communication in real and virtual environment*, pp. 283–304.

D'Avella, A., Portone, A., Fernandez, L. and Lacquaniti, F. (2006) 'Control of fast-reaching movements by muscle synergy combinations', *Journal of Neuroscience*, 26(30), pp. 7791–7810. doi:

10.1523/JNEUROSCI.0830-06.2006.

D'Avella, A., Saltiel, P. and Bizzi, E. (2003) 'Combinations of muscle synergies in the construction of a natural motor behavior', *Nature Neuroscience*, 6(3), pp. 300–308. doi: 10.1038/nn1010.

Damoiseaux, J. S., Rombouts, S. A. R. B., Barkhof, F., Scheltens, P., Stam, C. J., Smith, S. M. and Beckmann, C. F. (2006) 'Consistent resting-state networks', (2).

Dancause, N. and Nudo, R. J. (2011) 'Chapter 15 - Shaping plasticity to enhance recovery after injury', in Green, A., Chapman, C. E., Kalaska, J. F., and Lepore, F. B. T. (eds) *Enhancing performance for action and perception*, pp. 273–295. doi: <https://doi.org/10.1016/B978-0-444-53355-5.00015-4>.

Darby, S. A. and Frysztak, R. J. (2013) *Neuroanatomy of the Spinal Cord*. Third Edit, *Clinical Anatomy of the Spine, Spinal Cord, and ANS*. Third Edit. doi: 10.1016/B978-0-323-07954-9.00009-8.

Dayan, E. and Cohen, L. G. (2011) 'Neuroplasticity subserving motor skill learning', *Neuron*, 72(3), pp. 443–454. doi: 10.1016/j.neuron.2011.10.008.

Dehghani, H., Weber, K. A., Batouli, S. A. H., Oghabian, M. A. and Khatibi, A. (2020) 'Evaluation and Optimization of Motion Correction in Spinal Cord fMRI Preprocessing', *bioRxiv*, p. 2020.05.20.103986. doi: 10.1101/2020.05.20.103986.

Delagi, E. and Perotto, A. (1980) *Anatomic guide for the electromyographer: the limbs and trunk*.

Delorme, A. and Makeig, S. (2004) 'EEGLAB: an open source toolbox for analysis of single-trial EEG dynamics including independent component analysis', *Journal of Neuroscience Methods*, 134(1), pp. 9–21. doi: <https://doi.org/10.1016/j.jneumeth.2003.10.009>.

Demarin, V., Morović, S. and Béné, R. (2014) 'Neuroplasticity', *Periodicum Biologorum*, 116(2), pp. 209–211.

Devonshire, I. M., Papadakis, N. G., Port, M., Berwick, J., Kennerley, A. J., Mayhew, J. E. W. and Overton, P. G. (2012) 'Neurovascular coupling is brain region-dependent', *NeuroImage*, 59(3), pp. 1997–2006. doi: 10.1016/j.neuroimage.2011.09.050.

Dice, L. R. (1945) 'Measures of the Amount of Ecologic Association Between Species', *Ecology*, 26(3), pp. 297–302. doi: 10.2307/1932409.

Diedrichsen, J. and Kornysheva, K. (2015) 'Motor skill learning between selection and execution', *Trends in Cognitive Sciences*, 19(4), pp. 227–233. doi: <https://doi.org/10.1016/j.tics.2015.02.003>.

Ding, Z., Huang, Y., Bailey, S. K., Gao, Y., Cutting, L. E., Rogers, B. P., Newton, A. T. and Gore, J. C. (2018) 'Detection of synchronous brain activity in white matter tracts at rest and under functional loading', *Proceedings of the National Academy of Sciences of the United States of America*, 115(3), pp. 595–600. doi: 10.1073/pnas.1711567115.

Dipietro, L., Krebs, H. I., Fasoli, S. E., Volpe, B. T. and Hogan, N. (2009) 'Submovement changes characterize generalization of motor recovery after stroke', *Cortex*, 45(3), pp. 318–324. doi: 10.1016/j.cortex.2008.02.008.

Dipietro, L., Krebs, H. I., Fasoli, S. E., Volpe, B. T., Stein, J., Bever, C. and Hogan, N. (2007) 'Changing Motor Synergies in Chronic Stroke', *Journal of Neurophysiology*, 98(2), pp. 757–768. doi: 10.1152/jn.01295.2006.

Dipietro, L., Poizner, H. and Krebs, H. I. (2014) 'Spatiotemporal dynamics of online motor correction processing revealed by high-density electroencephalography', *Journal of cognitive neuroscience*. 2014/02/24, 26(9), pp. 1966–1980. doi: 10.1162/jocn_a_00593.

Dobkin, B. H. (2004) 'Strategies for stroke rehabilitation', *Lancet Neurology*, 3(9), pp. 528–536. doi: 10.1016/S1474-4422(04)00851-8.

Dobkin, B. H. (2009) 'Motor rehabilitation after stroke, traumatic brain, and spinal cord injury: common denominators within recent clinical trials Bruce', *Current Opinion in Neurology*, 22(6), pp. 563–569. doi: 10.1097/WCO.0b013e3283314b11.Motor.

Donnan, G. A., Fisher, M., Macleod, M. and Davis, S. M. (2008) 'Stroke', *Lancet*, 371(9624), pp. 1612–23. doi: 10.1016/S0140-6736(08)60694-7.

Dou, Z. and Yang, L. (2019) 'The Application of Functional Magnetic Resonance Imaging in Neuropathic Pain', *Medical Imaging - Principles and Applications*, October.

Doyon, J. and Benali, H. (2005) 'Reorganization and plasticity in the adult brain during learning of motor skills', *Current Opinion in Neurobiology*, 15(2), pp. 161–167. doi: <https://doi.org/10.1016/j.conb.2005.03.004>.

Doyon, J., Gabbitov, E., Vahdat, S., Lungu, O. and Boutin, A. (2018) 'Current issues related to motor sequence learning in humans', *Current Opinion in Behavioral Sciences*, 20, pp. 89–97. doi: 10.1016/j.cobeha.2017.11.012.

Doyon, J., Penhune, V. and Ungerleider, L. G. (2003) 'Distinct contribution of the cortico-striatal and cortico-cerebellar systems to motor skill learning', *Neuropsychologia*, 41(3), pp. 252–262. doi: [https://doi.org/10.1016/S0028-3932\(02\)00158-6](https://doi.org/10.1016/S0028-3932(02)00158-6).

Dubois, J. and Adolphs, R. (2016) 'Building a Science of Individual Differences from fMRI', *Trends in Cognitive Sciences*, 20(6), pp. 425–443. doi: 10.1016/j.tics.2016.03.014.

Dubovik, S., Pignat, J.-M., Ptak, R., Aboulafia, T., Allet, L., Gillabert, N., Magnin, C., Albert, F., Momjian-Mayor, I., Nahum, L., Lascano, A. M., Michel, C. M., Schnider, A. and Guggisberg, A. G. (2012) 'The behavioral significance of coherent resting-state oscillations after stroke.', *NeuroImage*, 61(1), pp. 249–57. doi: 10.1016/j.neuroimage.2012.03.024.

Duret, C., Grosmaire, A.-G. and Krebs, H. I. (2019) 'Robot-Assisted Therapy in Upper Extremity Hemiparesis: Overview of an Evidence-Based Approach ', *Frontiers in Neurology* , p. 412. Available at: <https://www.frontiersin.org/article/10.3389/fneur.2019.00412>.

Ehrsson, H. H., Kuhtz-Buschbeck, J. P. and Forssberg, H. (2002) 'Brain Regions Controlling Nonsynergistic versus Synergistic Movement of the Digits: A Functional Magnetic Resonance Imaging Study', *Journal of Neuroscience*, 22(12), pp. 5074–5080. doi: 10.1523/jneurosci.22-12-05074.2002.

Eippert, F., Finsterbusch, J., Bingel, U. and Büchel, C. (2009) 'Direct Evidence for Spinal Cord Involvement in Placebo Analgesia', *Science*, 326(October), p. 2009.

Eippert, F., Kong, Y., Jenkinson, M., Tracey, I. and Brooks, J. C. W. (2017a) 'Denoising spinal cord fMRI data: Approaches to acquisition and analysis', *NeuroImage*, 154, pp. 255–266. doi: 10.1016/j.neuroimage.2016.09.065.

Eippert, F., Kong, Y., Winkler, A. M., Andersson, J. L., Finsterbusch, J., Büchel, C., Brooks, J. C. W. and Tracey, I. (2017b) 'Investigating resting-state functional connectivity in the cervical spinal cord at 3T.', *NeuroImage*, 147, pp. 589–601. doi: 10.1016/j.neuroimage.2016.12.072.

Eippert, F. and Tracey, I. (2014) 'The spinal cord is never at rest', *eLife*, 2014(3). doi: 10.7554/eLife.03811.

Eklund, A., Nichols, T. E. and Knutsson, H. (2016) 'Cluster failure: Why fMRI inferences for spatial extent have inflated false-positive rates.', *Proceedings of the National Academy of Sciences of the United States of America*, 113(28), pp. 7900–5. doi: 10.1073/pnas.1602413113.

- Ellingson, B. M. and Cohen-Adad, J. (2014) 'Chapter 3.1 - Diffusion-Weighted Imaging of the Spinal Cord', in Cohen-Adad, J. and Wheeler-Kingshott, C. A. M. B. T.-Q. M. R. I. of the S. C. (eds), pp. 123–145. doi: <https://doi.org/10.1016/B978-0-12-396973-6.00009-5>.
- Ellis, M. D., Sukal, T., DeMott, T. and Dewald, J. P. A. (2007) 'Augmenting Clinical Evaluation of Hemiparetic Arm Movement With a Laboratory-Based Quantitative Measurement of Kinematics as a Function of Limb Loading', *Neurorehabilitation and Neural Repair*, 22(4), pp. 321–329. doi: 10.1177/1545968307313509.
- Enoka, R. M. (2008) *Neuromechanics of human movement*.
- Fasoli, S. E., Krebs, H. I., Stein, J., Frontera, W. R. and Hogan, N. (2003) 'Effects of robotic therapy on motor impairment and recovery in chronic stroke', *Archives of Physical Medicine and Rehabilitation*, 84(4), pp. 477–482. doi: <https://doi.org/10.1053/apmr.2003.50110>.
- Faull, O. K., Jenkinson, M., Clare, S. and Pattinson, K. T. S. (2015) 'Functional subdivision of the human periaqueductal grey in respiratory control using 7tesla fMRI', *NeuroImage*, 113, pp. 356–364. doi: 10.1016/j.neuroimage.2015.02.026.
- Feher, J. (2012) *Quantitative Human Physiology*. doi: 10.1016/b978-0-12-382163-8.00028-1.
- Feigin, V. L., Krishnamurthi, R. V., Theadom, A. M., Abajobir, A. A., Mishra, S. R., Ahmed, M. B., Abate, K. H., Mengistie, M. A., Wakayo, T., Abd-Allah, F., Abdulle, A. M., Zaki, M. E., *et al.* (2017) 'Global, regional, and national burden of neurological disorders during 1990–2015: a systematic analysis for the Global Burden of Disease Study 2015', *The Lancet Neurology*, 16(11), pp. 877–897. doi: 10.1016/S1474-4422(17)30299-5.
- Ferguson, A., Huie, J. R., Crown, E., Baumbauer, K., Hook, M., Garraway, S., Lee, K., Hoy, K. and Grau, J. (2012) 'Maladaptive spinal plasticity opposes spinal learning and recovery in spinal cord injury', *Frontiers in Physiology*, p. 399.
- Ferreira, M., Emi, M., Chaves, A., Ma, F., Oliveira, C., Maria, A., Bruno, C. and Vimieiro, S. (2018) 'Effectiveness of robot therapy on body function and structure in people with limited upper limb function: A systematic review and meta-analysis (PloS one (2018) 13 7 (e0200330))', *PloS one*, 13(11), p. e0207962. doi: 10.1371/journal.pone.0207962.
- Feys, H., De Weerd, W., Verbeke, G., Steck, G. C., Capiu, C., Kiekens, C., Dejaeger, E., Van Hoydonck, G., Vermeersch, G. and Cras, P. (2004) 'Early and repetitive stimulation of the arm can substantially improve the long-term outcome after stroke: a 5-year follow-up study of a randomized trial.', *Stroke; a journal of cerebral circulation*, 35(4), pp. 924–9. doi: 10.1161/01.STR.0000121645.44752.f7.
- Figley, C. R., Yau, D. and Stroman, P. W. (2008) 'Attenuation of lower-thoracic, lumbar, and sacral spinal cord motion: Implications for imaging human spinal cord structure and function', *American Journal of Neuroradiology*, 29(8), pp. 1450–1454. doi: 10.3174/ajnr.A1154.
- Filippi, M., Bar-Or, A., Piehl, F., Preziosa, P., Solari, A., Vukusic, S. and Rocca, M. A. (2018) 'Multiple sclerosis', *Nature Reviews Disease Primers*, 4(1), p. 43. doi: 10.1038/s41572-018-0041-4.
- Finnigan, S. and van Putten, M. J. A. M. (2013) 'EEG in ischaemic stroke: Quantitative EEG can uniquely inform (sub-)acute prognoses and clinical management', *Clinical Neurophysiology*, 124(1), pp. 10–19. doi: <https://doi.org/10.1016/j.clinph.2012.07.003>.
- Finsterbusch, J. (2012) 'Improving the performance of diffusion-weighted inner field-of-view echo-planar imaging based on 2D-Selective radiofrequency excitations by tilting the excitation plane', *Journal of Magnetic Resonance Imaging*, 35(4), pp. 984–992. doi: 10.1002/jmri.23522.
- Finsterbusch, J. (2013) 'Functional neuroimaging of inner fields-of-view with 2D-selective RF excitations', *Magnetic Resonance Imaging*, 31(7), pp. 1228–1235. doi: 10.1016/j.mri.2013.03.005.

Finsterbusch, J. (2014) 'Chapter 2.2 - B0 Inhomogeneity and Shimming', in Cohen-Adad, J. and Wheeler-Kingshott, C. A. M. B. T.-Q. M. R. I. of the S. C. (eds), pp. 68–90. doi: <https://doi.org/10.1016/B978-0-12-396973-6.00006-X>.

Finsterbusch, J., Eippert, F. and Büchel, C. (2012) 'Single, slice-specific z-shim gradient pulses improve T2*-weighted imaging of the spinal cord.', *NeuroImage*, 59(3), pp. 2307–15. doi: 10.1016/j.neuroimage.2011.09.038.

Finsterbusch, J., Sprenger, C. and Büchel, C. (2013) 'Combined T2*-weighted measurements of the human brain and cervical spinal cord with a dynamic shim update.', *NeuroImage*, 79, pp. 153–61. doi: 10.1016/j.neuroimage.2013.04.021.

Floyer-Lea, A. and Matthews, P. M. (2005) 'Distinguishable Brain Activation Networks for Short- and Long-Term Motor Skill Learning', *Journal of Neurophysiology*, 94(1), pp. 512–518. doi: 10.1152/jn.00717.2004.

Fonov, V. S., Le Troter, A., Taso, M., De Leener, B., Lévêque, G., Benhamou, M., Sdika, M., Benali, H., Pradat, P.-F., Collins, D. L., Callot, V. and Cohen-Adad, J. (2014) 'Framework for integrated MRI average of the spinal cord white and gray matter: The MNI-Poly-AMU template', *NeuroImage*, 102, pp. 817–827. doi: <https://doi.org/10.1016/j.neuroimage.2014.08.057>.

Fouad, K. and Tse, A. (2008) 'Adaptive changes in the injured spinal cord and their role in promoting functional recovery', *Neurological Research*, 30(1), pp. 17–27. doi: 10.1179/016164107X251781.

Fox, M. D. and Greicius, M. (2010) 'Clinical applications of resting state functional connectivity', *Frontiers in systems neuroscience*, 4, p. 19. doi: 10.3389/fnsys.2010.00019.

Fox, M. D. and Raichle, M. E. (2007) 'Spontaneous fluctuations in brain activity observed with functional magnetic resonance imaging', *Nature Reviews Neuroscience*, 8(9), pp. 700–711. doi: 10.1038/nrn2201.

Fratini, M., Moraschi, M., Maraviglia, B. and Giove, F. (2014) 'On the impact of physiological noise in spinal cord functional MRI', *Journal of Magnetic Resonance Imaging*, 40(4), pp. 770–777. doi: 10.1002/jmri.24467.

Friesen, W. O. and Cang, J. (2001) 'Sensory and central mechanisms control intersegmental coordination', *Current Opinion in Neurobiology*, 11(6), pp. 678–683. doi: 10.1016/S0959-4388(01)00268-9.

Frisoli, A. (2018) 'Chapter 6 - Exoskeletons for upper limb rehabilitation', in Colombo, R. and Sanguineti, V. B. T.-R. R. (eds), pp. 75–87. doi: <https://doi.org/10.1016/B978-0-12-811995-2.00006-0>.

Friston, K. J., Frith, C. D., Liddle, P. F. and Frackowiak, R. S. J. (1993) 'Functional Connectivity: The Principal-Component Analysis of Large (PET) Data Sets', *Journal of Cerebral Blood Flow and Metabolism*, 13(1), pp. 5–14.

Friston, K. J., Holmes, A. P., Poline, J.-B., Grasby, P. J., Williams, S. C. R., Frackowiak, R. S. J. and Turner, R. (1995) 'Analysis of fMRI Time-Series Revisited', *NeuroImage*, 2(1), pp. 45–53. doi: <https://doi.org/10.1006/nimg.1995.1007>.

Friston, K. J., Williams, S., Howard, R. and Frackowiak, R. S. J. (1996) 'Movement-Related Effects in fMRI Time-Series', *Magnetic resonance in medicine*, 35, pp. 346–355.

Fugl-Meyer, A. R., Jääskö, L., Leyman, I., Olsson, S. and Steglind, S. (1975) 'The post-stroke hemiplegic patient. 1. a method for evaluation of physical performance.', *Scandinavian Journal of Rehabilitation Medicine*, pp. 13–31. doi: 10.1038/35081184.

Ganesh, G., Minamoto, T. and Haruno, M. (2019) 'Activity in the dorsal ACC causes deterioration of sequential motor performance due to anxiety', *Nature Communications*, 10(1), p. 4287. doi:

10.1038/s41467-019-12205-6.

Gawryluk, J. R., Mazerolle, E. L. and D'Arcy, R. C. N. (2014) 'Does functional MRI detect activation in white matter? A review of emerging evidence, issues, and future directions', *Frontiers in Neuroscience*, 8(8 JUL), pp. 1–12. doi: 10.3389/fnins.2014.00239.

Geuter, S. and Büchel, C. (2013) 'Facilitation of pain in the human spinal cord by placebo treatment', *Journal of Neuroscience*, 33(34), pp. 13784–13790. doi: 10.1523/JNEUROSCI.2191-13.2013.

Giang, C., Pirondini, E., Kinany, N., Pierella, C., Panarese, A., Coscia, M., Miehlbradt, J., Magnin, C., Nicolo, P., Guggisberg, A. and Micera, S. (2020) 'Motor improvement estimation and task adaptation for personalized robot-aided therapy: a feasibility study', *BioMedical Engineering OnLine*, 19(1), p. 33. doi: 10.1186/s12938-020-00779-y.

Giove, F., Garreffa, G., Giulietti, G., Mangia, S., Colonnese, C. and Maraviglia, B. (2004) 'Issues about the fMRI of the human spinal cord.', *Magnetic resonance imaging*, 22(10), pp. 1505–16. doi: 10.1016/j.mri.2004.10.015.

Giszter, S. F. (2015) 'Motor primitives-new data and future questions', *Current Opinion in Neurobiology*, 33, pp. 156–165. doi: 10.1016/j.conb.2015.04.004.

Giszter, S., Hart, C. and Udoekwere, U. (2012) 'The Role of Spinal Cord in Motor Control: reflexes, patterning and final motor production', *ACNR*, 12(1), pp. 25–29.

Giulietti, G., Giove, F., Garreffa, G., Colonnese, C., Mangia, S. and Maraviglia, B. (2008) 'Characterization of the functional response in the human spinal cord: Impulse-response function and linearity.', *NeuroImage*, 42(2), pp. 626–34. doi: 10.1016/j.neuroimage.2008.05.006.

Glover, G. H., Li, T. Q. and Ress, D. (2000a) 'Image-based method for retrospective correction of physiological motion effects in fMRI: RETROICOR', *Magnetic Resonance in Medicine*, 44(1), pp. 162–167.

Glover, G. H., Li, T. and Ress, D. (2000b) 'Image-Based Method for Retrospective Correction of Physiological Motion Effects in fMRI: RETROICOR', *Magnetic resonance in medicine*, 44(March), pp. 162–167.

Goldvasser, D., McGibbon, C. A. and Krebs, D. E. (2001) 'High curvature and jerk analyses of arm ataxia', *Biological Cybernetics*, 84(2), pp. 85–90. doi: 10.1007/s004220000201.

Gore, J. C., Li, M., Gao, Y., Wu, T. L., Schilling, K. G., Huang, Y., Mishra, A., Newton, A. T., Rogers, B. P., Chen, L. M., Anderson, A. W. and Ding, Z. (2019) 'Functional MRI and resting state connectivity in white matter - a mini-review', *Magnetic Resonance Imaging*, 63(July), pp. 1–11. doi: 10.1016/j.mri.2019.07.017.

Gorelick, P. B. (2019) 'The global burden of stroke: persistent and disabling', *The Lancet Neurology*, 18(5), pp. 417–418. doi: 10.1016/S1474-4422(19)30030-4.

Govers, N., Béghin, J., Van Goethem, J. W. M., Michiels, J., Hauwe, L., Vandervliet, E. and Parizel, P. M. (2007) 'Functional MRI of the cervical spinal cord on 1.5 T with fingertapping: To what extent is it feasible?', *Neuroradiology*, 49(1), pp. 73–81. doi: 10.1007/s00234-006-0162-4.

Grasso, R., Ivanenko, Y. P., Zago, M., Molinari, M., Scivoletto, G., Castellano, V., Macellari, V. and Lacquaniti, F. (2004) 'Distributed plasticity of locomotor pattern generators in spinal cord injured patients.', *Brain: a journal of neurology*, 127(Pt 5), pp. 1019–34. doi: 10.1093/brain/awh115.

Grau, J. W. (2014) 'Learning from the spinal cord: how the study of spinal cord plasticity informs our view of learning', *Neurobiology of learning and memory*. 2013/08/20, 108, pp. 155–171. doi: 10.1016/j.nlm.2013.08.003.

Greenberg, S. A. (2003) 'The History of Dermatome Mapping', *Archives of Neurology*, 60(1), pp. 126–131.

doi: 10.1001/archneur.60.1.126.

Grefkes, C. and Fink, G. R. (2014) 'Connectivity-based approaches in stroke and recovery of function', *The Lancet Neurology*, 13(2), pp. 206–216. doi: 10.1016/S1474-4422(13)70264-3.

Greicius, M. D., Krasnow, B., Reiss, A. L. and Menon, V. (2003) 'Functional connectivity in the resting brain: A network analysis of the default mode hypothesis', *Proceedings of the National Academy of Sciences of the United States of America*, 100(1), pp. 253–258. doi: 10.1073/pnas.0135058100.

Grimm, F., Naros, G. and Gharabaghi, A. (2016) 'Closed-loop task difficulty adaptation during virtual reality reach-to-grasp training assisted with an exoskeleton for stroke rehabilitation', *Frontiers in Neuroscience*, 10(NOV), pp. 1–13. doi: 10.3389/fnins.2016.00518.

Guadagnoli, M. A. and Lee, T. D. (2004) 'Challenge Point: A Framework for Conceptualizing the Effects of Various Practice Conditions in Motor Learning', *Journal of Motor Behavior*, 36(2), pp. 212–224. doi: 10.3200/JMBR.36.2.212-224.

Guertin, P. A. and Steuer, I. (2009) 'Key central pattern generators of the spinal cord', *Journal of Neuroscience Research*, 87(11), pp. 2399–2405. doi: 10.1002/jnr.22067.

Guggisberg, A. G., Koch, P. J., Hummel, F. C. and Buetefisch, C. M. (2019) 'Brain networks and their relevance for stroke rehabilitation', *Clinical Neurophysiology*, 130(7), pp. 1098–1124. doi: <https://doi.org/10.1016/j.clinph.2019.04.004>.

Handwerker, D. A., Ollinger, J. M. and D'Esposito, M. (2004) 'Variation of BOLD hemodynamic responses across subjects and brain regions and their effects on statistical analyses', *NeuroImage*, 21(4), pp. 1639–1651. doi: 10.1016/j.neuroimage.2003.11.029.

Hardwick, R. M., Rottschy, C., Miall, R. C. and Eickhoff, S. B. (2013) 'A quantitative meta-analysis and review of motor learning in the human brain', *NeuroImage*, 67, pp. 283–297. doi: <https://doi.org/10.1016/j.neuroimage.2012.11.020>.

Harel, N. Y. and Strittmatter, S. M. (2008) 'Functional MRI and other non-invasive imaging technologies: Providing visual biomarkers for spinal cord structure and function after injury', *Experimental Neurology*, 211(2), pp. 324–328. doi: <https://doi.org/10.1016/j.expneurol.2008.02.017>.

Harita, S., Ioachim, G., Powers, J. and Stroman, P. W. (2019) 'Investigation of Resting-State BOLD Networks in the Human Brainstem and Spinal Cord', *Neuroscience*, 404, pp. 71–81. doi: <https://doi.org/10.1016/j.neuroscience.2019.02.009>.

Harris, C. S. (1965) 'Perceptual adaptation to inverted, reversed, and displaced vision.', *Psychological Review*, 72(6), pp. 419–444. doi: 10.1037/h0022616.

Harrison, J. K., McArthur, K. S. and Quinn, T. J. (2013) 'Assessment scales in stroke: Clinimetric and clinical considerations', *Clinical Interventions in Aging*, 8, pp. 201–211. doi: 10.2147/CIA.S32405.

Harvey, A. K., Pattinson, K. T. S., Brooks, J. C. W., Mayhew, S. D., Jenkinson, M. and Wise, R. G. (2008) 'Brainstem functional magnetic resonance imaging: Disentangling signal from physiological noise', *Journal of Magnetic Resonance Imaging*, 28(6), pp. 1337–1344. doi: 10.1002/jmri.21623.

Hermens, H. J., Freriks, B., Disselhorst-Klug, C. and Rau, G. (2000) 'Development of recommendations for SEMG sensors and sensor placement procedures', *Journal of Electromyography and Kinesiology*, 10(5), pp. 361–374. doi: [https://doi.org/10.1016/S1050-6411\(00\)00027-4](https://doi.org/10.1016/S1050-6411(00)00027-4).

Van Den Heuvel, M. P. and Hulshoff Pol, H. E. (2010) 'Exploring the brain network: A review on resting-state fMRI functional connectivity', *European Neuropsychopharmacology*, 20(8), pp. 519–534. doi: 10.1016/j.euroneuro.2010.03.008.

- Huang, Y., Bailey, S. K., Wang, P., Cutting, L. E., Gore, J. C. and Ding, Z. (2018) 'Voxel-wise detection of functional networks in white matter', *NeuroImage*, 183(February), pp. 544–552. doi: 10.1016/j.neuroimage.2018.08.049.
- Hummel, F. C. and Cohen, L. G. (2006) 'Non-invasive brain stimulation: a new strategy to improve neurorehabilitation after stroke?', *The Lancet Neurology*, 5(8), pp. 708–712.
- Hutchison, R. M., Womelsdorf, T., Allen, E. A., Bandettini, P. A., Calhoun, V. D., Corbetta, M., Della Penna, S., Duyn, J. H., Glover, G. H., Gonzalez-Castillo, J., Handwerker, D. A., Keilholz, S., Kiviniemi, V., Leopold, D. A., de Pasquale, F., Sporns, O., Walter, M. and Chang, C. (2013) 'Dynamic functional connectivity: Promise, issues, and interpretations', *NeuroImage*, 80, pp. 360–378. doi: <https://doi.org/10.1016/j.neuroimage.2013.05.079>.
- Islam, H., Law, C. S. W., Weber, K. A., Mackey, S. C. and Glover, G. H. (2018) 'Dynamic per slice Shimming for Simultaneous Brain and Spinal Cord fMRI', *Magnetic Resonance in Medicine*, (May 2018), pp. 825–838. doi: 10.1002/mrm.27388.
- Ivanenko, Y. P., Cappellini, G., Poppele, R. E. and Lacquaniti, F. (2008) 'Spatiotemporal organization of alpha-motoneuron activity in the human spinal cord during different gaits and gait transitions.', *The European journal of neuroscience*, 27(12), pp. 3351–68. doi: 10.1111/j.1460-9568.2008.06289.x.
- Ivanenko, Y. P., Dominici, N., Cappellini, G., Di Paolo, A., Giannini, C., Poppele, R. E. and Lacquaniti, F. (2013) 'Changes in the Spinal Segmental Motor Output for Stepping during Development from Infant to Adult', *Journal of Neuroscience*, 33(7), pp. 3025–3036. doi: 10.1523/JNEUROSCI.2722-12.2013.
- Ivanenko, Y. P., Poppele, R. E. and Lacquaniti, F. (2004) 'Five basic muscle activation patterns account for muscle activity during human locomotion', *The Journal of Physiology*, 556(1), pp. 267–282. doi: 10.1113/jphysiol.2003.057174.
- Ivanenko, Y. P., Poppele, R. E. and Lacquaniti, F. (2006) 'Spinal Cord Maps of Spatiotemporal Alpha-Motoneuron Activation in Humans Walking at Different Speeds', *Journal of Neurophysiology*, 95, pp. 602–618. doi: 10.1152/jn.00767.2005.
- Jankowska, E. (2008) 'Spinal interneuronal networks in the cat: Elementary components', *Brain Research Reviews*, 57(1), pp. 46–55. doi: 10.1016/j.brainresrev.2007.06.022.
- Jenkinson, M., Bannister, P., Brady, M. and Smith, S. (2002) 'Improved Optimization for the Robust and Accurate Linear Registration and Motion Correction of Brain Images Improved Optimization for the Robust and Accurate Linear Registration and Motion Correction of Brain Images', *NeuroImage*, 17(2), pp. 825–841. doi: 10.1006/nimg.2002.1132.
- Jenkinson, M., Beckmann, C. F., Behrens, T. E. J., Woolrich, M. W. and Smith, S. M. (2012) 'FSL', *NeuroImage*, 62(2), pp. 782–90. doi: 10.1016/j.neuroimage.2011.09.015.
- Jochimsen, T. H., Norris, D. G. and Möller, H. E. (2005) 'Is there a change in water proton density associated with functional magnetic resonance imaging?', *Magnetic resonance in medicine*, 53(2), pp. 470–3. doi: 10.1002/mrm.20351.
- Jörntell, H. (2016) 'Synergy Control in Subcortical Circuitry: Insights from Neurophysiology', in *Human and Robot Hands*.
- Kan, P., Huq, R., Hoey, J., Goetschalckx, R. and Mihailidis, A. (2011) 'The development of an adaptive upper-limb stroke rehabilitation robotic system', *Journal of NeuroEngineering and Rehabilitation*, 8(1), p. 33. doi: 10.1186/1743-0003-8-33.
- Karahanoğlu, F. I., Caballero-Gaudes, C., Lazeyras, F. and Van De Ville, D. (2013) 'Total activation: FMRI deconvolution through spatio-temporal regularization', *NeuroImage*, 73, pp. 121–134. doi: 10.1016/j.neuroimage.2013.01.067.

Karahanoğlu, F. I. and Van De Ville, D. (2015) 'Transient brain activity disentangles fMRI resting-state dynamics in terms of spatially and temporally overlapping networks', *Nature Communications*, 6. doi: 10.1038/ncomms8751.

Karbasforoushan, H., Cohen-Adad, J. and Dewald, J. P. A. (2019) 'Brainstem and spinal cord MRI identifies altered sensorimotor pathways post-stroke', *Nature Communications*, 10(1), pp. 1–7. doi: 10.1038/s41467-019-11244-3.

Katan, M. and Luft, A. (2018) 'Global Burden of Stroke', *Seminars in Neurology*, 38(2), pp. 208–211. doi: 10.1055/s-0038-1649503.

Kavounoudias, A., Roll, J. P., Anton, J. L., Nazarian, B., Roth, M. and Roll, R. (2008) 'Proprio-tactile integration for kinesthetic perception: An fMRI study', *Neuropsychologia*, 46(2), pp. 567–575. doi: <https://doi.org/10.1016/j.neuropsychologia.2007.10.002>.

Kendall, F. P., McCreary, E. K., Provance, P. G., Rodgers, M. M., Romani, W. A. (2005) *Muscles: Testing and Function with Posture and Pain*. 5th edn.

Kendall, F., McCreary, E. and Provance, P. (2005) *Muscles testing and function with posture and pain*. 5th edn.

Kibleur, P., Tata, S. R., Greiner, N., Conti, S., Barra, B., Zhuang, K., Kaeser, M., Ijspeert, A. and Capogrosso, M. (2019) 'Spatiotemporal Maps of Proprioceptive Inputs to the Cervical Spinal Cord During Three-Dimensional Reaching and Grasping', *bioRxiv*, p. 790816. doi: 10.1101/790816.

Kieliba, P., Tropea, P., Pirondini, E., Coscia, M., Micera, S. and Artoni, F. (2018) 'How are Muscle Synergies Affected by Electromyography Pre-Processing?', *IEEE Transactions on Neural Systems and Rehabilitation Engineering*, 26(4), pp. 882–893. doi: 10.1109/TNSRE.2018.2810859.

Kinany, N., Pirondini, E., Martuzzi, R., Mattera, L., Micera, S. and Van de Ville, D. (2019) 'Functional imaging of rostrocaudal spinal activity during upper limb motor tasks', *NeuroImage*, 200(May), pp. 590–600. doi: 10.1016/j.neuroimage.2019.05.036.

Kinany, N., Pirondini, E., Micera, Silvestro and Van De Ville, D. (2020) 'Dynamic functional connectivity of resting-state spinal cord fMRI reveals fine-grained intrinsic architecture', *Neuron*.

Klamroth-Marganska, V., Blanco, J., Campen, K., Curt, A., Dietz, V., Ettlin, T., Felder, M., Fellinghauer, B., Guidali, M., Kollmar, A., Luft, A., Nef, T., Schuster-Amft, C., Stahel, W. and Riener, R. (2014) 'Three-dimensional, task-specific robot therapy of the arm after stroke: A multicentre, parallel-group randomised trial', *The Lancet Neurology*, 13(2), pp. 159–166. doi: 10.1016/S1474-4422(13)70305-3.

Knikou, M. (2008) 'The H-reflex as a probe: Pathways and pitfalls', *Journal of Neuroscience Methods*, 171(1), pp. 1–12. doi: 10.1016/j.jneumeth.2008.02.012.

Koch, S. C. (2019) 'Motor task-selective spinal sensorimotor interneurons in mammalian circuits', *Current Opinion in Physiology*, 8, pp. 129–135. doi: 10.1016/j.cophys.2019.01.014.

Kong, Y., Eippert, F., Beckmann, C. F., Andersson, J., Finsterbusch, J., Büchel, C., Tracey, I. and Brooks, J. C. W. (2014) 'Intrinsically organized resting state networks in the human spinal cord.', *Proceedings of the National Academy of Sciences of the United States of America*, 111(50), pp. 18067–72. doi: 10.1073/pnas.1414293111.

Kong, Y., Jenkinson, M., Andersson, J., Tracey, I. and Brooks, J. C. W. (2012) 'Assessment of physiological noise modelling methods for functional imaging of the spinal cord', *NeuroImage*, 60(2), pp. 1538–1549.

Kornelsen, J. and Mackey, S. (2010) 'Potential Clinical Applications for Spinal Functional MRI', *Current Pain and Headache Reports*, 11(3), pp. 165–170.

- Kornelsen, J. and Stroman, P. W. (2004) 'fMRI of the Lumbar Spinal Cord During a Lower Limb Motor Task', *Magnetic resonance in medicine*, 52, pp. 411–414. doi: 10.1002/mrm.20157.
- Kornelsen, J. and Stroman, P. W. (2007) 'Detection of the neuronal activity occurring caudal to the site of spinal cord injury that is elicited during lower limb movement tasks.', *Spinal cord*, 45(7), pp. 485–90. doi: 10.1038/sj.sc.3102019.
- Krakauer, J. W. (2006) 'Motor learning: its relevance to stroke recovery and neurorehabilitation', *Current Opinion in Neurology*, 19(1), pp. 84–90. doi: 10.1097/01.wco.0000200544.29915.cc.
- Krakauer, J. W. (2007) 'Avoiding performance and task confounds: Multimodal investigation of brain reorganization after stroke rehabilitation', *Experimental Neurology*, 204(2), pp. 491–495. doi: 10.1016/j.expneurol.2006.12.026.
- Krakauer, J. W. (2009) 'Motor learning and consolidation: the case of visuomotor rotation', *Advances in experimental medicine and biology*, 629, pp. 405–421. doi: 10.1007/978-0-387-77064-2_21.
- Krebs, H. I., Krams, M., Agrafiotis, D. K., DiBernardo, A., Chavez, J. C., Littman, G. S., Yang, E., Byttebier, G., Dipietro, L., Rykman, A., McArthur, K., Hajjar, K., Lees, K. R. and Volpe, B. T. (2014) 'Robotic Measurement of Arm Movements After Stroke Establishes Biomarkers of Motor Recovery', *Stroke*, 45(1), pp. 200–204. doi: 10.1161/STROKEAHA.113.002296.
- Krebs, H. I., Palazzolo, J. J., Dipietro, L., Ferraro, M., Krol, J., Ranekleiv, K., Volpe, B. T. and Hogan, N. (2003) 'Rehabilitation robotics: Performance-based progressive robot-assisted therapy', *Autonomous Robots*, 15(1), pp. 7–20. doi: 10.1023/A:1024494031121.
- Kwakkel, G. (2006) 'Impact of intensity of practice after stroke: issues for consideration.', *Disability and rehabilitation*, 28(13–14), pp. 823–30. doi: 10.1080/09638280500534861.
- Kwakkel, G., Kollen, B. and Twisk, J. (2006) 'Impact of time on improvement of outcome after stroke', *Stroke*, 37(9), pp. 2348–2353. doi: 10.1161/01.STR.0000238594.91938.1e.
- Kwakkel, G., Van Peppen, R., Wagenaar, R. C., Dauphinee, S. W., Richards, C., Ashburn, A., Miller, K., Lincoln, N., Partridge, C., Wellwood, I. and Langhorne, P. (2004) 'Effects of augmented exercise therapy time after stroke: A meta-analysis', *Stroke*, 35(11), pp. 2529–2536. doi: 10.1161/01.STR.0000143153.76460.7d.
- Lamercy, O., Maggioni, S., Lünenburger, L., Gassert, R. and Bolliger, M. (2016) 'Robotic and Wearable Sensor Technologies for Measurements/Clinical Assessments', in *Neurorehabilitation Technology*.
- Lamers, I., Kelchtermans, S., Baert, I. and Feys, P. (2014) 'Upper Limb Assessment in Multiple Sclerosis: A Systematic Review of Outcome Measures and their Psychometric Properties', *Archives of Physical Medicine and Rehabilitation*, 95(6), pp. 1184–1200. doi: <https://doi.org/10.1016/j.apmr.2014.02.023>.
- Lang, C. E., Bland, M. D., Bailey, R. R., Schaefer, S. Y. and Birkenmeier, R. L. (2013) 'Assessment of upper extremity impairment, function, and activity after stroke: Foundations for clinical decision making', *Journal of Hand Therapy*, 26(2), pp. 104–115. doi: 10.1016/j.jht.2012.06.005.
- Langhorne, P., Bernhardt, J. and Kwakkel, G. (2011) 'Stroke rehabilitation', *The Lancet*, 377(9778), pp. 1693–1702. doi: 10.1016/S0140-6736(11)60325-5.
- Langhorne, P., Coupar, F. and Pollock, A. (2009) 'Motor recovery after stroke: a systematic review.', *Lancet neurology*, 8(8), pp. 741–54. doi: 10.1016/S1474-4422(09)70150-4.
- LaPash Daniels, C. M., Ayers, K. L., Finley, A. M., Culver, J. P. and Goldberg, M. P. (2009) 'Axon sprouting in adult mouse spinal cord after motor cortex stroke', *Neuroscience Letters*, 450(2), pp. 191–195. doi: 10.1016/j.neulet.2008.11.017.

-
- Lawrence, E. S., Coshall, C., Dundas, R., Stewart, J., Rudd, A. G., Howard, R. and Wolfe, C. D. A. (2001) 'Estimates of the Prevalence of Acute Stroke Impairments and Disability in a Multiethnic Population', *Stroke*, 32(6), pp. 1279–1284. doi: 10.1161/01.STR.32.6.1279.
- Lawrence, E. S., Coshall, C., Dundas, R., Stewart, J., Rudd, A. G., Howard, R. and Wolfe, C. D. A. (2015) 'Estimates of the Prevalence of Acute Stroke Impairments and Disability in a Multiethnic Population'.
- Lee, D. D. and Seung, H. S. (2001) 'Algorithms for Non-negative Matrix Factorization', in Leen, T. K., Dietterich, T. G., and Tresp, V. (eds) *Advances in Neural Information Processing Systems 13*, pp. 556–562. Available at: <http://papers.nips.cc/paper/1861-algorithms-for-non-negative-matrix-factorization.pdf>.
- Lee, J. Y., Oh, Y., Kim, S. S., Scheidt, R. A. and Schweighofer, N. (2016) 'Optimal Schedules in Multitask Motor Learning', *Neural Computation*, 28(4), pp. 667–685. doi: 10.1162/NECO_a_00823.
- Lee, K. B., Lim, S. H., Kim, K. H., Kim, K. J., Kim, Y. R., Chang, W. N., Yeom, J. W., Kim, Y. D. and Hwang, B. Y. (2015) 'Six-month functional recovery of stroke patients: a multi-time-point study', *International journal of rehabilitation research. Internationale Zeitschrift fur Rehabilitationsforschung. Revue internationale de recherches de readaptation*, 38(2), pp. 173–180. doi: 10.1097/MRR.0000000000000108.
- Lee, M. H., Smyser, C. D. and Shimony, J. S. (2013) 'Resting-state fMRI: a review of methods and clinical applications', *AJNR. American journal of neuroradiology*. 2012/08/30, 34(10), pp. 1866–1872. doi: 10.3174/ajnr.A3263.
- De Leener, B., Fonov, V. S., Collins, D. L., Callot, V., Stikov, N. and Cohen-Adad, J. (2018) 'PAM50: Unbiased multimodal template of the brainstem and spinal cord aligned with the ICBM152 space', *NeuroImage*, 165, pp. 170–179. doi: 10.1016/j.neuroimage.2017.10.041.
- De Leener, B., Lévy, S., Dupont, S. M., Fonov, V. S., Stikov, N., Louis Collins, D., Callot, V. and Cohen-Adad, J. (2017) 'SCT: Spinal Cord Toolbox, an open-source software for processing spinal cord MRI data.', *NeuroImage*, 145(Pt A), pp. 24–43. doi: 10.1016/j.neuroimage.2016.10.009.
- Lemon, R. N. (2008) 'Descending Pathways in Motor Control', *Annual Review of Neuroscience*, 31(1), pp. 195–218. doi: 10.1146/annurev.neuro.31.060407.125547.
- Lenzo, B., Bergamasco, M. and Salsedo, F. (2015) 'Actuating method and device for human interaction multi-joint mechanisms'.
- Leo, A., Handjaras, G., Bianchi, M., Marino, H., Gabiccini, M., Guidi, A., Scilingo, E. P., Pietrini, P., Bicchi, A., Santello, M. and Ricciardi, E. (2016) 'A synergy-based hand control is encoded in human motor cortical areas', *eLife*, 5(FEBRUARY2016), pp. 1–32. doi: 10.7554/eLife.13420.
- Levin, M. F. (1996) 'Interjoint coordination during pointing movements is disrupted in spastic hemiparesis', *Brain*, 119(1), pp. 281–293. doi: 10.1093/brain/119.1.281.
- Levine, A. J., Lewallen, K. A. and Pfaff, S. L. (2012) 'Spatial organization of cortical and spinal neurons controlling motor behavior', *Current Opinion in Neurobiology*, 22(5), pp. 812–821. doi: 10.1016/j.conb.2012.07.002.
- Lévy, S., Benhamou, M., Naaman, C., Rainville, P., Callot, V. and Cohen-Adad, J. (2015) 'White matter atlas of the human spinal cord with estimation of partial volume effect', *NeuroImage*, 119, pp. 262–271. doi: 10.1016/j.neuroimage.2015.06.040.
- Li, M., Newton, A. T., Anderson, A. W., Ding, Z. and Gore, J. C. (2019) 'Characterization of the hemodynamic response function in white matter tracts for event-related fMRI', *Nature Communications*, 10(1), pp. 1–11. doi: 10.1038/s41467-019-09076-2.
- Li, S. (2017) 'Spasticity, Motor Recovery, and Neural Plasticity after Stroke', *Frontiers in neurology*, 8, p. 120. doi: 10.3389/fneur.2017.00120.

- Li, S. and Francisco, G. E. (2015) 'New insights into the pathophysiology of post-stroke spasticity', *Frontiers in human neuroscience*, 9, p. 192. doi: 10.3389/fnhum.2015.00192.
- Liégeois, R., Li, J., Kong, R., Orban, C., Van De Ville, D., Ge, T., Sabuncu, M. R. and Yeo, B. T. T. (2019) 'Resting brain dynamics at different timescales capture distinct aspects of human behavior', *Nature Communications*, 10(1). doi: 10.1038/s41467-019-10317-7.
- Lilja, J., Endo, T., Hofstetter, C., Westman, E., Young, J., Olson, L. and Spenger, C. (2006) 'Blood oxygenation level-dependent visualization of synaptic relay stations of sensory pathways along the neuroaxis in response to graded sensory stimulation of a limb', *The Journal of neuroscience : the official journal of the Society for Neuroscience*, 26(23), pp. 6330–6336. doi: 10.1523/JNEUROSCI.0626-06.2006.
- Lillicrap, T. P., Moreno-Briseño, P., Diaz, R., Tweed, D. B., Troje, N. F. and Fernandez-Ruiz, J. (2013) 'Adapting to inversion of the visual field: A new twist on an old problem', *Experimental Brain Research*, 228(3), pp. 327–339. doi: 10.1007/s00221-013-3565-6.
- Linus, P. and Coryell, C. D. (1936) 'The Magnetic Properties and Structure of Hemoglobin, Oxyhemoglobin and Carbonmonoxyhemoglobin', *PNAS*, 22(4), pp. 210–216.
- Liu, X., Qian, W., Jin, R., Li, X., Luk, K. D., Wu, E. X. and Hu, Y. (2016a) 'Amplitude of Low Frequency Fluctuation (ALFF) in the Cervical Spinal Cord with Stenosis: A Resting State fMRI Study', *PloS one*, 11(12), pp. e0167279–e0167279. doi: 10.1371/journal.pone.0167279.
- Liu, X., Zhou, F., Li, X., Qian, W., Cui, J., Zhou, I. Y., Luk, K. D. K., Wu, E. X. and Hu, Y. (2016b) 'Organization of the intrinsic functional network in the cervical spinal cord: A resting state functional MRI study', *Neuroscience*, 336, pp. 30–38. doi: 10.1016/j.neuroscience.2016.08.042.
- Lo, A. C., Guarino, P. D., Richards, L. G., Haselkorn, J. K., Wittenberg, G. F., Federman, D. G., Ringer, R. J., Wagner, T. H., Krebs, H. I., Volpe, B. T., Bever, C. T., Bravata, D. M., Duncan, P. W., Corn, B. H., Maffucci, A. D., Nadeau, S. E., Conroy, S. S., Powell, J. M., Huang, G. D. and Peduzzi, P. (2010) 'Robot-assisted therapy for long-term upper-limb impairment after stroke', *New England Journal of Medicine*, 362(19), pp. 1772–1783. doi: 10.1056/NEJMoa0911341.
- Logothetis, N. K., Pauls, J., Augath, M., Trinath, T. and Oeltermann, A. (2001) 'Neurophysiological investigation of the basis of the fMRI signal', *Nature*, 412(6843), pp. 150–157. doi: 10.1038/35084005.
- Lohani, M., Payne, B. R. and Strayer, D. L. (2019) 'A review of psychophysiological measures to assess cognitive states in real-world driving', *Frontiers in Human Neuroscience*, 13(March), pp. 1–27. doi: 10.3389/fnhum.2019.00057.
- Lohse, K. R., Wadden, K., Boyd, L. A. and Hodges, N. J. (2014) 'Motor skill acquisition across short and long time scales: A meta-analysis of neuroimaging data', *Neuropsychologia*, 59, pp. 130–141. doi: https://doi.org/10.1016/j.neuropsychologia.2014.05.001.
- Lu, X., Miyachi, S., Ito, Y., Nambu, A. and Takada, M. (2007) 'Topographic distribution of output neurons in cerebellar nuclei and cortex to somatotopic map of primary motor cortex', *European Journal of Neuroscience*, 25(8), pp. 2374–2382. doi: 10.1111/j.1460-9568.2007.05482.x.
- Lungu, O., Frigon, A., Piché, M., Rainville, P., Rossignol, S. and Doyon, J. (2010) 'Changes in Spinal Reflex Excitability Associated With Motor Sequence Learning', *Journal of Neurophysiology*, 103(5), pp. 2675–2683. doi: 10.1152/jn.00006.2010.
- Maclean, N., Pound, P., Wolfe, C. and Rudd, A. (2000) 'Qualitative analysis of stroke patients' motivation for rehabilitation.', *Bmj*, 321(7268), pp. 1051–1054. doi: 10.1136/bmj.321.7268.1051.
- Maclean, N., Pound, P., Wolfe, C. and Rudd, A. (2002) 'The Concept of Patient Motivation: A Qualitative Analysis of Stroke Professionals' Attitudes Niall Maclean, Pandora Pound, Charles Wolfe and Anthony Rudd', pp. 444–449. doi: 10.1161/hs0202.102367.

Madi, S., Flanders, A. E., Vinitski, S., Herbison, G. J. and Nissanov, J. (2001) 'Functional MR imaging of the human cervical spinal cord.', *AJNR. American journal of neuroradiology*, 22(9), pp. 1768–1774.

Maggioni, S., Melendez-Calderon, A., van Asseldonk, E., Klamroth-Marganska, V., Lünenburger, L., Riener, R. and van der Kooij, H. (2016) 'Robot-aided assessment of lower extremity functions: a review', *Journal of NeuroEngineering and Rehabilitation*, 13(1), p. 72. doi: 10.1186/s12984-016-0180-3.

Maier, M., Ballester, B. R. and Verschure, P. F. M. J. (2019) 'Principles of Neurorehabilitation After Stroke Based on Motor Learning and Brain Plasticity Mechanisms ', *Frontiers in Systems Neuroscience* , p. 74. Available at: <https://www.frontiersin.org/article/10.3389/fnsys.2019.00074>.

Maieron, M., Iannetti, G. D., Bodurka, J., Tracey, I., Bandettini, P. A. and Porro, C. A. (2007) 'Functional Responses in the Human Spinal Cord during Willed Motor Actions: Evidence for Side- and Rate-Dependent Activity', *Journal of Neuroscience*, 27(15), pp. 4182–4190. doi: 10.1523/JNEUROSCI.3910-06.2007.

Mandal, P. K., Mahajan, R. and Dinov, I. D. (2012) 'Structural brain atlases: design, rationale, and applications in normal and pathological cohorts', *Journal of Alzheimer's disease : JAD*, 31 Suppl 3(0 3), pp. S169–S188. doi: 10.3233/JAD-2012-120412.

Manto, M., Bower, J. M., Conforto, A. B., Delgado-García, J. M., Da Guarda, S. N. F., Gerwig, M., Habas, C., Hagura, N., Ivry, R. B., Marien, P., Molinari, M., Naito, E., Nowak, D. A., Ben Taib, N. O., Pelisson, D., Tesche, C. D., Tilikete, C. and Timmann, D. (2012) 'Consensus paper: Roles of the cerebellum in motor control-the diversity of ideas on cerebellar involvement in movement', *Cerebellum*, 11(2), pp. 457–487. doi: 10.1007/s12311-011-0331-9.

Maraka, S., Jiang, Q., Jafari-Khouzani, K., Li, L., Malik, S., Hamidian, H., Zhang, T., Lu, M., Soltanian-Zadeh, H., Chopp, M. and Mitsias, P. D. (2014) 'Degree of corticospinal tract damage correlates with motor function after stroke.', *Annals of clinical and translational neurology*, 1(11), pp. 891–9. doi: 10.1002/acn3.132.

Marchal-Crespo, L. and Reinkensmeyer, D. J. (2009) 'Review of control strategies for robotic movement training after neurologic injury', *Journal of NeuroEngineering and Rehabilitation*, 6(1), p. 20. doi: 10.1186/1743-0003-6-20.

Marieb, E. N., Hoehn, K. N. (2014) *Human Anatomy & Physiology*. 9th edn.

Martin, A. R., Aleksanderek, I., Cohen-Adad, J., Tarmohamed, Z., Tetreault, L., Smith, N., Cadotte, D. W., Crawley, A., Ginsberg, H., Mikulis, D. J. and Fehlings, M. G. (2016) 'Translating state-of-the-art spinal cord MRI techniques to clinical use: A systematic review of clinical studies utilizing DTI, MT, MWF, MRS, and fMRI', *NeuroImage: Clinical*, 10, pp. 192–238. doi: 10.1016/j.nicl.2015.11.019.

Martucci, K. T., Weber, K. A. and Mackey, S. C. (2019) 'Altered Cervical Spinal Cord Resting-State Activity in Fibromyalgia', *Arthritis and Rheumatology*, 71(3), pp. 441–450. doi: 10.1002/art.40746.

Matthews, P. M., Honey, G. D. and Bullmore, E. T. (2006) 'Applications of fMRI in translational medicine and clinical practice', *Nature Reviews Neuroscience*, 7(9), pp. 732–744. doi: 10.1038/nrn1929.

McBain, R. A., Taylor, J. L., Gorman, R. B., Gandevia, S. C. and Butler, J. E. (2016) 'Human intersegmental reflexes from intercostal afferents to scalene muscles', *Experimental Physiology*, 101(10), pp. 1301–1308. doi: 10.1113/EP085907.

McPherson, J. G., Chen, A., Ellis, M. D., Yao, J., Heckman, C. J. and Dewald, J. P. A. (2018) 'Progressive recruitment of contralesional cortico-reticulospinal pathways drives motor impairment post stroke', *Journal of Physiology*, 596(7), pp. 1211–1225. doi: 10.1113/JP274968.

Metzger, J.-C., Lambercy, O., Califfi, A., Dinacci, D., Petrillo, C., Rossi, P., Conti, F. M. and Gassert, R. (2014) 'Assessment-driven selection and adaptation of exercise difficulty in robot-assisted therapy: a pilot

- study with a hand rehabilitation robot', *Journal of NeuroEngineering and Rehabilitation*, 11(1), p. 154. doi: 10.1186/1743-0003-11-154.
- Meunier, S., Kwon, J., Russmann, H., Ravindran, S., Mazzocchio, R. and Cohen, L. (2007) 'Spinal use-dependent plasticity of synaptic transmission in humans after a single cycling session', *Journal of Physiology*, 579(2), pp. 375–388. doi: 10.1113/jphysiol.2006.122911.
- Miall, R. C. (2013) 'Cortical Motor Control', in *Neuroscience in the 21st Century*, pp. 1187–1208. doi: 10.1007/978-1-4614-1997-6.
- Miall, R. C., Jenkinson, N. and Kulkarni, K. (2004) 'Adaptation to rotated visual feedback: A re-examination of motor interference', *Experimental Brain Research*, 154(2), pp. 201–210. doi: 10.1007/s00221-003-1630-2.
- Micera, S., Caleo, M., Chisari, C., Hummel, F. C. and Pedrocchi, A. (2020) 'Advanced Neurotechnologies for the Restoration of Motor Function', *Neuron*, 105(4), pp. 604–620. doi: 10.1016/j.neuron.2020.01.039.
- Michel, C. M. and Koenig, T. (2018) 'EEG microstates as a tool for studying the temporal dynamics of whole-brain neuronal networks: A review', *NeuroImage*, 180, pp. 577–593. doi: <https://doi.org/10.1016/j.neuroimage.2017.11.062>.
- Minka, T. P. (2001) 'Automatic choice of dimensionality for PCA', *Advances in Neural Information Processing Systems*.
- Moeller, S., Yacoub, E., Olman, C. A., Auerbach, E., Strupp, J., Harel, N. and Uğurbil, K. (2010) 'Multiband multislice GE-EPI at 7 tesla, with 16-fold acceleration using partial parallel imaging with application to high spatial and temporal whole-brain fMRI', *Magnetic Resonance in Medicine*, 63(5), pp. 1144–1153. doi: 10.1002/mrm.22361.
- Moffitt, M. A., Dale, B. M., Duerk, J. L. and Grill, W. M. (2005) 'Functional magnetic resonance imaging of the human lumbar spinal cord', *Journal of Magnetic Resonance Imaging*, 21(5), pp. 527–535. doi: 10.1002/jmri.20314.
- Monti, S., Tamayo, P., Mesirov, J. and Golub, T. (2003) 'Consensus Clustering: A Resampling-Based Method for Class Discovery and Visualization of Gene Expression Microarray Data', *Machine Learning*, 52(1), pp. 91–118. doi: 10.1023/A:1023949509487.
- Morishita, T. and Hummel, F. C. (2017) 'Non-invasive Brain Stimulation (NIBS) in Motor Recovery After Stroke: Concepts to Increase Efficacy', *Current Behavioral Neuroscience Reports*, 4(3), pp. 280–289. doi: 10.1007/s40473-017-0121-x.
- Moritz, C. T., Lucas, T. H., Perlmutter, S. I. and Fetz, E. E. (2007) 'Forelimb movements and muscle responses evoked by microstimulation of cervical spinal cord in sedated monkeys.', *Journal of neurophysiology*, 97(1), pp. 110–120. doi: 10.1152/jn.00414.2006.
- Mottolese, C., Richard, N., Harquel, S., Szathmari, A., Sirigu, A. and Desmurget, M. (2012) 'Mapping motor representations in the human cerebellum', *Brain*, 136(1), pp. 330–342. doi: 10.1093/brain/aws186.
- Munkres, J. (1957) 'Algorithms for the Assignment and Transportation Problems', *Journal of the Society for Industrial and Applied Mathematics*, 5(1), pp. 32–38. Available at: <http://www.jstor.org/stable/2098689>.
- Murphy, K., Bodurka, J. and Bandettini, P. A. (2007) 'How long to scan? The relationship between fMRI temporal signal to noise ratio and necessary scan duration', *NeuroImage*, 34(2), pp. 565–574. doi: <https://doi.org/10.1016/j.neuroimage.2006.09.032>.
- Murphy, M. A., Willén, C. and Sunnerhagen, K. S. (2011) 'Kinematic variables quantifying upper-extremity performance after stroke during reaching and drinking from a glass', *Neurorehabilitation and*

Neural Repair, 25(1), pp. 71–80. doi: 10.1177/1545968310370748.

Murphy, M., Resteghini, C., Feys, P. and Lamers, I. (2015) 'An overview of systematic reviews on upper extremity outcome measures after stroke', *BMC Neurology*, 15(1), p. 29. doi: 10.1186/s12883-015-0292-6.

Murphy, T. H. and Corbett, D. (2009) 'Plasticity during stroke recovery: From synapse to behaviour', *Nature Reviews Neuroscience*, 10(12), pp. 861–872. doi: 10.1038/nrn2735.

Musienko, P., van den Brand, R., Märzendorfer, O., Roy, R. R., Gerasimenko, Y., Edgerton, V. R. and Courtine, G. (2011) 'Controlling Specific Locomotor Behaviors through Multidimensional Monoaminergic Modulation of Spinal Circuitries', *The Journal of Neuroscience*, 31(25), p. 9264 LP-9278. doi: 10.1523/JNEUROSCI.5796-10.2011.

Mussa-Ivaldi, F. A., Giszter, S. F. and Bizzi, E. (1994) 'Linear combinations of primitive in vertebrate motor control', *Proceedings of the National Academy of Sciences of the United States of America*, 91(August), pp. 7534–7538.

Nathan, P. W., Smith, M. and Deacon, P. (1996) 'Vestibulospinal, reticulospinal and descending propriospinal nerve fibres in man', *Brain*, 119(6), pp. 1809–1833. doi: 10.1093/brain/119.6.1809.

Ng, M. C., Wu, E. X., Lau, H. F., Hu, Y., Lam, E. Y. and Luk, K. D. (2008) 'Cervical spinal cord BOLD fMRI study: Modulation of functional activation by dexterity of dominant and non-dominant hands', *NeuroImage*, 39(2), pp. 825–831. doi: 10.1016/j.neuroimage.2007.09.026.

Nicolo, P., Rizk, S., Magnin, C., Pietro, M. Di, Schnider, A. and Guggisberg, A. G. (2015) 'Coherent neural oscillations predict future motor and language improvement after stroke.', *Brain : a journal of neurology*, 138(Pt 10), pp. 3048–60. doi: 10.1093/brain/awv200.

Nielsen, J. B. (2016) 'Human Spinal Motor Control', *Annual Review of Neuroscience*, 39(1), pp. 81–101. doi: 10.1146/annurev-neuro-070815-013913.

Nielsen, J. B., Crone, C. and Hultborn, H. (2007) 'The spinal pathophysiology of spasticity – from a basic science point of view', *Acta Physiologica*, 189(2), pp. 171–180. doi: 10.1111/j.1748-1716.2006.01652.x.

Nielsen, J. B., Willerslev-Olsen, M., Christiansen, L., Lundbye-Jensen, J. and Lorentzen, J. (2015) 'Science-Based Neurorehabilitation: Recommendations for Neurorehabilitation From Basic Science', *Journal of Motor Behavior*, 47(1), pp. 7–17. doi: 10.1080/00222895.2014.931273.

Nielsen, J., Crone, C. and Hultborn, H. (1993) 'H-reflexes are smaller in dancers from The Royal Danish Ballet than in well-trained athletes', *European Journal of Applied Physiology and Occupational Physiology*, 66(2), pp. 116–121. doi: 10.1007/BF01427051.

Nordin, N., Xie, S. Q. and Wunsche, B. (2014) 'Assessment of movement quality in robot- assisted upper limb rehabilitation after stroke: a review.', *Journal of neuroengineering and rehabilitation*, 11, p. 137. doi: 10.1186/1743-0003-11-137.

Novak, D., Mihelj, M., Zihlerl, J., Olensek, A. and Muni, M. (2011) 'Psychophysiological measurements in a biocooperative feedback loop for upper extremity rehabilitation', *IEEE Transactions on Neural Systems and Rehabilitation Engineering*, 19(4), pp. 400–410. doi: 10.1109/TNSRE.2011.2160357.

O'Connor, E. E. and Zeffiro, T. A. (2019) 'Why is Clinical fMRI in a Resting State? ', *Frontiers in Neurology*, p. 420. Available at: <https://www.frontiersin.org/article/10.3389/fneur.2019.00420>.

Octavia, J. R. and Coninx, K. (2014) 'Adaptive Personalized Training Games for Individual and Collaborative Rehabilitation of People with Multiple Sclerosis', *BioMed Research International*.

Overduin, S. A., d'Avella, A., Carmena, J. M. and Bizzi, E. (2012) 'Microstimulation Activates a Handful of

- Muscle Synergies', *Neuron*, 76(6), pp. 1071–1077. doi: 10.1016/j.neuron.2012.10.018.
- Overduin, S. A., d'Avella, A., Roh, J., Carmena, J. M. and Bizzi, E. (2015) 'Representation of muscle synergies in the primate brain', *Journal of Neuroscience*, 35(37), pp. 12615–12624. doi: 10.1523/JNEUROSCI.4302-14.2015.
- Panarese, A., Colombo, R., Sterpi, I., Pisano, F. and Micera, S. (2012a) 'Tracking Motor Improvement at the Subtask Level During Robot-Aided Neurorehabilitation of Stroke Patients', *Neurorehabilitation and Neural Repair*, 26(7), pp. 822–833. doi: 10.1177/1545968311431966.
- Panarese, A., Colombo, R., Sterpi, I., Pisano, F. and Micera, S. (2012b) 'Tracking motor improvement at the subtask level during robot-aided neurorehabilitation of stroke patients.', *Neurorehabilitation and neural repair*, 26(7), pp. 822–33. doi: 10.1177/1545968311431966.
- Panarese, A., Pirondini, E., Tropea, P., Cesqui, B., Posteraro, F. and Micera, S. (2016) 'Model-based variables for the kinematic assessment of upper-extremity impairments in post-stroke patients', *Journal of NeuroEngineering and Rehabilitation*, 13(1), p. 81. doi: 10.1186/s12984-016-0187-9.
- Papaleo, E., Zollo, L., Spedaliere, L. and Guglielmelli, E. (2013) 'Patient-tailored adaptive robotic system for upper-limb rehabilitation', *Proceedings - IEEE International Conference on Robotics and Automation*, pp. 3860–3865. doi: 10.1109/ICRA.2013.6631120.
- Park, C., Chang, W. H., Ohn, S. H., Kim, S. T., Bang, O. Y., Pascual-leone, A. and Kim, Y. (2011) 'Connectivity During Motor Recovery After Stroke', *Stroke*, 42. doi: 10.1161/STROKEAHA.110.596155.
- Parkes, L., Fulcher, B., Yücel, M. and Fornito, A. (2018) 'An evaluation of the efficacy, reliability, and sensitivity of motion correction strategies for resting-state functional MRI', *NeuroImage*, 171, pp. 415–436. doi: <https://doi.org/10.1016/j.neuroimage.2017.12.073>.
- Parkes, L. M., Schwarzbach, J. V., Bouts, A. A., Deckers, R. H. R., Pullens, P., Kerskens, C. M. and Norris, D. G. (2005) 'Quantifying the spatial resolution of the gradient echo and spin echo BOLD response at 3 Tesla', *Magnetic resonance in medicine*, 54(6), p. 1465—1472. doi: 10.1002/mrm.20712.
- Peer, M., Nitzan, M., Bick, A. S., Levin, N. and Arzy, S. (2017) 'Evidence for functional networks within the human brain's white matter', *Journal of Neuroscience*, 37(27), pp. 6394–6407. doi: 10.1523/JNEUROSCI.3872-16.2017.
- Penhune, V. B. and Steele, C. J. (2012) 'Parallel contributions of cerebellar, striatal and M1 mechanisms to motor sequence learning', *Behavioural Brain Research*, 226(2), pp. 579–591. doi: <https://doi.org/10.1016/j.bbr.2011.09.044>.
- Pereira, F., Mitchell, T. and Botvinick, M. (2009) 'Machine learning classifiers and fMRI: a tutorial overview.', *NeuroImage*, 45(1, Suppl 1), pp. S199–S209. doi: 10.1016/j.neuroimage.2008.11.007.
- Perlbarg, V., Bellec, P., Anton, J.-L., Péligrini-Issac, M., Doyon, J. and Benali, H. (2007) 'CORSICA: correction of structured noise in fMRI by automatic identification of ICA components.', *Magnetic resonance imaging*, 25(1), pp. 35–46. doi: 10.1016/j.mri.2006.09.042.
- Piché, M., Cohen-Adad, J., Nejad, M. K., Perlbarg, V., Xie, G., Beaudoin, G., Benali, H. and Rainville, P. (2009) 'Characterization of cardiac-related noise in fMRI of the cervical spinal cord.', *Magnetic resonance imaging*, 27(3), pp. 300–10. doi: 10.1016/j.mri.2008.07.019.
- Pierella, C., Pirondini, E., Kinany, N., Coscia, M., Giang, C., Miehlbradt, J., Magnin, C., Nicolo, P., Dalise, S., Sgherri, G., Chisari, C., Van De Ville, D., Guggisberg, A. and Micera, S. (2020) 'A multimodal approach to capture post-stroke temporal dynamics of recovery', *Journal of neural engineering*, 17(4), p. 45002. doi: 10.1088/1741-2552/ab9ada.
- Pierrot-Desseilligny, E. and Burke, D. (2005) *The circuitry of the human spinal cord: its role in motor*

control and movement disorders.

Pila, O., Duret, C., Gracies, J.-M., Francisco, G. E., Bayle, N. and Hutin, É. (2018) 'Evolution of upper limb kinematics four years after subacute robot-assisted rehabilitation in stroke patients', *International Journal of Neuroscience*, 128(11), pp. 1030–1039. doi: 10.1080/00207454.2018.1461626.

Di Pino, G., Pellegrino, G., Assenza, G., Capone, F., Ferreri, F., Formica, D., Ranieri, F., Tombini, M., Ziemann, U., Rothwell, J. C. and Di Lazzaro, V. (2014) 'Modulation of brain plasticity in stroke: a novel model for neurorehabilitation', *Nature Reviews Neurology*, 10(10), pp. 597–608. doi: 10.1038/nrneurol.2014.162.

Pirondini, E., Coscia, M., Marcheschi, S., Roas, G., Salsedo, F., Frisoli, A., Bergamasco, M. and Micera, S. (2016) 'Evaluation of the effects of the Arm Light Exoskeleton on movement execution and muscle activities: a pilot study on healthy subjects.', *Journal of neuroengineering and rehabilitation*, 13, p. 9. doi: 10.1186/s12984-016-0117-x.

Pirondini, E., Coscia, M., Minguillon, J., Millán, J. del R., Van De Ville, D. and Micera, S. (2017) 'EEG topographies provide subject-specific correlates of motor control', *Scientific Reports*, 7(1), p. 13229. doi: 10.1038/s41598-017-13482-1.

Pirondini, E., Goldshuv-Ezra, N., Zinger, N., Britz, J., Soroker, N., Deouell, L. Y. and Ville, D. Van De (2020) 'Resting-state EEG topographies: Reliable and sensitive signatures of unilateral spatial neglect', *NeuroImage. Clinical*, 26, p. 102237. doi: 10.1016/j.nicl.2020.102237.

Pirondini, E., Pierella, C., Kinany, N., Coscia, M., Miehlbradt, J., Magnin, C., Nicolo, P., Guggisberg, A., Micera, S., Deouell, L. and Van De Ville, D. (2019) 'On the Potential of EEG Biomarkers to Inform Robot-Assisted Rehabilitation in Stroke Patients BT - Converging Clinical and Engineering Research on Neurorehabilitation III', in Masia, L., Micera, S., Akay, M., and Pons, J. L. (eds), pp. 956–960.

Poewe, W., Seppi, K., Tanner, C. M., Halliday, G. M., Brundin, P., Volkman, J., Schrag, A.-E. and Lang, A. E. (2017) 'Parkinson disease', *Nature Reviews Disease Primers*, 3(1), p. 17013. doi: 10.1038/nrdp.2017.13.

Poldrack, R. A., Mumford, J. A. and Nichols, T. E. (2011) *Handbook of Functional MRI Data Analysis*. doi: DOI: 10.1017/CBO9780511895029.

Poppele, R. and Bosco, G. (2003) 'Sophisticated spinal contributions to motor control', *Trends in Neurosciences*, 26(5), pp. 269–276. doi: 10.1016/S0166-2236(03)00073-0.

Power, J. D., Mitra, A., Laumann, T. O., Snyder, A. Z., Schlaggar, B. L. and Petersen, S. E. (2014) 'Methods to detect, characterize, and remove motion artifact in resting state fMRI', *NeuroImage*, 84, pp. 320–341. doi: 10.1016/j.neuroimage.2013.08.048.

Powers, J. M., Ioachim, G. and Stroman, P. W. (2018) 'Ten key insights into the use of spinal cord fmri', *Brain Sciences*, 8(9). doi: 10.3390/brainsci8090173.

Preti, M. G., Bolton, T. A. and Van De Ville, D. (2016) 'The dynamic functional connectome: State-of-the-art and perspectives.', *NeuroImage*. doi: 10.1016/j.neuroimage.2016.12.061.

Puig, J., Blasco, G., Daunis-I-Estadella, J., Thomalla, G., Castellanos, M., Figueras, J., Remollo, S., van Eendenburg, C., Sánchez-González, J., Serena, J. and Pedraza, S. (2013) 'Decreased corticospinal tract fractional anisotropy predicts long-term motor outcome after stroke.', *Stroke*, 44(7), pp. 2016–8. doi: 10.1161/STROKEAHA.111.000382.

Raffin, E. and Hummel, F. C. (2018) 'Restoring Motor Functions After Stroke: Multiple Approaches and Opportunities', *Neuroscientist*, 24(4), pp. 400–416. doi: 10.1177/1073858417737486.

Rana, M., Yani, M. S., Asavasopon, S., Fisher, B. E. and Kutch, J. J. (2015) 'Brain connectivity associated with muscle synergies in humans', *Journal of Neuroscience*, 35(44), pp. 14708–14716. doi: 10.1523/JNEUROSCI.1971-15.2015.

- Rapolienė, J., Endzelytė, E., Jasevičienė, I. and Savickas, R. (2018) 'Stroke Patients Motivation Influence on the Effectiveness of Occupational Therapy', *Rehabilitation research and practice*, 2018, p. 9367942. doi: 10.1155/2018/9367942.
- Rathelot, J.-A. and Strick, P. L. (2006) 'Muscle representation in the macaque motor cortex: An anatomical perspective', *Proceedings of the National Academy of Sciences*, 103(21), p. 8257 LP-8262. doi: 10.1073/pnas.0602933103.
- Rathelot, J.-A. and Strick, P. L. (2009) 'Subdivisions of primary motor cortex based on cortico-motoneuronal cells', *Proceedings of the National Academy of Sciences*, 106(3), p. 918 LP-923. doi: 10.1073/pnas.0808362106.
- Reggie Edgerton, V., Roy, R. R., Leon Niranjala, R. D. and Hodgson, J. A. (1997) 'Does Motor Learning Occur in the Spinal Cord?', *The Neuroscientist*, 3(5), pp. 287–294.
- Rehme, A. K. and Grefkes, C. (2013) 'Cerebral network disorders after stroke: evidence from imaging-based connectivity analyses of active and resting brain states in humans.', *The Journal of physiology*, 591(1), pp. 17–31. doi: 10.1113/jphysiol.2012.243469.
- Reinkensmeyer, D. J. and Boninger, M. L. (2012) 'Technologies and combination therapies for enhancing movement training for people with a disability.', *Journal of neuroengineering and rehabilitation*, 9(1). doi: 10.1186/1743-0003-9-17.
- Reinkensmeyer, D. J., Burdet, E., Casadio, M., Krakauer, J. W., Kwakkel, G., Lang, C. E., Swinnen, S. P., Ward, N. S. and Schweighofer, N. (2016) 'Computational neurorehabilitation: modeling plasticity and learning to predict recovery', *Journal of NeuroEngineering and Rehabilitation*, 13(1), p. 42. doi: 10.1186/s12984-016-0148-3.
- Reitmeir, R., Kilic, E., Kilic, Ü., Bacigaluppi, M., Elali, A., Salani, G., Pluchino, S., Gassmann, M. and Hermann, D. M. (2011) 'Post-acute delivery of erythropoietin induces stroke recovery by promoting perilesional tissue remodelling and contralesional pyramidal tract plasticity', *Brain*, 134(1), pp. 84–99. doi: 10.1093/brain/awq344.
- Riener, R., Nef, T. and Colombo, G. (2005) 'Robot-aided neurorehabilitation of the upper extremities', *Medical and Biological Engineering and Computing*, 43(1), pp. 2–10. doi: 10.1007/BF02345116.
- Rinne, P., Hassan, M., Fernandes, C., Han, E., Hennessy, E., Waldman, A., Sharma, P., Soto, D., Leech, R., Malhotra, P. A. and Bentley, P. (2017) 'Motor dexterity and strength depend upon integrity of the attention-control system', *Proceedings of the National Academy of Sciences*, p. 201715617. doi: 10.1073/pnas.1715617115.
- Rodgers, H., Bosomworth, H., Krebs, H. I., van Wijck, F., Howel, D., Wilson, N., Aird, L., Alvarado, N., Andole, S., Cohen, D. L., Dawson, J., Fernandez-Garcia, C., Finch, T., Ford, G. A., Francis, R., Hogg, S., Hughes, N., Price, C. I., Ternent, L., Turner, D. L., Vale, L., Wilkes, S. and Shaw, L. (2019) 'Robot assisted training for the upper limb after stroke (RATULS): a multicentre randomised controlled trial', *The Lancet*, 394(10192), pp. 51–62. doi: 10.1016/S0140-6736(19)31055-4.
- Rodriguez Guerrero, C., Fraile Marinero, J., Perez Turiel, J. and Rivera Farina, P. (2010) 'Bio cooperative robotic platform for motor function recovery of the upper limb after stroke', *2010 Annual International Conference of the IEEE Engineering in Medicine and Biology Society, EMBC'10*, pp. 4472–4475. doi: 10.1109/IEMBS.2010.5626052.
- Roh, J., Rymer, W. Z., Perreault, E. J., Yoo, S. B. and Beer, R. F. (2013) 'Alterations in upper limb muscle synergy structure in chronic stroke survivors.', *Journal of neurophysiology*, 109(3), pp. 768–81. doi: 10.1152/jn.00670.2012.
- Romanes, G. J. (1964) 'The Motor Pools of the Spinal Cord', *Progress in brain research*, 11, pp. 93–119.

Rosenthal, O., Wing, A. M., Wyatt, J. L., Punt, D., Brownless, B., Ko-Ko, C. and Miall, R. C. (2019) 'Boosting robot-assisted rehabilitation of stroke hemiparesis by individualized selection of upper limb movements - A pilot study', *Journal of NeuroEngineering and Rehabilitation*, 16(1), pp. 1–14. doi: 10.1186/s12984-019-0513-0.

Rossini, P. M., Calautti, C., Pauri, F. and Baron, J. (2003) 'Post-stroke plastic reorganisation in the adult brain', *The LANCET Neurology*, 2, pp. 493–502.

Sadaka-stephan, A., Pirondini, E. and Coscia, M. (2015) 'Influence of trajectory and speed profile on muscle organization during robot-aided training', *IEEE International Conference on Rehabilitation Robotics*, pp. 241–246.

Sadaka-Stephan, A., Pirondini, E., Coscia, M. and Micera, S. (2015) 'Influence of trajectory and speed profile on muscle organization during robot-aided training', *IEEE International Conference on Rehabilitation Robotics*, 2015–Sept, pp. 241–246. doi: 10.1109/ICORR.2015.7281206.

Saltiel, P., Wyler-Duda, K., D'Avella, A., Tresch, M. C. and Bizzi, E. (2001) 'Muscle synergies encoded within the spinal cord: Evidence from focal intraspinal NMDA iontophoresis in the frog', *Journal of Neurophysiology*, 85(2), pp. 605–619. doi: 10.1152/jn.2001.85.2.605.

Sami, S., Robertson, E. M. and Miall, R. C. (2014) 'The Time Course of Task-Specific Memory Consolidation Effects in Resting State Networks', *The Journal of Neuroscience*, 34(11), p. 3982 LP-3992. doi: 10.1523/JNEUROSCI.4341-13.2014.

Samson, R. S., Lévy, S., Schneider, T., Smith, A. K., Smith, S. A., Cohen-Adad, J. and Gandini Wheeler-Kingshott, C. A. M. (2016) 'ZOOM or Non-ZOOM? Assessing Spinal Cord Diffusion Tensor Imaging Protocols for Multi-Centre Studies', *PloS one*, 11(5), pp. e0155557–e0155557. doi: 10.1371/journal.pone.0155557.

Van de Sand, M. F., Sprenger, C. and Büchel, C. (2015) 'BOLD responses to itch in the human spinal cord', *NeuroImage*, 108, pp. 138–143. doi: 10.1016/j.neuroimage.2014.12.019.

Sandhu, M. S., Baekey, D. M., Maling, N. G., Sanchez, J. C., Reier, P. J. and Fuller, D. D. (2015) 'Midcervical neuronal discharge patterns during and following hypoxia', *Journal of Neurophysiology*, 113(7), pp. 2078–2090. doi: 10.1152/jn.00834.2014.

Sangari, S., Lundell, H., Kirshblum, S. and Perez, M. A. (2019) 'Residual descending motor pathways influence spasticity after spinal cord injury', *Annals of Neurology*, 86(1), pp. 28–41. doi: 10.1002/ana.25505.

Sangari, S. and Perez, M. A. (2019) 'Imbalanced Corticospinal and Reticulospinal Contributions to Spasticity in Humans with Spinal Cord Injury', *The Journal of neuroscience: the official journal of the Society for Neuroscience*, 39(40), pp. 7872–7881. doi: 10.1523/JNEUROSCI.1106-19.2019.

Santello, M., Baud-Bovy, G. and Jörntell, H. (2013) 'Neural bases of hand synergies', *Frontiers in Computational Neuroscience*, 7(MAR), pp. 1–15. doi: 10.3389/fncom.2013.00023.

Santello, M., Flanders, M. and Soechting, J. F. (1998) 'Postural hand synergies for tool use.', *The Journal of neuroscience: the official journal of the Society for Neuroscience*, 18(23), pp. 10105–10115. doi: 10.1523/JNEUROSCI.18-23-10105.1998.

Saritas, E. U., Cunningham, C. H., Lee, J. H., Han, E. T. and Nishimura, D. G. (2008) 'DWI of the spinal cord with reduced FOV single-shot EPI', *Magnetic Resonance in Medicine*, 60(2), pp. 468–473. doi: 10.1002/mrm.21640.

La Scaleia, V., Ivanenko, Y. P., Zelik, K. E. and Lacquaniti, F. (2014) 'Spinal motor outputs during step-to-step transitions of diverse human gaits.', *Frontiers in human neuroscience*, 8(May), p. 305. doi: 10.3389/fnhum.2014.00305.

- Schirmer, C. M., Shils, J. L., Arle, J. E., Cosgrove, G. R., Dempsey, P. K., Tarlov, E., Kim, S., Martin, C. J., Feltz, C., Moul, M. and Magge, S. (2011) 'Heuristic map of myotomal innervation in humans using direct intraoperative nerve root stimulation: Clinical article', *Journal of Neurosurgery: Spine*, 15(1), pp. 64–70. doi: 10.3171/2011.2.SPINE1068.
- Seidler, R. D., Kwak, Y., Fling, B. W. and Bernard, J. A. (2013) 'Neurocognitive mechanisms of error-based motor learning', *Advances in experimental medicine and biology*, 782, pp. 39–60. doi: 10.1007/978-1-4614-5465-6_3.
- Shabbott, B. A. and Sainburg, R. L. (2010) 'Learning a visuomotor rotation: Simultaneous visual and proprioceptive information is crucial for visuomotor remapping', *Experimental Brain Research*, 203(1), pp. 75–87. doi: 10.1007/s00221-010-2209-3.
- Sharrard, W. J. (1964) 'The segmental innervation of the lower limb muscles in man', *Annals of the Royal College of Surgeons of England*, 35(2), pp. 106–122. Available at: <https://pubmed.ncbi.nlm.nih.gov/14180405>.
- Shirota, C., Balasubramanian, S. and Melendez-Calderon, A. (2019) 'Technology-aided assessments of sensorimotor function: current use, barriers and future directions in the view of different stakeholders', *Journal of NeuroEngineering and Rehabilitation*, 16(1), p. 53. doi: 10.1186/s12984-019-0519-7.
- Siegel, J. S., Ramsey, L. E., Snyder, A. Z., Metcalf, N. V., Chacko, R. V., Weinberger, K., Baldassarre, A., Hacker, C. D., Shulman, G. L. and Corbetta, M. (2016) 'Disruptions of network connectivity predict impairment in multiple behavioral domains after stroke', *Proceedings of the National Academy of Sciences*, 113(30), p. E4367 LP-E4376. doi: 10.1073/pnas.1521083113.
- Siemens (2012) 'TimTX TrueShape'.
- Sist, B., Fouad, K. and Winship, I. R. (2014) 'Plasticity beyond peri-infarct cortex: Spinal up regulation of structural plasticity, neurotrophins, and inflammatory cytokines during recovery from cortical stroke', *Experimental Neurology*, 252, pp. 47–56. doi: 10.1016/j.expneurol.2013.11.019.
- Smith, S. M. (2002) 'Fast robust automated brain extraction', *Human Brain Mapping*, 17(3), pp. 143–155. doi: 10.1002/hbm.10062.
- Smith, S. M., Fox, P. T., Miller, K. L., Glahn, D. C., Fox, P. M., Mackay, C. E., Filippini, N., Watkins, K. E., Toro, R., Laird, A. R. and Beckmann, C. F. (2009) 'Correspondence of the brain's functional architecture during activation and rest', *Proceedings of the National Academy of Sciences of the United States of America*, 106(31), pp. 13040–13045. doi: 10.1073/pnas.0905267106.
- Soteropoulos, D. S., Edgley, S. A. and Baker, S. N. (2013) 'Spinal commissural connections to motoneurons controlling the primate hand and wrist', *Journal of Neuroscience*, 33(23), pp. 9614–9625. doi: 10.1523/JNEUROSCI.0269-13.2013.
- Specht, K. (2020) 'Current Challenges in Translational and Clinical fMRI and Future Directions', *Frontiers in Psychiatry*, p. 924. Available at: <https://www.frontiersin.org/article/10.3389/fpsy.2019.00924>.
- Sprenger, C., Eippert, F., Finsterbusch, J., Bingel, U., Rose, M. and Büchel, C. (2012) 'Attention modulates spinal cord responses to pain.', *Current biology: CB*, 22(11), pp. 1019–22. doi: 10.1016/j.cub.2012.04.006.
- Steele, C. J. and Penhune, V. B. (2010) 'Specific Increases within Global Decreases: A Functional Magnetic Resonance Imaging Investigation of Five Days of Motor Sequence Learning', *The Journal of Neuroscience*, 30(24), p. 8332 LP-8341. doi: 10.1523/JNEUROSCI.5569-09.2010.
- Stroman, P. W. (2005) 'Magnetic Resonance Imaging of Neuronal Function in the Spinal Cord: Spinal fMRI', *Clinical Medicine and Research*, 3(3), pp. 146–156.

-
- Stroman, P. W., Kornelsen, J., Bergman, a, Krause, V., Ethans, K., Malisza, K. L. and Tomanek, B. (2004) 'Noninvasive assessment of the injured human spinal cord by means of functional magnetic resonance imaging.', *Spinal cord*, 42(2), pp. 59–66. doi: 10.1038/sj.sc.3101559.
- Stroman, P. W., Kornelsen, J., Lawrence, J. and Malisza, K. L. (2005) 'Functional magnetic resonance imaging based on SEEP contrast: response function and anatomical specificity.', *Magnetic resonance imaging*, 23(8), pp. 843–50. doi: 10.1016/j.mri.2005.07.009.
- Stroman, P. W., Krause, V., Frankenstein, U. N., Malisza, K. L. and Tomanek, B. (2001a) 'Spin-echo versus gradient-echo fMRI with short echo times', *Magnetic Resonance Imaging*, 19, pp. 827–831.
- Stroman, P. W., Krause, V., Malisza, K. L., Frankenstein, U. N. and Tomanek, B. (2001b) 'Characterization of contrast changes in functional MRI of the human spinal cord at 1.5 T', *Magnetic Resonance Imaging*, 19, pp. 833–838.
- Stroman, P. W. and Ryner, L. N. (2001) 'Functional MRI of motor and sensory activation in the human spinal cord', *Magnetic Resonance Imaging*, 19, pp. 27–32.
- Stroman, P. W., Tomanek, B., Krause, V., Frankenstein, U. N. and Malisza, K. L. (2002) 'Mapping of Neuronal Function in the Healthy and Injured Human Spinal Cord with Spinal fMRI', *NeuroImage*, 17, pp. 1854–1860. doi: 10.1006/n.
- Stroman, P. W., Wheeler-Kingshott, C., Bacon, M., Schwab, J. M., Bosma, R., Brooks, J., Cadotte, D., Carlstedt, T., Ciccarelli, O., Cohen-Adad, J., Curt, a, Evangelou, N., Fehlings, M. G., Filippi, M., Kelley, B. J., Kollias, S., Mackay, a, Porro, C. a, Smith, S., Strittmatter, S. M., Summers, P. and Tracey, I. (2014) 'The current state-of-the-art of spinal cord imaging: methods.', *NeuroImage*, 84, pp. 1070–81. doi: 10.1016/j.neuroimage.2013.04.124.
- Sukal, T. M., Ellis, M. D. and Dewald, J. P. A. (2007) 'Shoulder abduction-induced reductions in reaching work area following hemiparetic stroke: neuroscientific implications', *Experimental Brain Research*, 183(2), pp. 215–223. doi: 10.1007/s00221-007-1029-6.
- Summers, P. E., Brooks, J. C. W. and Cohen-Adad, J. (2014) 'Chapter 4.1 - Spinal Cord fMRI', in Cohen-Adad, J. and Wheeler-Kingshott, C. A. M. B. T.-Q. M. R. I. of the S. C. (eds), pp. 221–239. doi: <https://doi.org/10.1016/B978-0-12-396973-6.00015-0>.
- Summers, P. E., Iannetti, G. D. and Porro, C. A. (2010) 'Functional exploration of the human spinal cord during voluntary movement and somatosensory stimulation', *Magnetic Resonance Imaging*, 28(8), pp. 1216–1224. doi: 10.1016/j.mri.2010.05.001.
- Takei, T., Confais, J., Tomatsu, S., Oya, T. and Seki, K. (2017) 'Neural basis for hand muscle synergies in the primate spinal cord', *Proceedings of the National Academy of Sciences of the United States of America*, 114(32), pp. 8643–8648. doi: 10.1073/pnas.1704328114.
- Takei, T. and Seki, K. (2010) 'Spinal interneurons facilitate coactivation of hand muscles during a precision grip task in monkeys', *Journal of Neuroscience*, 30(50), pp. 17041–17050. doi: 10.1523/JNEUROSCI.4297-10.2010.
- Tanji, J. (2001) 'Sequential Organization of Multiple Movements: Involvement of Cortical Motor Areas', *Annual Review of Neuroscience*, 24(1), pp. 631–651. doi: 10.1146/annurev.neuro.24.1.631.
- Telgen, S., Parvin, D. and Diedrichsen, J. (2014) 'Mirror reversal and visual rotation are learned and consolidated via separate mechanisms: Recalibrating or learning de novo?', *Journal of Neuroscience*, 34(41), pp. 13768–13779. doi: 10.1523/JNEUROSCI.5306-13.2014.
- Tennant, K. A. (2014) 'Thinking outside the brain: Structural plasticity in the spinal cord promotes recovery from cortical stroke', *Experimental Neurology*, 254, pp. 195–199. doi: 10.1016/j.expneurol.2014.02.003.

- Thrane, G., Sunnerhagen, K. S., Persson, H. C., Opheim, A. and Alt Murphy, M. (2019) 'Kinematic upper extremity performance in people with near or fully recovered sensorimotor function after stroke', *Physiotherapy Theory and Practice*, 35(9), pp. 822–832. doi: 10.1080/09593985.2018.1458929.
- Ting, L. H., Chiel, H. J., Trumbower, R. D., Allen, J. L., McKay, J. L., Hackney, M. E. and Kesar, T. M. (2015) 'Neuromechanical principles underlying movement modularity and their implications for rehabilitation', *Neuron*, 86(1), pp. 38–54. doi: 10.1016/j.neuron.2015.02.042.
- Tinnermann, A., Geuter, S., Sprenger, C., Finsterbusch, J. and Büchel, C. (2017) 'Interactions between brain and spinal cord mediate value effects in placebo hyperalgesia', *Science*, 358(6359), pp. 105–108. doi: 10.1126/science.aan1221.
- Tohyama, T., Kinoshita, M., Kobayashi, K., Isa, K., Watanabe, D., Kobayashi, K., Liu, M., Isa, T. and Strick, P. L. (2017) 'Contribution of propriospinal neurons to recovery of hand dexterity after corticospinal tract lesions in monkeys', *Proceedings of the National Academy of Sciences of the United States of America*, 114(3), pp. 604–609. doi: 10.1073/pnas.1610787114.
- Tresch, M. C., Cheung, V. C. K., Avella, A. and Matthew, C. (2006) 'Matrix Factorization Algorithms for the Identification of Muscle Synergies : Evaluation on Simulated and Experimental Data Sets', *Journal of Neurophysiology*, 95, pp. 2199–2212. doi: 10.1152/jn.00222.2005.
- Triantafyllou, C., Hoge, R. D., Krueger, G., Wiggins, C. J., Potthast, A., Wiggins, G. C. and Wald, L. L. (2005) 'Comparison of physiological noise at 1.5 T, 3 T and 7 T and optimization of fMRI acquisition parameters', *NeuroImage*, 26(1), pp. 243–250. doi: <https://doi.org/10.1016/j.neuroimage.2005.01.007>.
- Trompetto, C., Marinelli, L., Mori, L., Pelosin, E., Currà, A., Molfetta, L. and Abbruzzese, G. (2014) 'Pathophysiology of spasticity: Implications for neurorehabilitation', *BioMed Research International*, 2014. doi: 10.1155/2014/354906.
- Tropea, P., Monaco, V., Coscia, M., Posteraro, F. and Micera, S. (2013) 'Effects of early and intensive neuro-rehabilitative treatment on muscle synergies in acute post-stroke patients: a pilot study', *Journal of neuroengineering and rehabilitation*, 10, p. 103. doi: 10.1186/1743-0003-10-103.
- Ueno, Y., Chopp, M., Zhang, L., Buller, B., Liu, Z., Lehman, N., Xuan Shuang, L., Zhang, Y., Roberts, C. and Zheng Gang, Z. (2012) 'Axonal Outgrowth and Dendritic Plasticity in the Cortical Peri-Infarct Area After Experimental Stroke', *Stroke*, 43(8), pp. 2221–2228. doi: 10.1161/STROKEAHA.111.646224.
- Vahdat, S., Darainy, M., Milner, T. E. and Ostry, D. J. (2011) 'Functionally Specific Changes in Resting-State Sensorimotor Networks after Motor Learning', *The Journal of Neuroscience*, 31(47), p. 16907 LP-16915. doi: 10.1523/JNEUROSCI.2737-11.2011.
- Vahdat, S., Khatibi, A., Lungu, O., Finsterbusch, J., Buchel, C., Cohen-Adad, J., Marchand-Pauvert, V. and Doyon, J. (2020) 'Resting-state brain and spinal cord networks in humans are functionally integrated', *PLoS Biology*, In Press, pp. 1–22. doi: 10.1371/journal.pbio.3000789.
- Vahdat, S., Lungu, O., Cohen-Adad, J., Marchand-Pauvert, V., Benali, H. and Doyon, J. (2015) 'Simultaneous brain–cervical cord fMRI reveals intrinsic spinal cord plasticity during motor sequence learning', *PLoS Biology*, 13(6), pp. 1–25. doi: 10.1371/journal.pbio.1002186.
- Valsasina, P., Agosta, F., Caputo, D., Stroman, P. W. and Filippi, M. (2008) 'Spinal fMRI during proprioceptive and tactile tasks in healthy subjects: activity detected using cross-correlation, general linear model and independent component analysis', *Neuroradiology*, 50(10), p. 895. doi: 10.1007/s00234-008-0420-8.
- Vannesjo, S. J., Miller, K. L., Clare, S. and Tracey, I. (2018) 'Spatiotemporal characterization of breathing-induced B0 field fluctuations in the cervical spinal cord at 7T', *NeuroImage*, 167, pp. 191–202. doi: <https://doi.org/10.1016/j.neuroimage.2017.11.031>.

Veerbeek, J. M., Langbroek-Amersfoort, A. C., van Wegen, E. E. H., Meskers, C. G. M. and Kwakkel, G. (2017) 'Effects of Robot-Assisted Therapy for the Upper Limb After Stroke', *Neurorehabilitation and Neural Repair*, 31(2), pp. 107–121. doi: 10.1177/1545968316666957.

Van De Ville, D., Britz, J. and Michel, C. M. (2010) 'EEG microstate sequences in healthy humans at rest reveal scale-free dynamics', *Proceedings of the National Academy of Sciences*, 107(42), p. 18179 LP-18184. doi: 10.1073/pnas.1007841107.

Vinh, N. X., Epps, J. and Bailey, J. (2010) 'Information theoretic measures for clusterings comparison: Variants, properties, normalization and correction for chance', *Journal of Machine Learning Research*, 11, pp. 2837–2854.

Wagner, F. B., Mignardot, J.-B., Le Goff-Mignardot, C. G., Demesmaeker, R., Komi, S., Capogrosso, M., Rowald, A., Seáñez, I., Caban, M., Pirondini, E., Vat, M., McCracken, L. A., Heimgartner, R., Fodor, I., Watrin, A., Seguin, P., Paoles, E., Van Den Keybus, K., Eberle, G., Schurch, B., Pralong, E., Becce, F., Prior, J., Buse, N., Buschman, R., Neufeld, E., Kuster, N., Carda, S., von Zitzewitz, J., Delattre, V., Denison, T., Lambert, H., Minassian, K., Bloch, J. and Courtine, G. (2018) 'Targeted neurotechnology restores walking in humans with spinal cord injury', *Nature*, 563(7729), pp. 65–71. doi: 10.1038/s41586-018-0649-2.

Wagner, T. H., Lo, A. C., Peduzzi, P., Bravata, D. M., Huang, G. D., Krebs, H. I., Ringer, R. J., Federman, D. G., Richards, L. G., Haselkorn, J. K., Wittenberg, G. F., Volpe, B. T., Bever, C. T., Duncan, P. W., Siroka, A. and Guarino, P. D. (2011) 'An economic analysis of robot-assisted therapy for long-term upper-limb impairment after stroke', *Stroke*, 42(9), pp. 2630–2632. doi: 10.1161/STROKEAHA.110.606442.

Wang, L., Yu, C., Chen, H., Qin, W., He, Y., Fan, F., Zhang, Y., Wang, M., Li, K., Zang, Y., Woodward, T. S. and Zhu, C. (2010) 'Dynamic functional reorganization of the motor execution network after stroke', *Brain : a journal of neurology*, 133, pp. 1224–1238. doi: 10.1093/brain/awq043.

Ward, N. S., Newton, J. M., Swayne, O. B. C., Lee, L., Thompson, A. J., Greenwood, R. J., Rothwell, J. C. and Frackowiak, R. S. J. (2006) 'Motor system activation after subcortical stroke depends on corticospinal system integrity', *Brain*, 129(3), pp. 809–819. doi: 10.1093/brain/awl002.

Weber, K. A., Chen, Y., Paliwal, M., Law, C. S., Hopkins, B. S., Mackey, S., Dhaher, Y., Parrish, T. B. and Smith, Z. A. (2020) 'Assessing the spatial distribution of cervical spinal cord activity during tactile stimulation of the upper extremity in humans with functional magnetic resonance imaging', *NeuroImage*, 217, p. 116905. doi: <https://doi.org/10.1016/j.neuroimage.2020.116905>.

Weber, K. A., Chen, Y., Wang, X., Kahnt, T. and Parrish, T. B. (2016a) 'Functional magnetic resonance imaging of the cervical spinal cord during thermal stimulation across consecutive runs', *NeuroImage*, 143, pp. 267–279. doi: 10.1016/j.neuroimage.2016.09.015.

Weber, K. A., Chen, Y., Wang, X., Kahnt, T. and Todd, B. P. (2016b) 'Lateralization of Cervical Spinal Cord Activity during an Isometric Upper Extremity Motor Task with Functional Magnetic Resonance Imaging', *NeuroImage*, January(125), pp. 233–243. doi: 10.1016/j.neuroimage.2015.10.014.

Weber, K. A., Sentis, A. I., Bernadel-Huey, O. N., Chen, Y., Wang, X., Parrish, T. B. and Mackey, S. (2018) 'Thermal Stimulation Alters Cervical Spinal Cord Functional Connectivity in Humans', *Neuroscience*, 369, pp. 40–50. doi: 10.1016/j.neuroscience.2017.10.035.

Weber, K., Bernadel-Huey, O., Chen, Y., Wang, X., Parrish, T. and Mackey, S. (2017) 'Advanced Spatial Smoothing Improves Detection of Cervical Spinal Cord Activity with fMRI', in *Proceedings of the Annual Meeting of the Human Brain Mapping Organization*.

Weber, L. M. and Stein, J. (2018) 'The use of robots in stroke rehabilitation: A narrative review', *NeuroRehabilitation*, 43, pp. 99–110. doi: 10.3233/NRE-172408.

Wei, P., Li, J., Gao, F., Ye, D., Zhong, Q. and Liu, S. (2010) 'Resting state networks in human cervical spinal cord observed with fMRI', *European journal of applied physiology*, 108(2), pp. 265–271. doi:

10.1007/s00421-009-1205-4.

Weiler, J., Gribble, P. L. and Pruszynski, J. A. (2019) 'Spinal stretch reflexes support efficient hand control', *Nature neuroscience*. doi: 10.1101/270116.

Welniarz, Q., Dusart, I. and Roze, E. (2017) 'The corticospinal tract: Evolution, development, and human disorders', *Developmental Neurobiology*, 77(7), pp. 810–829. doi: 10.1002/dneu.22455.

Wenderoth, N., Debaere, F., Sunaert, S. and Swinnen, S. P. (2005) 'The role of anterior cingulate cortex and precuneus in the coordination of motor behaviour', *European Journal of Neuroscience*, 22(1), pp. 235–246. doi: 10.1111/j.1460-9568.2005.04176.x.

Wenger, N., Moraud, E. M., Gandar, J., Musienko, P., Capogrosso, M., Baud, L., Le Goff, C. G., Barraud, Q., Pavlova, N., Dominici, N., Minev, I. R., Asboth, L., Hirsch, A., Duis, S., Kreider, J., Mortera, A., Haverbeck, O., Kraus, S., Schmitz, F., DiGiovanna, J., van den Brand, R., Bloch, J., Detemple, P., Lacour, S. P., Bézard, E., Micera, S. and Courtine, G. (2016) 'Spatiotemporal neuromodulation therapies engaging muscle synergies improve motor control after spinal cord injury', *Nature Medicine*, 22(2), pp. 138–145. doi: 10.1038/nm.4025.

Werner, S. and Bock, O. (2010) 'Mechanisms for visuomotor adaptation to left-right reversed vision', *Human Movement Science*, 29(2), pp. 172–178. doi: 10.1016/j.humov.2010.02.004.

Westlake, K., Hinkley, L., Bucci, N., Guggisberg, A., Findlay, A., Byl, N., Henry, R. and Nagarajan, S. (2013) 'Resting State Alpha-band Functional Connectivity and Recovery after Stroke', *Experimental Neurology*, 237(1), pp. 160–169. doi: 10.1016/j.expneurol.2012.06.020. Resting.

Wheeler-Kingshott, C. A. M., Hickman, S. J., Parker, G. J. M., Ciccarelli, O., Symms, M. R., Miller, D. H. and Barker, G. J. (2002) 'Investigating cervical spinal cord structure using axial diffusion tensor imaging', *NeuroImage*, 16(1), pp. 93–102. doi: 10.1006/nimg.2001.1022.

Wheeler-Kingshott, C. A., Stroman, P. W., Schwab, J. M., Bacon, M., Bosma, R., Brooks, J., Cadotte, D. W., Carlstedt, T., Ciccarelli, O., Cohen-Adad, J., Curt, A., Evangelou, N., Fehlings, M. G., Filippi, M., Kelley, B. J., Kollias, S., Mackay, A., Porro, C. A., Smith, S., Strittmatter, S. M., Summers, P., Thompson, A. J. and Tracey, I. (2014) 'The current state-of-the-art of spinal cord imaging: applications.', *NeuroImage*, 84, pp. 1082–93. doi: 10.1016/j.neuroimage.2013.07.014.

WHO (2008) *World Health Statistics*.

Wilterson, S. A. and Taylor, J. A. (2019) 'Implicit adaptation processes appear unable to account for learning in sensorimotor adaptation tasks', *bioRxiv*, pp. 1–29.

Winstein, C. J. and Kay, D. B. (2015) *Translating the science into practice: shaping rehabilitation practice to enhance recovery after brain damage*. 1st edn, *Progress in brain research*. 1st edn. doi: 10.1016/bs.pbr.2015.01.004.

Winstein, C. J., Wolf, S. L., Dromerick, A. W., Lane, C. J., Nelsen, M. A., Lewthwaite, R., Cen, S. Y., Azen, S. P. and Team, for the I. C. A. R. E. (ICARE) I. (2016) 'Effect of a Task-Oriented Rehabilitation Program on Upper Extremity Recovery Following Motor Stroke: The ICARE Randomized Clinical Trial', *JAMA*, 315(6), pp. 571–581. doi: 10.1001/jama.2016.0276.

Winstein, C., Lewthwaite, R., Blanton, S. R., Wolf, L. B. and Wishart, L. (2014) 'Infusing Motor Learning Research Into Neurorehabilitation Practice: A Historical Perspective With Case Exemplar From the Accelerated Skill Acquisition Program', *Journal of Neurologic Physical Therapy*, 38(3). Available at: https://journals.lww.com/jnpt/Fulltext/2014/07000/Infusing_Motor_Learning_Research_Into.8.aspx.

Wittmann, F., Lambercy, O., Gonzenbach, R. R., Van Raai, M. A., Hover, R., Held, J., Starkey, M. L., Curt, A., Luft, A. and Gassert, R. (2015) 'Assessment-driven arm therapy at home using an IMU-based virtual reality system', *IEEE International Conference on Rehabilitation Robotics*, 2015–Sept, pp. 707–712. doi:

10.1109/ICORR.2015.7281284.

Wolbrecht, E. T., Chan, V., Reinkensmeyer, D. J. and Bobrow, J. E. (2008) 'Optimizing compliant, model-based robotic assistance to promote neurorehabilitation', *IEEE Transactions on Neural Systems and Rehabilitation Engineering*, 16(3), pp. 286–297. doi: 10.1109/TNSRE.2008.918389.

Woldag, H. and Hummelsheim, H. (2002) 'Evidence-based physiotherapeutic concepts for improving arm and hand function in stroke patients', *Journal of Neurology*, 249(5), pp. 518–528. doi: 10.1007/s004150200058.

Wolpaw, J. R. (2007) 'Spinal cord plasticity in acquisition and maintenance of motor skills', *Acta Physiologica*, 189(2), pp. 155–169. doi: 10.1111/j.1748-1716.2006.01656.x.

Wolpaw, J. R. (2012) 'Harnessing neuroplasticity for clinical applications', *Brain*, 135(4), pp. 2004–2007. doi: 10.1093/brain/aws017.

Wolpaw, J. R. and Carp, J. S. (2006) 'Plasticity from muscle to brain', *Progress in Neurobiology*, 78(3), pp. 233–263. doi: <https://doi.org/10.1016/j.pneurobio.2006.03.001>.

Wolpaw, J. R. and Tennissen, A. M. (2001) 'Activity-Dependent Spinal Cord Plasticity in Health and Disease', *Annual Review of Neuroscience*, 24(1), pp. 807–843. doi: 10.1146/annurev.neuro.24.1.807.

Wolpert, D. M. and Ghahramani, Z. (2000) 'Computational principles of movement neuroscience', *Nature Neuroscience*, 3(november), pp. 1212–1217.

Woo, C.-W., Chang, L. J., Lindquist, M. A. and Wager, T. D. (2017) 'Building better biomarkers: brain models in translational neuroimaging', *Nature Neuroscience*, 20(3), pp. 365–377. doi: 10.1038/nn.4478.

Woolrich, M. (2008) 'Robust group analysis using outlier inference', *NeuroImage*, 41(2), pp. 286–301. doi: 10.1016/j.neuroimage.2008.02.042.

Woolrich, M. W., Behrens, T. E. J., Beckmann, C. F., Jenkinson, M. and Smith, S. M. (2004a) 'Multilevel linear modelling for fMRI group analysis using Bayesian inference', *NeuroImage*, 21(4), pp. 1732–1747. doi: 10.1016/j.neuroimage.2003.12.023.

Woolrich, M. W., Behrens, T. E. J. and Smith, S. M. (2004b) 'Constrained linear basis sets for HRF modelling using Variational Bayes', *NeuroImage*, 21(4), pp. 1748–1761. doi: 10.1016/j.neuroimage.2003.12.024.

Woolrich, M. W., Ripley, B. D., Brady, M. and Smith, S. M. (2001) 'Temporal autocorrelation in univariate linear modeling of fMRI data', *NeuroImage*, 14(6), pp. 1370–1386. doi: 10.1006/nimg.2001.0931.

Wu, T. L., Wang, F., Mishra, A., Wilson, G. H., Byun, N., Chen, L. M. and Gore, J. C. (2018) 'Resting-state functional connectivity in the rat cervical spinal cord at 9.4 T', *Magnetic Resonance in Medicine*, 79(5), pp. 2773–2783. doi: 10.1002/mrm.26905.

Wu, T. L., Yang, P. F., Wang, F., Shi, Z., Mishra, A., Wu, R., Chen, L. M. and Gore, J. C. (2019) 'Intrinsic functional architecture of the non-human primate spinal cord derived from fMRI and electrophysiology', *Nature Communications*, 10(1), pp. 1–10. doi: 10.1038/s41467-019-09485-3.

Wu, W., Wang, D., Wang, T. and Liu, M. (2017a) 'A personalized limb rehabilitation training system for stroke patients', *2016 IEEE International Conference on Robotics and Biomimetics, ROBIO 2016*, pp. 1924–1929. doi: 10.1109/ROBIO.2016.7866610.

Wu, X., Yang, Z., Bailey, S. K., Zhou, J., Cutting, L. E., Gore, J. C. and Ding, Z. (2017b) 'Functional connectivity and activity of white matter in somatosensory pathways under tactile stimulations', *NeuroImage*, 152(March), pp. 371–380. doi: 10.1016/j.neuroimage.2017.02.074.

- Wymbs, N. F. and Grafton, S. T. (2015) 'The Human Motor System Supports Sequence-Specific Representations over Multiple Training-Dependent Timescales', *Cerebral cortex (New York, N.Y. : 1991)*, 2014/06/26, 25(11), pp. 4213–4225. doi: 10.1093/cercor/bhu144.
- Xu, R. and Wunsch, D. (2005) 'Survey of clustering algorithms', *IEEE Transactions on Neural Networks*, 16(3), pp. 645–678. doi: 10.1109/TNN.2005.845141.
- Yakovenko, S., Mushahwar, V., Horst, V. V. A., Holstege, G., Prochazka, A. and Vanderhorst, V. (2002) 'Spatiotemporal Activation of Lumbosacral Motoneurons in the Locomotor Step Cycle', *Journal of Neurophysiology*, 87, pp. 1542–1553.
- Yeganegi, H., Fathi, Y. and Erfanian, A. (2018) 'Decoding hind limb kinematics from neuronal activity of the dorsal horn neurons using multiple level learning algorithm', *Scientific Reports*, 8(1), pp. 1–12. doi: 10.1038/s41598-017-18971-x.
- Yoshizawa, T., Nose, T., Moore, G. J. and Sillerud, L. O. (1996) 'Functional Magnetic Resonance Imaging of Motor Activation in the Human Cervical Spinal Cord', *Neuroimage*, 4(68), pp. 174–182.
- Zaharchuk, G., Saritas, E. U., Andre, J. B., Chin, C. T., Rosenberg, J., Brosnan, T. J., Shankaranarayan, A., Nishimura, D. G. and Fischbein, N. J. (2011) 'Reduced Field-of-View Diffusion Imaging of the Human Spinal Cord: Comparison with Conventional Single-Shot Echo-Planar Imaging', *American Journal of Neuroradiology*, 32(5), p. 813 LP-820. doi: 10.3174/ajnr.A2418.
- Zappasodi, F., Croce, P., Giordani, A., Assenza, G., Giannantoni, N. M., Profice, P., Granata, G., Rossini, P. M. and Tecchio, F. (2017) 'Prognostic Value of EEG Microstates in Acute Stroke', *Brain Topography*, 30(5), pp. 698–710. doi: 10.1007/s10548-017-0572-0.
- Zeiler, S. R. and Krakauer, J. W. (2013) 'The interaction between training and plasticity in the poststroke brain', *Current Opinion in Neurology*, 26(6), pp. 609–616. doi: 10.1097/WCO.0000000000000025.
- Zholudeva, L. V., Qiang, L., Marchenko, V., Dougherty, K. J., Sakiyama-Elbert, S. E. and Lane, M. A. (2018) 'The Neuroplastic and Therapeutic Potential of Spinal Interneurons in the Injured Spinal Cord', *Trends in Neurosciences*, 41(9), pp. 625–639. doi: 10.1016/j.tins.2018.06.004.
- Zhu, L., Lindenberg, R., Alexander, M. and Schlaug, G. (2011) 'Lesion load of the corticospinal tract predicts motor impairment in chronic stroke', *Stroke*, 41(5), pp. 910–915. doi: 10.1161/STROKEAHA.109.577023.Lesion.
- Zimmermann, J. B., Seki, K. and Jackson, A. (2011) 'Reanimating the arm and hand with intraspinal microstimulation.', *Journal of neural engineering*, 8(5), p. 54001. doi: 10.1088/1741-2560/8/5/054001.
- Zöllner, D. M., Bolton, T. A. W., Karahanoglu, F. I., Eliez, S., Schaer, M. and Van De Ville, D. (2018) 'Robust recovery of temporal overlap between network activity using transient-informed spatio-temporal regression', *IEEE Transactions on Medical Imaging*, 38(1), pp. 291–302. doi: 10.1109/TMI.2018.2863944.
- Zöllner, D., Sandini, C., Karahanoglu, F. I., Padula, M. C., Schaer, M., Eliez, S. and Van De Ville, D. (2019) 'Large-Scale Brain Network Dynamics Provide a Measure of Psychosis and Anxiety in 22q11.2 Deletion Syndrome', *Biological Psychiatry: Cognitive Neuroscience and Neuroimaging*, 4(10), pp. 881–892. doi: 10.1016/j.bpsc.2019.04.004.
- Zuo, X.-N. and Xing, X.-X. (2014) 'Test-retest reliabilities of resting-state FMRI measurements in human brain functional connectomics: A systems neuroscience perspective', *Neuroscience & Biobehavioral Reviews*, 45, pp. 100–118. doi: <https://doi.org/10.1016/j.neubiorev.2014.05.009>.

Nawal Kinany

Avenue Alexandre-Vinet 29, 1004 Lausanne, Switzerland
+41 78.843.31.57 | nawal.kinany@epfl.ch
30 years old (07.01.1990) | Nationality: French

EDUCATION

- 2016 → **PhD candidate in electrical engineering**, EPFL, Lausanne [CH]
2013 – 2015 **Master (MSc) in Bioengineering**, EPFL, Lausanne [CH] – GPA: 5.75/6
Minor in Neuroprosthetics
2015 **Master thesis**, Imperial College London [UK] – Grade: 6/6
2010 – 2013 **Bachelor (BSc) in Life Sciences & Technology**, EPFL, Lausanne [CH] – GPA: 5.56/6

RESEARCH EXPERIENCE

- 2016 → **Research assistant**, Translational Neuroengineering & Medical Image Processing Labs, EPFL, Geneva [CH]
• Studied the central and peripheral mechanisms of motor control and motor recovery
• Developed multimodal assessments (motion analysis, electromyography, brain/spinal cord imaging)
• Managed a multicentric (CH,IT) clinical trial to test a personalized post-stroke robot-assisted training
- 2019
mar – jun
sep – nov
2015 – 2016
oct – mar **Visiting researcher**, Montreal Neurological Institute, McGill University, Montreal [CA]
• Analyzed the dynamics of cerebral and spinal signals using data-driven multivariate approaches
- Research assistant**, Human Robotics Group, Imperial College London [UK]
• Improved the established virtual neurorehabilitation training platform
• Co-founded gripAble (www.gripable.co), a start-up developing innovative mobile technologies for functional therapy and objective measurement of upper-limb function.
- 2015
feb – aug **Student researcher**, Human Robotics Group, Imperial College London [UK]
• Programmed and tested a videogame for post-stroke technology-assisted rehabilitation
- 2015
jul – aug **Intern**, Neuroimaging Research Lab, Lausanne University Hospital [CH]
• Implemented a generalized code to display experimental design and retrieve behavioral data in fMRI studies
- 2012
jul – aug **Research scholar**, Max Planck Institute of Neurobiology, Munich [DE]
• Investigated morphological changes in interneurons using time-lapse imaging (two-photon microscopy)

AWARDS AND FELLOWSHIPS

- 2015 Prize for the **best GPA during the Master in Bioengineering**
Recipient of the **Grenier prize** (rewards a Master project particularly original in its presentation)
- 2014 Recipient of the **WISH Community Career Investment** for Master project abroad (6'000 CHF)
- 2013 Recipient of the **Debiopharm Excellence Fellowship** (10'000 CHF)

TEACHING EXPERIENCE

- 2016 – 2020 **Teaching assistant for master classes**, EPFL, Lausanne
• Image processing | Signal processing for functional brain imaging | Sensorimotor neuroprosthetics
Student supervision, four master theses and two semester projects
- 2013 – 2014 **Teaching assistant for bachelor classes**, EPFL, Lausanne
• General physics

EXTRACURRICULAR ACTIVITIES

- 2018 **Organization of a special session**, International Conference on Neurorehabilitation, Pisa, Italy
Topic: *Uncovering neural mechanisms of post-stroke recovery using clinical imaging tools.*
- 2014 **Sponsoring and communication**, for STIL, technologies and innovation exhibition at EPFL
- 2010 – 2014 **Class representative & head of the student representation** for the life sciences students
- 2010 – 2011 **Visual communication**, for Balelec Festival, the largest one-day student festival in Europe (15'000 people)

LANGUAGES

French (mother tongue), **English** (fluent), **German** (intermediate)

ORAL PRESENTATIONS

- 2018 *Brain in action, network dynamics, and spinal cord with fMRI*
Center for Neuroprosthetics Annual Research Symposium, Campus Biotech, Geneva
- 2017 *Investigating spinal cord activity using fMRI*
BBL/CIBM Research Day, Geneva University Hospital

PEER-REVIEWED JOURNAL PUBLICATIONS

- 2020 **N Kinany**, E Pirondini, S Micera*, D Van de Ville*, *Dynamic functional connectivity of resting-state spinal cord fMRI reveals fine-grained intrinsic architecture*, Neuron (2020), accepted, online publication on September 9th
- C Pierella, E Pirondini, **N Kinany**, M Coscia, C Giang, J Miehbradt, C Magnin, P Nicolo, S Dalise, G Sgherri, C Chisari, D Van De Ville, A Guggisberg, S Micera, *A multimodal approach to capture post-stroke temporal dynamics of recovery*, Journal of Neural Engineering (2020), vol. 17, art. 4
- C Giang, E Pirondini*, **N Kinany***, C Pierella*, A Panarese, M Coscia, J Miehbradt, C Magnin, P Nicolo, A Guggisberg, S Micera, *Motor improvement estimation and task adaptation for personalized robot-aided therapy: a feasibility study*, BioMedical Engineering Online (2020), vol 19, art. 33
- 2019 **N Kinany**, E Pirondini, R Martuzzi, L Mattera, S Micera*, D Van de Ville*, *Functional imaging of rostrocaudal spinal activity during upper limb motor tasks*, NeuroImage (2019), vol. 200, p. 590-600
- 2017 M Mace*, **N Kinany***, P Rinne, A Rayner, P Bentley, E Burdet, *Balancing the playing field: collaborative gaming for physical training*, Journal of NeuroEngineering and Rehabilitation (2017), vol. 14, art. 116
- S Wurth, M Capogrosso, S Raspopovic, J Gandar, G Federici, **N Kinany**, A Cutrone, A Piersigilli, N Pavlova, R Guiet, G Taverni, J Rigosa, X Navarro, G Courtine, S Micera, *Long-term usability and bio-integration of polyimide-based intra-neural stimulating electrodes*, Biomaterials (2017), vol. 122, p. 114-129

PEER-REVIEWED CONFERENCE PROCEEDINGS

- 2018 Converging Clinical and Engineering Research on Neurorehabilitation III,
4th International Conference on NeuroRehabilitation (ICNR2018), October 16-20, 2018, Pisa, Italy
Biosystems & Biorobotics, vol. 21, Springer
- N Kinany**, C Pierella, E Pirondini, M Coscia, J Miehbradt, C Magnin, P Nicolo, D Van de Ville, A Guggisberg, S Micera *Resting-state functional connectivity in stroke patients after upper limb robot-assisted therapy: a pilot study*
- J Miehbradt, C Pierella, **N Kinany**, M Coscia, E Pirondini, M Vissani, A Mazzoni, C Magnin, P Nicolo, A Guggisberg, S Micera, *Evolution of cortical asymmetry with post-stroke rehabilitation: a pilot study*
- E Pirondini, C Pierella, **N Kinany**, M Coscia, J Miehbradt, C Magnin, P Nicolo, A Guggisberg, S Micera, L Deouell, D Van De Ville, *On the potential of EEG biomarkers to inform robot-assisted rehabilitation in stroke patients*
- C Pierella, C Giang, E Pirondini, **N Kinany**, M Coscia, J Miehbradt, C Magnin, P Nicolo, A Guggisberg, S Micera, *Personalizing exoskeleton-based upper limb rehabilitation using a statistical model: a pilot study*
- M Coscia, L Pellegrino, C Pierella, E Pirondini, **N Kinany**, J Miehbradt, C Magnin, P Nicolo, P Giannoni, L Marinelli, A Guggisberg, M Casadio, S Micera, *Training muscle synergies to relearn movement: current perspectives and future trends*
- 2016 Converging Clinical and Engineering Research on Neurorehabilitation II
3rd International Conference on NeuroRehabilitation (ICNR2016), October 18-21, 2016, Segovia, Spain
Biosystems & Biorobotics, vol. 15., Springer
- M Mace, P Rinne, **N Kinany**, P Bentley, E Burdet, *Collaborative gaming to enhance patient performance during virtual therapy*

* Equally contributing authors